Title

New tools and paradigms for the analysis of sea spray aerosols by single particle mass spectrometry

Permalink

https://escholarship.org/uc/item/6hq731qk

Author

Sultana, Camille M.

Publication Date

2017

UNIVERSITY OF CALIFORNIA, SAN DIEGO

New tools and paradigms for the analysis of sea spray aerosols by single particle mass spectrometry

A dissertation submitted in partial satisfaction of the requirements for the degree Doctor of Philosophy

in

Chemistry

by

Camille Marissa Sultana

Committee in charge:

Professor Kimberly Prather, Chair
Professor Farooq Azam
Professor Francesco Paesani
Professor Michael Tauber
Professor Susan Taylor

2017

The Dissertation of Camille Marissa Sultana is approved, and is acceptable in quality and form for publication on microfilm and electronically:

Chair

University of California, San Diego

2017

DEDICATION

To Peter and Monica, my wonderful parents who have
always encouraged and believed in me.

TABLE OF CONTENTS

Signature Page.....iii

Dedication.....iv

Table of Contents.....v

List of Figures.....xii

List of Tables.....xvi

Acknowledgements.....xvii

Vita.....xxii

Abstract of The Dissertation.....xxiv

Chapter 1. Introduction..... 1

1.1 Sea Spray Aerosols..... 1

1.1.1 SSA Production Mechanism..... 1

1.1.2 SSA Chemical Composition..... 2

1.1.3 Supermicron SSA Morphology..... 5

1.2 Online Single Particle Measurement by ATOFMS..... 6

1.2.1 Instrument Description..... 6

1.2.2 Basics of Data Analysis..... 7

1.2.3 Limitations of SPMS..... 7

1.2.4 Depth Profiling of Particles with SPMS..... 10

1.3 Dissertation Objectives..... 11

1.4 Dissertation Synopsis..... 12

1.5 Acknowledgments 13

Chapter 2. FATES: a flexible analysis toolkit for the exploration of single-particle mass spectrometer data 14

2.1 Abstract 14

2.2 Introduction 14

2.3 FATES Software Description 18

2.4 FATES Data Architecture 19

2.4.1 FATES Optimization 20

2.5 Data Analysis within FATES 24

2.6 Exploration of Data Utilizing FATES GUIs 25

2.6.1 guiFATES: Spectra Visualization, Grouping, and Exploration 25

2.6.2 dendroFATES: Hierarchical Cluster Relations 29

2.6.3 scatterFATES: User Defined Particle Relations 31

2.6.4 calibFATES: Raw Spectra Calibration 32

2.7 Conclusions 34

2.8 Code Availability 34

2.9 Acknowledgements 34

2.10 Supporting Information 35

Chapter 3. Effect of Structural Heterogeneity in Chemical Composition on Online Single-Particle Mass Spectrometry Analysis of Sea Spray Aerosol Particles 37

3.1 Abstract 37

3.2 Introduction 38

3.3 Methods ... 41
  3.3.1 SSA Generation ... 41
  3.3.2 Measurement of SSA Composition via ATOFMS ... 43
  3.3.3 Analysis of Particle Mass Spectra ... 44
3.4 Results and Discussion ... 45
  3.4.1 Effect of Laser Power on Supermicron SSA Mass Spectra ... 45
  3.4.2 Relationship of Chemical Signal to Total Positive Spectrum Ion Intensity ... 47
  3.4.3 SSA Mass Spectral Consistency between Laboratory and Field Studies ... 50
  3.4.4 Contribution of Particulate Biological Components to SSA MS ... 54
  3.4.5 Interpreting mass spectra from SPMS studies of SSA ... 54
3.5 Acknowledgements ... 56
3.6 Supporting Information ... 57
  3.6.1 Method for Converting Particle Diameter ... 64
  3.6.2 Methods for Supplementary AFM Analysis ... 64

Chapter 4. Integration of offline and SPMS analyses to obtain a more complete picture of particle morphology and coordination of chemical species within model SSA particles. 66
4.1 Abstract ... 66
4.2 Introduction ... 67
4.3 Methods ... 69
  4.3.1 SSA Generation ... 69
  4.3.2 Sample Collection for Offline Analyses ... 70
  4.3.3 Online Single Particle SSA Analysis by ATOFMS ... 71

4.3.4 Offline single particle SSA analysis by AFM 79
4.3.5 Offline Carboxylate, Dicarboxylate, and Inorganic Salt Extraction and Quantification 81
4.3.6 Organic Volume Calculation from Offline Ensemble Data 82
4.4 Results and Discussion 83
4.4.1 Description of Terminology 83
4.4.2 Organic Volume Fraction: Offline Ensemble and Offline AFM Single Particle Comparison 85
4.4.3 Organic Shell Thickness: Offline Ensemble and Online SPMS Single Particle Comparison 85
4.4.4 Inorganic Signal: Offline Ensemble and Online SPMS Single Particle Comparison 89
4.4.5 Laser Desorption/ionization Processes in Carboxylate-rich Particles 94
4.5 Conclusions 102
4.6 Acknowledgements 103
Chapter 5. Expanding Single Particle Mass Spectrometer Analyses for the Identification of Microbe Signatures in Sea Spray Aerosols 104
5.1 Abstract 104
5.2 Introduction 105
5.3 Methods 106
5.3.1 MART Induced Phytoplankton Bloom and SSA Generation 106
5.3.2 Measurement of Bulk Water Biology and Characteristics 107

5.3.3 Measurement of SSA Composition via ATOFMS 108

5.3.4 Summary of Single Particle Data Analyses 108

5.4 Results and Discussion... 109

5.4.1 Description of SSA Microbial Mass Spectra (BioSS) 109

5.4.2 BioSS and Particle Size Dependence... 112

5.4.3 Dependence of SSA BioSS Signatures on Total Ion Intensity and Laser Pulse Energy113

5.4.4 Utilizing BioSS Signatures and Total Ion Intensity to Understand the Structure of Microbial Containing SSA Particles... 117

5.4.5 Influence of Seawater Chemistry on BioSS signatures 120

5.5 Conclusions 122

5.6 Acknowledgements 123

5.7 Supporting Information.. 124

Chapter 6. Microbial Control of Sea Spray Aerosol Composition: A Tale of Two Blooms 131

6.1 Abstract 131

6.2 Introduction 132

6.3 Results and Discussion.. 134

6.3.1 Overview of Mesocosm Experiment and Measurements 134

6.3.2 Impact of Mesocosm Dynamics on SSA Composition.............................. 135

6.3.3 Explaining the Differences in SSA Organic Content Between the Two Blooms 140

6.3.4 Impact of Phytoplankton Bloom on Ice Nucleation Properties 144

6.3.5 Factors Controlling SSA Composition and Climate Relevant Properties.... 145

6.4 Acknowledgements 148

6.5 Supporting Information 149

6.5.1 General Experiment Summary 153

6.5.2 Water Collection 153

6.5.3 Nutrient Addition 154

6.5.4 Wave Channel Set-up.. 154

6.5.5 Bulk Seawater Measurements 154

6.5.6 Measurement of Aerosol Size Distributions 155

6.5.7 Measurement of SSA Composition via an ATOFMS................................ 156

6.5.8 Measurement of SSA Composition via AMS 157

6.5.9 Measurement of SSA Composition via Micro-Raman Spectroscopy.......... 159

6.5.10 Measurement of INP with CSU-IS 161

6.5.11 Calculating Labile Organic Species in Seawater during the Mesocosm Experiment.. 163

Chapter 7. Biologically-mediated influences on the climate impacts of SSA 165

7.1 Abstract 165

7.2 Introduction 166

7.3 Methods.. 167

7.3.1 General Experiment Description... 167

7.3.2 ATOFMS 168

7.3.3 Additional Measurements: Hygroscopicity Experiment 171

7.3.4 Additional Measurements: Hygroscopicity Experiment 172

7.4 Results and Discussion 174

7.4.1 Hygroscopicity Studies 174

7.4.2 IN Studies 180

7.5 Conclusions 190

7.6 Acknowledgments 191

Chapter 8. Conclusions and Future Directions 193

8.1 Synopsis 193

8.2 Conclusions 193

8.2.1 New SPMS data analysis toolkit 193

8.2.2 Influence of SSA particle morphology on mass spectral signatures 194

8.2.3 Identification of microbial ion signatures in SSA populations 196

8.2.4 Influence of seawater biology and SSA chemical composition 197

8.3 Future Work 198

8.3.1 Extending FATES to offline spectroscopic single particle data sets 198

8.3.2 Chemistry at the air-particle interface of hydrated aerosols 200

8.3.3 Definitive identification of microbial cells in SSA 201

8.3.4 Semi-quantitative descriptions of SSA particle morphology 202

8.4 Acknowledgments 203

References 204

LIST OF FIGURES

Figure 2.1 Screen capture of a guiFATES window with data from 46,432 individual particles... 26

Figure 2.2 Screen capture of a dendroFATES window showing the cluster tree or dendrogram for 30 input clusters. 30

Figure 2.3 Screen capture of a scatterFATES window showing the -35 to -93 m/z ratio plotted against particle size for 166,666 particles. 32

Figure 2.4 Screenshot of a calibFATES window displaying a single particle uncalibrated mass spectrum. 33

Figure 2.5 Screen captures of a guiFATES window with the same data as in Figure 2.1 filtered and sorted in various ways. 35

Figure 2.6 guiFATES windows generated automatically from the selection of a node in Figure 2.2 (reproduced in Figure 2.6c).......... 36

Figure 3.1 The distribution of the relative sodium ion contribution to the total positive ion intensity for supermicron SSA, generated by frit bubbled seawater analyzed by ATOFMS using five different desorption/ionization laser pulse energies. 47

Figure 3.2 The distribution of total positive ion intensity grouped by the fraction of positive mass spectral sodium intensity for supermicron SSA particles. 48

Figure 3.3 The sodium ion fraction versus the relative total ion intensity for each positive mass spectrum generated by supermicron SSA from the (a) frit bubbled seawater and (b) MART (1.2 mJ laser pulse energy).......... 49

Figure 3.4 (a) The temporal trends for the fraction of ambient particles identified as SSA with sodium fractions of 0.4-1 (Na-rich) and 0-0.4 (Na-deficient) shown for two coastal field studies, CalWater2 and CIFEX. (b) Scatter plots of the number fraction of Na-deficient particles and (c) the relative mean signal from ion markers in the total aerosol population. 52

Figure 3.5 A schematic illustrating how two different particle populations could both generate a similar suite of relative mass spectra by laser desorption/ionization, the ionization method utilized by SPMS. 55

Figure 3.6 The distribution for the measured vacuum aerodynamic diameter of dry SSA particles generated during the fritted bubbler (a) and MART (b) experiments.......... 58

Figure 3.7 Average relative positive ion (a) and negative ion (b) mass spectra (with half-unit resolution) are shown for super-micrometer SSA generated by a MART and frit bubbled seawater as well as sampled during CIFEX and CalWater2 coastal field studies. 59

Figure 3.8 The distribution of total positive ion intensity for particles grouped by the fraction of positive mass spectral sodium intensity. Results are shown for supermicron SSA generated by frit bubbled seawater for all the ATOFMS laser pulse energies utilized.......... 60

Figure 3.9 The size of each particle plotted versus the total ion intensity for the positive mass spectrum generated. Results are shown for the bubbled seawater experiments with the ATOFMS operated at three laser pulse energies: 0.6 mJ, 1.05 mJ, and 1.5 mJ. 61

Figure 3.10 Scatter plot of the sulfate ion marker ($^{48}SO^-$, $^{64}SO_2^-$, $^{80}SO_3^-$) contribution to the negative total ion intensity versus the calcium ion marker ($^{40}Ca^+$, $^{57}CaOH^+$, $^{75,77}CaCl^+$, $^{96}Ca_2O^+$) for supermicron SSA. 62

Figure 3.11 Images typical of ambient SSA (a,b) and SSA generated from natural seawater utilizing MART or plunging waterfall (c-f) and fritted bubbler techniques. 63

Figure 4.1 The estimate ensemble and average single particle OVF values for each MOUDI stage, plotted at the 50% cut aerodynamic diameter of the MOUDI stage. Single particle OVF values are also plotted against their calculated d_{vol}. 85

Figure 4.2 An illustration of how ATOFMS mass spectra are descriptive of the particle morphology and organic shell thickness.. 87

Figure 4.3 Single particle total positive ion intensity versus particle size for the various experiments. 88

Figure 4.4 The number fraction of calcium-rich single particle mass spectra over the range of total positive ion intensities and (a) and the distribution of the relative positive calcium ion signal (b) for the various experiments. 92

Figure 4.5 The distribution of relative positive magnesium, potassium, and calcium ion signal for the I_{SSW} and O_{SSW} particles grouped by total positive ion intensity. 93

Figure 4.6 Total negative ion intensities for individual mass spectra plotted against total positive ion intensities for bubbled O_{SSW} (a) and atomized I_{SSW} (b) particles. The relative positive sodium ion signal (c) and negative linear carboxylate ion signal (d) are indicated by marker color, with warmer shades signifying higher relative signal for O_{SSW} particles. 96

Figure 4.7 Average of single particle Na-deficient mass spectra for bubbled O_{SSW} particles grouped by total positive ion intensity. 100

Figure 5.1 Three representative dual-polarity mass spectra illustrating the continuum of SSA ion signatures identified as BioSS. 110

Figure 5.2 Relative ion signals for BioSS with either low or high total ion intensity. Results shown are for all BioSS generated during the experiment with 1.22+-0.04 mJ laser pulse energy. 115

Figure 5.3 Distributions of relative ion signals on September 17th for BioSS generated with either low or high laser pulse energies. 116

Figure 5.4 (a) The fraction of BioSS, grouped by total ion intensity, with large *-Cl* or *+Na* relative ion signal. (b) The total ion intensity distribution of BioSS grouped by particle diameter. 118

Figure 5.5 Temporal trends of (a) chlorophyll-a (Chl-a), heterotrophic bacteria (HB), and dissolved organic carbon (DOC) concentrations in the seawater as well as (b) the fraction of particles generating BioSS. 121

Figure 5.6 The number fraction of select SSA particles over the size range of the ATOFMS: particles generating biological mass spectra (BioSS), particles with potassium and phosphate rich mass spectra that were not classified as BioSS (kPhos). 127

Figure 5.7 Two representative dual-polarity mass spectra illustrating the continuum of SSA ion signatures with strong potassium and phosphate ion signals but not identified as BioSS.......... 128

Figure 5.8 Distributions of relative ion signals for BioSS grouped by total ion intensity. Results shown are for all BioSS generated during the experiment with 1.22+-0.04 mJ laser pulse energy. 129

Figure 5.9 Distributions of relative ion signals on September 17th for BioSS for all laser pulse energies utilized. 130

Figure 6.1 Time series for the mescosom experiment in the wave channel of (A) of Chl-a and heterotrophic bacteria (HB) concentrations in bulk seawater and as fOM, the relative organic mass fraction of SSA as determined by the AMS... 135

Figure 6.2 Two organic size modes in SSA produced from the wave-channel experiment: (A) mass size distributions of AMS organic ion signals: m/z 43 ($C_3H_7^+$ or $C_2H_3O^+$), an indicator of total organic species; m/z 57 ($C_4H_9^+$), an indicator of aliphatic-rich organic species and m/z 44 (CO_2^+), an indicator of oxidized organic species. 137

Figure 6.3 Lipase activity and calculated aliphatic-rich labile (ARL) species concentration (Model parameters: a: $k^+ = 250$ a.u. μg^{-1} l day^{-1} and $C_{1/2} = 30$ a.u.; b: $k^+ = 6$ a.u. μg^{-1} l day^{-1} and $C_{1/2} = 5$ a.u.; and c: $k^+ = 6$ a.u. μg^{-1} l day^{-1} and $C_{1/2} = 500$ a.u. (a.u. means arbitrary unit)...................... 143

Figure 6.4 Schematic for the pathways of organic enrichment in SSA and their possible relationships with biological processes in seawater.. 146

Figure 6.5 Schematic drawing of the IMPACTS experiment set-up. 149

Figure 6.6 Size resolved organic AMS spectra of SSA from the wave-channel: The major peaks in the mass spectrum for the submicron mode are 43, 55, 57, 79, 81 and 83, which are typical hydrocarbon fragments [*Canagaratna et al.*, 2007]. 149

Figure 6.7 AMS organic spectrum of the bulk seawater (last panel): seawater from the wave channel was atomized to produce droplets, which were then dried and sampled by the AMS. All other AMS spectra used in this study (including Figure 6.2B and 6.5) are compared here. 150

Figure 6.8 Elemental ratios of organics in SSA, calculated from the high resolution AMS mass spectra (C: carbon, H: hydrogen, and O: oxygen). 151

Figure 6.9 (A) ATOFMS spectra (weight matrices) and (B) size (D_{va}) resolved number fraction of the SSOC and OC SSA types from the wave channel experiment.. 151

Figure 6.10 Representative Raman spectra of SSA particles and assignments to the vibrational peaks are provided in each table. A peak marked with an asterisk in each spectrum is due to the quartz substrate (6.5.9).. 152

Figure 6.11 Measured ectoenzyme activity of the bulk seawater with target sites of the substrates given in parentheses where necessary (6.5.5)... 153

Figure 6.12 Average mass size distribution (calculated from the particle number size distribution, 6.5.6) of SSA produced from the wave channel during the entire experiment........................... 153

Figure 7.1 Size resolved ATOFMS particle counts during the hygroscopicity MART experiments. 170

Figure 7.2 The average relative mass spectrum for each mass spectral category generated in the hygroscopicity MART experiments.. 176

Figure 7.3 Reproduced from [*Forestieri et al.*, 2016]. Time series for the indoor MART chlorophyll-a along with physical and chemical measurements of the SSA population. 178

Figure 7.4 Reproduced from [*Forestieri et al.*, 2016]. Time series for the indoor MART chlorophyll-a along with physical and chemical measurements of the SSA population. 179

Figure 7.5 Average relative mass spectra for the *BioSS* mass spectral type, identified during the wave channel IMPACTS experiment, split by total positive ion intensity (low: 0-2E5, medium: 2E5-6E5, high: 6E5-12E5).. 182

Figure 7.6 Average relative mass spectra for the Bio-Ag and KP-lowOrg mass spectral types identified during the wave channel IMPACTS experiment... 183

Figure 7.7 For each sampling period the mean relative positive silver ion signal was calculated for the BioAg type (dotted line). In addition the distribution of the relative silver ion signal for the BioAg mass spectral type is also shown for each time period... 184

Figure 7.8 Average relative mass spectra for the Dust and NO_x mass spectral types, identified during the wave channel IMPACTS experiment... 185

Figure 7.9 The number fraction for the mass spectral types, identified during the wave channel IMPACTS experiment, over the size range of the ATOFMS. 186

Figure 7.10 Panels (a) from *McCluskey et al.* [2016]. (a) Timeline of INP number concentrations (n_{INPs}; per liter of air; left axis). Colors indicate activation temperature denoted by the color scale. (b) Number fraction of the ATOFMS mass spectral types... 189

LIST OF TABLES

Table 2.1 Summary of SPMSs developed and data analysis packages used. 15

Table 2.2 Comparison of run times for various operations in YAADA and FATES. 21

Table 3.1 Comparison of run times for various operations in YAADA and FATES. 57

Table 4.1 Summary of the number of single particle mass spectra generated by the ATOFMS... 75

Table 4.2 Summary of the number of single particle mass spectra generated by the ATOFMS, split by total positive ion intensity. 76

Table 4.3 Summary of the number of single particle mass spectra generated utilizing the O_{SSW} solution split by total positive ion intensity and particle size. 77

Table 4.4 Summary of the number of single particle (d_{va} 1-2 μm) mass spectra generated utilized to determine the relative yield of positive and negative ions (N^+/N^-). 78

Table 4.5 Summary of the number of particles analyzed by AFM for each MOUDI stage. 80

Table 5.1 Final concentration of nutrients in the growth media (Proline Aquatic Ecosystems) added to the seawater. $Na_2SiO_3 \cdot 9H_2O$ is not part of the nutrient mix, and was added separately. 124

Table 5.2 Mass-to-charge of ions summed to calculate relative positive or negative ion signal. 125

Table 5.3 Ion markers common to the various representative mass spectra shown in Figure 5.1. The ion markers are roughly grouped by the intensity of their signal relative to the total positive or total negative ion intensity. 126

Table 6.1 Summarizing collection times and volumes for the experiment. 153

ACKNOWLEDGEMENTS

The work documented in this dissertation would not be possible without the support and guidance of my advisor, Professor Kimberly Prather. It has been a real joy and an exceptional opportunity to work in such a well supported, multi-disciplinary, and collaborative research group. I have always been encouraged to consider how my work connected to the world and scientific community at large, even when my own work felt narrow in focus. Kim has shown me to how critical not only the science but also science communication is. My growth in oral and written science communication for a range of audiences is one of my proudest achievements in graduate school, and one which Kim is owed a great credit.

I'd also like to acknowledge my doctoral committee members Professor Farooq Azam, Professor Francesco Paesani, Professor Michael Tauber, and Professor Susan Taylor for their advice and feedback during my exams.

Working in the Prather lab has been an especially special and rewarding experience because of the enormously talented, encouraging, and friendly students, post-docs, and staff who make up the team. Across the board Prather lab members are selfless and caring individuals, and countless members have kept me afloat during my grad school career running experiments, editing papers, helping me prepare for exams, listening to my science ramblings, and providing guidance and advice. In addition to the huge amount of scientific and professional assistance, I am so grateful for the companionship and friendships I have developed within the Prather lab. For your assistance and camaraderie thank you to: Hashim Al-Mashat, Dr. Andrew Martin, Dr. Jessica Axson, Charlotte Beall, Dr. Doug Collins, Gavin Cornwell, Dr. Cassie Gaston, Dr. Lindsay Hatch, Dr. Louise Kristensen, Chris Lee, Dolan Lucero, Kathryn Mayer, Brock Mitts, Kathryn Moore, Robin Richardson, Mitchell Santander, Jon Sauer, Dr. Kaitlyn Suski, Dr. Xiaofei

Wang. Also thank you to the best machinist and handiest man around Joe Mayer and Monica Castrejon, who always goes above and beyond no matter the task.

My path to grad school was paved by my parents, Peter and Monica Sultana, who have always encouraged me to be curious, brave, and independent. Even when the going has gotten tough, knowing that I always have their unwavering support and love has been a relief and source of great strength. Also thank you to my friends outside of the scientific community who have kept me balanced and brought welcome levity and fun into my life. A special shout out to Marvin Vuong, Emily Baker, and Kief and Becky Zangaro who listened to way more shop talk and work-related diatribes than they could possibly be interested in and have not once complained. Finally, a massive thank you to Brett Schellenberg, my boyfriend who has been an up close and personal witness to my progression through grad school. Thank you for your patience, your million little actions to brighten my days and lighten my load, and for keeping me grounded when I feel lost in a scientific wilderness.

Chapter 2, in full is a reprint of material as it appears in Atmospheric Measurement Techniques, 2017. Reprinted with permission from Sultana, C. M., Cornwell, G. C., Rodriguez, P., Prather, K. A. FATES: a flexible analysis toolkit for the exploration of single-particle mass spectrometer data. Atmos. Meas. Tech. 2017, 10, 1323–1334. The dissertation author was the primary investigator and author of this paper, established the framework and data architecture within FATES, built the tools for script based and visual data analysis, and wrote the accompanying manual. Paul Rodriguez assisted in establishing the framework and data architecture within FATES. Gavin Cornwell built the calibration tool within FATES assisted extensively in testing the software and writing the manual.

Chapter 3, in full, is a reprint of material as it appears in Environmental Science and Technology, 2017. Reprinted with permission from Sultana, C. M., Collins, D. B., Prather, K. A.

The Effect of Structural Heterogeneity in Chemical Composition on Online Single Particle Mass Spectrometry Analysis of Sea Spray Aerosol Particles. Environ. Sci. Technol. 2017, 51, 3660–3668. The dissertation author was the primary investigator and author of this paper and was responsible for the ATOFMS operation during the laboratory experiments and all analyses of ATOFMS data sets. John Holecek and Gavin Cornwell were responsible for field study ATOFMS operation. Douglas Collins contributed intellectually to the manuscript.

Chapter 4, in full, is currently being prepared for submission for publication to Analytical Chemistry. Printed with permission from Sultana, C. M., Cochran, R., Lee, H., Sauer, J., Morris, H., Stone, E. A., Grassian, V. H., Tivanski, A., Prather, K. A. Integration of offline and SPMS analyses to obtain a more complete picture of particle morphology and coordination of chemical species within model SSA particles. The dissertation author was the primary investigator and author of this paper. Richard Cochran designed and led the original experiment in which all the offline data was collected and also performed the quantitative composition analysis of the bulk water and aerosol population. Hansol Lee and Holly Morris were responsible for collecting and analyzing the atomic force microscopy images. Jon Sauer contributed intellectually to the manuscript.

Chapter 5, in full, is material that has been submitted for publication to Analytical Chemistry. Printed with permission from Sultana, C.M., Al-Mashat, H., Prather, K. A. Expanding Single Particle Mass Spectrometer Analyses for the Identification of Microbe Signatures in Sea Spray Aerosols. The dissertation author was the primary investigator and author of this paper. Hashim Al-Mashat contributed intellectually to the manuscript.

Chapter 6, in full is a reprint of material as it appears in ACS Central Science, 2015. Reprinted with permission from Wang, X., Sultana, C. M., Trueblood, J., Hill, T.C.J., Malfatti, F., Lee, C., Laskina, O., Moore, K.A., Beall, C.M., McCluskey, C.S., Cornwell, G.C., Zhou, Y., Cox, J.L., Pendergraft, M.A., Santander, M.V., Bertram, T.H., Cappa, C.D., Azam, F., DeMott, P.J., Grassian, V.H., Prather, K. A. Microbial Control of Sea Spray Aerosol Composition: A Tale of Two Blooms. ACS Central Science. 2015, 1, 124–131. The dissertation author and Dr. Xiaofei Wang were primary investigators and lead authors of this paper. The dissertation author was responsible for helped design and led the IMPACTS campaign and analysis of the ATOFMS data. Dr. Xiaofei Wang was responsible for the aerosol mass spectrometer operation and data analysis. Gavin Cornwell operated the ATOFMS. Thomas Hill and Christina McCluskey were responsible for the ice nucleating particle collections and analysis. Francesca Malfatti completed the enzyme analysis. Olga Laskina and John Trueblood were responsible for the Raman data collection and analysis. Kathryn Moore operated the sizing instruments. Charlotte Beall, Mitchell Santander, Joshua Cox, and Yanyan Zhou assisted in seawater and aerosol offline sample collection and analyses. Chris Cappa, Timothy Bertram, and Francesca Malfatti assisted in manuscript preparation and contributed intellectually to the manuscript.

The hygroscopicity study in Chapter 7 is material that appears in Atmospheric Chemistry and Physics, 2016. Reprinted with permission from Forestieri, S. D., Cornwell, G. C., Helgestad, T. M., Moore, K. A., Lee, C., Novak, G.A., Sultana, C. M., Wang, X., Bertram, T. H., Prather, K. A., Cappa, C. D. Linking variations in sea spray aerosol particle hygroscopicity to composition during two microcosm experiments. Atmos. Chem. Phys. 2016, 16, 9003-9018. Sara Forestieri was the primary investigator and author of this paper and responsible for the hygroscopicity measurements and analyses. The dissertation author was responsible for the operation of the ATOFMS and associated data analyses and contributed intellectually and to the writing of this manuscript. Xiaofei Wang was responsible for operation of the aerosol mass spectrometer and associated data analyses and contributed to the writing of this manuscript. Portions of the ice nucleation study results in Chapter 7 contribute to a manuscript, which has been submitted for publication to the Journal of the Atmospheric Sciences. Printed with permission from McCluskey, C. S., Hill, T. C. J., Sultana, C. M., Laskina, O., Trueblood, J., Santander, M. V., Beall, C. M., Michaud, J. M., Prather, K. A., Grassian, V., DeMott, P. J. A mesocosm double feature: revealing the identity of marine ice nucleating particles. Christina McCluskey is the primary investigator and author of this paper and responsible for the online ice nucleation measurements and analyses. The dissertation author was responsible for the operation of the ATOFMS and associated data analyses and contributed intellectually and to the writing of this manuscript. Thomas Hill performed the offline ice nucleation measurements and analyses. John Trueblood was responsible for the analysis of the ice nucleating residues. The dissertation author helped design and led the IMPACTS campaign during which the hygroscopicty and ice nucleation studies were conducted.

VITA

2010	Bachelor of Science, Chemistry, Harvey Mudd College
2011-2012	Teaching Assistant, University of California, San Diego
2011-2017	Research Assistant, University of California, San Diego
2013	Master of Science, Chemistry, University of California, San Diego
2017	Doctor of Philosophy, Chemistry, University of California, San Diego

PUBLICATIONS

Sultana, C. M., R. Cochran, H. Lee, J. Sauer, H. Morris, E. A. Stone, V. H. Grassian, A. Tivanski, and K. A. Prather. Integration of offline and SPMS analyses to obtain a more complete picture of particle morphology and coordination of chemical species within model SSA particles, *In Preparation.*

Sultana, C. M., H. Al-Mashat, and K. A. Prather (2017), Expanding Single Particle Mass Spectrometer Analyses for the Identification of Microbe Signatures in Sea Spray Aerosols, *Submitted to Analytical Chemistry.*

Sultana, C. M., G. C. Cornwell, P. Rodriguez, and K. A. Prather (2017), FATES: a flexible analysis toolkit for the exploration of single-particle mass spectrometer data, *Atmos. Meas. Tech.*, *10*, 1323–1334.

Sultana, C. M., D. B. Collins, and K. A. Prather (2017), The Effect of Structural Heterogeneity in Chemical Composition on Online Single Particle Mass Spectrometry Analysis of Sea Spray Aerosol Particles, *Environ. Sci. Technol.*, *51*, 3660–3668.

Cochran, R. E., O. Laskina, J. V Trueblood, A. D. Estillore, H. S. Morris, T. Jayarathne, C. M. Sultana, C. Lee, P. Lin, J. Laskin, A. Laskin, J. A. Dowling, Z. Qin, C. D. Cappa, T. H. Bertram, A. V. Tivanski, E. A. Stone, K. A. Prather, and V. H. Grassian (2017), Molecular Diversity Between Individual Sea Spray Aerosol Particles : Influence of Ocean Biology on Particle Composition and Hygroscopicity, *Chem*, *In Press.*

McCluskey, C. S., T. C. J. Hill, F. Malfatti, C. M. Sultana, C. Lee, M. V. Santander, C. M. Beall, K. A. Moore, G. C. Cornwell, D. B. Collins, K. A. Prather, T. Jayarathne, E. A. Stone, F. Azam, S. M. Kreidenweis, and P. J. DeMott (2017), A dynamic link between ice nucleating particles released in nascent sea spray aerosol and oceanic biological activity during two mesocosm experiments, *J. Atmos. Sci.*, *74*, 151–165.

McCluskey, C. S., T. C. J. Hill, O. Laskina, J. Trueblood, V. H. Grassian, M. V. Santander, C. M. Beall, C. M. Sultana, K. A. Prather, and P. J. DeMott (2017), A mesocosm double feature: revealing the identity of marine ice nucleating particles, *Submitted to Journal of the Atmospheric Sciences*.

Cochran, R. E., O. Laskina, T. Jayarathne, A. Laskin, J. Laskin, P. Lin, C. M. Sultana, C. Lee, K.

A. Moore, C. D. Cappa, T. H. Bertram, K. A. Prather, V. H. Grassian, and E. A. Stone (2016), Analysis of Organic Anionic Surfactants in Fine and Coarse Fractions of Freshly Emitted Sea Spray Aerosol, *Environ. Sci. Technol.*, *50*, 2477–2486.

Collins, D. B., T. H. Bertram, C. M. Sultana, C. Lee, J. L. Axson, and K. A. Prather (2016), Phytoplankton blooms weakly influence the cloud forming ability of sea spray aerosol, *Geophys. Res. Lett.*, *43*(18), 9975–9983.

Forestieri, S. D., G. C. Cornwell, T. M. Helgestad, K. A. Moore, C. Lee, G. A. Novak, C. M. Sultana, X. Wang, T. H. Bertram, K. A. Prather, and C. D. Cappa (2016), Linking variations in sea spray aerosol particle hygroscopicity to composition during two microcosm experiments, *Atmos. Chem. Phys.*, *16*, 9003–9018.

Jayarathne, T., C. M. Sultana, C. Lee, F. Malfatti, J. L. Cox, M. A. Pendergraft, K. A. Moore, F. Azam, A. V. Tivanski, C. D. Cappa, T. H. Bertram, V. H. Grassian, K. A. Prather, and E. A. Stone (2016), Enrichment of Saccharides and Divalent Cations in Sea Spray Aerosol during Two Phytoplankton Blooms, *Environ. Sci. Technol.*, *50*(21), 11511–11520.

Patterson, J. P., D. B. Collins, J. M. Michaud, J. L. Axson, C. M. Sultana, T. Moser, A. C. Dommer, J. Conner, V. H. Grassian, M. D. Stokes, G. B. Deane, J. E. Evans, M. D. Burkart, K. A. Prather, and N. C. Gianneschi (2016), Sea Spray Aerosol Structure and Composition Using Cryogenic Transmission Electron Microscopy, *ACS Cent. Sci.*, *2*, 40–47.

DeMott, P. J., T. C. J. Hill, C. S. McCluskey, K. A. Prather, D. B. Collins, R. C. Sullivan, M. J. Ruppel, R. H. Mason, V. E. Irish, T. Lee, C. Y. Hwang, T. S. Rhee, J. R. Snider, G. R. McMeeking, S. Dhaniyala, E. R. Lewis, J. J. B. Wentzell, J. Abbatt, C. Lee, C. M. Sultana, A. P. Ault, J. L. Axson, M. Diaz Martinez, I. Venero, G. Santos-Figueroa, M. D. Stokes, G. B. Deane, O. L. Mayol-Bracero, V. H. Grassian, T. H. Bertram, A. K. Bertram, B. F. Moffett, and G. D. Franc (2015), Sea spray aerosol as a unique source of ice nucleating particles, *Proc. Natl. Acad. Sci.*, *113*(21), 5797–5803.

Lee, C., C. M. Sultana, D. B. Collins, M V Santander, J. L. Axson, F. Malfatti, G. C. Cornwell, J. R. Grandquist, G. B. Deane, M. D. Stokes, F. Azam, V. H. Grassian, and K. A. Prather (2015), Advancing Model Systems for Fundamental Laboratory Studies of Sea Spray Aerosol Using the Microbial Loop, *J. Phys. Chem. A*, *119*, 8860–8870.

Schill, S. R., D. B. Collins, C. Lee, H. S. Morris, G. A. Novak, K. A. Prather, P. K. Quinn, C. M. Sultana, A. V. Tivanski, K. Zimmermann, C. D. Cappa, and T. H. Bertram (2015), The Impact of Aerosol Particle Mixing State on the Hygroscopicity of Sea Spray Aerosol, *ACS Cent. Sci.*, *1*(3), 132–141.

Wang, X.*, C. M. Sultana*, J. Trueblood, T. C. J. Hill, F. Malfatti, C. Lee, O. Laskina, K. A. Moore, C. M. Beall, C. S. McCluskey, G. C. Cornwell, Y. Zhou, J. L. Cox, M. A. Pendergraft, M. V. Santander, T. H. Bertram, C. D. Cappa, F. Azam, P. J. DeMott, V. H. Grassian, and K. A. Prather (2015), Microbial Control of Sea Spray Aerosol Composition: A Tale of Two Blooms, *ACS Cent. Sci.*, *1*(3), 124–131.

FIELDS OF STUDY

Major Field of Study: Chemistry (Atmospheric & Analytical Chemistry)

ABSTRACT OF THE DISSERTATION

New tools and paradigms for the analysis of sea spray aerosols by single particle mass spectrometry

by

Camille Marissa Sultana

Doctor of Philosophy in Chemistry

University of California, San Diego, 2017

Professor Kimberly Prather, Chair

Aerosols can influence the chemistry of the atmosphere as well as also impact global climate by directly scattering light and modifying cloud properties. Sea spray aerosols (SSA) are the second most abundant natural aerosol globally and have the potential to strongly influence atmospheric chemistry and scattering of solar radiation in marine regions. In this dissertation, an ATOFMS was utilized to characterize the chemistry of SSA, focusing on describing the mixing state of the population and also distributions of chemical components within particles. Existing paradigms describing SSA via single particle mass spectrometers (SPMS) were expanded upon and SPMS descriptions of SSA with results from offline spectromicroscopy and quantitative ensemble techniques were unifed. This research was facilitated by the development of a new

SPMS data analysis toolkit, which enabled both script-based and visual data exploration all within a single programming environment. Utilizing this toolkit, ATOFMS depth profiling studies of supermicron SSA illustrated that much of the variation in SSA mass spectral signatures is likely due to inconsistent desorption of particles with core-shell morphologies, helping to unify online and offline descriptions of the SSA mixing state. In a study of SSA generated from a model seawater solution, the interpretation of single particle ion signatures were informed by complimentary offline microscopy images and quantitative chemical composition measurements. It was deduced that the high calcium signal and total negative ion yield were likely a product of the coordination of calcium to carboxylate in the desorbed and ionized particle. For the first time, depth profiling and size dependence analyses were coupled to isolate likely microbial ion signatures (BioSS) from within the SSA population. These new paradigms were applied to interpret SSA ATOFMS data sets from collaborative studies, where the influence of biologically mediated changes in seawater chemistry on SSA chemistry and climate impacts were explored. Concentrations of BioSS and warm ice nucleating particles were correlated, suggesting microbe-containing SSA may effectively nucleate ice in marine clouds. Finally, ATOFMS and aerosol mass spectrometry descriptions of SSA helped establish a mechanistic framework illustrating how SSA chemical composition is modulated not only by phytoplankton primary production but also by microbial degradation processes.

.

Chapter 1. Introduction

1.1 Sea Spray Aerosols

Atmospheric aerosols are solid or liquid particles suspended in the atmosphere. These particles have a significant impact on global climate by interacting directly with incoming radiation and indirectly through influencing cloud properties as cloud condensation (CCN) and ice nuclei (IN) [*Haywood and Boucher*, 2000; *Lohmann and Feichter*, 2005; *Pöschl*, 2005]. Sea spray aerosols (SSA) represent one of the largest mass fluxes of aerosol particles into the atmosphere [*Textor et al.*, 2006; *O'Dowd et al.*, 2007]. To be able to constrain the uncertainty in the radiative forcing of anthropogenic aerosols [IPCC, 2013], first the impact of large natural sources of aerosols, such as SSA, on current total aerosol radiative forcing must be better understood [*Raes et al.*, 2000].

1.1.1 SSA Production Mechanism

Breaking waves entrain air at the ocean surface, generating bubbles, which rise through the water column and subsequently burst at the air-sea interface, ejecting SSA into the atmosphere. Two distinct bubble-bursting mechanisms, film and jet drop formation, are considered to control SSA formation. Bubble bursting studies of these production mechanisms are extensively described and summarized in *Lewis and Schwartz* [2004a], however a brief introduction is provided here. At the ocean surface, the fragmentation of the thin fluid bubble cap forms film drops, generally described as submicron particles. Surfactants within the bubble film can stabilize the cap, not only extending its lifetime [*Garrett*, 1967; *Sellegri et al.*, 2006] but also altering the composition of the subsequent film drops due to drainage of water and soluble chemical species from the cap film [*Modini et al.*, 2013]. The collapse of the bubble cavity after cap rupture generates jet drops, generally considered to make up most of the supermicron SSA number fraction. The influence of bubble size and seawater chemistry on the number, size, and composition of SSA produced from jet and film drop production mechanisms is still an area of active research.

In most studies of SSA, bubbles are generated in natural or artificial seawater by two broad mechanisms: air is forced through submerged sintered filters or "frits" [e.g. *Keene et al.*, 2007; *Bates et al.*, 2012; *Frossard et al.*, 2014b; *Quinn et al.*, 2014] or alternatively air is entrained by an impinging water jet or waterfall, mimicking wave breaking [e.g. *Fuentes et al.*, 2010b; *Zábori et al.*, 2013; *Schwier et al.*, 2015; *Forestieri et al.*, 2016]. The bubble size distribution and the method of SSA production have been shown to influence the physical and chemical properties of SSA particles. In comparisons of frit and plunging production methods, plunging mechanisms have been shown to produce bubble and SSA size distributions [*Fuentes et al.*, 2010a; *Stokes et al.*, 2013] and SSA particle compositions [*Collins et al.*, 2014] more closely matching those from breaking waves. A marine aerosol reference tank (MART), which utilizes a pulsed plunging waterfall mechanism, has been developed to closely and reproducibly mimic bubble generation in natural wave breaking processes, to produce realistic nascent sea spray aerosols [*Stokes et al.*, 2013].

1.1.2 SSA Chemical Composition

Previous field and lab studies have shown that SSA is a complex mixture of inorganic salts and an array of dissolved and particulate organic components [*Gantt and Meskhidze*, 2013]. Surface-active dissolved and particulate organic material are scavenged by rising bubbles [e.g. *Blanchard*, 1975, 1978; *Tseng et al.*, 1992; *Mopper et al.*, 1995] and subsequently enriched in SSA relative to their concentrations in the bulk [e.g. *Keene et al.*, 2007; *Russell et al.*, 2010;

Cochran et al., 2016b; *Jayarathne et al.*, 2016]. Studies employing ensemble measurements of ambient marine aerosol and artificially-produced SSA have found increasing organic content by mass of SSA with decreasing particle diameter, as summarized by *Gantt and Meskhidze* [2013]. Oceanic biological activity and chemical makeup have been shown to affect marine aerosol chemical composition [*O'Dowd et al.*, 2004; *Yoon et al.*, 2007; *Schwier et al.*, 2015]. Biologically driven changes in SSA particle chemistry can in turn influence the heterogeneous reactivity [*Ault et al.*, 2014], hygroscopicity [*Fuentes et al.*, 2011], and cloud and ice nucleating activities of SSA [*Fuentes et al.*, 2011; *McCoy et al.*, 2015; *Wilson et al.*, 2015; *McCluskey et al.*, 2017a]. Traditionally, chlorophyll-a (Chl-a) concentration measurements in a few productive and localized regions have been used to empirically parameterize SSA submicron organic content in regional and global models [*Langmann et al.*, 2008; *O'Dowd et al.*, 2008; *Vignati et al.*, 2010; *Gantt et al.*, 2011], despite conflicting information concerning the strength of the correlation between Chl-a and SSA organic fraction [*O'Dowd et al.*, 2008; *Rinaldi et al.*, 2013; *Quinn et al.*, 2014]. In an effort to develop predictions of submicron SSA organic mass fractions that are accurate for both low and high regions of primary production, more recent models have divided marine organic matter into a number of classes with class-specific surface activities and biologically dependent production and lifetimes [*Burrows et al.*, 2014, 2016].

While global model representations of SSA organic content have largely focused on the submicron regime, the bulk of SSA surface area resides in the supermicron size range. Therefore, the three-dimensional chemical structure and mixing state of supermicron SSA plays a key role in light scattering and interactions with gaseous species [*Lewis and Schwartz*, 2004a, 2004b; *Fan and Toon*, 2011]. However, ensemble techniques typically utilized to inform these models cannot describe the size-resolved chemical composition and chemical morphology of individual particles [e.g., *Albert et al.*, 2012; *Gantt et al.*, 2012; *Partanen et al.*, 2014]. In addition, ensemble techniques, which determine the average the chemical composition of an aerosol sample, are not well suited to identifying or describing scarce particle types, such as ice nucleating particles (INP), which are critical in controlling cloud lifetimes and the radiation budget over the open ocean [*DeMott et al.*, 2015; *Wilson et al.*, 2015]. For rare populations, like INP which make up roughly one in a million particles, single particle resolution is instrumental in determining the chemical and physical characteristics.

Offline single particle analyses of supermicron SSA particles have shown that they mostly comprise a single population, with organic material and sea salts contained within each particle [*Posfai et al.*, 1995; *Leck and Bigg*, 2008; *Wise et al.*, 2009; *Russell et al.*, 2010; *Hawkins and Russell*, 2010; *Maskey et al.*, 2011; *Laskin et al.*, 2012; *Ault et al.*, 2013a, 2013b, 2013c; *Gantt and Meskhidze*, 2013; *Collins et al.*, 2014; *Chi et al.*, 2015; *Patterson et al.*, 2016], though the relative concentrations of organic material may vary with changing seawater biological activity and seawater composition [*Ault et al.*, 2013c; *Lee et al.*, 2015]. Intact cells or cell fragments of marine microbiology can also be ejected in supermicron SSA [*Blanchard and Syzdek*, 1982; *Patterson et al.*, 2016], however reports of particles containing identifiable particulate cellular material are very rare. While offline studies describe supermicron SSA as a rather uniform particle population, there is great variation in the supermicron SSA mass spectral signatures generated with online analysis by single particle mass spectrometers (SPMS). Based on this online data, studies have suggested three distinct particle types each contribute a significant number fraction to the supermicron SSA population: sea salt (SS), sea salt with organic carbon (SSOC), and biological or magnesium (Bio) particles [*Gaston et al.*, 2011; *Prather et al.*, 2013; *Collins et al.*, 2014; *Guasco et al.*, 2014]. Resolving the discrepancy between offline spectromicroscopy and online spectrometry descriptions of the supermicron SSA mixing state is critical, as sea spray aerosols remain a topic of great interest to the atmospheric science community.

1.1.3 Supermicron SSA Morphology

Determining the surface composition of aerosols is key to determining their climate relevant properties, such as ice nucleating and cloud nucleating capabilities. In addition, photochemistry and reactions with gas phase components are often driven by the components at the aerosol surface. The three-dimensional chemical structure of dried supermicron SSA has been examined offline with a variety of spectromicroscopy techniques. Whether SSA is collected in the ambient environment or generated in the laboratory by wave breaking, plunging waterfall, or fritted bubbler methods, there is consensus in the spectromicroscopy literature that the vast majority of supermicron particles phase separate upon drying into inorganic cuboids with amorphous coatings and nodules [*Posfai et al.*, 1995; *Leck and Bigg*, 2008; *Wise et al.*, 2009; *Russell et al.*, 2010; *Hawkins and Russell*, 2010; *Maskey et al.*, 2011; *Laskin et al.*, 2012; *Ault et al.*, 2013a, 2013b, 2013c; *Gantt and Meskhidze*, 2013; *Collins et al.*, 2014; *Chi et al.*, 2015; *Patterson et al.*, 2016]. Sodium chloride makes up the bulk of the inorganic cores while the particle surface is greatly enriched in organic constituents and minor inorganic species, such as sulfate, magnesium, and calcium. This observed phase separation is well supported by physical chemistry studies of the efflorescence of particles generated from seawater and model salt solutions [*Ge et al.*, 1996, 1998a; *Cziczo et al.*, 1997; *Liu et al.*, 2008; *Xiao et al.*, 2008; *Harmon et al.*, 2010; *Tong et al.*, 2011; *Gupta et al.*, 2015].

Similarly, SSA particles are traditionally dried by reducing the relative humidity (RH) of the sampled air to roughly less than 20% before aerosol analysis by SPMS. Drying particles before they enter the SPMS ensures consistency between studies, as different inlets and instrumental setups can lead to varying degrees of drying and phase separation within the instrument if the particles enter wet. In addition, particle phase water suppresses ion formation, so gathering data on highly hydrated particles provides additional experimental challenges [*Neubauer et al.*, 1997, 1998]. Given the extent of drying for the work presented in this dissertation (RH ~< 20%), it is expected that the SSA particles analyzed were phase separated before entering the SPMS utilized.

1.2 Online Single Particle Measurement by ATOFMS

1.2.1 Instrument Description

SPMS provide size resolved information on the chemical composition of individual aerosol particles, in real time without particle preparation, collection, or storage. In the work presented herein, a nozzle-inlet aerosol time-of-flight mass spectrometer (ATOFMS), a specific version of SPMS, was utilized to analyze particles with vacuum aerodynamic diameters (d_{va}) from 0.5 to 4.5 m. A detailed description of the ATOFMS utilized has been previously published [*Gard et al.*, 1997], however a brief summary is provided here. After entering the instrument, particles are focused into a particle beam and accelerated to their d_{va}-dependent terminal velocity. Particle velocities are determined by the time required to transit between two continuous wave 532 nm laser beams. Velocities are converted to d_{va} via calibration with polystyrene latex spheres of known diameter and density. Within the mass spectrometer, particles are desorbed and ionized by a Q-switched Nd:YAG laser pulse (266 nm wavelength, 8 ns pulse width, 700 μm spot size) which desorbs and ionizes each particle's chemical components. Generated negative and positive ions are collected and detected simultaneously by two reflectron-time-of-flight mass spectrometers producing a dual-polarity mass spectrum for each particle.

1.2.2 Basics of Data Analysis

Following data acquisition, peaks of known mass-to-charge (*m/z*) are used to generate calibrations to convert the raw time-of-flight (TOF) mass spectra to *m/z* space. Baseline and noise corrections as well as the generated mass calibration are applied to raw 15,000 point TOF spectra. The storage and computational demands of data sets containing tens of thousands to millions of mass spectra are minimized by an empirically-derived lab-generated peak picking script. Mass spectra are usually reduced to ten to several hundred points containing peak locations, areas, and intensities. Particle data and mass spectra are then imported into MATLAB. Particles are often grouped by mass spectral similarity utilizing clustering algorithms such as k-means, ART-2a, or hierarchical clustering [e.g. *Murphy et al.*, 2003; *Rebotier and Prather*, 2007; *Giorio et al.*, 2012]. This usually reduces the data set to several hundred clusters, which are then further combined into particle types based upon expert knowledge. Relationships between ion responses within mass spectra and the dependency of mass spectral signatures based upon laser pulse energy, particle size, and experimental conditions at a single particle level can also be examined.

1.2.3 Limitations of SPMS

Ion signals generated by laser desorption/ionization (LDI) are only qualitatively dependent on particle chemical composition [e.g., *Ge et al.*, 1998; *Gross et al.*, 2000; *Hinz and Spengler*, 2007]. It has been frequently demonstrated that the mass spectra generated via LDI show broad particle-to-particle variation even for particles of identical chemical composition [e.g. *Gross et al.*, 2000; *Wenzel and Prather*, 2004; *Zelenyuk et al.*, 2008]. This variation is exacerbated by variations in particle size [*Reinard and Johnston*, 2008; *Zelenyuk et al.*, 2008a], inconsistency in laser fluence experienced by the particles [*Wenzel and Prather*, 2004; *Steele et al.*, 2005], and spatial chemical heterogeneity within particles [*Cai et al.*, 2006; *Zelenyuk et al.*, 2008b; *Cahill et al.*, 2015a]. Fluence, a measure of energy per unit area can vary substantially since the laser beam profile is often nominally Gaussian, although variations, or 'hot spots' can arise within individual laser pulses. *Wenzel and Prather* [2004] showed that for 1 μm particles composed of 2,4- dihydroxybenzoic acid and ionized by an inhomogeneous laser, ART-2a generated 15-20 clusters even for very low mass spectral discrimination thresholds (vigilance factor: 0.2-0.6), well below the minimum for initial clustering which is usually utilized for field study datasets (vigilance factor: ~0.7-0.8), where there is a need to identify spectra from actually distinct particle types [e.g. *Dall'Osto and Harrison*, 2006; *Pratt and Prather*, 2009; *Qin and Prather*, 2006]. At the laser pulse energies commonly utilized in SPMS, particle desorption, especially for supermicron particles, is usually incomplete [*Weiss et al.*, 1997; *Carranza and Hahn*, 2002; *Vera et al.*, 2005; *Dall'Osto et al.*, 2006; *McJimpsey et al.*, 2008; *Wade et al.*, 2008]. Therefore problems in spectral variation are intensified for particle types where all particles are of similar composition, but within each particle there is spatial heterogeneity in the chemical distribution, such as "core-shell" morphologies. For example, *Zelenyuk et al.* [2008b] showed that 146 nm NaCl particles coated in a 59 nm shell of dioctyl phthalate (DOP) can generate mass spectra with 100% contribution from DOP ions to 85% contribution from NaCl ions at a constant laser power of 0.38 J/cm^2. Algorithmic analysis of such mass spectra would divide these results into an array of distinct particle types, despite the existence of only a single particle population. A wide array of particle types can exhibit chemical spatial heterogeneity, such as effloresced SSA and particles that have undergone secondary processing (e.g. reaction with nitric acid, condensation of gas phase organic species, etc.).

Furthermore, analysis of SPMS datasets is made more difficult by the fact that a combination of matrix effects [*Sullivan and Prather*, 2005; *Nash et al.*, 2006; *Hinz and Spengler*, 2007] and differences in ionization efficiency [*Ge et al.*, 1998b; *Gross et al.*, 2000; *Bhave et al.*, 2002; *Spencer and Prather*, 2006; *Hinz and Spengler*, 2007] result in non-quantitative mass spectral signatures. As such, mass spectra can have large relative contributions from minor components of the particle composition, while major components of a particle may only contribute negligibly to the mass spectra. This can result in distinct particle types having very similar mass spectra [*Silva et al.*, 1999; *Murphy et al.*, 2003; *Zawadowicz et al.*, 2016]. For example, one area of ongoing discussion is the accurate identification and discrimination between aerosolized dust and cells, because both types often share major ion markers (potassium, phosphate, organic nitrogen). These particle types are often only distinguishable by minor ions, such as silicates and aluminum [*Holecek et al.*, 2007; *Pratt et al.*, 2009b; *Ault et al.*, 2011; *Creamean et al.*, 2013, 2014; *Zawadowicz et al.*, 2016].

The array of SPMS designs compounded with the non-quantitative nature of SPMS mass spectra and wide particle-to-particle mass spectral variation even for particles of similar composition, demonstrates the need for flexible data analysis techniques. Discussions on accurate methods to identify particle types not only span a range of mathematical and grouping techniques [*Murphy et al.*, 2003; *Rebotier and Prather*, 2007; *Zelenyuk et al.*, 2008a; *Gross et al.*, 2010; *Giorio et al.*, 2012], but are usually specific to a narrow set of particles or a single type [*Silva et al.*, 1999; *Silva and Prather*, 2000; *Pratt and Prather*, 2009; *Zawadowicz et al.*, 2016], and may also be instrument dependent [*Hinz et al.*, 2006]. Because of this, any standard clustering threshold (whether using ART-2a, K-means, or a clustering algorithm of choice) will almost certainly leave some particle types split across multiple clusters and some clusters composed of multiple particle types [*Phares et al.*, 2001; *Murphy et al.*, 2003; *Wenzel and Prather*, 2004; *Rebotier and Prather*, 2007; *Zelenyuk et al.*, 2008a]. This reality means SPMS analysis on external aerosol populations will almost always require some form of expert knowledge and further user-guided analysis beyond initial algorithmic grouping, as specified in almost all field study publications [e.g. *Dall'Osto and Harrison*, 2006; *Pratt and Prather*, 2009; *Qin et al.*, 2012].

1.2.4 Depth Profiling of Particles with SPMS

Numerous laboratory studies have demonstrated depth profiling of particles in real time by directly varying the pulse energy of the desorption/ionization laser. This depth profiling analysis has been utilized to study well-defined particles with core-shell morphologies, generated by coating size-selected single chemical component particles with a chemically distinct outer layer of a controlled thickness [*Carson et al.*, 1997b; *Woods et al.*, 2002; *Pegus et al.*, 2005; *Cai et al.*, 2006; *Zelenyuk et al.*, 2008b; *Cahill et al.*, 2015a]. With lower laser pulse energies, correspondingly low laser fluences only desorb small quantities of the particle, and ion signals are representative of mainly the surface components. At higher laser pulse energies, mass spectra have greater contributions from the core chemical components due to more complete particle desorption.

However, it has also been shown that even operating at a consistent laser pulse energy there can be considerable fluctuations in the laser fluence experienced by individual particles, as evidenced by variation in the mass spectra [*Carson et al.*, 1997b; *Wenzel and Prather*, 2004; *Zelenyuk et al.*, 2008b; *Cahill et al.*, 2015a]. Desorption/ionization lasers are often focused to spot sizes on the order of 100 microns. Particles analyzed by SPMS are nominally 1 um in diameter. This means that the laser beam spot size is much larger than the particles analyzed by SPMS, and any particle only sees a fraction of the total energy generated by each pulse. While SPMS users can operationally measure the total energy of each laser pulse, it is not possible to ascertain a direct measure of the laser fluence at the location within the laser beam profile where the particle was desorbed and ionized. SPMS depth-profiling studies of particles with core-shell morphologies have shown that total positive ion intensity increases with increasing relative ion signals from the particle core [*Pegus et al.*, 2005; *Zelenyuk et al.*, 2008b]. For one SPMS study of SSA performed at a consistent laser pulse energy, total mass spectral ion intensity was utilized as an indirect measure of the degree of particle desorption and laser fluence experienced by the particle [*Ault et al.*, 2013a].

1.3 Dissertation Objectives

The use of ATOFMS for the analysis of SSA mixing state has been leveraged frequently in recent years and a number of distinct particle types have been described [*Dall'Osto et al.*, 2004; *Gaston et al.*, 2011; *Prather et al.*, 2013; *Collins et al.*, 2014; *Guasco et al.*, 2014; *Sierau et al.*, 2014; *Lee et al.*, 2015]. These particle types were created by algorithmic clustering and then expert refinement and recombination. In these manuscripts, only brief descriptions of the mass spectral characteristics and inferred chemical composition of each particle type are supplied. This thesis seeks to expand upon the existing paradigms utilized to describe SSA via SPMS, and unify SPMS descriptions of SSA with results from offline spectromicroscopy and quantitative ensemble techniques. Specific questions which will be addressed in this work are presented below:

1. How does the distinct core-shell morphology of supermicron SSA particles influence the single particle mass spectra generated by SPMS?
2. What is the cause of the discrepancy between the offline spectromicroscopy and online SPMS descriptions of the supermicron SSA mixing state?
3. Considering the ubiquity of dissolved chemical species in seawater which have traditionally been utilized as unique markers for cellular material, can the mass spectral fingerprints of the rare SSA particles containing intact cells or cellular fragments be distinguished from the greater population?

4. How does increasing chemical and biological complexity of seawater influence the already demanding interpretation of SSA data sets?

1.4 Dissertation Synopsis

The goals of this dissertation demanded utilizing investigative data analysis techniques and tools that are less commonly leveraged in developing particle types from SPMS data sets. Chapter 2 describes a new open source Flexible Analysis Toolkit for the Exploration of Single Particle Mass Spectrometer data (FATES). FATES is the first publically available SPMS toolkit to allow users to explore their data using both creative script-based data mining robust interactive GUIs for data visualizations, all within a single programming environment. The utilization of FATES proved instrumental in attaining the results described throughout Chapters 3-7. ATOFMS depth profiling studies of supermicron SSA, accomplished by directly varying the laser pulse energy and utilizing total ion intensity analyses, are discussed in Chapter 3. The studies illustrate that much of the variation in SSA mass spectral signatures is likely due to inconsistent desorption of particles with core-shell morphologies, helping to unify online and offline descriptions of the SSA mixing state. Chapter 4 extends the results of Chapter 3 by examining the effect of elevated organic content within a synthetic seawater solution on SSA particle morphology, composition, and mass spectral signatures. Organic volume fractions calculated from offline single particle atomic force microscopy (AFM) images are compared for the first time to quantitative ensemble measurements and show good agreement. Informed by particle morphology results from AFM, chemical composition data from bulk measurements, and the laser desorption/ionization literature, it is deduced that the coordination of calcium to functionalized organic molecules likely results in the unusually intense calcium ion signals observed. In Chapter 5, microbial ion signatures are isolated from an SSA population. Depth profiling and size dependence analyses are coupled to verify the classification of this distinct particle type and also to propose that marine microbes are ejected with dissolved organic and inorganic material which can potentially obscure the identification of these rare particles via ATOFMS analysis. Chapter 6 describes results from a 29-day mesocosm study carried in an isolated wave channel filled with 3,400 gallons of natural seawater. Size resolved ATOFMS and aerosol mass spectrometry descriptions of SSA were coupled with measurements of seawater biological activity to establish a mechanistic framework illustrating how SSA chemical composition is modulated not only by phytoplankton primary production but also by microbial degradation processes. Results from ATOFMS data sets, achieved by applying paradigms established in Chapters 2-5, are utilized in Chapter 7 to inform investigations into the cloud and ice nucleating capabilities of SSA. Overall, this work expands upon previous descriptions of SSA via online single particle mass spectrometry, and presents new paradigms to help deconvolute the influence of biological activity and particle chemistry and morphology on mass spectral datasets.

1.5 Acknowledgments

Olivia Ryder and Gavin Cornwell are acknowledged for assisting in the editing of this chapter.

Chapter 2. FATES: a flexible analysis toolkit for the exploration of single-particle mass spectrometer data

Reproduced with permission from the European Geosciences Union

2.1 Abstract

Single-particle mass spectrometry (SPMS) analysis of aerosols has become increasingly popular since its invention in the 1990s. Today many iterations of commercial and lab-built SPMS systems are in use worldwide. However, supporting analysis toolkits for these powerful instruments are outdated, have limited functionality, or are versions that are not available to the scientific community at large. In an effort to advance this field and allow better communication and collaboration between scientists, we have developed FATES (Flexible Analysis Toolkit for the Exploration of SPMS data), a MATLAB toolkit easily extensible to an array of SPMS designs and data formats. FATES was developed to minimize the computational demands of working with large data sets while still allowing easy maintenance, modification, and utilization by novice programmers. FATES permits scientists to explore, without constraint, complex SPMS data with simple scripts in a language popular for scientific numerical analysis. In addition FATES contains an array of data visualization graphic user interfaces (GUIs) which can aid both novice and expert users in calibration of raw data; exploration of the dependence of mass spectral characteristics on size, time, and peak intensity; and investigations of clustered data sets.

2.2 Introduction

Single particle mass spectrometers (SPMSs) yield the size and chemical composition of individual aerosol particles in real-time. SPMSs can generate tens of single particle mass spectra per second utilizing laser desorption-ionization (LDI). However mass spectra generated by LDI exhibit ion signals only qualitatively dependent on particle chemical composition [e.g., *Ge et al.*, 1998; *Gross et al.*, 2000; *Hinz and Spengler*, 2007] and also can exhibit large particle-to-particle variation even for chemically uniform particles [e.g., *Steele et al.*, 2005; *Wenzel and Prather*, 2004; *Zelenyuk et al.*, 2008a, 2008b]. Thus SPMSs generate both large and highly complex datasets, requiring sophisticated data analysis techniques for exploration and distillation of information.

Table 2.1 Summary of SPMSs developed and data analysis packages used.

SPMS version	**Analysis Toolkit Utilized**
Lab developed Instruments	
ALABAMA[a]	CRISP (IGOR toolkit)[b]
ATOFMS[c] (UF-ATOFMS[d])	YAADA (MATLAB toolkit)[e]
LAMPAS[f] (LAMPAS 2[g], LAMPAS 3[h])	Not reported
PALMS[i]	Not reported
RSMS[j] (RSMS-II[k], RSMS-III[l])	Not reported
SPASS[m]	ENCHILADA[n,o]
SPLAT[p] (SPLAT II[q], mini-SPLAT[r])	SpectraMiner[s], ClusterSculptor[t]
Commercial Instruments	
Guangzhou-Hexin ATOFMS/ SPAMS (currently manufactured)[u]	YAADA[v]
TSI ATOFMS (discontinued)[w]	YAADA[x], ENCHILADA[y]

[a]*Brands et al.*, 2011; [b]*Klimach,* 2012; [c]*Gard et al.,* 1997; [d]*Su et al.,* 2004; [e]*Allen,* 2005; [f]*Hinz et al.,* 1994; [g]*Trimborn et al.*, 2000; [h]*Hinz et al.* 2011; [i]*Thomson et al.*, 2000; [j]*Carson et al.*, 1995; [k]*Phares et al.*, 2002; [l]*Lake et al.*, 2003; [m]*Erdmann et al.*, 2005; [n]*Healy et al.*, 2010; [o]*Gross et al.*, 2010; [p]*Zelenyuk and Imre*, 2005; [q]*Zelenyuk et al.*, 2009; [r]*Zelenyuk et al.*, 2015; [s]*Zelenyuk et al.*, 2006; [t]*Zelenyuk et al.*, 2008; [u]www.tofms.net/content.aspx?info_lb=387&flag=103; [v]*Zhang et al.*, 2015; [w]www.tsi.com/aerosol-time-of-flight-mass-spectrometers-series-3800; [x]*Dall'Osto et al.*, 2012; [y]*Sierau et al.,* 2014

As Table 2.1 illustrates, individual laboratories have independently developed a variety of SPMSs, and two commercial versions have also been produced. Due to the many iterations of SPMSs that exist and the lack of a standard data format, individual laboratories have had to build their own data analysis software, though these toolkits are often not reported in the literature (Table 2.1). Only two of these data analysis toolkits have been made publicly available, YAADA (www.yaada.org) and ENCHILADA (www.cs.carleton.edu/enchilada). YAADA is specific to the lab built and commercial versions of the aerosol time-of-flight mass spectrometer (ATOFMS), a version of SPMS [*Allen*, 2005]. ENCHILADA is reported to be compatible with three SPMS designs: SPASS, PALMS, and TSI ATOFMS [*Gross et al.*, 2010]. However, the authors could only find reported use of the ENCHILADA toolkit for TSI ATOFMS and SPASS datasets. Despite their age these toolkits are still utilized, with YAADA being the toolkit of choice for the burgeoning SPMS community in China. The differences and limitations between these two software tools have been extensively described previously [*Gross et al.*, 2010] but a brief summary is given here. YAADA is an object-oriented framework implemented in MATLAB that allows user-developed script-based data exploration and can also leverage the extensive set of built-in functions within MATLAB. This allows a degree of flexibility in creating graphical outputs and exploring ATOFMS data in tandem with other data types. However, the extensive amount of code required at the time of development to create the object-oriented framework for YAADA has made the toolkit highly susceptible to updates and changes in MATLAB. Thus continued use of YAADA either requires using outdated MATLAB versions or extensive maintenance of the scripts underlying the toolkit. Also considerable knowledge of YAADA-specific data classes and framework in addition to general MATLAB understanding is required to be able to manipulate the data. Additionally, YAADA's accessibility is limited for novice users as there are no (graphic user interfaces) GUIs for data exploration. In comparison ENCHILADA is a software package with a graphical user interface. Therefore data analysis functions and workflows built into ENCHILADA are leveraged by interacting with the GUI, without the need to create scripts or interact in a command line interface. However any addition of functionality requires modifying the underlying source code and rebuilding the software. ENCHILADA relies primarily on SQL for accessing and storing the mass spectral database, and

Java for implementation of the GUI, though a number of other drivers, toolkits, and C++ are also integrated into its implementation. Thus modifications are a significant programming task and likely infeasible for scientists not highly experienced in programming and computer science.

Motivated by the continued use of SPMS and the limitations of the currently available software we have developed a new **f**lexible **a**nalysis **t**oolkit for the **e**xploration of **s**ingle particle mass spectrometer data (FATES). To encourage the widespread adoption of this toolkit it was purposely designed in an extensible manner to adapt to the ever evolving and varied implementations of SPMS. It is clear that building open source tools in a standard, well known platform, and creating a work flow with user defined parameters for data analysis would be beneficial to the SPMS community, increasing the rate of knowledge discovery and enabling collaboration between researchers. For example, maintenance and alterations of the software should be easily accessible to chemists and aerosol scientists without extensive training in computer science. In addition, any new toolkit should not be explicitly limited to expected common analyses, which may be built into GUIs, but should give the user complete freedom to access, explore, and utilize SPMS data and also integrate with other temporally and spatially resolved data sets. Finally any framework needs to make careful consideration of both memory and speed constraints imposed by the possible large size of SPMS data sets. Given these constraints the FATES toolkit was developed completely in the MATLAB environment, and an extensive manual was written and is provided in the Supplement. MATLAB is a popular language for numerical data analysis by scientists because it has an extensive library of well-documented built-in functions, utilizes libraries optimized for speed in matrix manipulation, and can support both graphical and script based exploration of data. By taking advantage of native MATLAB data types, FATES is easier to maintain and computationally more efficient than YAADA, the previous publicly available MATLAB toolkit for SPMS analysis. The FATES framework allows users to creatively explore their data without previous assumptions or constraints with simple scripts and by leveraging built-in MATLAB functions. Additionally FATES offers a suite of GUIs for interactive visualizations which can aid both novice and expert users in calibration of raw data, exploration of data sets using temporal, size, and mass spectral filters, as well as investigations of clustered data sets. FATES is the first publicly available SPMS toolkit to allow creative, efficient, script-based data mining along with GUI based visual data exploration and calibration all within a single programming environment.

2.3 FATES Software Description

FATES is implemented completely in MATLAB. No other languages, drivers, or software are needed to utilize FATES. In addition FATES was purposely developed in a manner that demands few presumptions about the instrument, particle, and spectral variables collected by the SPMS. For example one SPMS may only record the speed and time of detection for each particle while another SPMS may also record the power of the desorption/ionization laser pulse. These differences are handled easily as FATES allows users to specify, define, and change the instrument, particle, and spectral variables they would like imported into and saved to a study. To make these alterations users only need modify simple scripts where the desired variables are listed and then these changes are carried over throughout the entirety of the source code. This flexible but simple design gives high utility for the SPMS community because it prevents users from needing expert knowledge of any language and having to search for and make line-by-line or structural changes within the source code. Detailed instructions for making these simple modifications are included in the FATES manual (Supplement M-5) and commented within the code. As distributed, the FATES source code already contains the necessary modifications to read in datasets from three SPMS designs: ATOFMS, ALABAMA, and TSI ATOFMS. In addition FATES avoids the explicit creation of new class objects, which minimizes the lines of source code and number of scripts by over an order of magnitude when compared to YAADA. This greatly minimizes the maintenance needed to keep FATES compatible with future versions of MATLAB. FATES has been tested for compatibility with MATLAB versions 2014b through 2016b.

2.4 FATES Data Architecture

SPMS data imported within FATES is stored within separate variables for the experiment description, the particle data, and the spectral data. A SPMS dataset imported into MATLAB via FATES is referred to as a FATES study, the data architecture of which is comprehensively detailed in the FATES manual (Supplement M-4). Logically, the data mostly consists of 1-many-relationships from study to experiment, experiment to particle, and particle to spectral peaks. The data is most typically loaded once and then accessed and filtered in bulk. Therefore, it is more efficient to organize the observed measurements into denormalized matrices for particle and spectral data, where key information is duplicated in each matrix.

Each FATES study stores a data structure that contains a number of user-defined fields (e.g. Instrument Name, Operator, Location) to describe the experiment in which the data within the study was collected. Each row of the structure describes a unique experiment, which pertains to a unique experiment identifier (ID). All particle data (e.g. speed, power of desorption/ionization laser pulse) is stored in a MATLAB matrix. More specifically, each particle within a FATES study has a unique two-column particle ID. The first column of the particle ID is the experiment ID, previously described, to which the particle belongs. This framework allows users to easily select for particle or spectral data collected during a specific experiment within a FATES study that contains data from multiple experiments. The mass spectral data for all particles in the FATES study is held in an external binary file. Users can easily and quickly retrieve spectral peak data (e.g. m/z, area, height) for user-selected particles using functions provided by the FATES toolkit (Supplement M-6). The spectral data when imported is then stored in MATLAB cell arrays or matrices. Each peak for all of the spectra within a FATES study has a unique four-column peak ID. The first three columns of the peak ID are the experiment ID, particle ID, and the polarity indicator of the spectrum to which the peak belongs. Note that each FATES study contains auxiliary data structures that list the name of the variable (e.g. particle speed, peak area, peak ID) that each column in a data matrix holds. Thus all data within a FATES study is self-contained and self-described, from experimental conditions to peak information. Therefore despite the flexibility of the FATES framework, users can still share FATES studies without confusion or need for external READ ME files to determine the source and identify of the data.

2.4.1 FATES Optimization

Considerable work has been completed to optimize the FATES framework for memory demands, speed, and ease of use. An ATOFMS dataset collected at Bodega Bay, CA in February and March of 2016 is used throughout this paper to illustrate the speed of data analysis within the FATES toolkit. This dataset contains 1,386,042 dual-polarity single particle mass spectra as well as particle data for an additional 11,454,356 particles that were detected in the light scattering region but did not generate spectra. All FATES analysis is performed in MATLAB 2014b with an Intel Core i7-4930K CPU running at 3.4 GHz with 16.0 GB of RAM. Run-time comparisons, summarized in Table 2.2, are made using the same computer utilizing a version of YAADA, which had been maintained by Kim Prather's research group to be compatible with MATLAB 2013a.

To begin working with a SPMS dataset a new FATES study has to be created (Supplement M-2). This process only needs to occur once for any dataset, but the source-code was still designed to minimize the time for study initialization. Despite the large size of the

Bodega Bay dataset, the creation of the FATES study only took 28.4 minutes. Even initiating a subset of the Bodega Bay study roughly a tenth of the FATES study (127,077 dual-polarity mass spectra) in YAADA still required 20.8 minutes. Small ALABAMA and TSI ATOFMS datasets were also initiated expediently in FATES (Table 2.2). Note the version of YAADA maintained by Kim Prather's research group is not able to import these datasets into MATLAB for comparison. FATES has also been designed so that additional data can be added to an existing study without having to reinitialize the entire data set (Supplement M-A). This is especially useful for field studies, where daily examination of the data is required, but initialization of increasingly large data sets can become onerous and time consuming.

Table 2.2 Comparison of run times for various operations in YAADA and FATES.

	YAADA	**FATES**
Study Creation	*20.8 min (ATOFMS)* 127,077 hit particles 1,050,174 missed particles	*28.4 min (ATOFMS)* 1,386,042 hit particles 11,454,356 missed particles *24.8 s (TSI ATOFMS)* 68,400 hit particles 639,145 missed particles *3.2 s (ALABAMA)* 10,00 hit particles 86,744 missed particles
Mass Spectra Retrieval	*42.5 s* 127,077 mass spectra *17.3 s* 50,000 mass spectra	*3.3 min* 1,386,042 mass spectra *26 s* 400,000 mass spectra *2.7 s* 50,000 mass spectra
Retrieval of particle IDs for hit submicron particles	*0.6 s* 127,077 hit particles	*0.01 s* 1,386,042 hit particles
ART-2a clustering	*70 min* 100,000 mass spectra	*2.1 min* 100,000 mass spectra

Once a FATES study is initiated, it is crucial to efficiently handle the spectral data. Users may desire to examine datasets with millions of mass spectra and each spectrum can contain hundreds of peaks. SPMS spectra data formats usually contain mass-to-charge (m/z) and area for each peak, but may also specify peak width, peak height, and other values. This amounts to many gigabytes of data, and therefore the trade off between making all the spectral data available and managing memory requirements had to be taken into consideration. MATLAB facilities for tables were considered, but they are more appropriate for heterogeneous data, whereas in our case all the spectral data is numeric or binary indicators. We also found MATLAB memory mapped files to have unpredictable performance, and it was difficult to append data rows because matrices are stored in column order. We determined the best way to build up and maintain a large matrix of spectral data, without keeping it in memory, was to create a single external binary file, append to it as needed, and provide a lightweight interface so that FATES programs, or other users, could easily execute functions against the file. Essentially, this interface is an API (application programming interface), which takes a regular MATLAB command or script, shuffles data in/out of memory in blocks of rows, executes the commands against the data in memory, and gathers results. The block sizes are set to default values that are reasonable for current workstation capacities, but can also be changed as appropriate in the future. The possible commands are unconstrained, but summaries and filtering operations are most appropriate and most likely to be called for.

In addition, the binary format minimizes both the time required to write and retrieve spectral data as well as the storage requirements for the file. Retrieving all 1,386,042 dual-polarity mass spectra in a single call from the external binary file created for the Bodega Bay study and loading it into a MATLAB array only took 3.3 minutes. It is important to note that this example is used for benchmarking purposes, but rarely would users need or choose to load into and hold all spectra information for entire large datasets within memory at the same time. The FATES framework automatically employs data pointers so that the whole binary file does not need to be read if the user is only attempting to retrieve spectra from particles which make up a subset of all the data in the FATES study. Run-times for retrieving all and contiguous subsets (i.e. the raw data files from which the study was created were contiguous) of the dual-polarity mass spectra from the FATES and YAADA studies are summarized in Table 2.2. Retrieving a subset of 50,000 mass spectra from the FATES study (2.7 seconds) was over six times faster than in the YAADA study (17.3 seconds). Searching and sorting data by particle information is also quickly performed in the FATES framework. By holding all hit particle data in memory, any operation querying the particle data does not require any data input/output calls and therefore is nearly instantaneous in MATLAB. For example retrieving the particle IDs for all sub-micron particles from the Bodega Bay study only took 0.01 seconds, while performing a similar analysis on the much smaller YAADA study required 0.6 seconds.

The quickness of the FATES framework depends partially upon minimizing retrieval calls to external files outside of the MATLAB workspace. Thus formatting of the data held within the MATLAB workspace has been carefully considered to minimize the memory demands of the FATES framework. Because spectral data is held in an external binary file users can choose to store spectra data in the study at a high resolution without increasing the study's working memory. When retrieving spectra from the external binary file users may specify the resolution to hold the data in the workspace. This feature allows users to tailor the resolution of the spectra in the workspace to its application and therefore the memory requirements. Mass spectral data loaded into the MATLAB workspace is stored in a single-precision floating-point format, saving memory compared to the standard MATLAB double-precision format, which requires twice the space. Particle data stored within a FATES study has also been formatted to minimize memory demands. If the user loads data into a FATES study for both detected particles that generated mass spectra (hit) and detected particles that did not generate spectra (missed) only hit particle data is stored in the particle matrices in MATLAB. Most data analyses utilize spectra and therefore only hit particle information is necessary, but hit particles usually make up a small fraction of total particles detected by the light scattering region of the SPMS. Therefore storing missed particle data in MATLAB memory would take up large amounts of space needlessly. All missed particle data is written to an external binary file and can be loaded by the user into MATLAB using a script provided in the FATES toolkit. Furthermore particle data stored in MATLAB memory is split between a single-precision and double-precision matrix. It is not necessary to store most data collected for particles (e.g. speed, laser power) in a double-precision format, so this choice further relieves the space required to store all particle data in memory. Therefore storing data for 1 million hit particles in memory where three variables require double-precision format (particle ID, time) and three variables only need single-precision format (speed, size, laser power) only requires 0.036 GB, which is very feasible for most modern desktop computers. Finally because all SPMS data when loaded into a FATES study is held in native MATLAB data types, interacting with the data requires very few FATES specific functions. Almost all common analyses can be patterned off a basic script, provided with demonstration data in the FATES toolkit, relying on a handful of MATLAB built-in functions and matrix indexing, making the FATES framework accessible and powerful for both expert and novice users.

2.5 Data Analysis within FATES

In this section we provide a brief overview of common analyses that can be performed on SPMS data within a FATES study. However it should be mentioned that it is impossible to describe or predict all data analyses and plotting options easily available to FATES users due to the extensive library of built-in and user-developed MATLAB functions. A large array of analyses can be performed using concise code (Supplement M-6) with only a few examples quickly discussed here. Utilizing logical indexing, particles and spectra can be filtered using any single or combination of particle and mass spectral characteristics (e.g. particle size, peak area at a certain m/z, etc.). Binning of particles and spectra by these characteristics, such as binning data based on time, can be accomplished in a single line with the built-in function *histc*. Additionally lists of particles can be compared with the built-in function *intersect*. Grouping data based on algorithmic clustering of the spectra is also easily performed. Clustering methods commonly used by the SPMS community such as k-means, hierarchical clustering, and k-medoids are built-in to MATLAB and the ART-2a algorithm, popular among ATOFMS users, is supplied in the FATES toolkit. Clustering data, which necessitates a large number of matrix operations, can be performed quickly even with naïve user scripts because MATLAB utilizes BLAS, LAPACK and proprietary libraries which speed-up common linear algebra computations. Clustering 100,000 particles from the Bodega Bay study with ART-2a (vigilance factor = 0.80, learning rate = 0.05) in the YAADA study required 70 minutes, however improvements in the ART-2a scripts in FATES allows the same analysis to be completed in only 2.1 minutes. Using the built-in MATLAB k-means function the same data was grouped into 15 clusters in 2.9 minutes (77 iterations) in FATES. Finally other types of data can be easily loaded into MATLAB and examined along with the SPMS data.

2.6 Exploration of Data Utilizing FATES GUIs

2.6.1 guiFATES: Spectra Visualization, Grouping, and Exploration

While the FATES toolkit allows flexibility in script-based SPMS data analysis, graphical tools can also be an effective way to explore the data and quickly identify trends and patterns. To this end the FATES toolkit includes GUIs, built within MATLAB, which allow users to easily examine trends in spectra based on particle metrics such as size and time, and cluster and spectral characteristics. Figure 2.1 is a screen capture of the FATES spectra explorer guiFATES, displaying data for 46,432 particles. This spectra explorer has been modeled after ClusterSculptor, a SPMS data analysis GUI developed by *Zelenyuk et al*. (2008a) that has not been made publicly available. To initiate guiFATES the user provides the *guifates* function with the mass spectra, two user selected particle metrics, and cluster data for a set of particles. A description of the functionality and abilities of guiFATES is given below.

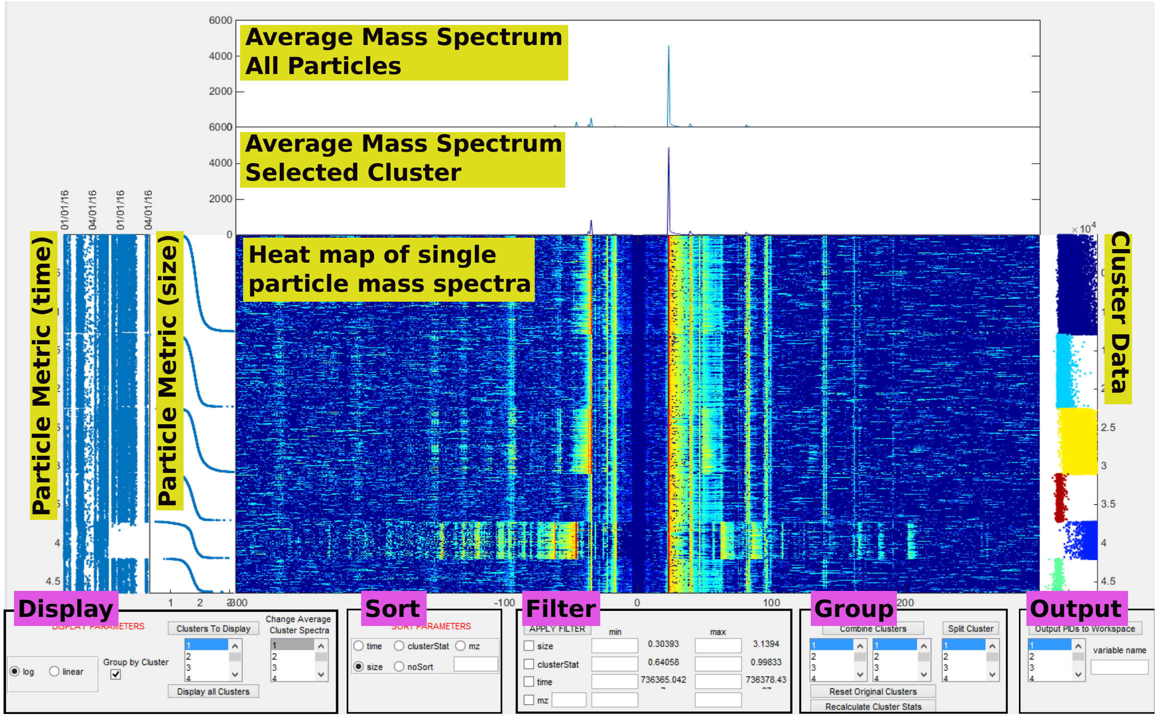

Figure 2.1 Screen capture of a guiFATES window with data from 46,432 individual particles.

The main panel of the guiFATES display is the heat map of the individual particle mass spectra. Each row is an individual mass spectrum with peak intensity indicated by color. The user can choose to display the provided mass spectra peak intensity utilizing a linear or log10 scale. The logarithmic scale makes it easier to visually detect relatively small peak intensities in the spectra, while the linear scale helps users visualize absolute differences between peak intensities. In Fig. 2.1 the logarithmic scale has been selected. Users can choose to provide any two characteristic particle metrics, such as, particle size, time of detection, laser pulse energy, or total ion intensity, which are displayed in the left panels. In Fig. 2.1 particle time and size have been provided. Clustering information is displayed in the right panel. The cluster or group assigned to each particle is indicated by the color of the points on the right while the location on the x-axis is a user provided clustering statistic for each particle. The clustering statistic provided for display in Fig. 2.1 is the dot product of each normalized particle spectrum with the normalized representative spectrum of the cluster to which the particle had been assigned. However, the user can provide any clustering or neighbor statistic they feel is effective for exploring their data set. The top plot in guiFATES is the average of all the provided spectra, and immediately below is plotted a select average cluster spectra, specified by the user in the display parameters. The line color in the average cluster spectra plot matches the colors used to indicate the assigned cluster for each particle in the right vertical plot. The bottom of the guiFATES windows contains all the display, sorting, filtering, and grouping parameters that the user may select and change.

guiFATES provides the user with many options for displaying and exploring the data and all functionalities are thoroughly detailed in the manual (Supplement M-7). A checkbox allows the user to display all data with or without grouping by cluster. In addition the user can select to sort the data by any of the particle metrics in the vertical side panels or by a m/z value in the spectra. In Fig. 2.1 the data is displayed by cluster and sorted by size. Figure 2.5a is a screen capture where the same data is not grouped by cluster and has been sorted by peak intensity of m/z -35. While users may initially provide guiFATES with a large amount of data, they will likely desire to display smaller selections at a time to enable better visual exploration. This can be accomplished in a number of ways within guiFATES. Users can use mouse clicks to quickly zoom in and out of a single plot using MATLAB’s native figure handling capabilities. guiFATES is designed so that when this occurs all plot axes within the GUI are scaled appropriately and instantaneously. Figure 2.5b is a screen capture where the user utilized this functionality to select the bottom half of the particles in Fig. 2.5a and also decreased the range of the m/z values displayed. For more complex selections users can enter in filtering parameters so that displayed particles only fall within a desired range of particle metrics, peak intensity of a certain m/z value, or any combination thereof. Figure 2.5c is a screen capture where the data, sorted by cluster, has been filtered by size (1-2 um), m/z -35 peak area (0-3000), and clustering statistic (0.8-1). Lastly users can also choose to only display select clusters. Figure 2.5d is a screen capture utilizing the same filters as in Fig. 2.5c however limiting the display to only clusters 2 and 5.

These visual sorting and filtering methods enable users to efficiently inspect datasets and visually discover mass spectral trends, differences, and similarities both between distinct particle types and within populations of chemically similar particles. Due to the high variability and qualitative nature of single particle mass spectra generated by laser desorption-ionization techniques, clustering algorithms utilized to group SPMS mass spectra within a dataset often do not generate a one-to-one relationship between the number of chemical particle types in the population and spectra clusters generated [e.g., *Giorio et al.*, 2012; *Murphy et al.*, 2003; *Rebotier and Prather*, 2007; *Wenzel and Prather*, 2004; *Zelenyuk et al.*, 2006, 2008a]. Therefore it is necessary to leverage expert knowledge to either combine multiple spectra clusters, generated algorithmically, into a single chemical particle type or to further split clusters into smaller groups as has been noted in many SPMS studies of unconstrained aerosol populations [e.g. *Dall'Osto and Harrison*, 2006; *Pratt et al.*, 2009; *Qin et al.*, 2012]. The authors emphasize that there is not a consensus on the most suitable algorithms and thresholds for SPMS analysis and suggest users investigate the previously listed references before embarking on mass spectral based algorithmic analysis. However, despite the conditions of initial clustering, guiFATES aids this process by allowing users to visualize all clustered particles at once and combine any number of clusters or split any cluster in any location during the data exploration process. Users can choose to output the particle identifiers of any cluster in the guiFATES window to the MATLAB workspace. All plotting, sorting, filtering, and grouping applications of guiFATES have been tested on a set of

100,000 particles with dual-polarity mass spectra, and at this size all updates to the displayed plots occurred nearly instantaneously, making guiFATES an appropriate and efficient tool for the large data sets common to SPMS analysis.

The advantages and benefits of this general method of data visualization and exploration for refining particle clusters has been discussed at length previously [*Zelenyuk et al.*, 2008] and with the publication of FATES will be available to the SPMS community at large. A specific detail of note is that *Zelenyuk et al.*, (2008) demonstrates that discontinuities in the particle cluster size distributions were characteristic of misclassifications of their mass spectra. Because this technique is not dependent on specific ion markers, it has the potential to be effective for a broad range of particle types, but is yet to be extensively explored. guiFATES also enables future investigations of the extension of this cluster discriminating technique to other common particle metrics, such as total ion intensity. Finally many studies have examined the influences of particle and experimental characteristics on the mass spectra generated from particles of uniform composition [e.g. *Neubauer et al.*, 1998; *Reinard and Johnston*, 2008; *Steele et al.*, 2003; *Zelenyuk et al.*, 2008b]. guiFATES can also be utilized in the exploration of these datasets consisting of a single particle type, where algorithmic grouping of particles utilizing mass spectra is unnecessary or even inappropriate.

2.6.2 dendroFATES: Hierarchical Cluster Relations

FATES also includes two supplementary GUIs which allows the users to graphically select the particles to feed into the guiFATES spectra explorer. dendroFATES is a GUI where the user supplies the clusters and representative cluster mass spectra output from any clustering algorithm of the user's choice. The clusters are then automatically grouped into a cluster tree by a hierarchical analysis performed within MATLAB which is displayed in the dendroFATES GUI window. Hierarchical analyses have been utilized previously with SPMS data sets [*Murphy et* *al.*, 2003; *Hinz et al.*, 2006; *Zelenyuk et al.*, 2006; *Rebotier and Prather*, 2007; *Giorio et al.*, 2012], but a brief description is given here. The dendrogram links clusters in a binary fashion creating new groups which are then further linked. Lower linkage heights indicate a higher degree of similarity between groups and large distances between levels in the dendrogram are indicative of natural divisions in the dataset.

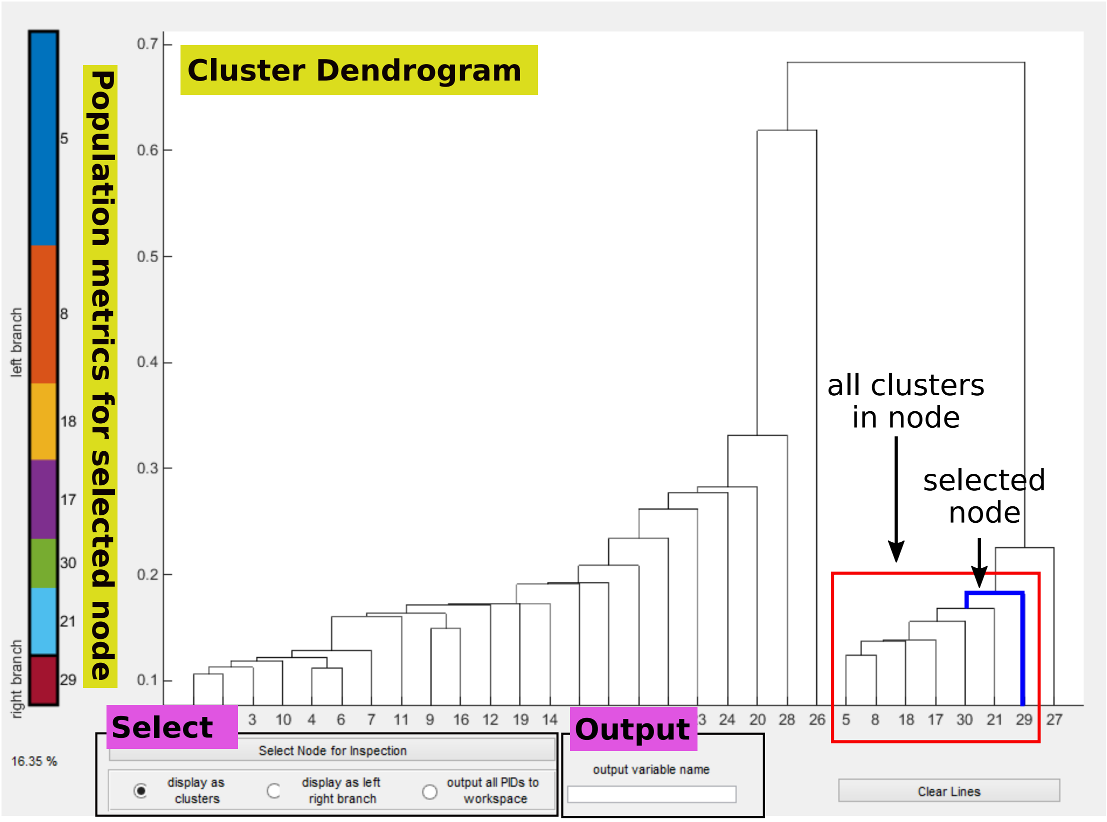

Figure 2.2 Screen capture of a dendroFATES window showing the cluster tree or dendrogram for 30 input clusters. The cluster contributions to the user selected node are shown in the plot on the left. The particle data for the selected node are automatically plotted in a guiFATES window (Figure 2.5).

Figure 2.2 is a screenshot of the dendroFATES window with a dendrogram generated from the thirty most populous clusters generated using the ART-2a algorithm to cluster a subset of 166,666 particles from the Bodega Bay dataset. Zooming in and out of the dendrogram is handled by MATLAB's native graphics functionality makes it possible to supply dendroFATES with hundreds of clusters and still explore the cluster tree quickly and intuitively. Because the dendrogram allows the user to easily visualize similarities and natural groupings of clusters generated, it is an excellent tool to select clusters for further exploration of the particle and spectral data using the guiFATES tool. Clicking linkages in dendroFATES automatically opens a guiFATES window displaying all particles belonging to the selected node. When a linkage is selected the fractional cluster contribution to the selected node is displayed on the right in the dendroFATES window and the fraction of the selected node to the total population is also displayed in text. Figure 2.6 illustrates the guiFATES window generated with the node selection made in Fig. 2.2 when the user chooses to display particles by their cluster label (Fig. 2.6a) or grouped by the left and right branch (Fig. 2.6b). As illustrated in Fig. 2.6a, when guiFATES is populated by dendroFATES the clusters are displayed in the same order as displayed in the dendogram. Therefore very similar clusters are adjacent in the guiFATES window, assisting intuitive visual comparisons and combinations of data. Because all FATES GUIs are in MATLAB and the user can also access the data programmatically, it is straightforward and fast for the user to iteratively select clusters from the dendrogram in dendroFATES, refine them in guiFATES, output new clusters to the workspace, and feed the new cluster results back into dendroFATES until the user is satisfied with the grouping of the data set.

2.6.3 scatterFATES: User Defined Particle Relations

The complexity of SPMS datasets means there are numerous relationships that could be explored, and predicting all desired comparisons is impossible. scatterFATES is another GUI used to populate guiFATES with user selected particles. However, rather than grouping particles via clusters as in dendroFATES, scatterFATES creates a scatter plot of particles using any two particle data metrics the user supplies as the axes. The points are then color coded by cluster or group. Figure 2.3 is an example scatterFATES window, where the -35 to -93 m/z ratio is plotted against particle size for the 166,666 particles that had been previously clustered. Once a scatter plot is created in scatterFATES the user can click on the figure to draw regions within the scatter plot as shown in Fig. 2.1. All particle data within a created region can then be selected and automatically populated into guiFATES for spectra visualization and exploration.

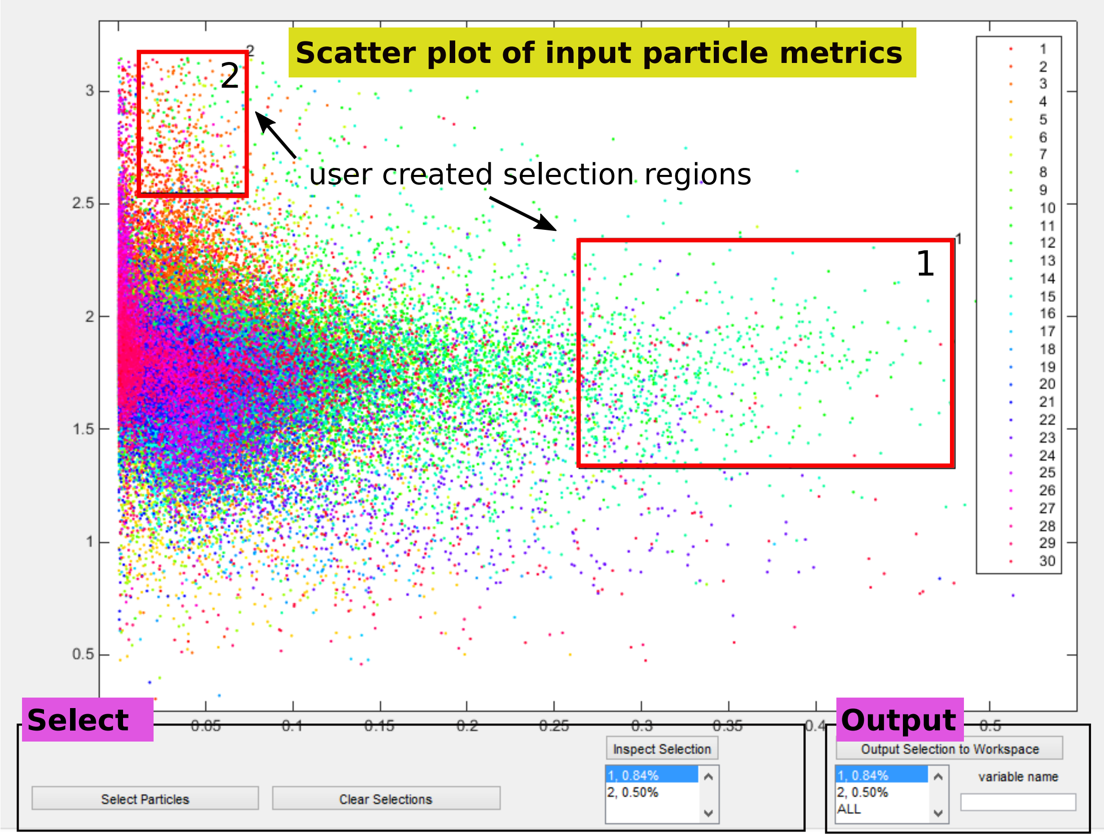

Figure 2.3 Screen capture of a scatterFATES window showing the -35 to -93 m/z ratio plotted against particle size for 166,666 particles. Any two particle metrics can be input into scatterFATES. Two regions have also been created by the user for further inspection in guiFATES.

2.6.4 calibFATES: Raw Spectra Calibration

FATES has been designed so that all aspects and functionalities of SPMS data analysis and exploration are contained within a single programming environment and language. To this end we developed calibFATES, a GUI to quickly scan through raw spectra data files before importation into FATES and generate calibrations to convert raw time-of-flight spectra to mass-to-charge spectra. calibFATES allows SPMS users to quickly visually examine generated spectra on the fly without any time consuming processing, even during data acquisition, to ensure the quality and consistency of the data being acquired. While calibFATES is currently written to be able to read the raw spectra files generated by the ATOFMS and TSI ATOFMS, it could be easily modified to read in any raw spectra file (Supplement M-B). Figure 2.4 is a screenshot of a calibFATES window displaying a single uncalibrated raw spectrum. Users can scan through and display spectra contained in any raw spectra files within the folder. A calibration can be generated by setting selected times to entered m/z values. To generate as accurate a calibration as possible it is suggested that users choose peaks with a diverse set of m/z values that span the SPMS mass spectral range and utilize multiple raw spectra to generate a single calibration. Generating calibration parameters from 20 peaks selected from five spectra has been found to produce generally satisfactory results for ATOFMS datasets. Calibration parameters can be output to a text file for future reference, and any calibration file generated can be loaded into and applied to the raw spectra in calibFATES so that the spectra are displayed as calibrated mass spectra rather than time-of-flight spectra.

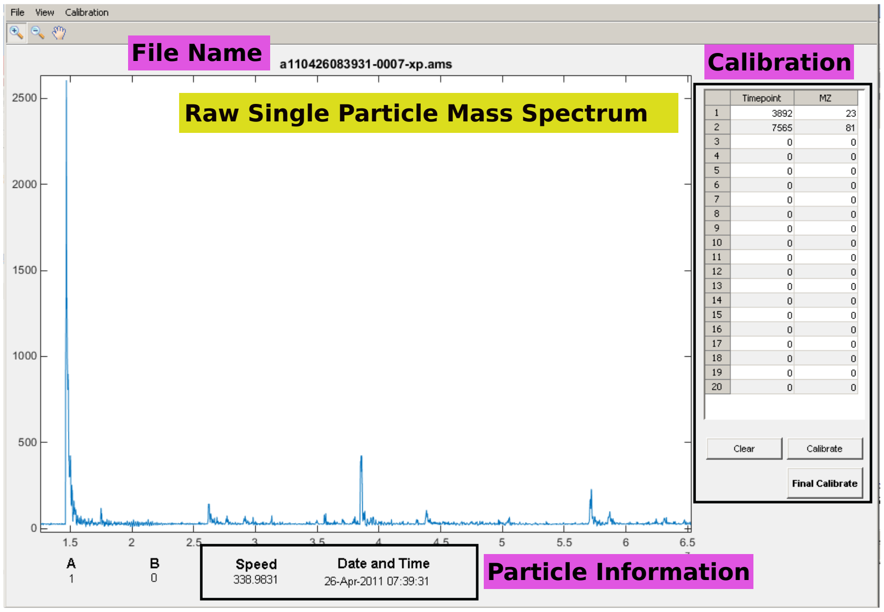

a110426083931-0007-xp.ams

	Timepoint	MZ
1	3892	23
2	7565	81
3	0	0
4	0	0
5	0	0
6	0	0
7	0	0
8	0	0
9	0	0
10	0	0
11	0	0
12	0	0
13	0	0
14	0	0
15	0	0
16	0	0
17	0	0
18	0	0
19	0	0
20	0	0

A	B	Speed	Date and Time
1	0	338.9831	26-Apr-2011 07:39:31

Figure 2.4 Screenshot of a calibFATES window displaying a single particle uncalibrated mass spectrum. Calibration data is input and displayed on the right and particle size and time are displayed on the bottom.

2.7 Conclusions

FATES is the first software package for SPMS data sets to include flexible script-based data analysis and graphical user interfaces for data exploration integrated within a single programming language. Because FATES is designed to be easily extensible to diverse input data formats and implemented completely in MATLAB, a highly documented language popular among scientists, it should be accessible and employable across the SPMS community despite the many independent instrumental designs. SPMS data importation and programmatic and graphical data analyses can be performed quickly in FATES even for large datasets thanks to both speed and memory optimizations and utilization of native MATLAB data types and built-in functions. Within a FATES study data is structured so that complex analyses can be performed using concise code with little reliance on FATES specific functions. In addition a set of GUIs with many display, sorting, filtering, and grouping functionalities have been developed to assist both expert and novice users to intuitively visualize a complex SPMS dataset and create robust particle groupings. For these reasons we believe FATES will greatly improve the efficiency of data processing and knowledge discovery from SPMS datasets.

2.8 Code Availability

The FATES software package (v1.0.0), an extensive manual, and an example data set are available online at doi:10.5281/zenodo.398847, and all future releases will be available at www.github.com/CMSultana/ FATESmatlabToolKit. This site is a forum where updates to the code and new functions can be shared amongst the SPMS community.

2.9 Acknowledgements

This work was funded by the National Science Foundation through the Center for Aerosol Impacts on Climate and the Environment (CHE 1305427). Any opinions, findings, and

conclusions or recommendations expressed in this material are those of the authors and do not necessarily reflect the views of the National Science Foundation.

Chapter 2, in full is a reprint of material as it appears in Atmospheric Measurement Techniques, 2017. Reprinted with permission from Sultana, C. M., Cornwell, G. C., Rodriguez, P., Prather, K. A. FATES: a flexible analysis toolkit for the exploration of single-particle mass spectrometer data. Atmos. Meas. Tech. 2017, 10, 1323–1334. The dissertation author was the primary investigator and author of this paper.

2.10 Supporting Information

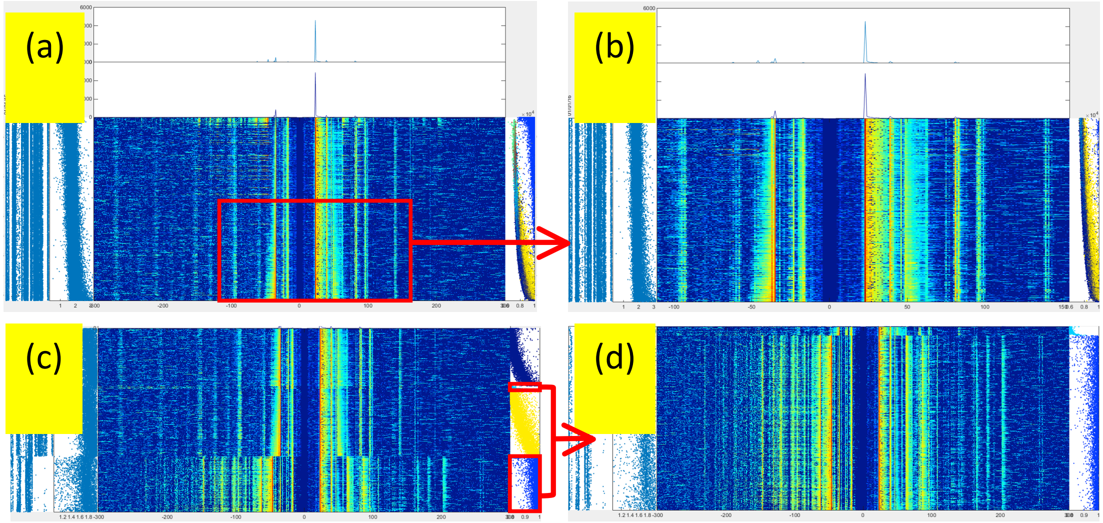

Figure 2.5 Screen captures of a guiFATES window with the same data as in Figure 2.1 filtered and sorted in various ways. a) Entire population sorted by m/z -35 peak intensity. b) Zoom in of 2.5a selecting the bottom half of the particles displayed and a decreased m/z range. c) The data, sorted by cluster, and filtered by size (1-2 um), m/z -35 peak area (0-3000), and clustering statistic (0.8-1). d) The same filtering parameters as S1c with the display limited to clusters 2 and 5.

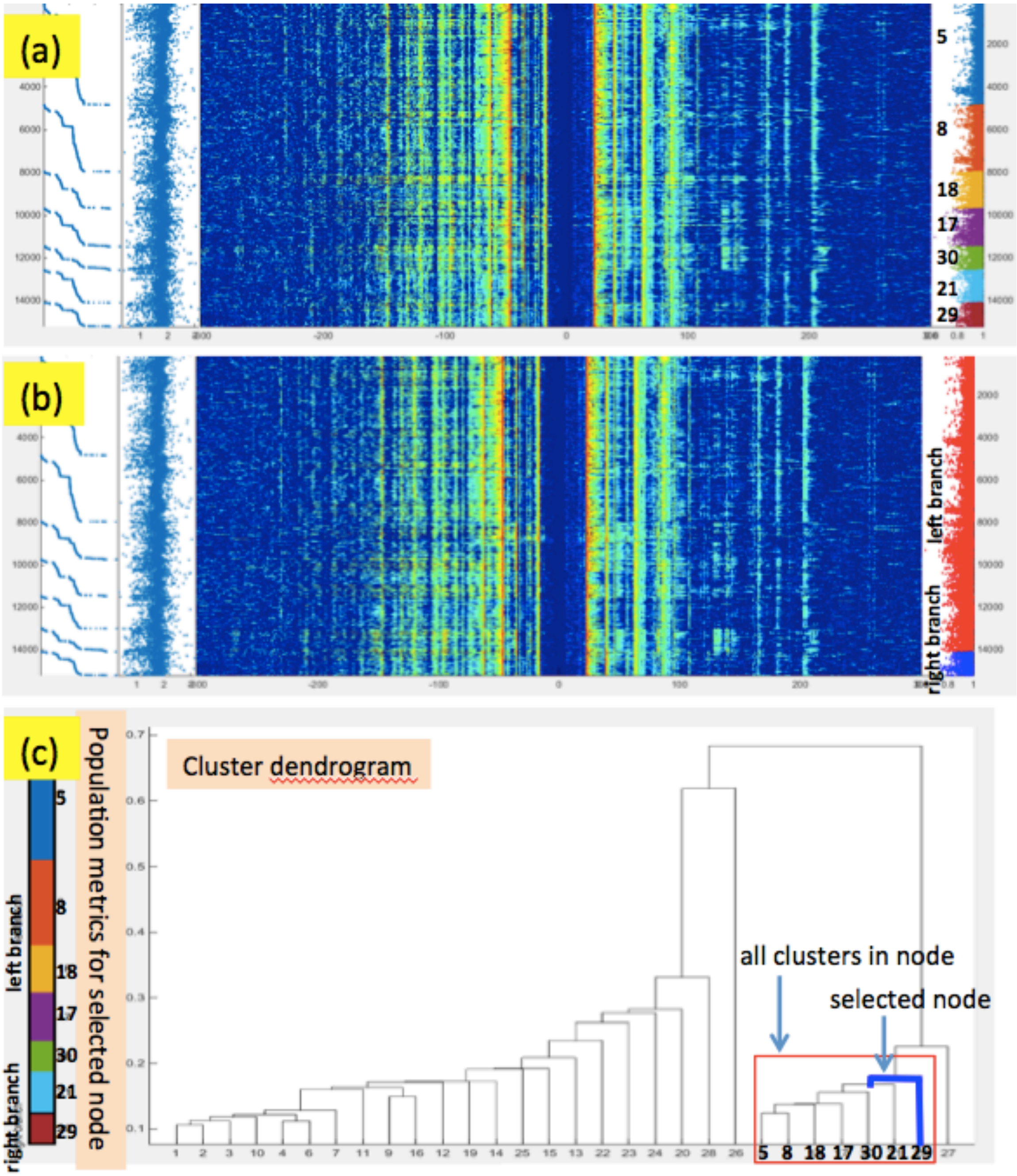

Figure 2.6 guiFATES windows generated automatically from the selection of a node in Figure 2.2 (reproduced in Figure 2.6c). a) The guiFATES window when the user chooses to group particles by their cluster label. The clusters are automatically displayed in the same order as displayed in the dendogram. b) The guiFATES window when the user chooses to group the same data by left or right branch. The clusters are displayed in the same order as displayed in the dendogram.

Chapter 3. Effect of Structural Heterogeneity in Chemical Composition on Online Single-Particle Mass Spectrometry Analysis of Sea Spray Aerosol Particles

Reproduced with permission from the American Chemical Society

3.1 Abstract

Knowledge of the surface composition of sea spray aerosols (SSA) is critical for understanding and predicting climate-relevant properties. Offline microscopy and spectroscopy studies have shown dry supermicron SSA tend to be spatially heterogeneous particles with sodium and chloride rich cores surrounded by organic enriched surface layers containing minor inorganic seawater components such as magnesium and calcium. At the same time, single particle mass spectrometry reveals several different mass spectral ion patterns, suggesting that there may be a number of chemically distinct particle types. This study investigates factors controlling single particle mass spectra of nascent supermicron SSA. Depth profiling experiments conducted on SSA generated by a fritted bubbler and total ion intensity analysis of SSA generated by a marine aerosol reference tank were compared with observations of ambient SSA observed at two coastal locations. Analysis of SSA produced utilizing controlled laboratory methods reveals that single particle mass spectra with weak sodium ion signals can be produced by the desorption of the surface of typical dry SSA particles comprised of salt cores and organic rich coatings. Thus, this lab-based study for the first time unifies findings from offline and online measurements as well as lab and field studies of SSA particle mixing state

3.2 Introduction

Atmospheric aerosols impact climate by interacting directly with incoming solar radiation and indirectly through influencing cloud properties by serving as cloud condensation (CCN) and ice nuclei [*Haywood and Boucher*, 2000; *Lohmann and Feichter*, 2005]. Sea spray aerosols (SSA) represent one of the most abundant types of tropospheric aerosols [*Textor et al.*, 2006]. The ability to determine the radiative forcing of anthropogenic aerosols is limited by the uncertainty of the impact of large natural sources of aerosols on current total aerosol radiative forcing [*Stocker et al.*, 2013]. SSA are ejected into the atmosphere when bubbles burst at the air-sea interface [*Blanchard and Woodcock*, 1957].

Previous field and lab studies have shown that SSA is a complex mixture of inorganic salts and an array of dissolved and particulate organic components [*Gantt and Meskhidze*, 2013; *Quinn et al.*, 2015]. Modeling studies have indicated that the mixing state of submicron SSA can have important effects on predicted CCN concentrations [*O'Dowd et al.*, 2004; *Meskhidze et al.*, 2011; *Gantt et al.*, 2012; *Westervelt et al.*, 2012], while the three-dimensional chemical structure and mixing state of supermicron SSA can affect light scattering due to changes in water uptake at sub-saturated relative humidities [*Saxena et al.*, 1995; *Forestieri et al.*, 2016]. Additionally, the supermicron size range is where the bulk of SSA surface area resides, and thus plays a key role in light scattering and interactions with gaseous species [*Lewis and Schwartz*, 2004a, 2004b; *Fan and Toon*, 2011].

In an effort to characterize the diversity in chemical mixing state of SSA, field studies employing off-line microscopy and spectroscopy techniques have helped illustrate the array of submicron SSA particle types [*Hawkins and Russell*, 2010; *Russell et al.*, 2010; *Orellana et al.*, 2011; *Ault et al.*, 2013c; *Gantt and Meskhidze*, 2013; *Park et al.*, 2014]. In contrast, offline chemical analysis techniques have found the vast majority of dry supermicron particles to be phase-separated inorganic cuboids with amorphous coatings [*Posfai et al.*, 1995; *Leck and Bigg*, 2008; *Wise et al.*, 2009; *Russell et al.*, 2010; *Hawkins and Russell*, 2010; *Maskey et al.*, 2011; *Laskin et al.*, 2012; *Ault et al.*, 2013a, 2013b, 2013c; *Gantt and Meskhidze*, 2013; *Collins et al.*, 2014; *Chi et al.*, 2015; *Lee et al.*, 2015; *Patterson et al.*, 2016]. Elemental analyses have shown that the inorganic cores are mainly composed of sodium chloride, while organic compounds along with minor inorganic species, such as magnesium, potassium, and calcium, are heavily enriched in the amorphous coating or surface localized nodules [*Posfai et al.*, 1995; *Hawkins and Russell*, 2010; *Russell et al.*, 2010; *Ault et al.*, 2013a, 2013b, 2013c; *Chi et al.*, 2015; *Patterson et al.*, 2016]. These results are in agreement with efflorescence studies of particles generated from natural seawater and model salt solutions, which demonstrated that after drying the particles consist of sodium chloride cores with the particle surface enriched in the minor inorganic components such as magnesium, potassium, and calcium [*Ge et al.*, 1996, 1998a; *Cziczo et al.*, 1997; *Liu et al.*, 2008; *Xiao et al.*, 2008; *Harmon et al.*, 2010; *Tong et al.*, 2011; *Gupta et al.*, 2015]. Although the amount of the coating material can vary between particles, offline chemical analysis has generally shown a single type of dry supermicron SSA particle with the population represented as an internal mixture of salt and organic species. While it is known that the bubble bursting process can eject both fragmented and intact microbiological cells [*Blanchard and Syzdek*, 1982; *Patterson et al.*, 2016], findings from spectromicroscopy techniques suggest that particles containing whole cells are rare. However, the collection and analysis methods are often not optimal for preserving cellular structures, and the sample throughput is often low. Consistent with this result, single bubble bursting experiments have reported the fraction of collected film and jet drops containing bacteria cells to be ~1% and less than 0.1%, respectively [*Blanchard and Syzdek*, 1974, 1978, 1982]. However, analysis of dried SSA by online single particle mass spectrometry (SPMS) has described an externally mixed population. Analysis based upon mass spectral signatures has identified three distinct particle types contributing significantly to the supermicron SSA population: sea salt (SS), sea salt with organic carbon (SSOC), and biological or magnesium (Bio) particles [*Gaston et al.*, 2011; *Prather et al.*, 2013; *Collins et al.*, 2014; *Guasco et al.*, 2014]. Bridging the data from both offline and online methods, as well as understanding the factors that affect the mixing state of supermicron SSA particles is a requirement for understanding the water uptake and light scattering properties of marine aerosols.

Particles with core-shell morphologies, comprised of specific components making up the core of the particle with other chemical species forming an outer layer were generated in previous laboratory studies and studied with SPMS [*Carson et al.*, 1997b; *Woods et al.*, 2002; *Cai et al.*, 2006; *Zelenyuk et al.*, 2008b; *Cahill et al.*, 2015a]. By varying the energy of the laser pulse that desorbs and ionizes the core-shell particles, these studies have illustrated that depth profiling of particles can be accomplished in real time. Lower laser fluence tends to partially desorb the particle, generating mass spectra (MS) that are representative of the surface components, whereas higher laser fluence typically desorbs a greater fraction of the particle, generating MS with greater ion signal contribution from core components. However, it has also been shown that even performing laser desorption/ionization using a consistent laser pulse energy on well-controlled particles of similar composition, there can be considerable variation in the laser fluence experienced by individual particles resulting in a range of mass spectra [*Carson et al.*, 1997b; *Wenzel and Prather*, 2004; *Zelenyuk et al.*, 2008b; *Cahill et al.*, 2015a]. Considering the structural observations of SSA by spectromicroscopy, combined with the variations in desorption/ionization common to SPMS, the range of MS patterns generated by SSA may be, at least in part, a result of the structural heterogeneity of dry supermicron SSA. Total ion intensity of each mass spectrum has been utilized as an indirect measure of the extent of particle desorption (proportional to the laser fluence experienced by the particle), and on average, mass spectra of

SSA particles that had low total ion intensity were relatively rich in Mg, K, and Ca [*Ault et al.*, 2013a].

This study extends the complexity of previous single particle mass spectrometry studies in an effort to inform the existing descriptions of the chemical mixing state of supermicron SSA particles. Aerosol time-of-flight mass spectrometry (ATOFMS) was used to perform a detailed analysis of laser desorption/ionization mass spectra of dry supermicron SSA sampled from three different sources: (1) SSA generated by bubbling seawater using a sintered frit, (2) SSA generated in a Marine Aerosol Reference Tank (MART), and (3) SSA sampled in ambient aerosol during two coastal field studies.

Depth profiling of frit-generated SSA was performed using ATOFMS. The results from the depth profiling study, the first to be performed on SSA particles utilizing SPMS, are extended to the MART and ambient generation schemes by examining the relationship of the relative sodium ion signal to mass spectral patterns and total ion intensity. Finally, this new approach is applied to sodium deficient and sodium rich SSA mass spectra collected during two coastal field studies. This study aims to unify the description of the mixing state and chemical composition of supermicron SSA by offline spectroscopy and microscopy techniques with real-time analysis by single particle mass spectrometry.

3.3 Methods

3.3.1 SSA Generation

3.3.1.2 Fritted Bubbler

On 1/18/16 seawater was collected from the coastal Pacific Ocean at Scripps Pier (La Jolla, CA; 32°51′56.8"N: 117° 15′38.48"W; 275 m offshore) at least 5 meters below the low tide line and passed through a sand bed filter to remove large debris**.** The water was then filtered through 0.8 μm and then 0.2 μm filters to remove biological particles such as bacteria and phytoplankton cells. 350 mL of the filtered seawater was then added to a 500 mL gas washing bottle or 'fritted bubbler' (Ace Glass) previously combusted at 400 °C for 6 h. Zero air (Sabio 1001) was flowed through the sintered glass filter or 'frit' (Pore Size C: 25-50 μm), submerged at a depth of roughly 17 cm, at a rate of 0.04 L/min to generate bubbles that rose through the seawater column, breaking at the surface to generate SSA particles used in the analyses described below. Additional zero air was added to the sample line after the bubbler to maintain a flow rate above 1 LPM (~1.25 LPM). Silica gel diffusion dryers were placed between the bubbler and the ATOFMS inlet to dry the particles (RH < 10%).

3.3.1.3 MART

Coastal Pacific seawater (60 L) was collected from the ocean surface at Scripps Pier (La Jolla, CA; 32°51´56.8"N: 117° 15´38.48"W; 275 m offshore) on 6/11/13 16:00 and added without treatment or filtering to a 100 L MART system [*Stokes et al.*, 2013]. At the time of collection, the chlorophyll-a concentration, water temperature, and salinity were 0.04 mg/m^3, 19.4 °C, and 33.6 PSU. SSA particles were generated in the MART using the pulsed plunging waterfall technique described in detail previously, with a 4 second waterfall duty cycle [*Stokes et al.*, 2013]. Two silica gel diffusion dryers were placed between the MART and the ATOFMS inlet to dry the particles (RH ~15%).

3.3.1.4 MART

Coastal Pacific seawater (60 L) was collected from the ocean surface at Scripps Pier (La Jolla, CA; 32°51´56.8"N: 117° 15´38.48"W; 275 m offshore) on 6/11/13 16:00 and added without treatment or filtering to a 100 L MART system [*Stokes et al.*, 2013]. At the time of collection, the chlorophyll-a concentration, water temperature, and salinity were 0.04 mg/m^3, 19.4 °C, and 33.6 PSU. SSA particles were generated in the MART using the pulsed plunging waterfall technique described in detail previously, with a 4 second waterfall duty cycle [*Stokes et al.*, 2013]. Two silica gel diffusion dryers were placed between the MART and the ATOFMS inlet to dry the particles (RH ~15%).

3.3.1.5 CIFEX

ATOFMS measurements of ambient aerosols were made during the Cloud Indirect Forcing Experiment (CIFEX) at a coastal site in Trinidad Head, CA (41.05° N: 124.15° W) in April 2004 [*Holecek et al.*, 2007]. Aerosols were collected at a height of 10 m, and the sampling inlet was heated to maintain the RH at 55%.

3.3.1.6 CalWater2

ATOFMS measurements of ambient aerosols were made during the CalWater2 field study at a coastal site in Bodega Bay, CA on the grounds of Bodega Marine Laboratory (39.32° N: 123.07° W) from January to March 2015 [*Martin et al.*, 2017]. Aerosols were collected at a height of five meters and silica gel diffusion dryers were placed before the ATOFMS inlet to reduce the RH of sampled air to ~15%.

3.3.2 Measurement of SSA Composition via ATOFMS

The size-resolved chemical composition of individual dry SSA particles with vacuum aerodynamic diameters (d_{va}) between 1 - 3 μm were measured in real time by ATOFMS. The measured vacuum aerodynamic size distribution of the sampled particles is provided in Figure 3.6 along with estimated aerodynamic and volume equivalent distributions (3.6.1). A detailed discussion of ATOFMS has been given previously [*Noble and Prather*, 1996; *Gard et al.*, 1997], so only a brief description follows here. Aerosol particles are drawn into a differentially pumped vacuum chamber through a converging nozzle inlet, wherein particles are accelerated to their size-dependent terminal velocities. Aerosol particles are sized based on the time required to transit two continuous wave laser beams (532 nm). The velocity is converted to vacuum aerodynamic diameter via calibration with polystyrene latex spheres (Invitrogen) of known diameter and density. When each particle arrives in the ion source region of the mass spectrometer, a Q-switched Nd:YAG laser pulse (266 nm wavelength, 8 ns pulse width, 700 µm spot size), triggered based on the velocity of particle, desorbs and ionizes each particle's chemical components. Laser pulse energy was kept constant at approximately 1.1-1.3 mJ for the MART, CIFEX, and CalWater2 studies. For the frit-generated SSA studies, the energy of the laser pulse was varied between 0.6-1.5 mJ, and mass spectra from 800-1300 particles were collected at each laser energy. Below 0.6 mJ, the percentage of particles generating MS dropped considerably, precluding the use of such low laser pulse energies for these experiments. The exact laser fluence that each particle experiences is variable even at a constant laser energy setting due to the Gaussian profile of the laser beam, hot spots in the laser beam, and shot-to-shot variations in laser pulse characteristics [*Wenzel and Prather*, 2004]. The positive and negative ions produced are detected by a dual-polarity reflectron time-of-flight mass spectrometer. Single particle mass spectra and size data were analyzed using the software toolkit, FATES [*Sultana et al.*, 2016].

3.3.3 Analysis of Particle Mass Spectra

Note that all analyses included in this study were performed on particles with d_{va} between 1 and 3 µm. Particles were binned by the fraction of positive mass spectral intensity attributable to sodium and sodium chloride containing ions (F_{Na}): $^{23}Na^+$, $^{46}Na_2^+$, $^{81,83}Na_2Cl^+$, $^{139,141,143}Na_3Cl_2^+$, $^{197,199,201}Na_4Cl_3^+$, $^{255,257,259}Na_4Cl_3^+$. Peak assignments correspond to the most likely ion produced at a specific mass-to-charge ratio (*m/z*). For consistency, only positive sodium ion markers were utilized as negative MS were not detected for every instance of a positive MS. Note that total positive ion intensities are the summation of all positive ion signal and are normalized to the maximum value within each dataset. Based upon similarity to the mass spectral fingerprints of the lab-generated SSA a subset of mass spectra most likely to represent freshly generated SSA particles were identified within the field study datasets. Mass spectra that contained indications of terrestrial or anthropogenic sources (e.g. nitrate, biomass burning, dust, soot) were eliminated. Mass spectra identified as likely generated by cellular material based upon comparison to the literature, with dominant potassium and phosphate ion markers [*Fergenson et al.*, 2004; *Russell*, 2009; *Gaston*, 2012; *Cahill et al.*, 2015b], were not included in the SSA analysis for the field studies due to the possibility of a biological terrestrial source. See supporting information for more detail on the analysis of the laboratory and field data.

3.4 Results and Discussion

3.4.1 Effect of Laser Power on Supermicron SSA Mass Spectra

Supermicron SSA particles (dry d_{va} = 1–3 μm) generated from natural seawater utilizing a fritted bubbler were analyzed via ATOFMS, varying the pulse energy of the desorption/ionization laser from 0.6 to 1.5 mJ. It is important to note that the bubbled seawater was filtered to remove most insoluble biological components such as bacteria and phytoplankton cells and preclude such material from being aerosolized and contributing to the mass spectra generated. Data from all laser energy conditions were compiled, and then the average normalized MS for particles with differing fractions of positive mass spectral intensity from sodium were calculated. For the purposes of this study, all particles with F_{Na}, fraction of sodium-containing positive ion signal, greater and less than 0.4 are referred to as Na-rich and Na-deficient, respectively. Mass spectra with a lower F_{Na} have higher relative contributions from components that are expected to exist at the surface of dried SSA particles, including calcium ($^{40}Ca^+$, $^{57}CaOH^+$, $^{75}CaCl^+$ $^{96}Ca_2O^+$, $^{145,147,149}CaCl_3^-$), magnesium ($^{24}Mg^+$, $^{129,131,133}MgCl_3^-$), potassium ($^{39}K^+$, $^{109,111,113}KCl_2^-$), and organic material ($^{27}C_2H_3^+$, $^{27}CHN^+$, $^{37}C_3H^+$, $^{43}C_2H_3O^+$, $^{43}CHNO^+$, $^{59}C_3H_9N^+$, $^{26}CN^-$, $^{42}CNO^-$, $^{43}C_2H_3O^-$) in both negative and positive mass spectra (Figure 3.7). Interestingly, the average normalized MS with high (0.8-1), medium (0.4-0.6), and low (0.0-0.1) F_{Na} are similar to the representative mass spectral fingerprints of the SS, SSOC, and Bio type particles that have been identified by previous SPMS analyses [*Gaston et al.*, 2011; *Prather et al.*, 2013; *Guasco et al.*, 2014]. Based solely on these results two potential explanations present themselves. Firstly the three types of mass spectra could be derived from a single population of phase-separated particles with chemical spatial heterogeneity, such as the core-shell morphology previously described. Alternatively a collection of three somewhat distinct particle types could exist in the aerosol population. Results from the different laser pulse energy trials were used to distinguish between these two possibilities by providing information on the three-dimensional chemical morphology of the particles.

Previous studies utilizing SPMSs have reduced the pulse energy of the desorption/ionization laser to selectively detect components on the surface of particles with known core-shell morphologies [*Carson et al.*, 1997b; *Woods et al.*, 2002; *Cai et al.*, 2006; *Zelenyuk et al.*, 2008b; *Cahill et al.*, 2015a]. As the laser pulse energy was increased from 0.6 to 1.5 mJ the fraction of Na-rich MS dramatically increased from 39% to 77.5% (Figure 3.1). As indicated in the schematic in Figure 3.1, the greater sodium signal at higher laser energy (more complete particle desorption/ionization) is consistent with structurally heterogeneous particles in which sodium is located in the core. Lower laser energies were more likely to desorb/ionize only small amounts of each particle, and the generated mass spectra had relatively greater contributions from components such as magnesium and organics. As discussed earlier, spectromicroscopy studies have shown that dried nascent SSA are dominated by a single type of structurally heterogeneous particles with magnesium, calcium, sulfate, potassium, and organics concentrated on the outside in an amorphous coating or sometimes in distinct nodules surrounding cores of sodium chloride [*Russell et al.*, 2010; *Ault et al.*, 2013a, 2013c; *Patterson et al.*, 2016].

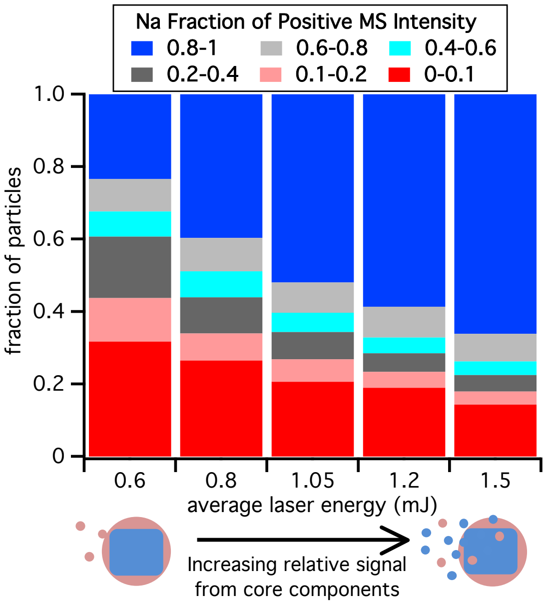

Figure 3.1 The distribution of the relative sodium ion contribution to the total positive ion intensity for supermicron SSA, generated by frit bubbled seawater analyzed by ATOFMS using five different desorption/ionization laser pulse energies.

The depth profiling results indicate that the variety of supermicron SSA mass spectra observed by ATOMFS could be attributed to a population of core-shell particles encountering a range of desorption/ionization conditions within the instrument.

3.4.2 Relationship of Chemical Signal to Total Positive Spectrum Ion Intensity

Studies of lab-generated particles with well characterized and controlled core-shell morphologies have shown that total positive ion intensity increases with increasing relative contribution from components in the core of the particle [*Pegus et al.*, 2005; *Zelenyuk et al.*, 2008b]. The use of total ion intensity as a method to discriminate between mass spectra that were generated in association with varying degrees of particle desorption (surface vs. core) has been employed previously for lab-generated SSA [*Ault et al.*, 2013a]. Particles analyzed in this study, however, were grouped by the fraction of positive ion signal from sodium rather than by the explicit total ion intensity as in the prior study.

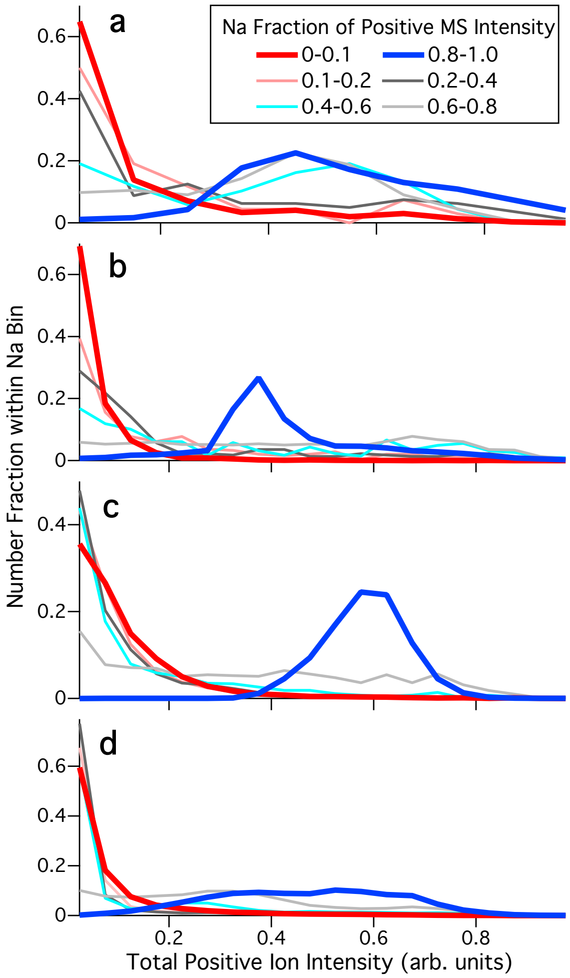

Figure 3.2 The distribution of total positive ion intensity grouped by the fraction of positive mass spectral sodium intensity for supermicron SSA particles generated by the (a) frit bubbled seawater and (b) MART, and sampled during (c) CIFEX and (d) CalWater-2. Total intensity values were normalized within each dataset.

The total positive ion intensity distribution for each group of mass spectra binned by F_{Na} was calculated for all supermicron particles. The results for the 1.2 mJ laser energy trial are shown in Figure 3.2, and are representative of the results across all laser pulse energy (0.6-1.5 mJ) ranges examined (Figure 3.8). At higher F_{Na} the total positive ion intensity distribution shifted to higher values (Figure 3.2-3.3). The increase in total positive ion intensities with increasing relative sodium ion signal is consistent with increasing particle desorption as shown in the conceptual cartoon in Figure 3.1. These results are in good agreement with previous analyses of SSA particles by ATOFMS that grouped particles explicitly by total mass spectral intensities [*Ault et al.*, 2013a]. However, even when sodium rich mass spectra were detected, particle desorption was likely not complete as the total positive ion MS intensity did not increase with size (Figure 3.9).

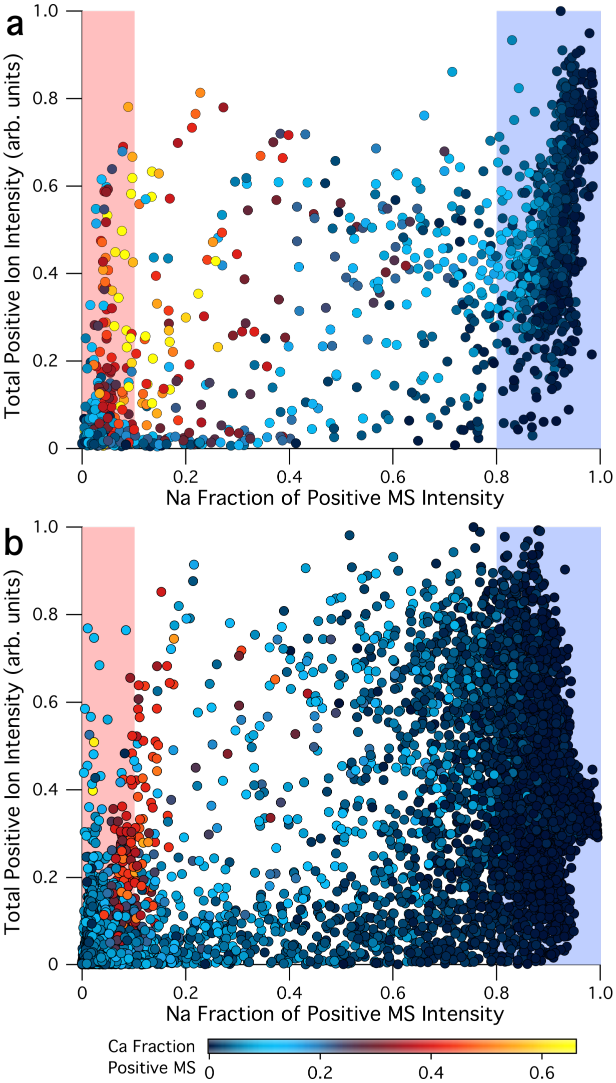

Figure 3.3 The sodium ion fraction versus the relative total ion intensity for each positive mass spectrum generated by supermicron SSA from the (a) frit bubbled seawater and (b) MART (1.2 mJ laser pulse energy). Warmer marker shades indicate higher calcium ion fraction in the positive mass spectra.

The generally low positive ion intensity of Na-deficient mass spectra supports the conclusion that these MS are mainly representative of the particle surface which has been shown to be enriched in organics and minor inorganic seawater components via offline techniques. However, it appears that the outlying sodium deficient mass spectra with relatively high total ion intensities also have high contributions from positive calcium ion markers ($^{40}Ca^+$, $^{57}CaOH^+$, $^{75,77}CaCl^+$, $^{96}Ca_2O^+$) (Figure 3.3). This behavior is likely still attributable to the morphology of dry SSA particles. For both SSA generated by the fritted bubbler and the MART the relative calcium ion contribution and the relative sulfate ion contribution ($^{48}SO^-$, $^{64}SO_2^-$, $^{80}SO_3^-$) have a positive correlation ($r^2_{bubbler} = 0.35$, $r^2_{MART} = 0.44$) (Figure 3.10). Calcium sulfate, calcium sulfate hydrates, and sodium calcium sulfate salts are well known to precipitate and crystallize initially during the dehydration of seawater and seawater droplets [*Hardie and Eugster*, 1980; *Xiao et al.*, 2008; *Tong et al.*, 2011]. Nodules or crystals rich in calcium and sulfur have been observed in dry SSA particles adhered to the outside of sodium chloride rich cores [*Ault et al.*, 2013a, 2013c]. It is possible that desorption and ionization of calcium sulfate crystals on the surface of dry SSA particles generates sodium deficient mass spectra but with more ion intensity than when only desorption of the amorphous and relatively thin coating occurs. The infrequency of these relatively intense calcium rich mass spectra may be because these crystals or nodules are less ubiquitous than the amorphous coating and localized to a specific region of a particle. Overall the relationship between the positive mass spectral ion markers and total positive ion intensity is consistent with the known core-shell morphologies of dry supermicron SSA.

3.4.3 SSA Mass Spectral Consistency between Laboratory and Field Studies

The data analyses described in the previous sections for SSA generated from bubbled seawater were also performed on dry supermicron SSA generated by a MART and from two field studies (CIFEX, CalWater2). For the MART and field studies, the particles were binned by F_{Na}

(Table 3.1) and the average mass spectra were similar to the results from SSA generated by bubbled seawater (Figure 3.7). In addition, for all four datasets the population of mass spectra with the highest F_{Na} (0.8-1) had higher total ion intensities than the preponderance of mass spectra with the lowest F_{Na} (0-0.1). These results strongly suggest that the supermicron SSA generated by the fritted bubbler, MART, and sampled during field studies are all similar in composition and morphology. Therefore, for all datasets the supermicron SSA population is likely dominated by a single particle type that, once dried, is structurally heterogeneous. Such particles exhibit a sodium chloride core with a surface enriched in organic material and minor inorganic seawater components. Some differences in the thickness of the sodium chloride deficient particle coating are likely to exist, as illustrated by images of typical ambient, MART, and frit generated dry SSA particles from prior studies (Figure 3.11) [*Collins et al.*, 2014]. While the morphology of dried SSA particles will not be representative of their hydrated structure under relatively humid ambient conditions, studying dried phase-separated particles provides a standard and experimentally simple common basis for analyzing chemical composition across an array of different methods.

Results from this study demonstrate that sodium deficient mass spectra, which are relatively rich in species such as magnesium, can be generated from desorption and ionization of the surface of dried SSA. Since the acquisition of mass spectra that differentially represent the core and surface coating of dry SSA is mostly a function of the instrumental operating conditions (e.g., laser pulse energy), the ratio of sodium rich to sodium deficient mass spectra should be relatively constant. To examine this hypothesis, the fraction of identified fresh SSA Na-rich and Na-deficient mass spectra within two-hour time bins was calculated for two field studies performed on the west coast of North America, CIFEX and CalWater2 (Figure 3.4). In both studies the fraction of Na-deficient mass spectra to the fraction of Na-rich mass spectra shows a generally positive trend as expected, though the correlations are poor (r^2_{CIFEX} = 0.28, r^2_{CW2} = 0.17). Notably, the CIFEX results here are in close agreement with a previous analysis where the MS were grouped by a clustering algorithm and "fresh SS" and "Mg-type" particle types, very similar to the average MS for high and low F_{Na} (Figure 3.7) respectively, were found to be well correlated [*Gaston et al.*, 2011].

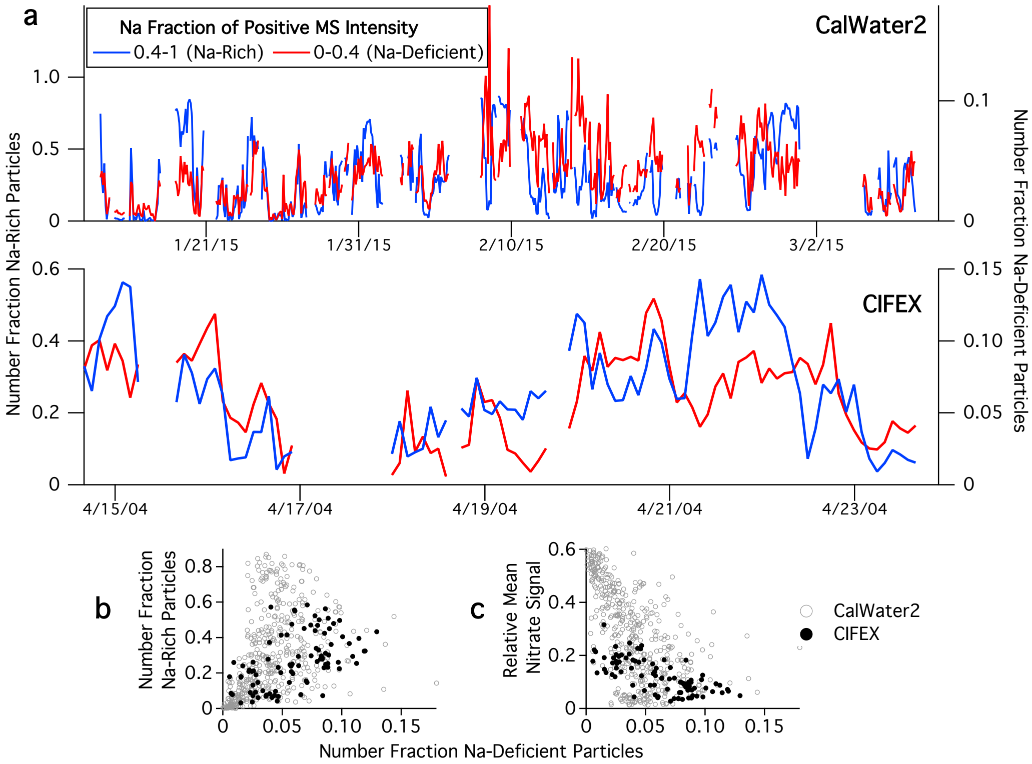

Figure 3.4 (a) The temporal trends for the fraction of ambient particles identified as SSA with sodium fractions of 0.4-1 (Na-rich) and 0-0.4 (Na-deficient) shown for two coastal field studies, CalWater2 and CIFEX. (b) Scatter plots of the number fraction of Na-deficient particles against the number fraction of Na-rich particles and (c) the relative mean signal from nitrate and sulfate markers in the total aerosol population.

To further support the assignment of the Na-deficient mass spectra as fresh SSA, versus terrestrial or anthropogenic particle types, the mean relative nitrate and sulfate ion signal ($^{46}NO_2^-$, $^{62}NO_3^-$, $^{97}HSO_4^-$, $^{125}H(NO_3)_2^-$, $^{147}Na(NO_3)_2^-$, $^{160}HNO_3HSO_4^-$, $^{188}(HNO_3)_2NO_3^-$) for all mass spectra detected was calculated for each time bin. Particle phase nitric and sulfuric acid is indicative of air masses influenced by anthropogenic pollution and secondary aging processes. It is anticipated that the fraction of Na-deficient, fresh SSA mass spectra will be negatively correlated with air masses not abundant in fresh SSA, and therefore the mean relative nitrate ion signal and sulfate ion signal. The results show a general negative trend ($r^2_{CIFEX} = 0.48$, $r^2_{CW2} = 0.35$).

While the resulting relationships generally support the conclusion that the identified Na-rich and Na-deficient mass spectra originate from the same particle type, large variation exists in the data. Variations in the Na-rich to Na-deficient ratio may be driven by the analytical difficulties associated with utilizing field study datasets for this specific type of investigation. This analysis depends upon accurately identifying SSA mass spectra in an uncontrolled environment. However, there are a variety of particle types, such as dust, biomass burning, and cellular material, which can generate mass spectra rich in magnesium, calcium, potassium, and/or organic ion markers. It is possible that some Na-deficient mass spectra included were not generated by surface desorption of SSA particles. Additionally it is key to include only MS from fresh SSA that have not been aged by secondary processes which have been shown to change the three-dimensional physicochemical structure of SSA [*Ault et al.*, 2013a]. However, negative MS, which frequently contain the secondary processing ion markers, are generated with less frequency than positive MS, particularly for low ion intensity mass spectra.

In addition, changes in seawater chemistry have been shown to influence SSA organic content and therefore also likely modify the thickness of the sodium deficient shell [*O'Dowd et al.*, 2004; *Yoon et al.*, 2007; *Cochran et al.*, 2016b]. It is expected that increases in the thickness of the organic coating on dry supermicron SSA particles would directly correspond to an increase in the fraction of Na-deficient mass spectra generated at a constant laser pulse energy [*Cai et al.*, 2006; *Zelenyuk et al.*, 2008b]. Therefore some of the variation in the ratio of Na-rich to Na-deficient MS noted in the field studies may be a result of changing seawater chemistry. While the paradigm that this study establishes with respect to interpretation of single particle mass spectra of SSA should find facile utility for studies of nascent SSA, there are still difficulties in applying this framework to complex field study datasets.

3.4.4 Contribution of Particulate Biological Components to SSA MS

The MART and bubbled seawater datasets were highly similar, however only the bubbled seawater was filtered to remove microbial cells. This suggests that intact cells or cell fragments were not abundant in the MART supermicron SSA or that mass spectra generated by aerosolized cells could not be reliably distinguished from those obtained from other salt and organic matter-containing supermicron SSA particles. As described, ion signatures which have been previously associated with cellular single particle mass spectra, such as organic, potassium, calcium, and phosphate ion markers, can be generated from the surface desorption of the structurally heterogeneous dried supermicron particles. It is important to note that while intact biological particles can be ejected in and have been identified in SSA [*Leck and Bigg*, 2005b; *Patterson et al.*, 2016], it is difficult to unequivocally assign a mass spectral pattern to aerosolized marine cells without more subtle data analysis methods or further information about the particles' properties. Therefore, further correlated information (e.g., fluorescence) may be required to identify and quantify the abundance of microbial cells ejected from the surface ocean.

3.4.5 Interpreting mass spectra from SPMS studies of SSA

Other than ejected particles composed of particulate biological components, the chemical composition of most supermicron SSA in the size regime examined (d_{va} = 1-3 μm) is expected to be relatively similar between particles [*Gantt and Meskhidze*, 2013]. However within each particle, spectromicroscopy analyses have shown a great deal of spatial heterogeneity in the structure of dry SSA particles [*Posfai et al.*, 1995; *Hawkins and Russell*, 2010; *Russell et al.*, 2010; *Ault et al.*, 2013a, 2013b, 2013c; *Deng et al.*, 2014; *Patterson et al.*, 2016]. Studies of dehydrated natural and model seawater droplets show that particles exhibit a core-shell morphology, with sodium chloride rich cores and nodules of calcium sulfate and an amorphous coating rich in magnesium, potassium, organics and other minor inorganic components at the surface [*Ge et al.*, 1996, 1998a; *Cziczo et al.*, 1997; *Liu et al.*, 2008; *Xiao et al.*, 2008; *Harmon et al.*, 2010; *Tong et al.*, 2011; *Gupta et al.*, 2015]. SPMS analysis of morphologically-controlled core-shell particles has shown that even at a constant laser pulse energy setting there is wide particle-to-particle variability in the ratio of signal from surface and core components in single particle mass spectra [*Carson et al.*, 1997b; *Zelenyuk et al.*, 2008b; *Cahill et al.*, 2015a]. This variation exists despite the chemical and morphological similarities between the lab-generated core-shell particles. As seen in this study, mass spectra with a wide range of sodium fractions were generated for all laser energies, which is consistent with previous studies of core-shell particles. However, the wide variability in signal response illustrates the complexity in analyzing SPMS data sets.

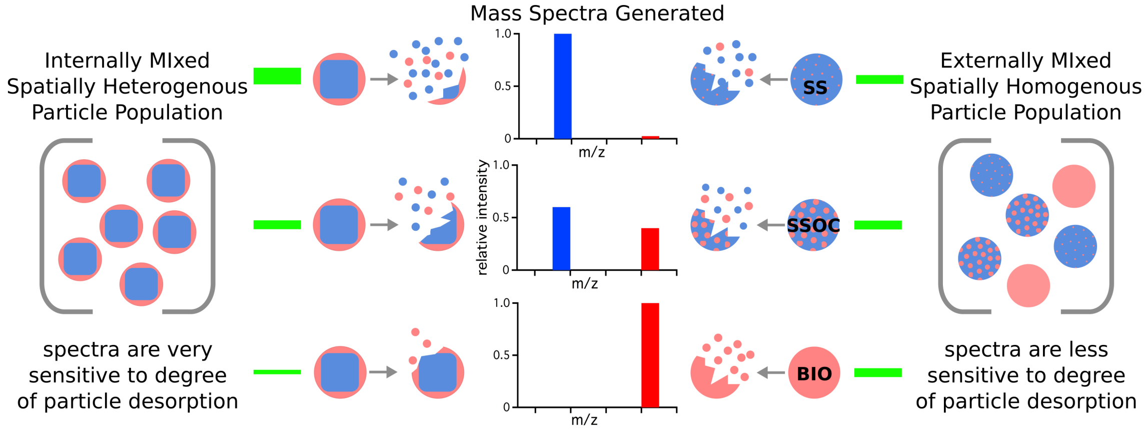

Figure 3.5 A schematic illustrating how two different particle populations could both generate a similar suite of relative mass spectra by laser desorption/ionization, the ionization method utilized by SPMS.

The schematic in Figure 3.5 illustrates that when analyzing single particle mass spectra of SSA, or any population of particles with structural heterogeneity, distinctions between relative mass spectra are not necessarily indicative of an externally mixed, chemically distinct particle population. Rather we have shown that varying degrees of laser desorption and ionization of core-shell SSA particles can produce MS with high, medium, and low sodium ion contributions which have been previously characterized as originating from distinct SS, SSOC, and Bio SSA particle types respectively [*Gaston et al.*, 2011; *Prather et al.*, 2013; *Collins et al.*, 2014; *Guasco et al.*, 2014]. Utilizing the paradigm established, increases in the fraction of low intensity and sodium deficient mass spectra generated by dried supermicron SSA should likely be interpreted as increases in the thickness of the amorphous coating on typical SSA particles rather than an appearance of a new distinct sodium deficient particle type. Leveraging depth profiling analysis and examining trends in total ion intensity coupled with known morphology from spectroscopy and microscopy studies has helped enable this distinction. These results bring real-time chemical analysis of SSA by SPMS into agreement with offline microscopy and spectroscopy descriptions of the supermicron SSA population, which dictates SSA's direct light scattering properties and interactions with gaseous species [*Lewis and Schwartz*, 2004a, 2004b; *Fan and Toon*, 2011]. Importantly, this analysis and new understanding can serve as a foundation for SPMS analysis of SSA, which could be extended in the future to the more complex submicron SSA population. It is important to note that the explicitly varying the laser pulse energy proved to be a useful tool for understanding the three-dimensional structural morphology and composition of atmospheric SSA particles.

3.5 Acknowledgements

This work was supported by the National Science Foundation through the Centers for Chemical Innovation Program via the Center for Aerosol Impacts on Climate and the Environment (CHE-1305427). The authors would like to thank O. Ryder for supplemental atomic force microscopy analysis, all collaborators involved in the MART microcosm studies, notably C. Lee, as well as J. Holecek and G. Cornwell for field study data collection. In addition, the authors would like to acknowledge the Bodega Marine Reserve, University of California Davis, and UC Natural Reserve System for use of Bodega Marine Laboratory facilities.

Chapter 3, in full, is a reprint of material as it appears in Environmental Science and Technology, 2017. Reprinted with permission from Sultana, C. M., Collins, D. B., Prather, K. A. The Effect of Structural Heterogeneity in Chemical Composition on Online Single Particle Mass Spectrometry Analysis of Sea Spray Aerosol Particles. Environ. Sci. Technol. 2017, 51, 3660–3668. The dissertation author was the primary investigator and author of this paper.

3.6 Supporting Information

Table 3.1 Comparison of run times for various operations in YAADA and FATES.

		Sodium ion contribution to postitive mass spectra intensity					
Experiment	**Laser Energy**	*0-0.1*	*0.1-0.2*	*0.2-0.4*	*0.4-0.6*	*0.6-0.8*	*0.8-*
Frit Bubbled							
	0.6 mJ	496 (32%)	188 (12%)	265 (17%)	108 (7%)	140 (9%)	366 (23%
	0.8 mJ	456 (26%)	129 (7%)	171 (10%)	124 (7%)	159 (9%)	682 (40%
	1.05 mJ	390 (21%)	117 (6%)	142 (8%)	101 (5%)	158 (8%)	981 (52%
	1.2 mJ	296 (19%)	68 (4%)	80 (5%)	68 (4%)	133 (9%)	914 (59%
	1.5 mJ	410 (14%)	104 (4%)	131 (5%)	107 (4%)	219 (8%)	1895 (66%
MART	*1.1-1.3 mJ*	4237 (37%)	238 (2%)	217 (2%)	318 (3%)	1007 (9%)	5289 (47%
CIFEX	*1.1-1.3 mJ*	6919 (13%)	2040 (4%)	1419 (3%)	793 (2%)	608 (1%)	40813 (78%
CalWater2	*1.1-1.3 mJ*	24030 (6%)	5451 (1%)	10949 (3%)	12059 (3%)	33793 (9%)	289485 (77%

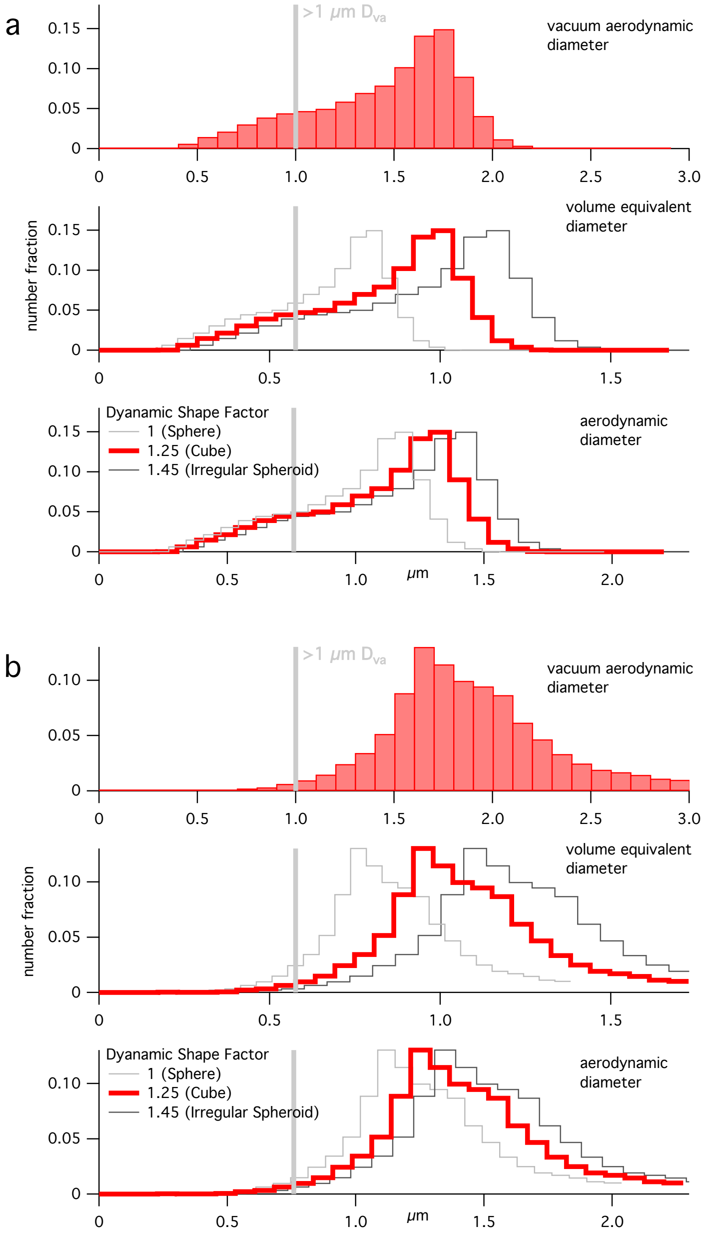

Figure 3.6 The distribution for the measured vacuum aerodynamic diameter of dry SSA particles generated during the fritted bubbler (a) and MART (b) experiments. Corresponding volume equivalent and aerodynamic diameters calculated using the density of sodium chloride and a variety of possible shape factors (6.5.1) are also shown. The grey line indicates 1 um d_{va} in the measured data and the calculated diameters for a shape factor of 1.25.

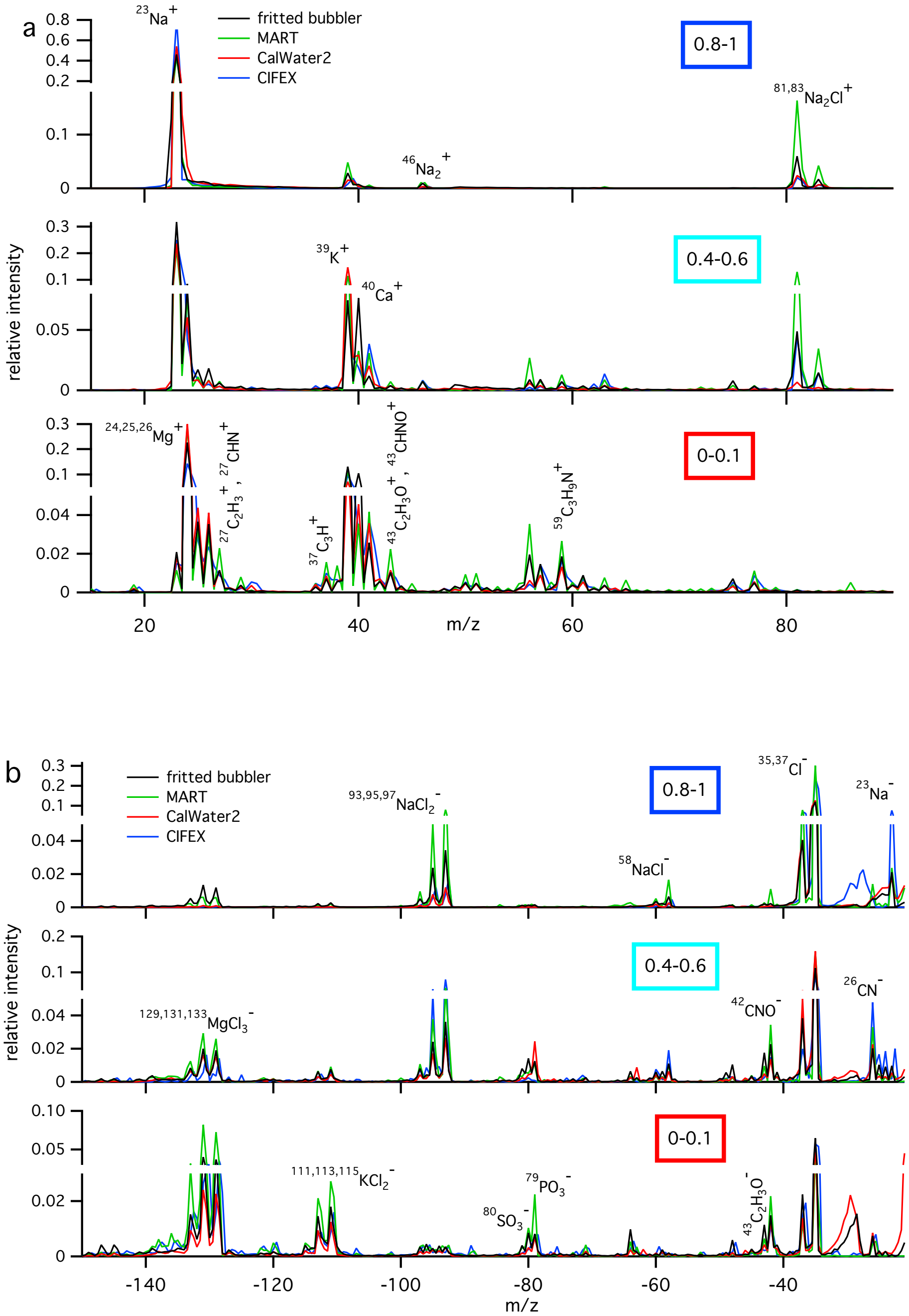

Figure 3.7 Average relative positive ion (a) and negative ion (b) mass spectra (with half-unit resolution) are shown for super-micrometer SSA generated by a MART and frit bubbled seawater as well as sampled during CIFEX and CalWater2 coastal field studies. Particles were grouped by the fraction of positive mass spectral ion intensity from sodium.

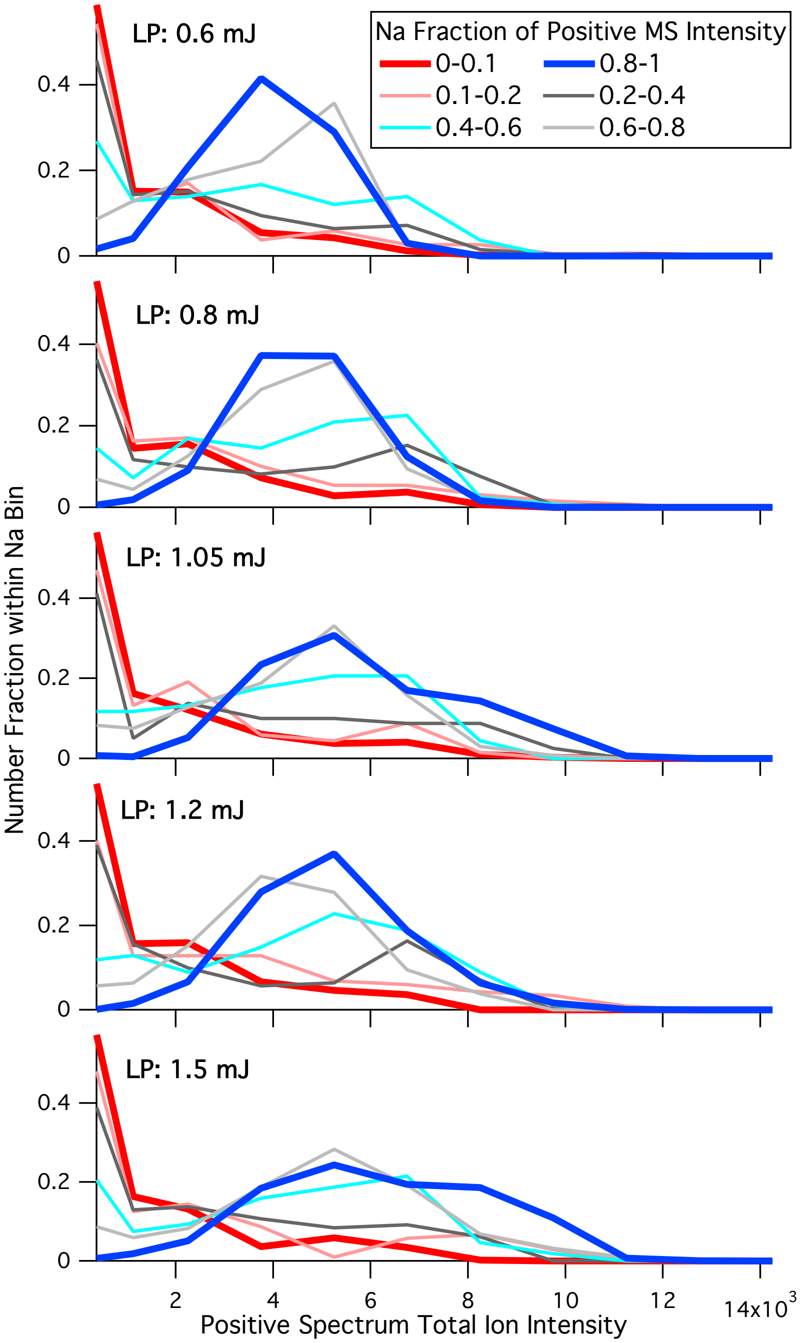

Figure 3.8 The distribution of total positive ion intensity for particles grouped by the fraction of positive mass spectral sodium intensity. Results are shown for supermicron SSA generated by frit bubbled seawater for all the ATOFMS laser pulse energies utilized.

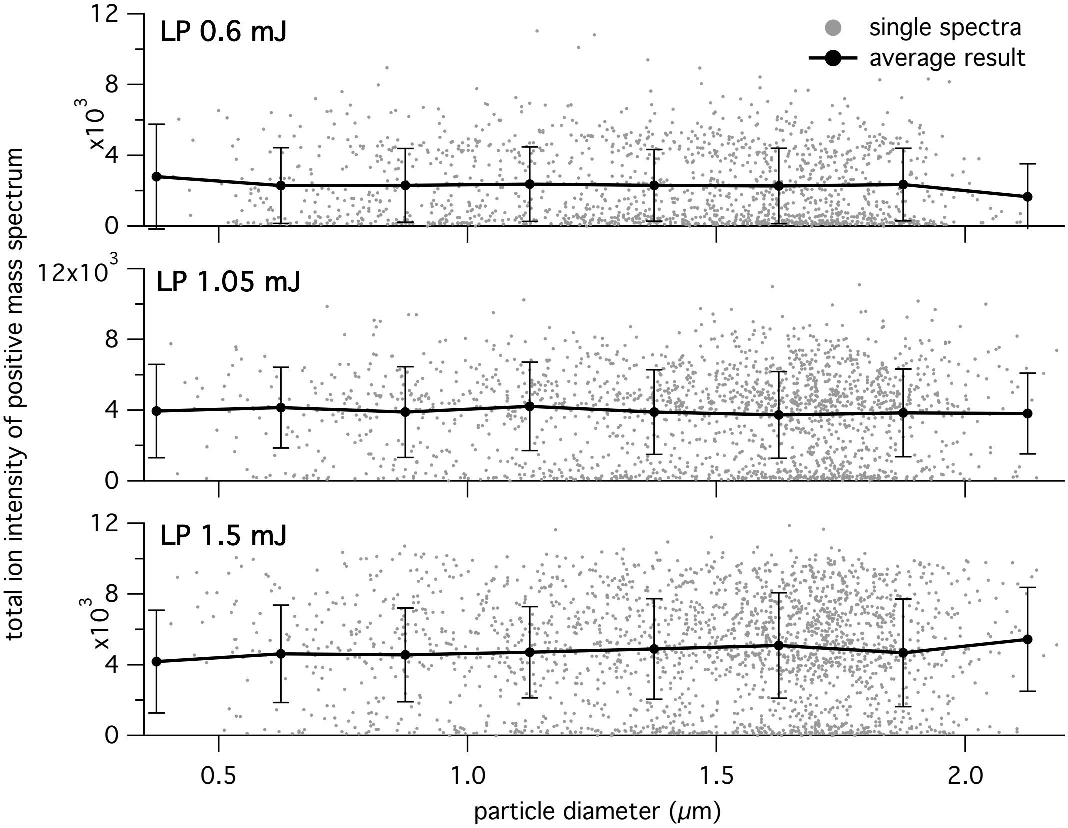

Figure 3.9 The size of each particle plotted versus the total ion intensity for the positive mass spectrum generated. Results are shown for the bubbled seawater experiments with the ATOFMS operated at three laser pulse energies: 0.6 mJ, 1.05 mJ, and 1.5 mJ. The average total ion intensity for each 0.25 μm size bin is also plotted.

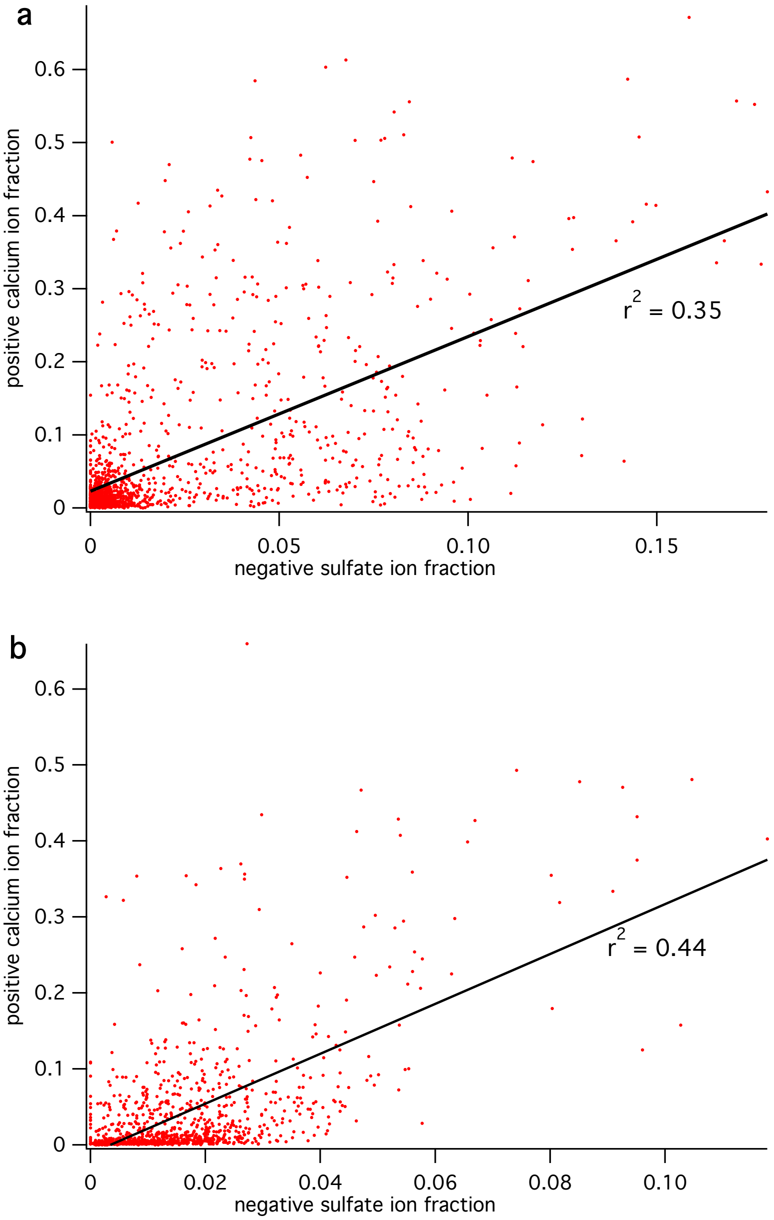

Figure 3.10 Scatter plot of the sulfate ion marker ($^{48}SO^-$, $^{64}SO_2^-$, $^{80}SO_3^-$) contribution to the negative total ion intensity versus the calcium ion marker ($^{40}Ca^+$, $^{57}CaOH^+$, $^{75,77}CaCl^+$, $^{96}Ca_2O^+$) for supermicron SSA generated from the frit bubbled seawater (a) and MART (b) experiments (1.2 mJ laser pulse energy).

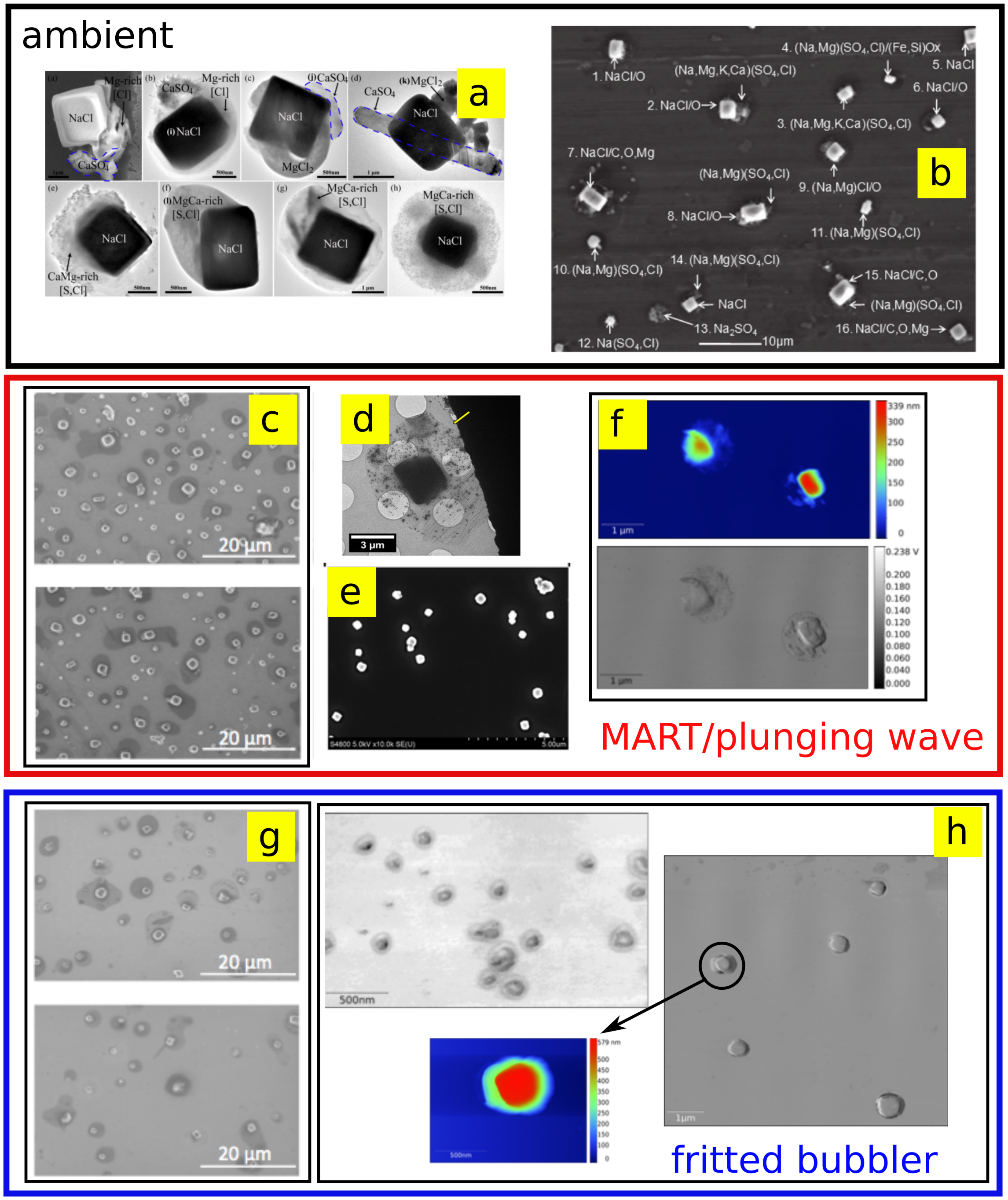

Figure 3.11 Images typical of ambient SSA (a,b) and SSA generated from natural seawater utilizing MART or plunging waterfall (c-f) and fritted bubbler techniques. Panel a is reprinted from *Chi et al.*, *Atmos. Chem. Phys.*, 2015. Panel b is reprinted from *Maskey et al.*, *Environ. Sci. Technol.,* 2011. Panels c and g are reprinted from *Collins et al.*, *Atmos. Meas. Tech.,* 2014. Panel d is reprinted from *Patterson et al.*, *ACS Cent. Sci.*, 2016. Panel e is reprinted from *Lee et al.*, *ACS Cent. Sci.,* 2015. Panel f is AFM phase and height images from SSA generated from a MART using seawater collected 07/14/15.

3.6.1 Method for Converting Particle Diameter

The vacuum aerodynamic diameter (d_{va}) of dry SSA particles was measured via ATOFMS. The continuum regime aerodynamic diameter (d_{ca}) and volume equivalent diameter (d_{ve}) can be estimated using

$$d_{ca} = d_{va}(X_c/\rho_p)^{1/2} \qquad [1]$$

$$d_{ve} = d_{va}(X_v/\rho_p) \qquad [2]$$

where ρ_p is the particle density and X_c and X_v are the dynamic shape factors in the continuum and vacuum regime limits, respectively [*DeCarlo et al.*, 2004]. D_{ca} and d_{ve} were calculated by assuming a particle density of NaCl (2.17 g/cm^3) with a range of possible particle morphologies. Nominal dynamic shape factors for spheres (1), cubes (1.25), and irregular spheroids (1.45) for both X_c and X_v were utilized [*DeCarlo et al.*, 2004].

3.6.2 Methods for Supplementary AFM Analysis

Atomic Force Microscopy. Laboratory generated SSA particles were impacted onto hydrophobically coated (polysiloxanes) Silicon wafer chips (Ted Pella, product number 16008) using stage 6 of a rotating Micro-Orifice Uniform Deposition Impactor (MSP Nano-MOUDI II, model 125R). A Bruker Dimension Icon ScanAsyst Atomic Force Microscope was used to image particles under laboratory temperature and relative humidity conditions (~298K, 19-20 % RH). A ScanAsyst-Air tip (Bruker) was utilized operating in "height" mode for topographical images and in "InPhase" mode for phase images. Raw data images were processed using Gwyddion 2.46 (Open Source software) to obtain usable images. Descriptions of the seawater collection conditions and SSA generation mechanisms are given below.

MART. Coastal Pacific seawater (60 L) was collected from the ocean surface at Scripps Pier (La Jolla, CA; 32°51′56.8"N: 117° 15′38.48"W; 275 m offshore) on 07/14/15 16:30 and added to a 100 L MART system.[*Stokes et al.*, 2013] At the time of collection, the chlorophyll-a concentration, water temperature, and salinity were 0.04 mg/m^3, 19.4 °C, and 33.6 PSU. SSA particles were generated in the MART using the pulsed plunging waterfall technique described in detail previously, with a 4 second waterfall duty cycle.

Fritted Bubbler. Seawater was collected from the coastal Pacific Ocean at Scripps Pier (La Jolla, CA; 32°51´56.8”N: 117° 15´38.48”W; 275 m offshore) at least 5 meters below the low tide line and passed through a sand bed filter to remove large debris**.** 350 mL of the filtered seawater was then added to a 500 mL gas washing bottle or ‘bubbler’ (Ace Glass, Pore Size C: 25-50 μm), previously combusted at 400 °C for 6 h. Zero air (Sabio 1001) was flowed through a submerged sintered glass filter or ‘frit’ at a rate of 0.4 L/min to generate bubbles that rose through the seawater column, breaking at the surface to generate SSA particles.

Chapter 4. Integration of offline and SPMS analyses to obtain a more complete picture of particle morphology and coordination of chemical species within model SSA particles

4.1 Abstract

While a wide array of analyses are available to study atmospheric aerosols, it is difficult to comprehensively describe an aerosol population utilizing a single methodology due to the limitations inherent to each technique. In this study, we integrate complementary offline and single particle mass spectrometry analyses to elucidate new details of intra-particle chemistry for particles produced from a solution of salts and carboxylic acids, a proxy for organic-rich seawater. The first direct comparison of particle organic volume fractions estimated from single particle atomic force microscopy (AFM) analyses and quantitative measurements of the average population composition yield good agreement for particles smaller than 0.5 μm. Above the size range of the AFM, the core-shell morphology of the particles is confirmed by online single particle mass spectrometer (SPMS) analyses, which reveal that the relative sodium ion signal increases with total positive ion intensity. In addition, the online single particle results suggest that the organic-rich shell thickness is increasing with particle size, which is supported by calculations utilizing the average particle compositions and model particle morphologies. In addition, an analysis of the single particle mass spectra, informed by the quantitative composition results and knowledge of particle morphology, suggests that carboxylate species are coordinated to calcium in the dried particle and that these species are potentially thermally desorbed as their preformed ions.

4.2 Introduction

Aerosols are an important component of the Earth's atmosphere, influencing cloud processes, directly scattering and absorbing solar radiation, and providing a site for multiphase chemical reactions. There are a multitude of techniques utilized to describe the mixing state of particle populations, particle chemical composition and morphology, and even intra-particle spatial chemical distributions. Sea spray aerosols (SSA) make up one of the largest mass fluxes of atmospheric aerosols [*Textor et al.*, 2006; *O'Dowd et al.*, 2007] and can influence the scattering of solar radiation in marine regions. As such their chemistry and production mechanisms have been the subject of recurring reviews and are a current topic of great interest to atmospheric scientists [*Lewis and Schwartz*, 2004c; *O'Dowd et al.*, 2007; *Gantt and Meskhidze*, 2013; *Grythe et al.*, 2014; *Quinn et al.*, 2015].

Producing accurate descriptions of SSA, both at the single particle level and as a population as a whole, presents a range of analytical challenges. SSA particles generated from bubble bursting mechanisms span several orders of magnitude in size, from tens of nanometers to several microns, and also exhibit size-dependent chemical compositions [*Lewis and Schwartz*, 2004c; *Gantt and Meskhidze*, 2013]. The chemistry at the air-particle interface is critical to determining a particle's interactions in the atmosphere. However, the distribution of chemical species within each particle as well as particle morphology are highly dependent upon the relative humidity, with phase separation often induced upon drying [e.g. *Russell et al.*, 2010; *Ault et al.*, 2013b; *Chi et al.*, 2015]. The high degree of intra-particle spatial chemical heterogeneity can complicate the interpretation and analysis of SSA by techniques that depend upon sampling and examining dry particles.

Recently, quantitative measurements of SSA composition, made by collecting a large number of particles and analyzing the collected sample offline as an ensemble, have enabled exact identification of organic and inorganic species in SSA and also facilitated new understandings of chemical selectivity at the air-sea interface [*Cochran et al.*, 2016a, 2016b; *Jayarathne et al.*, 2016]. These measurements, though, have limited size-resolution and are not able to resolve the population mixing state and single particle chemistry and morphology. The study of these chemically and morphologically complex atmospherically relevant particles has motivated the development of new techniques and expanded application of existing methods for offline single particle analysis [*Morris et al.*, 2015; *Ryder et al.*, 2015; *Patterson et al.*, 2016]. However, offline single particle sample analysis requires a great investment of time, potentially resulting in small data sets limiting the certainty and detail of conclusions extracted. In addition, sample collection and storage conditions must be carefully considered as can influence particle morphology [*Laskina et al.*, 2015].

Online single particle analysis of SSA by aerosol time-of-flight mass spectrometers (ATOFMS), a specific design of a single particle mass spectrometer (SPMS), has been employed to generate descriptions of the mixing state of SSA populations under varied biochemical conditions of the source seawater [*Gaston et al.*, 2011; *Prather et al.*, 2013; *Collins et al.*, 2014; *Guasco et al.*, 2014]. As SPMS provide size-resolved mass spectra of single particles with high throughput and no sample collection, they are an appealing analytical tool for scientists interested in measuring the temporal evolution of aerosol populations. However, a few studies have illustrated that the core-shell morphology frequently observed in spectromicroscopy studies of dry supermicron SSA [e.g. *Russell et al.*, 2010; *Ault et al.*, 2013b; *Chi et al.*, 2015] can strongly influence SSA ion signatures generated by SPMS if there is an inconsistent degree of particle desorption and ionization within the instrument [*Ault et al.*, 2013a; *Sultana et al.*, 2017c]. This finding coupled with the known qualitative or semi-quantitative nature of SPMS mass spectra due to the confounding nature of matrix effects, means extracting detailed knowledge of SSA chemistry from SPMS data sets is particularly difficult.

This work presents a study of particles generated by bubbling a model solution for organic-rich seawater. Unsaturated linear dicarboxlyates and dicarboxylates, which have been shown to be present in nascent SSA [*Cochran et al.*, 2016a], were added to a solution of inorganic salts, with typical seawater salinity. Here we unite quantitative measurements of the average population composition, previously published in [*Cochran et al.*, 2016b], with single particle phase and topographical analyses by atomic force microscopy (AFM) and size-resolved single particle mass spectra to generate a description of particle morphology and organic content for particles from tens of nanometers to several microns in size. The ATOFMS results suggest that the organic shell thickness increases from 1 to 3 microns, in agreement with the model calculations from the offline data. Also, notably total ion intensity analyses from the ATOFMS single particle mass spectra, informed by the offline determination of particle morphology and composition, are utilized to indicate that calcium are coordinated to the carboxylate species in the analyzed particle and may be directly thermally desorbed as intact preformed ions.

4.3 Methods

4.3.1 Model SSA Generation

Model SSA particles were generated from an inorganic synthetic seawater (I_{SSW}) solution utilizing an atomizer, an inorganic synthetic seawater solution with additional calcium ($I_{SSW}+Ca$) utilizing an atomizer, and a synthetic seawater solution (O_{SSW}) with added organic acids utilizing a sintered glass bubbler system and an atomizer. Details on the solution preparation and final concentrations and generation mechanism for all bulk and single particle offline SSA analysis are given in *Cochran et al.* [2016b]. The methods utilized for the online ATOFMS-analyzed SSA closely followed these procedures with the exact details given below. All glassware utilized was soaked in an acid wash, rinsed with MilliQ, and then combusted at 400° C for six hours. The inorganic synthetic seawater solution was made by dissolving 35 grams of reef salt (Tropic Marin Pro-Reef Sea Salt) into 1000 mL of MilliQ water. The $I_{SSW}+Ca$ solution was generated by doubling the original calcium ion concentration to roughly 0.025 M with the addition of calcium chloride. To prepare the O_{SSW} solution first the concentration of trace organics in a I_{SSW} solution was minimized by aggressively bubbling the I_{SSW} solution for 90 minutes with Zero air (Sabio 1001) through a sintered glass frit to generate standing foam. The foam was periodically removed from the top of the container with a clean glass rod. This method is adapted from a technique popular in fluid mechanics and bubble dynamics [*Scott*, 1975; *Kelsall et al.*, 1996]. Then the O_{SSW} solution was generated by adding butanoic, hexanoic, octanoic, butanedioic, hexanedioic, and octanedioic acids to the bubbled I_{SSW} solution to a final concentration of 0.001 M for each added organic constituent. The final O_{SSW} solution was adjusted to pH 6-6.4 with 2% aqueous sodium hydroxide to prevent precipitate formation. 400 mL of the O_{SSW} solution was added to a 500 mL sintered glass bubbler system (Ace Glass, Porosity C: 25-50 um pore size). Particles were generated by pushing Zero Air at 0.5 LPM through the sintered glass frits. All particles analyzed were dried by passing the air flow through a diffusional drier (70 cm length) to lower the RH of the sampled air to ~15%.

4.3.2 Sample Collection for Offline Analyses

A description of the sample collection for offline analyses is provided in *Cochran et al.* [2016b], but also briefly summarized here. For offline analyses, aerosol streams from three separate bubbler systems were combined and the aerosol collected using a 10-stage Micro-Orifice Uniform Deposition Impactor (MOUDI, Model 110, MSP Corporation, MN, USA). The MOUDI system sampled air at 30 lpm with 1.5 lpm combined flow from the three bubbler systems (0.5 lpm each) and the remaining from HEPA-filtered air. The impactor stages provided 50% size cuts at 18, 10, 5.6, 3.2, 1.8, 1.0, 0.56, 0.32, 0.18, 0.10 and 0.056 μm aerodynamic diameter (d_a). All MOUDI stages were cleaned with isopropanol and dried for 30 min prior to sample collection. For particle analysis by atomic force microscopy (AFM), hydrophobically coated silicon wafers were utilized as the substrate, to minimize particle spreading upon impaction. The samples for AFM analysis were stored in a low RH humidity and ambient temperature environment to minimize water uptake [*Laskina et al.*, 2015]. For quantification of carboxylate, dicarboxylate, and inorganic salt species, 47 mm quartz fiber filters (pre-combusted at 550 °C for 6 h) were placed onto each stage. Following collection, each quartz fiber filter was removed from the MOUDI stage and immediately placed in a petri dish lined with pre-combusted aluminum foil. The petri dishes were sealed with PTFE tape and stored at -20 °C until extraction and analysis. Aqueous bulk solution was also collected before and after bubbling (1 mL for each) into 4 mL amber glass vials (pre-combusted at 550 °C for 6 h).

4.3.3 Online Single Particle SSA Analysis by ATOFMS

The vacuum aerodynamic diameter (d_{va}) amd chemical composition of individual particles were measured in real time by a nozzle-inlet ATOFMS. A detailed discussion of ATOFMS can be found in previous publications [*Noble and Prather*, 1996; *Gard et al.*, 1997]. Particles were desorbed and ionized by a Nd:YAG laser pulse (266 nm wavelength, 8 ns pulse width, 700 μm spot size), with a measured laser pulse energy varied between 0.4-1.6 mJ to achieve a wide range of particle desorption and ionization. Single particle dual-polarity mass spectra and size data were imported into MATLAB analyzed using the software toolkit, FATES [*Sultana et al.*, 2017b]. The number of mass spectra generated for each solution and SSA generation method are summarized in Table 4.1. A number of mass spectral peaks were summed to determine the signal attributable to sodium ($^{23}Na^+$, $^{46}Na_2^+$, $^{81,83}Na_2Cl^+$, $^{139,141,143}Na_3Cl_2^+$), calcium ($^{40}Ca^+$, $^{57}CaOH^+$, $^{75,77}CaCl^+$, $^{96}Ca_2O^+$), magnesium ($^{24,25,26}Mg^+$), potassium ($^{39}K^+$), and carboxylate ($^{87}C_4H_7O_2^-$, $^{115}C_6H_{11}O_2^-$, $^{127}CaC_4H_7O_2^-$, $^{143}C_8H_{15}O_2^-$, $^{183}CaC_8H_{15}O_2^-$) indicative ions. The fraction of total positive ion intensity attributable to sodium (Na_F), calcium (Ca_F), magnesium (Mg_F), potassium (K_F) and the fraction of total negative ion intensity attributable to carboxylate (LC_F) were calculated. Total positive and negative ion intensities are the summation of all ion signals up to mass-to-charge (*m/z*) +200 and -200, respectively. Note absolute total negative ion and positive ion intensities are not directly comparable due to differences in ion transfer efficiency and detector settings. Mass spectra were categorized as Na-rich or Na-deficient utilizing a threshold Na_F of 0.6. A threshold of Ca_F of 0.15 was utilized to categorize mass spectra as Ca-Rich or Ca-Poor. All error bars are the approximate standard error (95% confidence interval) for a binomial distribution assuming simple random sampling with replacement calculated with Equation 4.1.

$$S = 2 * \sqrt{\frac{\frac{x}{N}\left(1-\frac{x}{N}\right)}{N}} \qquad [4.4]$$

where N is the total number of particles within a bin or population and x is the number of particles within that bin classified as a certain type.

The number of mass spectra generated for each experiment and separated by ion intensity is shown in Table 4.2. Mass spectra generated from SSA with the bubbled O_{SSW} solution were also binned by particle size and total ion intensity. The number of mass spectra in within each bin of this analysis is summarized in Table 4.3.

Additional experiments were performed to calculate the relative yield of positive to negative ions. The relative yield of positive and negative ions generated by laser desorption/ionization of particles can be determined by measuring the detection efficiency of the two reflectron time-of-flight mass analyzers within the ATOFMS [*Reinard and Johnston*, 2008].

In normal operation mode (#1), the reflectron mass spectrometer on the right, facing the front of the instrument, is utilized to detect positive ions and the reflectron mass spectrometer on the left is utilized to detect negative ions. Detection efficiencies of the mass spectrometers on the right (R_R) and left (R_L) can be obtained by measuring the positive and negative ion signals in both normal mode (#1) and by flipping the polarities (#2) so that the right spectrometer is used to detect the negative ions and left spectrometer is used to detect the positive ions. As described in *Reinard and Johnston* [2008], for particles of a similar composition and size, and ionized by a consistent laser pulse energy the absolute yield of positive (N^+) and negative (N^-) ions (Equations 4.2 and 4.3)

$$N^+ = S_{1+}(R_R)^{-1} = S_{2+}(R_L)^{-1} \qquad [4.2]$$

$$N^- = S_{1-}(R_L)^{-1} = S_{2-}(R_R)^{-1} \qquad [4.3]$$

where S_{1-}, S_{2-}, S_{1+}, and S_{2+} are the total negative and positive ion signals from mode 1 and 2. Therefore the relative yield of positive to negative ions produced can be calculated by

$$\frac{N^+}{N^-} = \sqrt{\frac{S_{1+}\, S_{2+}}{S_{1-}\, S_{2-}}} \qquad [4.4]$$

Note that signal from free electrons are not recorded or imported into the dataset and therefore are not included in the analysis.

This ion intensity analysis was performed on SSA generated by atomizing I_{SSW} with laser pulse energies 1.1-1.2 mJ and on SSA generated by bubbling O_{SSW} with laser pulse energies 0.7-1.2 mJ. Section 1.3.1 details the SSA and solution generation methods.

The data analysis was limited to particles with d_{va} 1-2 µm and that generated both positive and negative mass spectra. For each SSA dataset (I_{SSW} and O_{SSW}) the ion intensity analysis was applied to Na-rich ($Na_F > 0.6$) and Na-deficient ($Na_F < 0.6$) mass spectra separately. Table 4-4 summarizes the number of particles utilized in the relative ion intensity analyses and the relative yield of positive to negative ions calculated utilizing Equation 4.4.

Table 4.1 Summary of the number of single particle mass spectra generated by the ATOFMS

Mass Spe Polarity	I_{SSW} (atomized)	$I_{SSW}+Ca$(atomized)	O_{SSW} (atomized)	O_{SSW} (bubbled)
Pos and Neg	2197	1935	773	10717
Pos Only	1036	978	183	44
Neg Only	0	0	0	2575

Table 4.2 Summary of the number of single particle mass spectra generated by the ATOFMS, split by total positive ion intensity.

	Mass Spectral Positive Ion Intensity (x10^3)										
	0-.08	.08-0.5	0.5-1.5	1.5-2.5	2.5-3.5	3.5-5.5	5.5-7.5	7.5-9.5	9.5-11.5	11.5-13.5	13.5-15.5
I_{SSW} (atomized)	12	437	1359	722	386	257	50	8	2	0	0
I_{SSW}+*CaCl* (atomized)	11	352	1064	644	392	330	101	18	1	0	0
O_{SSW} (atomized)	3	78	323	220	183	128	28	1			
O_{SSW} (bubbled)	533	2688	2078	1209	761	1043	925	780	440	235	56

Table 4.3 Summary of the number of single particle mass spectra generated utilizing the $\boldsymbol{O_{SSW}}$ solution split by total positive ion intensity and particle size.

Particle Size	Mass Spectral Positive Ion Intensity (x10^3)				
(d_{va}, µm)	.08-1	1-2.5	2.5-4.5	4.5-6.5	6.5-17
1-1.5	604	283	166	94	83
1.5-1.75	1157	642	378	287	394
1.75-2	1080	552	361	282	640
2-2.5	635	316	191	159	517
2.5-3.5	188	102	67	43	216

Table 4.4 Summary of the number of single particle (d_{va} 1-2 μm) mass spectra generated utilized to determine the relative yield of positive and negative ions (N^+/N^-). Only ion intensity from particles which generated both positive and negative mass spectra were utilized to calculated N^+/N^-.

Mass Spectra Generated	I_{SSW} (atomized) Na-rich mode# 1/2	I_{SSW} (atomized) Na-deficient mode# 1/2	O_{SSW} (bubbled) Na-rich mode# 1/2	O_{SSW} (bubbled) Na-deficient mode# 1/2
Pos and Neg	262/398	36/9	209/263	353/454
Pos Only	140/272	5/11	2/5	9/196
N^+/N^-	11.5	6.0	1.6	1.1

4.3.4 Offline single particle SSA analysis by AFM

Molecular force probe 3D AFM (Asylum Research, Santa Barbara, CA) was used for particle imaging at ambient temperature. Silicon nitride AFM probes (MikroMasch, Model CSC37) with a nominal spring constant of 0.35 – 0.7 N/m and tip radius of curvature of 10 nm were used for all imaging done in this work. The particle-deposited substrates were imaged in AC mode to locate single and individual particles of interest. Imaging parameters were optimized (free amplitude = 3 - 4 V) to image the particles without applying excessive amount of force onto the sample, which could potentially be damaged. Scan rate was approximately 1.0 Hz. From the 3D height images, volume and volume-equivalent diameters were calculated using built-in Asylum Research particle analysis software for all systems studied here. Due to spreading upon impaction onto the substrate, the particle volume was used to calculate the volume-equivalent diameter (d_{vol}), which is a more accurate means of calculating the size of the particle prior to impaction than area-equivalent diameter. Based upon an inspection of the topography and phase images, particles were either classified as having a core-shell (CS) morphology or homogenously mixed (HM) without obvious phase separation of the components [*Ryder et al.*, 2015; *Morris et al.*, 2016]. Single particle, organic volume fractions were estimated by subtracting the volume of the particle core from the volume of the whole particle as detailed in *Ryder et al.* [2015]. Mean OVF values for all particles collected on each MOUDI stage are reported with error bars that represent two standard deviations. The number of individual particles analyzed on each MOUDI stage and morphology is summarized in Table 4.1.

Table 4.5 Summary of the number of particles analyzed by AFM for each MOUDI stage.

MOUDI Stage	MOUDI Stage Size Range (µm, d_a)	Total Number of Particles Analyzed	Number of CS particles	Number of HM particles
6	0.56-1	55	54	1
7	0.32-0.56	44	44	0
8	0.18-0.32	39	37	2
9	0.1-0.18	26	21	5
10	0.56-0.1	107	0	107

4.3.5 Offline Carboxylate, Dicarboxylate, and Inorganic Salt Extraction and Quantification

Details on the extraction and quantification of carboxylates, dicarboxylates and inorganic salts have previously been reported [*Cochran et al.*, 2016b]. Only a brief summary of these methods is provided here. For quantifying inorganic cations (sodium, potassium, magnesium and calcium) and anions (chlorine and sulfate) in aerosol, a 1 cm^2 punch of the quartz fiber filter was removed and placed into the bottom of a test tube. Then, 1 mL of ultrapure water was added to the bottom of the test tube. The test tube was capped and shaken at 125 rpm for 10 min, followed by sonication in a room temperature bath for 30 min at 60 Hz. Extracts were analyzed within 24 h via a Dionex ICS-5000 high-pressure ion chromatograph with a conductivity detector using a method described previously [*Jayarathne et al.*, 2014]. Prior to analysis of the extracts the instrument was calibrated for each analyte and method detection limits were calculated, details provided in *Cochran et al.* [2016b].

For quantifying linear carboxylates (LCs) and linear dicarboxylates (LDCs) in aerosol collected during the bubbler experiments, the remaining quartz fiber filter area after removing a 1 cm^2 punch (for quantification of inorganic salts) was placed into the bottom of a 4.0 mL (15×45 mm) amber glass vial. Then 1 mL of dichloromethane was added, and the vial was immediately closed and sonicated in a room temperature bath for 30 min at 60 Hz. Following sonication, the extract was transferred to a separate clean 4.0 mL glass vial. The extraction procedure was repeated three more times on the same filter. The final 4 mL extract volume was then evaporated to 0.1 mL under a gentle stream of nitrogen.

Extraction of linear carboxylates and dicarboxylates from the aqueous bulk solution collected from the bubbler was performed using liquid-liquid extraction. First, an internal standard solution containing deuterium labelled standards of alkanoic (butanoic-$_{d7}$, hexanoic-$_{d11}$, and octanoic-$_{d15}$) and dicarboxylic (butanedioic-$_{d4}$, hexanedioic-$_{d8}$, and octanedioic-$_{d12}$) acids was spiked to 1 mL of aqueous bulk solution in a 4 mL glass vial. Then 1 mL of dichloromethane was added and the mixture shaken for 10 min at 125 rpm. The dichloromethane layer containing the carboxylates was removed and transferred to a clean 4 mL glass vial. The process was repeated three more times and the final volume of dichloromethane extract was reduced to 0.1 mL under a gentle stream of nitrogen.

Prior to analysis, the carboxylates and dicarboxylates were derivatized by N-Methyl-N-(trimethylsilyl)trifluoroacetamide to produce trimethylsilyl esters of each carboxylate and dicarboxylate. The extracts containing the trimethylsilyl esters were analyzed by a gas chromatography mass spectrometer using electron impact as an ionization source (GC-EI-MS) (Agilent 6890 GC coupled to a 5975 C MS with an EI source). All analyses were accomplished on a 30 m DB-5 column with 0.25 mm I.D. and 0.25 µm film thickness (J&W Scientific, Inc., Folsom, CA) using a split/splitless injector in pulsed splitless mode and a carrier gas flow of 1.0 mL/min. MS data was acquired in selected ion monitoring (SIM). Prior to the analysis of extracts the instrument was calibrated for each analyte individually in the range of 0.06–30 µg mL^{-1}. Method detection limits (ng mL^{-1}) were calculated for each acid and detailed in *Cochran et al.* [2016b].

4.3.6 Organic Volume Calculation from Offline Ensemble Data

Organic volume fractions (OVF) of the dry particles were estimated utilizing the size-resolved offline filter carboxylate, dicarboxylate and inorganic salt quantitative measurements with a number of simplifying assumptions detailed below. The inorganic component of the particle is treated as 100% sodium chloride, as the concentration of sodium and chloride are much greater than the contributions from sulfate, magnesium, and potassium. The concentration of sodium chloride is assumed to be the measured concentration of sodium. In addition, it was assumed the inorganic and organic species are completely phase separated once the particle is dry. Following this, the inorganic volume has a density of crystalline sodium chloride, and the organic volume density is the average of the pure carboxylic acids weighted by the measured concentrations. Utilizing the calculated organic volume fractions for each size range, the thickness of the outer organic shell can be estimated assuming model particles where inorganic cores of either spherical or cubical morphology are coated by organic material to yield spherical particles as illustrated in Figure 4d. The calculated OVFs from stage 5 (64%) and stage 4 (79%) were utilized to calculate the organic shell thickness from 1-1.8 and 1.8-2.5 μm, respectively, shown in in Figure 4.2b.

4.4 Results and Discussion

4.4.1 Description of Terminology

Note that the synthetic seawater solution free of carboxylic acids is called the I_{SSW} solution. Particles generated by atomizing this solution are termed I_{SSW} particles. The synthetic seawater solution with additional calcium chloride is the $I_{SSW}+Ca$ solution. Particles generated by atomizing this solution are termed $I_{SSW}+Ca$ particles. The synthetic seawater solution with added carboxylic acids is the O_{SSW} solution, and particles generated by bubbling this solution are bubbled O_{SSW} particles while particles generated by atomizing this solution are atomized O_{SSW} particles.

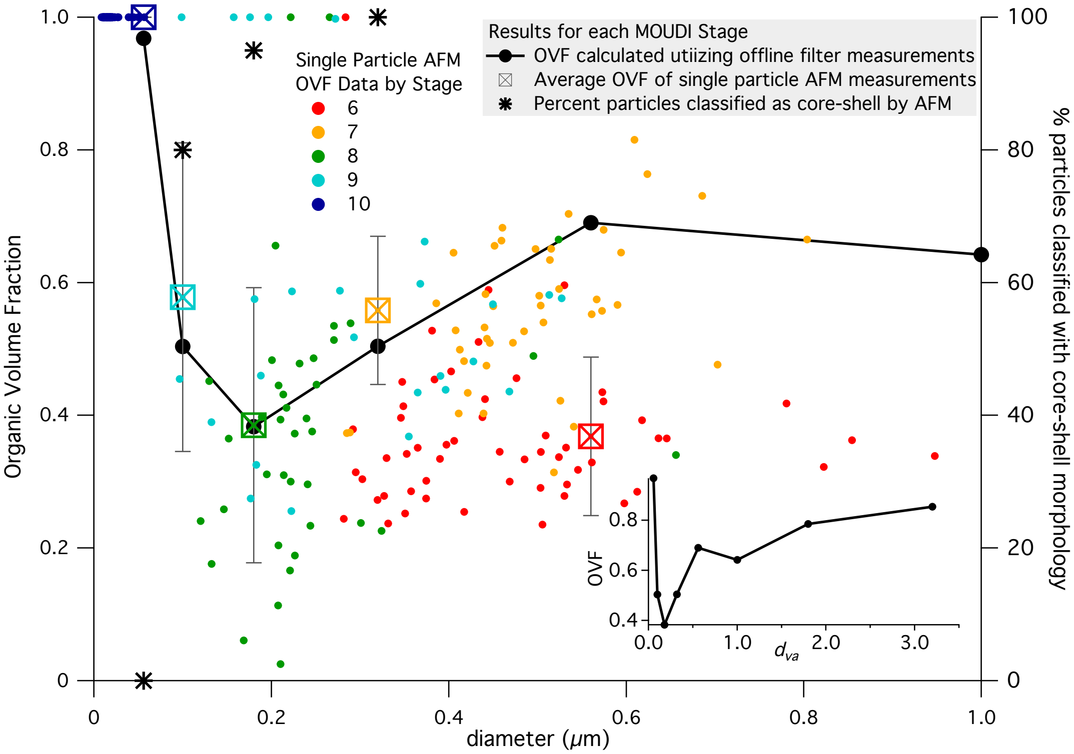

Figure 4.1 The estimate of ensemble and average single particle organic volume fraction (OVF) values for each MOUDI stage, plotted at the 50% cut aerodynamic diameter of the MOUDI stage. Single particle OVF values are also plotted against their calculated d_{vol}. The percentage of particles on each stage classified as having a core-shell morphology with AFM analysis is also shown.

4.4.2 Organic Volume Fraction: Offline Ensemble and Offline AFM Single Particle Comparison

The size-resolved OVF for the bubbled O_{SSW} particles was estimated utilizing two offline techniques. An ensemble of particles was collected on filters mounted in a MOUDI (Section 1.3.2) and the amount of carboxylates, dicarboxylates, and inorganic salts were quantified (Section 1.3.5) (see *Cochran et al.* [2016b] for reported values). The quantitatively determined composition for the sampled population was then utilized to estimate the average particle OVF for the size range of the MOUDI stage (1.3.6). This ensemble estimate is compared to single particle OVF values (Figure 4.1) estimated from analysis of the topography and phase AFM images [*Ryder et al.*, 2015]. Particles without detectable phase separation are classified as homogeneously mixed with 100% OVF. 95% of particles greater than 100 nm (d_{vol}) were classified as having a core-shell morphology (Figure 4.2d), with a variable OVF depending on the volume of the particle shell. For MOUDI stages 10-7 the average single particle OVF values estimated via AFM correspond closely to the estimated OVF from the quantitative ensemble measurement. This is the first direct comparison of OVF estimated from single particle AFM morphological analyses and quantification of the population composition by an ensemble measurement.

4.4.3 Organic Shell Thickness: Offline Ensemble and Online SPMS Single Particle Comparison

On MOUDI stages 6 and 7, 97 out of the 98 particles analyzed with AFM were classified as having a core shell morphology, examples of which are shown in Figure 4.2d. We assume the phase separated core shell morphology observed is maintained for larger particles in the size range of the ATOFMS. The assumption that the particle core is composed primarily of sodium chloride is supported by ATOFMS analysis of bubbled O_{SSW} particles which shows that mass spectra with low total positive ion intensity generated few Na-rich mass spectra ($Na_F > 0.6$) relative to mass spectra with higher total positive ion intensities (Figure 4.2a). Similar heterogeneous chemical spatial morphologies have been described for more realistic SSA both by offline microspectroscopy analyses and online SPMS depth-profiling studies [*Russell et al.*, 2010; *Ault et al.*, 2013a, 2013c; *Chi et al.*, 2015; *Sultana et al.*, 2017c]. The thickness of the organic shell on the particles analyzed can be roughly estimated utilizing the OVFs estimated from the offline ensemble analyses (Figure 4.2b), assuming particles have a model morphology with a spherical organic shell and either cubic or spherical inorganic cores (Figure 4.2d). Calculations for these model particles illustrate that the thickness of the organic shell should increase with increasing particle diameter over the size range of the ATOFMS (Figure 4.2b), even if a constant organic volume fraction is estimated. The decreasing fraction of Na-rich mass spectra with increasing particle diameter (Figure 4.2c), is consistent with the increase in organic shell thickness predicted from calculations utilizing the offline ensemble measurements. At typical laser pulse energies particle desorption and ionization is regularly reported to be incomplete for supermicron particles [*Weiss et al.*, 1997; *Carranza and Hahn*, 2002; *Vera et al.*, 2005; *Chen et al.*, 2006; *Dall'Osto et al.*, 2006], illustrated in this study by the relative insensitivity of the total positive ion intensity to particle diameter (Figure 4.3). Therefore, as the thickness of the organic shell increases, sodium chloride concentrated in the particle core is less likely to be desorbed and ionized. Only at very high total ion intensities, with likely more complete particle desorption, do all particle sizes generate a similar fraction of Na-rich mass spectra. These results illustrate the potential for SPMS datasets to resolve finer details of particle morphology without explicitly performing depth profiling studies where the pulse energy of the desorption/ionization laser is directly varied.

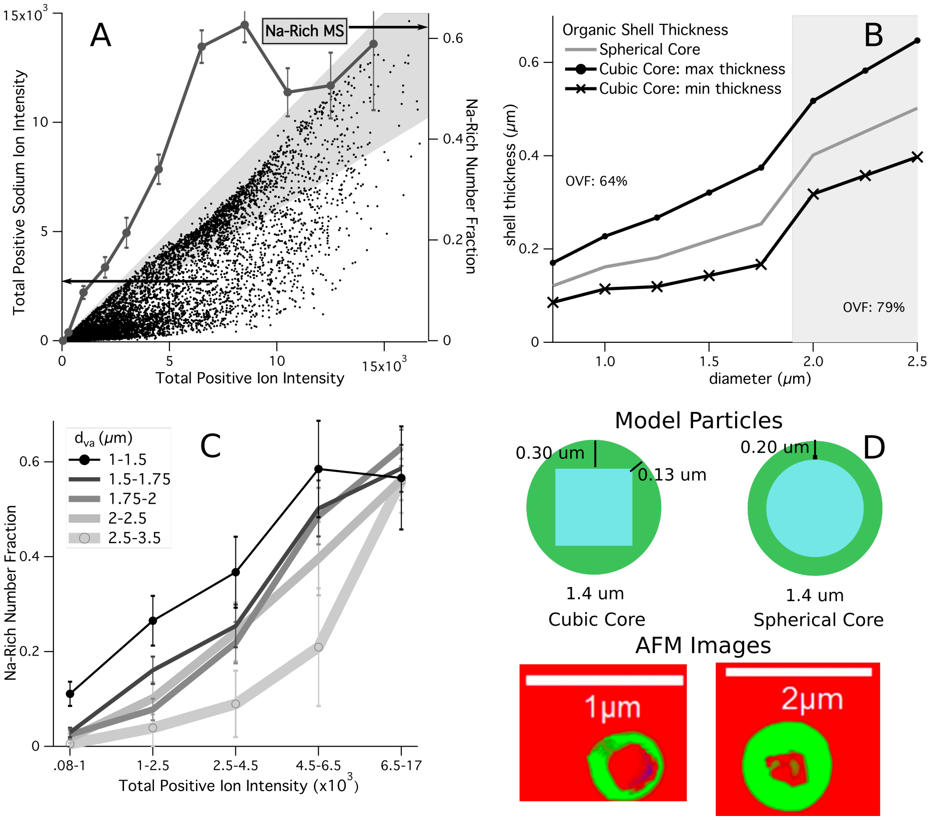

Figure 4.2 An illustration of how ATOFMS mass spectra are descriptive of the particle morphology and organic shell thickness. In black dots, the total positive ion intensity for bubbled O_{SSW} single particle mass spectra plotted against the intensity of positive sodium ion markers (a). Mass spectra classified as Na-rich are highlighted and the fraction of Na-rich mass spectra across the total positive intensity range is also shown. The thickness of the organic shell is estimated utilizing OVFs estimated from the offline ensemble measurements (b) for particles with model morphologies (d). The number fraction of Na-rich mass spectra with respect to total positive ion intensity is calculated for mass spectra binned by particle size (c). A cartoon of the model particle morphologies and AFM phase images illustrating the core shell morphology in the analyzed particles are also provided (d).

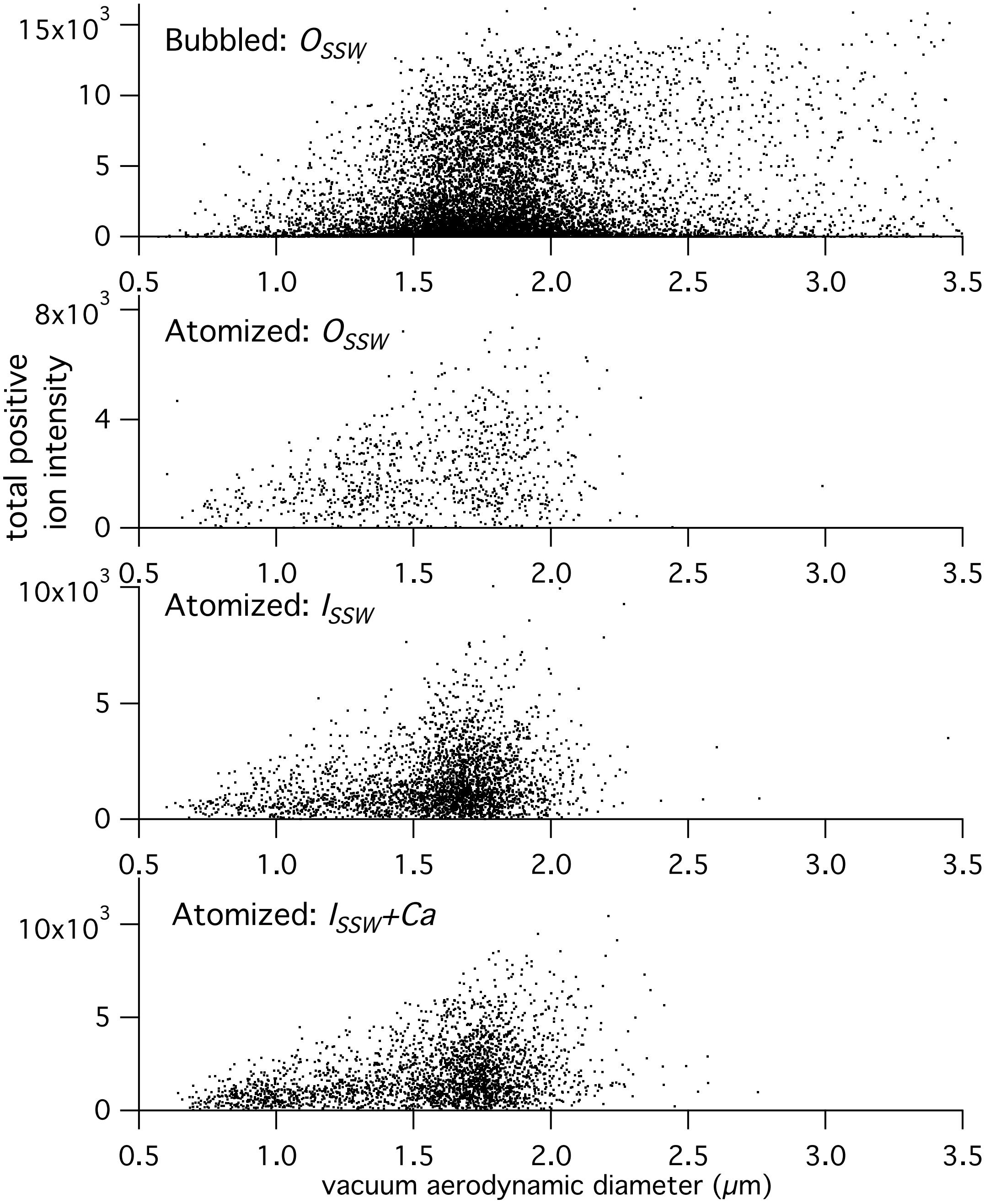

Figure 4.3 Single particle total positive ion intensity versus particle size for the various experiments.

4.4.4 Inorganic Signal: Offline Ensemble and Online SPMS Single Particle Comparison

The following sections (4.4.4 and 4.4.5) describe a number of remarkable characteristics of the single particle mass spectra from the O_{SSW} particles: the exceedingly intense positive calcium ion signal, the high total negative ion yield for Na-deficient mass spectra, and the relatively strong signal from the intact carboxylate species. We illustrate how these results are inconsistent with the known average particle composition and expected morphology if common paradigms for understanding laser desorption/ionization processes within SPMS are applied to the results. Instead it is proposed that the Na-poor O_{SSW} particle ion signatures can be explained by the thermal desorption of calcium and carboxylate ions from coordinated complexes within the dried analyzed particle.

As detailed in *Cochran et al.* [2016b], the offline ensemble quantitative organic and inorganic analyses revealed that when bubbling the O_{SSW} solution, chemical species were selectively transferred from the bulk to the aerosol phase. Treated as a whole, the carboxylic and dicarboxylic acids were highly enriched in the aerosol phase relative to the bulk solution, with calculated enrichment factors of 54 and 106 for aerosols collected on MOUDI stages 5 (1-1.8 μm) and 4 (1.8-3.1 μm), which is in the size range of the nozzle ATOFMS. In comparison, the offline quantitative analyses showed that calcium was enriched only slightly from the bulk solution to the aerosol phase, with enrichment factors of 1.3±0.8 (MOUDI stage 5) and 2±0.51 (MOUDI stage 4) [*Cochran et al.*, 2016b]. We examined how chemical selectivity from the bulk to the aerosol phase, influenced the ion signatures generated by the ATOFMS. Analysis of an atomized O_{SSW} solution by ATOFMS, provides mass spectra comparable to that for the bulk O_{SSW} solution, to which ion signatures generated by particles produced by bubbling the O_{SSW} solution can be compared.

For both atomized and bubbled O_{SSW} particles, the number fraction of Ca-rich mass spectra ($Ca_F > 0.15$) did decrease with increasing total positive ion intensity (Figure 4.4a). This suggests that calcium is concentrated at the surface of the dry O_{SSW} particles relative to the core, which is consistent with previous spectromicroscopy studies of dry SSA particles [*Xiao et al.*, 2008; *Ault et al.*, 2013c; *Chi et al.*, 2015]. When analyzed by ATOFMS, bubbled O_{SSW} particles generated positive mass spectra with intense ion signals from calcium compared to atomized O_{SSW} particles. The distribution of Ca_F values, the fraction of total positive ion intensity made up by calcium ion markers, is shown in Figure 4.4b. Note the mass spectra for atomized O_{SSW} and atomized I_{SSW} particles are very similar. Atomization generates particles with a chemical composition similar to the bulk, and the O_{SSW} solution differs from the I_{SSW} solution only by the addition of a small amount of carboxylic acids relative to the total salt concentration. For this reason, a number of additional comparisons were performed simply with the atomized I_{SSW} particles.

Since the offline quantitative analyses indicated a calcium enrichment factor of roughly 2 for particles in the ATOFMS size range, atomized $I_{SSW}+Ca$ particles were also analyzed, where the calcium concentration in the atomized solution was double that of the I_{SSW} and $\mathrm{O_{SSW}}$ solutions. The Ca_F values from the I_{SSW} particles were also doubled and the distribution was recalculated. However, neither of these cases generated Ca_F distributions similar to the intensely calcium-rich mass spectra generated by the bubbled O_{SSW} particles.

While the single particle mass spectra generated only qualitatively describe the particle chemical composition, this dramatic increase in calcium ion signal is surprising given the only modest quantitative increase observed in the offline ensemble measurements. For all I_{SSW} and O_{SSW} particles it is expected that minor inorganic constituents such as magnesium, potassium, and calcium will be enriched in the outer shell of the particles [e.g. *Ge et al.*, 1996; *Russell et al.*, 2010; *Ault et al.*, 2013b; *Chi et al.*, 2015], and this shell is greatly increased in thickness for the bubbled O_{SSW} particles due to the enrichment of the carboxylic acid species in the aerosol phase. Therefore for the bubbled O_{SSW} particles, due to incomplete particle desorption and ionization, mass spectra are less likely to be characteristic of the sodium rich particle core and more likely to be characteristic of the thick particle shell, where magnesium, potassium, and calcium ions are expected to segregate. Yet, the distributions of the relative magnesium and potassium ion signals for the organic-rich bubbled O_{SSW} particles appeared to be similar or only increase slightly compared to the atomized I_{SSW} particles (Figure 4.5). The similarity of the magnesium and potassium ion signals between the bubbled O_{SSW} and atomized I_{SSW} particles suggests that the dramatic increase in calcium ion intensity is not entirely a result of the limited desorption and ionization of the sodium rich core or the modest quantitative increase in calcium ion concentrations.

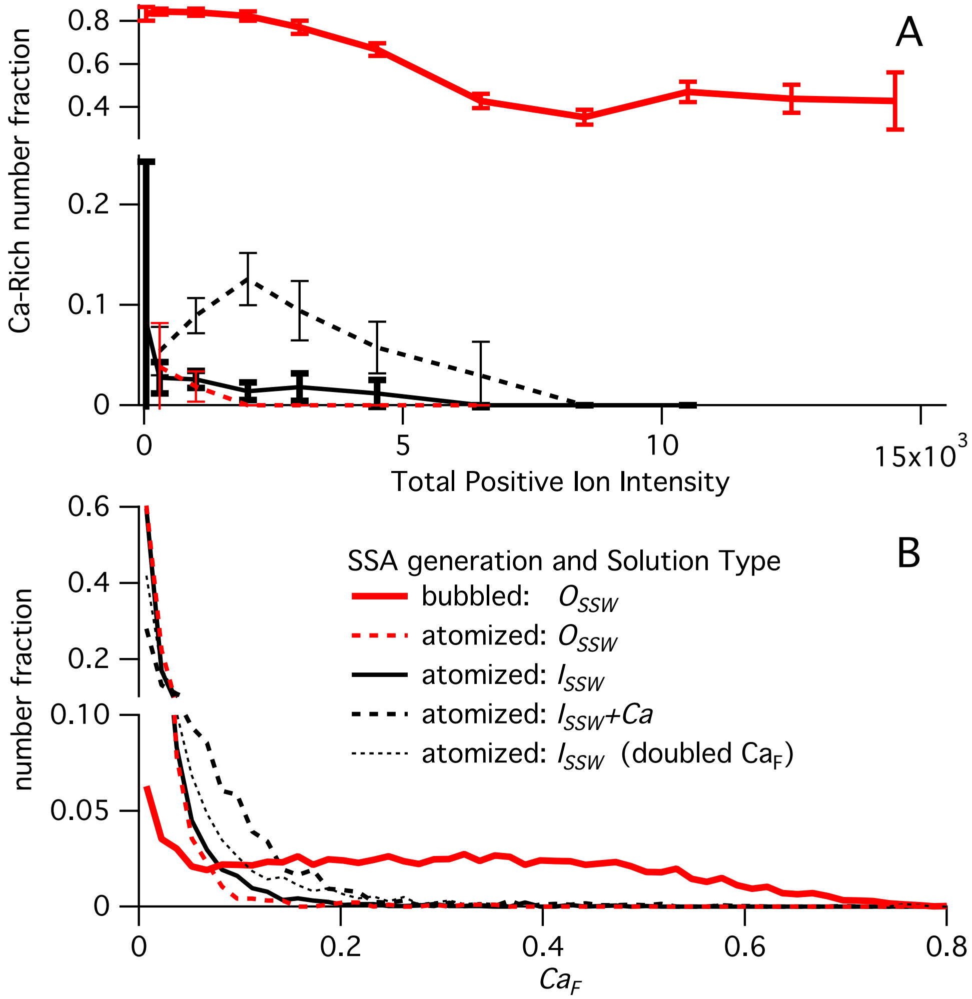

Figure 4.4 The number fraction of calcium-rich single particle mass spectra over the range of total positive ion intensities and (a) and the distribution of the relative positive calcium ion signal (b) for the various experiments.

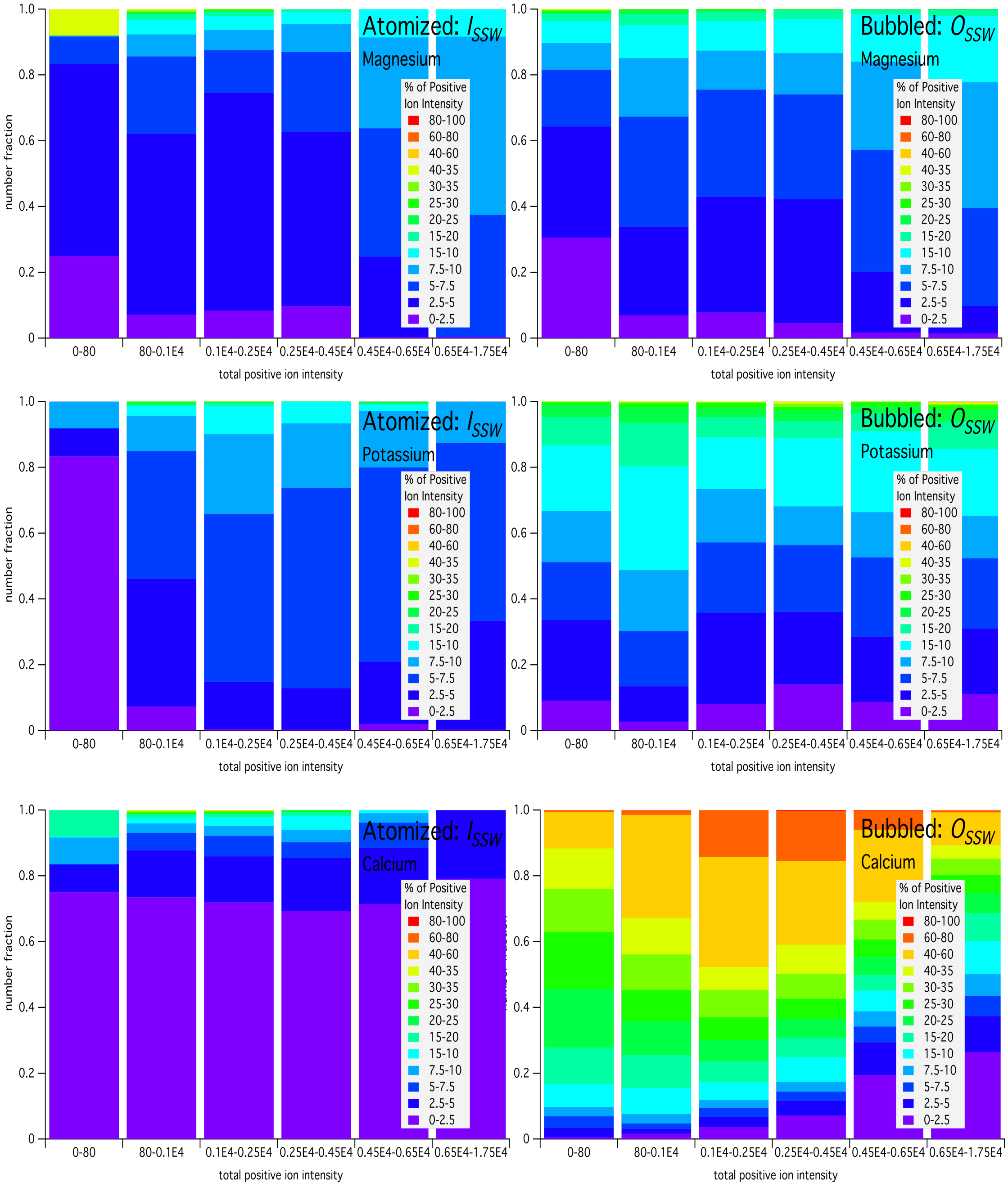

Figure 4.5 The distribution of relative positive magnesium, potassium, and calcium ion signal for the I_{SSW} and O_{SSW} particles grouped by total positive ion intensity.

Chemical spatial heterogeneity within the particle does not entirely justify the intense calcium ion signal detected for the OSSW particles. Therefore this behavior should be partially due to the preferential ionization and detection of calcium over potassium and magnesium. However, for laser desorption/ionization in SPMS, ionization efficiency for cations is generally considered to be a function of the first ionization potential of the chemical species; species with lower ionization potentials usually more efficiently generate positive ions [*Otten et al.*, 1987; *Gross et al.*, 2000; *Reents and Schabel*, 2001; *Hinz and Spengler*, 2007]. The ionization energies of potassium, sodium, magnesium, and calcium are 4.34 eV, 5.14 eV, 7.65 eV, and 6.11 eV, respectively [*Sansonetti and Martin*, 2005]. For simple inorganic salt particles, the reported range of experimentally determined relative sensitivity factors (RSF, the number of ions detected for each species normalized by the actual concentration of each species in the particle) for potassium (RSF ≈ 50-190), sodium (RSF ≈ 14-23), and magnesium (RSF ≈ 0.8-6) follow the trend expected from the differences in ionization potentials [*Otten et al.*, 1987; *Gross et al.*, 2000; *Hinz and Spengler*, 2007]. Therefore for the bubbled O_{SSW} particles, the relatively extreme sensitivity to calcium cannot be explained by the the ionization potential paradigm usually applied towards the understanding of SPMS ionization mechanisms.

4.4.5 Laser Desorption/ionization Processes in Carboxylate-rich Particles

We sought to gain a better understanding of the ionization processes governing the generation of mass spectra from the bubbled O_{SSW} particles by examining the relationship between total positive negative ion intensity and total positive ion intensity for the single particle mass spectra generated. It has been frequently concluded that in most cases negative ion formation is a secondary process controlled by the ability of neutral species to capture free electrons, which in itself is dependent on the electron affinity of the neutral species and ion plume density and dynamics [e.g. *Carson et al.*, 1997a; *Kane et al.*, 2002; *Reinard and Johnston*, 2008].

For these reasons, an examination of negative ion production could itself be illustrative of the chemistry of the particle before desorption and following ionization.

Strikingly the distribution of the total negative ion intensity with respect to total positive ion intensity is distinct for atomized I_{SSW} and bubbled O_{SSW} particles (Figure 4.6a,b). For I_{SSW} particles, which consist of inorganic salts, there appears to be very little dependence of total negative ion intensity on total positive ion intensity. As total positive ion intensity increases, total negative ion intensity remains relatively low and does not appear to depend strongly on total positive ion intensities (Figure 4.6b). For 32% of mass spectra generated only positive ion signal was detected (Table 4.1). Conspicuously, less than 1% of bubbled O_{SSW} particles generated positive ion only mass spectra, and for 19% of mass spectra only negative ions were detected. Also the relationship between total positive and negative ion formation for bubbled O_{SSW} particles appears to be dictated by the relative sodium ion signal in the positive mass spectra (Figure 4.6a,c).

Bubbled O_{SSW} particle mass spectra classified as Na-rich behave similarly to atomized I_{SSW} particle mass spectra.. Remarkably, for relatively low total positive ion intensities, within the lower 15% of the total range, total negative ion intensity appears to clearly scale linearly with total positive ion intensity. As total positive ion intensity increases Ca_F decreases and Na_F increases, the contribution of calcium and sodium ion markers to the positive mass spectra, which is as expected if sodium is concentrated in the particle core and calcium is located in the particle shell. However, with the increase in Na_F the total negative ion intensity drops and eventually, at the highest Na_F and total positive ion intensity values, the Na-deficient total negative ion intensities reach absolute values similar to the Na-rich population. This is remarkable behavior, which suggests some ionization processes for organic-rich particle shell are distinct from the processes controlling the ionization of the particle core.

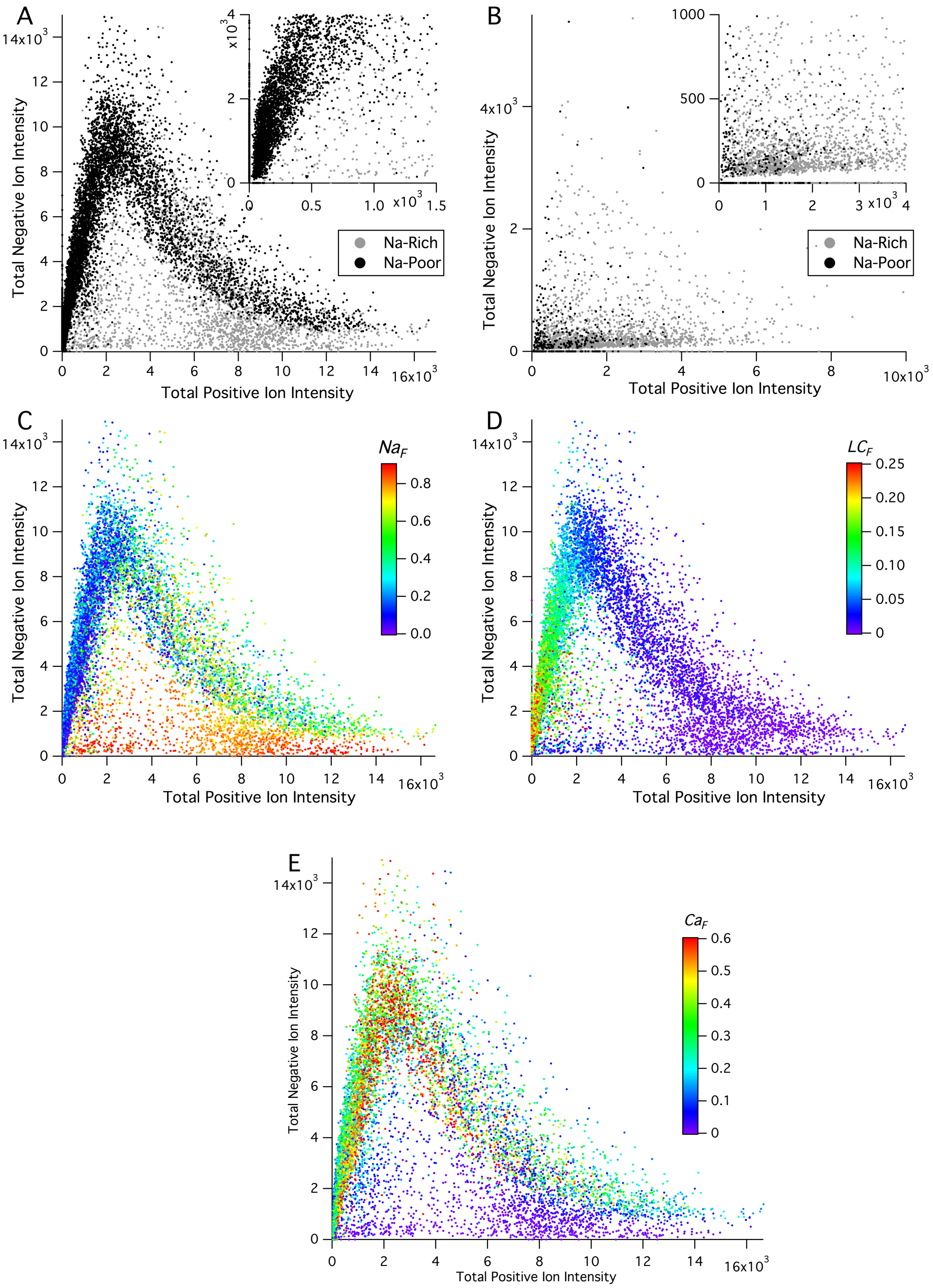

Figure 4.6 Total negative ion intensities for individual mass spectra plotted against total positive ion intensities for bubbled O_{SSW} (a) and atomized I_{SSW} (b) particles. The relative positive sodium ion signal (c) negative linear carboxylate ion signal (d), and positive calcium ion signal are indicated by marker color, with warmer shades signifying higher relative signal for O_{SSW} particles.

To this point we have discussed trends in the relative values of the mass spectral total positive and negative ion intensities. For the results described above, the absolute total negative ion and positive ion intensities are not directly comparable as negative and positive ions are collected with two different reflectron time-of-flight mass spectrometers. While the results summarized in Figure 1.6 strongly suggest different ionization processes in the particle shell and core, this can be further elucidated by determining the relative yield of positive to negative ions for the single particle mass spectra. Following the method outlined in Section 1.3.3 [*Reinard and Johnston*, 2008] we found that for bubbled O_{SSW} particles, the ratio of total positive ion yield to total negative ion yield was 4.4 and 2.3 for Na-rich and Na-deficient mass spectra. In contrast, for atomized I_{SSW} particles, Na-rich and Na-deficient mass spectra had an average positive ion yield 20.6 and 11.0 times greater than the negative ion yield. These results reveal that negative ions are generated more efficiently for bubbled O_{SSW} particles, likely as a result of ionization of components in the organic-rich particle shell.

At the pH of the O_{SSW} solution it is expected for the vast majority of the carboxylic acids to be present in their carboxylate form. At low total positive ion intensities the negative mass spectra for bubbled O_{SSW} particles are characterized by relatively intense signal from what are assumed to be the intact carboxylate ions ($^{87}C_4H_7O_2^-$, $^{115}C_6H_{11}O_2^-$, $^{143}C_8H_{15}O_2^-$, $^{183}CaC_8H_{15}O_2^-$) as well as the carboxylate ions clustered with calcium ($^{127}CaC_4H_7O_2^-$, $^{183}CaC_8H_{15}O_2^-$) (Figure 4.6d). The corresponding positive spectra are notable for their lack of any identifiable signal from the carboxylic acid species, as relatively intact molecular species (M, M+H, M-H) or smaller organic ion fragments (Figure 4.7e). At higher total positive ion intensities, presumably a result of the particle encountering regions of higher laser fluence in the beam profile, the relative ion signal from the intact carboxylate negative ion species decreases and negative ion signals attributed to organic ion fragments increases.

We have now described a number of remarkable characteristics for the Na-deficient single particle mass spectra generated by the carboxylate-rich bubbled O_{SSW} particles. In summary, the intensity of the positive calcium ion signal exceeds what may be predicted for the particle morphology and composition. The high calcium ion signal can not be explained with the common photoionization processes and ionization energy paradigm utilized to describe particle desorption/ionization mechanisms, which would predict poor sensitivity of calcium relative to sodium and potassium and a similar sensitivity to magnesium. Also, the yield of negative ions is high, compared to inorganic I_{SSW} particles, and at low total positive ion intensities it is well correlated to the positive ion yield. This is despite the common assertion that negative ion formation is a complex secondary process requiring the capture of the free electron ejected during positive ion formation. Finally, at low total positive ion intensities the intact negative carboxylate ions generate relatively strong signals but few other organic ion markers are observed.

For the system studied in this work *Cochran et al.* [2016b] found that the enrichment of the carboxylic acid species and calcium in SSA particles had similar trends with respect to size. It was hypothesized that this correspondence is a result of coordination of calcium ions to the head groups of the deprotonated carboxylic acid species, which are highly enriched in the bubble films, leading to the selective transfer of both species into the aerosol phase. This conclusion is supported by studies of surfactants at the air-water interface of salt solutions have found that calcium ions interact more strongly with anionic or zwitterionic surfactant head groups than sodium, potassium, or magnesium cations, coordinating strongly enough to displace some of the solvating water molecules [*Casillas-Ituarte et al.*, 2010; *Chen et al.*, 2010; *Tang et al.*, 2010, 2011; *Hua et al.*, 2015; *Adams et al.*, 2016; *Zhang et al.*, 2016]. These studies indicate that for the hydrated bubbled O_{SSW} particles calcium is likely coordinated to the carboxylate head groups, but the likely micro-chemical environment of calcium and the carboxylate species for dry particles was not discussed. The ion signatures of the bubbled O_{SSW} mass spectra may be illustrative of the coordination environment of the calcium within the dry particle.

The behavior of the Na-deficient bubbled O_{SSW} mass spectra appears to be at odds with a number of paradigms typically used to describe desorption/ionization mechanisms in SPMS. However, most studies of ionization processes in SPMS utilize relatively simple inorganic salt particles. We argue that the previously noted confounding characteristics of the Na-deficient bubbled O_{SSW} mass spectra are consistent with the ionization of calcium-coordinated carboxylates in the dry particles, possibly proceeding through thermal rather than photoionization processes. While the SPMS literature investigating the ionization mechanisms of organic-rich particles is sparse, a number of studies utilizing laser microbe mass spectrometry (LMMS) have investigated the ionization processes for organic and organic salt analytes. LMMS usually utilizes 266 nm lasers for desorption and ionization of solid and liquid analytes and therefore is relatively comparable to SPMS. LMMS studies reveal that laser desorption/ionization of neutral organic species (M) usually result in the production of both negative and positive organic ions, with usually a high degree of fragmentation occurring [*Heinen*, 1981; *Van Vaeck et al.*, 1989a]. However, when ionizing organic-alkali (i.e. $(M\text{-}H)^- Na^+$) or organic-halide salts there is minimal signal from organic ion fragments with the opposite polarity as the original organic precurser ion. In addition, fragmentation of the organic species is relatively minimal compared to analysis of the neutral species, and signal from the pre-formed organic precurser ion is relatively intense [*Van Vaeck et al.*, 1989b; *Claereboudt et al.*, 1993]. Given this, the observation that for bubbled O_{SSW} mass spectra primarily negative organic ions were detected and signal for the precurser carboxylate ion dominated the negative spectra at low total positive ion intensities, is consistent with the carboxylic acid species remaining deprotonated through particle deliquescence and remaining as a carboxylate in the dry particle.

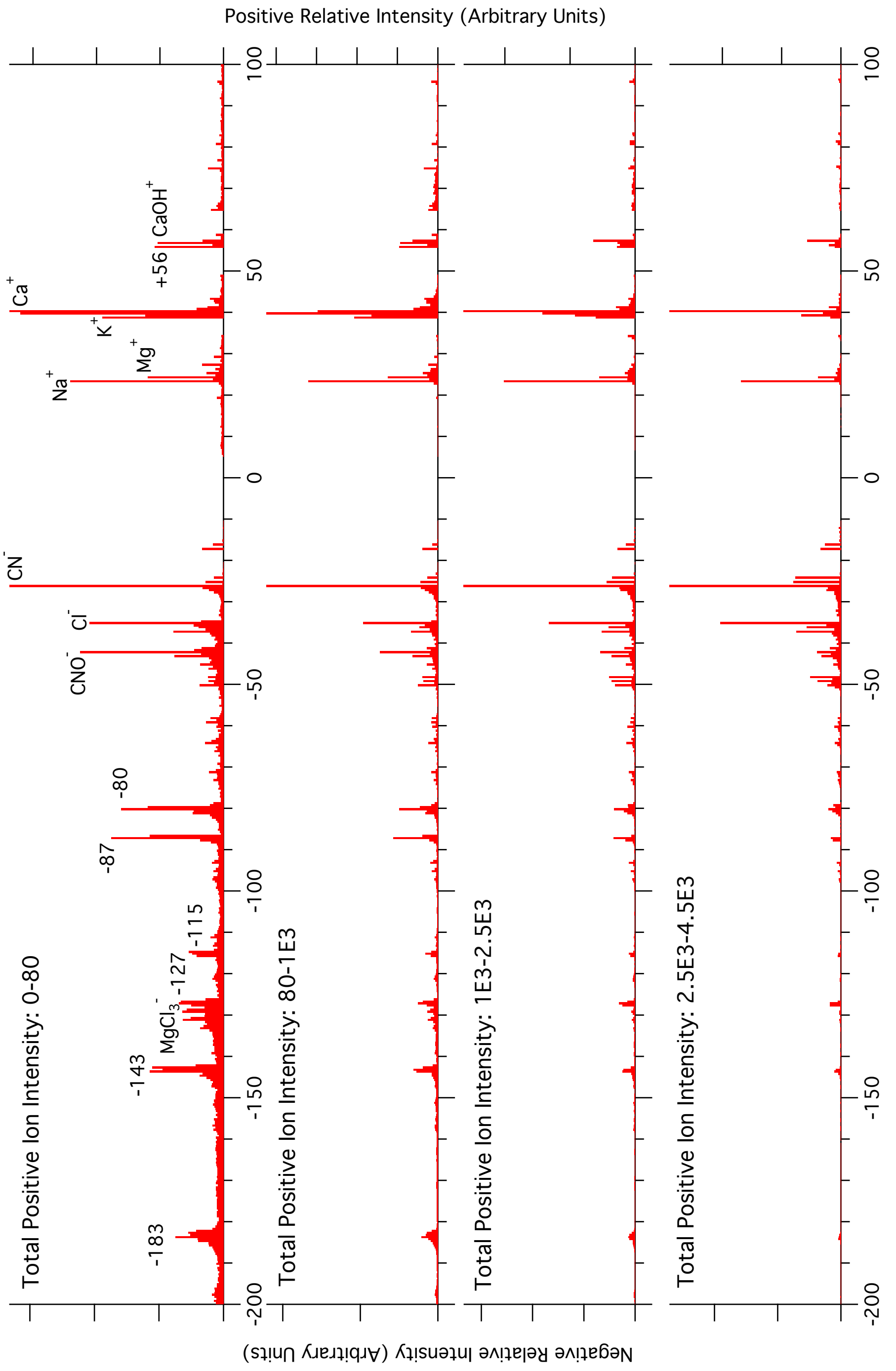

Figure 4.7 Average of single particle Na-deficient mass spectra for bubbled O_{SSW} particles grouped by total positive ion intensity. Note the broad peaks for the lower total positive ion bins are due to averaging particle-to-particle variation in the time-of-flights of the ions, but the peaks were well resolved at the single particle level.

A number of studies have shown that the intact pre-formed organic cations in nonvolatile quaternary salts can be generated by simple thermal desorption without additional ionization from electron beams, electrostatic fields, or photons [e.g. *Cotter and Yergey*, 1981; *Rollgen et al.*, 1982; *Yergeyt and Cotter*, 1982; *Van Breemen et al.*, 1983; *Chen et al.*, 2006]. It is theorized that the facile detection of pre-formed ions by heating these organic salts is a result of thermal energy directly rupturing the ionic bond between the anion and cations, rather than ionization as a result of electron ejection [*Chen et al.*, 2006]. Under this paradigm, ionization is loosely a function of lattice energy with increases in the ionic radius and bond length decreasing the ionic bond strength and likelihood of decomposition into anion and cation species [*Cotter and Yergey*, 1981]. While LMMS utilizes a laser for analyte desorption/ionization a number of studies have suggested that for organic salts and complex inorganic salts thermal processes may be contributing to ionization as well leading to the direct desorption of pre-formed ions [*Heinen*, 1981; *Van Breemen et al.*, 1983; *Claereboudt et al.*, 1993]. The high intensity of pre-formed complex precurser ions and the efficient generation of both positive and negative ions are both cited as evidence for the influence of thermal processes on ion formation in LMMS [*Heinen*, 1981]. Bearing this in mind when considering the mass spectra from the bubbled O_{SSW} particles, the high negative ion yield and intense signal from both the carboxylate precurser ion and positive calcium ions are all cohesive with this paradigm of direct desorption of pre-formed ions from relatively poorly ionically coordinated complexes. In summary we surmise that at relatively low total ion positive intensities desorption and ionization of primarily the particle shell is occurring, enriched in the carboxylate and calcium species. We suggest that thermal ionization processes can potentially yield the direct formation of calcium and carboxylate ions for coordinated complexes in the dried particle, resulting in relatively high calcium and total negative ion yields and intact carboxylate ions. At higher total positive ion intensities the mass spectra have increasing contribution from the sodium chloride rich core, consistent with the core-shell morphologies observed via AFM.

4.5 Conclusions

With the ability to analyze thousands of particles within a few hours without sample preparation, single particle mass spectrometers are powerful instruments for studying the mixing state of aerosol populations. The mass spectra are often semi-quantitative in nature at best, a result of inconsistent particle desorption and ionization and the complex ionization processes sensitive to both ion plume energetics and chemistry. Therefore, except for particles generated under highly controlled condition where the chemistry, morphology, and size have already been narrowly selected for, SPMS data sets are rarely leveraged to investigate particle morphology and intra-particle spatial chemical heterogeneity. In this study we utilized single particle microscopy analyses and quantitative measurements of the average chemical composition to inform the interpretation of SPMS ion signatures of model organic-rich SSA particles, with a distinct core-shell morphology. Recently established paradigms which infer the degree of particle desorption and ionization with the total positive ion intensity were used to confirm increases in organic-rich shell thickness with particle size calculated from the quantitative measurements. In addition, discrepancies between the SPMS ion signatures and the chemical composition and particle morpholgy determined from the offline analyses, motivated a new investigation of the ionization processes governing the carboxylate-rich particle shell. We identified a number of mass spectral characteristics which are possibly indicative of ionic coordination between ion species in the particle before desorption and ionization. While further experiments must be conducted to verify this hypothesis, the SPMS analyses present a potential path to elucidate fine details of chemical interactions within particles from datasets that are viewed as generally qualitative.

4.6 Acknowledgements

This work was supported by the National Science Foundation through the Centers of Chemical Innovation Program via the Center for Aerosol Impacts on Climate and the Environment (CHE-1305427).

Chapter 4, in full, is currently being prepared for submission for publication to Analytical Chemistry. Printed with permission from Sultana, C. M., Cochran, R., Lee, H., Sauer, J., Morris, H., Stone, E. A., Grassian, V. H., Tivanski, A., Prather, K. A. Integration of offline and SPMS analyses to obtain a more complete picture of particle morphology and coordination of chemical species within model SSA particles. The dissertation author was the primary investigator and author of this paper.

Jon Sauer is acknowledged for assisting in the editing of this chapter.

Chapter 5. Expanding Single Particle Mass Spectrometer Analyses for the Identification of Microbe Signatures in Sea Spray Aerosols

5.1 Abstract

Ocean-derived microbes in sea spray aerosols (SSA) have the potential to influence climate and weather by acting as ice nucleating particles in clouds. Single particle mass spectrometers (SPMS), which generate *in situ* single particle composition data, are excellent tools to study aerosols in rapidly changing environmental systems as they can provide high temporal resolution and require no sample preparation. While SPMS have proven capable of detecting microbes, these instruments have never been utilized to identify aerosolized microbes in SSA due to the complexity of the datasets and the relative rarity of ejected microbes. In this study, an aerosol time-of-flight mass spectrometer was used to analyze laboratory generated SSA produced using a marine aerosol reference tank with natural seawater. We present the first description of a population of biological SSA mass spectra (BioSS), which closely match microbial ion signatures observed in multiple previous studies. The dependence of BioSS organic nitrogen ion markers on total ion intensity and laser pulse energy was also consistent with previous SPMS microbial analyses. The fraction of BioSS dramatically increased in the largest supermicron particles, further supporting the assignment of BioSS mass spectra as microbes. Finally, supported by analysis of inorganic ion signals, we propose that dry BioSS particles have heterogeneous structures, with microbes adhered to sodium chloride nodules surrounded by a magnesium enriched coatings. Consistent with this structure, chlorine-containing ion markers were ubiquitous

in BioSS spectra and identified as possible tracers for distinguishing aerosolized marine from terrestrial microbes.

5.2 Introduction

Microbial cells ejected in sea spray aerosols (SSA) by bubble bursting at the ocean surface [*Blanchard*, 1978; *Blanchard and Syzdek*, 1982; *Aller et al.*, 2005; *Leck and Bigg*, 2005a; *Hultin et al.*, 2011; *Patterson et al.*, 2016] are of interest to atmospheric and climate scientists because of their potential to act as ice nucleating particles (INP) within clouds [*Schnell*, 1977; *Fall and Schnell*, 1985; *Junge and Swanson*, 2007; *Knopf et al.*, 2011; *DeMott et al.*, 2015; *Wilson et al.*, 2015]. However, common offline methods used to detect and enumerate aerosolized microbial cells have poor temporal resolution and often require a significant investment of time in sample collection, preparation, and analysis. Therefore these traditional offline techniques are not well suited to monitoring microbes in the atmosphere. To capture changes in aerosol composition, ground-based and aircraft studies require high temporal resolution measurements on the order of seconds to minutes. In addition, knowledge of the surface composition of individual particles is critical for understanding their ice nucleating capabilities [*Bassett et al.*, 1970; *Gavish et al.*, 1990; *Cziczo et al.*, 2009]. However, with bulk collection methods commonly employed for offline microbial analyses, such as impingers or filters, information on the chemical morphology of microbe-containing particles is not maintained.

Single particle mass spectrometers (SPMSs) have been shown to be able to detect aerosolized microorganisms, providing real-time, single particle, size resolved, chemical composition data without requiring any sample preparation [*Russell*, 2009; *Cahill et al.*, 2015b]. SPMS studies of isolated aerosolized standards of microbes and plant detritus all report similar mass spectra indicative of cellular material, rich in potassium, phosphate, and a number of organic nitrogen ion markers [*Silva*, 2000; *Fergenson et al.*, 2004; *Gaston*, 2012; *Cziczo et al.*, 2013; *Cahill et al.*, 2015b]. However, mass spectra with such cellular signatures have only been identified in one study of an ambient aerosol population [*Holecek et al.*, 2007] and a small number of studies of insoluble residues in precipitation and cloud water samples [*Holecek et al.*, 2007; *Pratt et al.*, 2009b; *Creamean et al.*, 2013, 2014] which are usually attributed to terrestrial microbial sources. Identifying mass spectra generated from microbe-containing particles within an SSA population is analytically challenging as ion markers often considered characteristic of cellular single particle mass spectra are also generated by chemical species dissolved in seawater. This study is the first to identify a narrow set of single particle biological SSA mass spectra (BioSS) that are likely generated by particles formed from the ejection of microbes in seawater droplets. SSA was produced from natural seawater in a marine aerosol reference tank (MART) and analyzed with an aerosol time-of-flight mass spectrometer (ATOFMS). In this study, identified BioSS signatures are consistent with phosphate- and potassium-rich mass spectra reported in previous SPMS studies of microbes. We also show the first application of data analyses utilizing particle size and ion signal dependence on total ion intensity and laser pulse energy to further confirm BioSS mass spectra as indeed produced from microbial SSA. In addition, using this information, details on the structure of BioSS particles are proposed. Finally we study the influence of changing seawater chemical and biological composition on BioSS signatures.

5.3 Methods

5.3.1 MART Induced Phytoplankton Bloom and SSA Generation

60 L of coastal Pacific seawater was collected from the ocean surface at Scripps Pier (La Jolla, CA; 32°51′56.8"N: 117° 15′38.48"W; 275 m offshore) on 9/10/13 18:00. The chlorophyll-a concentration, water temperature, and salinity were 2.9 mg/m^3, 19.9 °C, and 33.5 PSU at the time of collection. The seawater was added to a 100 L MART system without treatment or

filtering and allowed to equilibrate to room temperature. Details of particle generation and phytoplankton bloom initiation have been discussed extensively previously, however a brief summary is given here [*Lee et al.*, 2015]. Beginning on 9/11/2013, SSA particles were generated in the MART using the pulsed plunging waterfall technique described in detail previously, with a 4 second waterfall duty cycle. After initial generation of SSA particles from the untreated seawater, a diatom growth medium commonly known as Guillard's f medium (ProLine Aquatic Ecosystems) (Table 5.1) was added to promote phytoplankton growth, and then SSA particles were again generated. Phytoplankton growth was also stimulated by high definition fluorescent tubes (5700 K, Full Spectrum Solutions, Model #205457) mounted to the MART and operated continuously throughout the experiment. After 9/11/2013, SSA particles were not produced until 9/16/2013 as the MART water recirculation system has been found to inhibit phytoplankton growth during early periods of a phytoplankton bloom. Once a threshold chlorophyll-a concentration was reached, SSA particles were generated and sampled daily. Silica gel diffusion dryers were utilized to reduce the relative humidity of the sampled air to ~15%.

5.3.2 Measurement of Bulk Water Biology and Characteristics

Bulk seawater was collected daily from the MART. *In vivo* measurements of chlorophyll-a fluorescence were made immediately after collection using a custom built, portable fluorometer calibrated using chlorophyll-a from *Anacystis nidulans* (Sigma Aldrich, C6144) in acetone. Water for DOC analysis was filtered (0.7 µm Whatman GF/F, Z242489) into cleaned and combusted 40 mL glass vials and then immediately acidified with two drops of trace metal-free 12N HCl to an approximate pH of 2. Samples were stored protected from light at room temperature until analysis using the high-temperature combustion method (Shimadzu Instruments). Heterotrophic bacteria were enumerated via flow cytometry (Beckman-Coulter Altra) stained with Hoechst 34442 (1 µg/ml, final concentration) (Method S-1).

5.3.3 Measurement of SSA Composition via ATOFMS

ATOFMS was utilized to measure in real time the size-resolved chemical compositions of dried individual SSA particles with vacuum aerodynamic diameters (d_{va}) between 0.5 – 4.5 µm. Detailed descriptions of ATOFMS have been published previously and only a brief discussion is given here. Aerosol particles are drawn into the instrument through a converging nozzle inlet and accelerated to their size-dependent terminal velocities. Aerosol particles transit two continuous wave laser beams (532 nm) and the calculated particle velocity is converted to vacuum aerodynamic diameter. A Q-switched Nd:YAG laser pulse (266 nm wavelength, 8 ns, 700 µm spot size,) desorbs and ionizes each particle's chemical components which are then detected by a dual-polarity reflectron time-of-flight mass spectrometer. A laser pulse energy (LPE) of 1.1-1.3 mJ was utilized every day of SSA sampling. In addition on specific days throughout the bloom the energy of the laser pulse energy was varied between 0.2-1.2 mJ.

5.3.4 Summary of Single Particle Data Analyses

All single particle data generated via ATOFMS were imported into MATLAB and analyzed using a Flexible Analysis Toolkit for the Exploration of SPMS data (FATES).[*Sultana et al.*, 2017b] Peak assignments were made referencing the current literature and correspond to the most likely ion produced at a specific mass-to-charge ratio (*m/z*). No clustering algorithms were used to group data, rather BioSS were separated by utilizing guiFATES, a user-guided visual analytical graphical user interface within FATES. The relative contribution of a number of ion markers (Table 5.2) to either the positive or negative mass spectra ion intensity was calculated. BioSS were then binned (0-1%, 1-5%, 5-10%, 10-25%, 25-100%) by each of these relative contributions to either the positive or negative mass spectrum. Note that total ion intensities are the summation of all negative and positive ion signal and are reported on an arbitrary scale of 0 to 100.

5.4 Results and Discussion

5.4.1 Description of SSA Microbial Mass Spectra (BioSS)

Mass spectra likely produced by microbial or microbe-containing SSA particles (BioSS) were identified within the SSA population based upon close similarity to previous descriptions of cellular spectra generated from SPMS studies of nebulized bacterial cells [*Steele et al.*, 2003, 2005; *Fergenson et al.*, 2004; *Czerwieniec et al.*, 2005; *Srivastava et al.*, 2005; *Tobias et al.*, 2006]. All BioSS identified had significant signal from phosphate ($^{63}PO_2^-$,$^{79}PO_3^-$, $^{97}H_2PO_4^-$) and potassium ($^{39,41}K^+$) and most also had $^{42}CNO^-$, $^{26}CN^-$, and $^{35,37}Cl^-$ ion markers with a range in signal response from additional ions. It is important to note that in this work, BioSS is treated as a single particle type generated by a population of microbe-containing particles. However a great deal of variation between the mass spectra exists. Three characteristic mass spectra illustrating the diversity of BioSS signatures are shown in Figure 5.1. These should not be considered representative of distinct particle types but rather part of a continuum of BioSS mass spectra. A detailed list of common ion markers is provided in Table 5.3. To help eliminate noise, these mass spectra are made up of an average of 30 (Figure 5.1a), 378 (Figure 5.1b), and 189 (Figure 5.1c) single particle mass spectra.

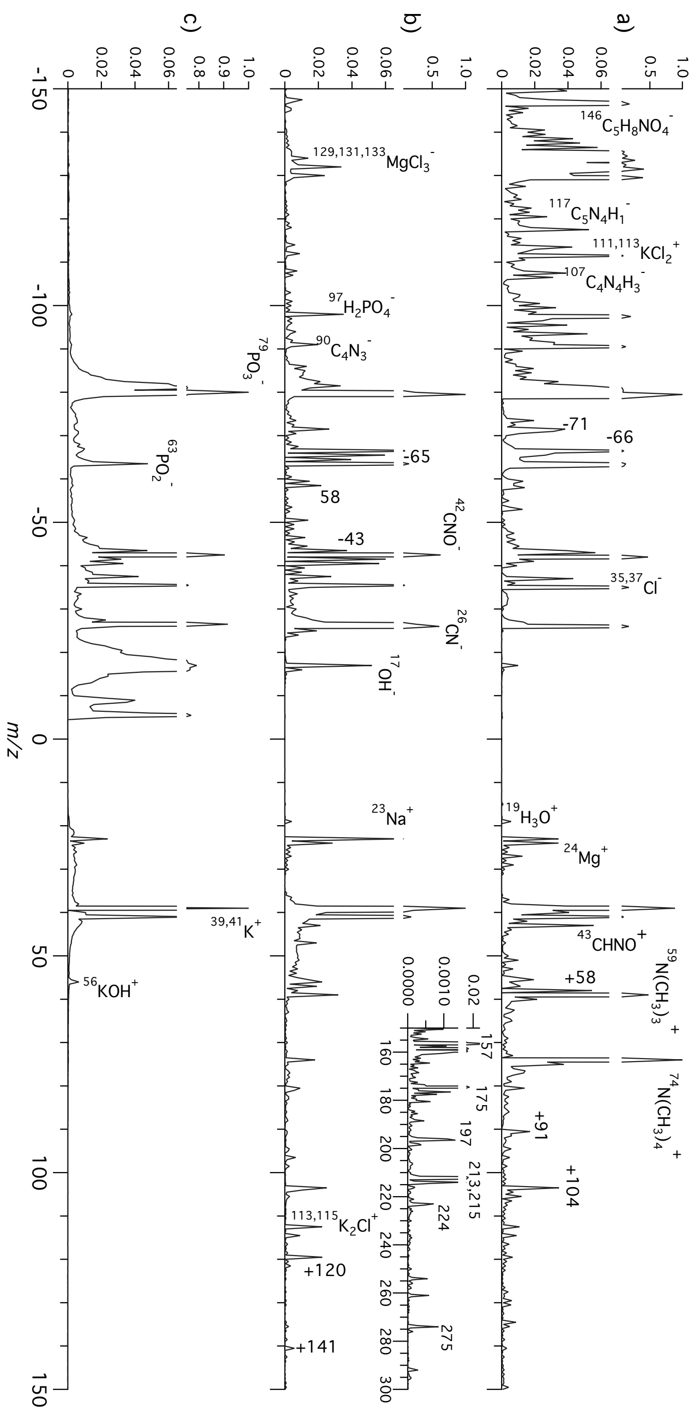

Figure 5.1 Three representative dual-polarity mass spectra illustrating the continuum of SSA ion signatures identified as BioSS. While some BioSS were relatively sparse (c) with few ion markers except from $^{39,41}K^+$, $^{63}PO_2^-$, $^{79}PO_3^-$, $^{42}CNO^-$, $^{26}CN^-$, and $^{35,37}Cl^-$ others were characterized by (a) a number of relatively intense positive and negative organic nitrogen markers, particularly *m/z* +59, +74 and -146, or (b) a series of less intense peaks above +100 (highlighted in inset).

In Figure 5.1a, the BioSS signature is characterized by intense signal from $^{129,131,133}\mathrm{MgCl_3^-}$ and relatively large organic nitrogen markers ($^{90}\mathrm{C_4N_3^-}$, $^{107}\mathrm{C_4N_4H_3^-}$, $^{117}\mathrm{C_5N_4H^-}$, $^{146}\mathrm{C_5H_8NO_4^-}$, $^{43}\mathrm{CHNO^+}$, $^{59}\mathrm{N(CH_3)_3^+}$, $^{74}\mathrm{N(CH_3)_4^+}$) in both the positive and negative mass spectra which in prior studies have been assigned to the ionization of amino acids [*Fergenson et al.*, 2004; *Czerwieniec et al.*, 2005; *Srivastava et al.*, 2005]. Additional signal from $^{91}\mathrm{C_7H_7^+}$ and ion markers -66, -71, and +104 are present which have been noted in single cell SPMS studies, but not specifically assigned [*Russell et al.*, 2004; *Czerwieniec et al.*, 2005; *Srivastava et al.*, 2005; *Steele et al.*, 2005]. In some cases, BioSS were identified with a positive ion mass spectrum, very similar to Figure 5.1a but lacking negative ion signal. The BioSS signature in Figure 5.1b is characterized by relatively more intense signals from $^{42}\mathrm{CNO^-}$, $^{26}\mathrm{CN^-}$ in the negative mass spectrum but with diminished signals from $^{-129,131,133}\mathrm{MgCl_3^-}$, $^{97}\mathrm{H_2PO_4^-}$, and most other organic positive and negative ion markers detailed for Figure 5.1a. Single particle mass spectra similar to Figure 5.1b consistently generate a set of low intensity positive ion markers (104, 120, 141, 157, 175, 197, 213, 215, 224, 275) some of which have been assigned ($^{120}\mathrm{C_8H_{10}NO_2^+}$, $^{175}\mathrm{C_6H_{15}N_4O_2^+}$) or noted (104, 157, 213) previously [*Czerwieniec et al.*, 2005; *Srivastava et al.*, 2005; *Tobias et al.*, 2006; *Russell*, 2009]. Finally some BioSS identified were characterized by relatively sparse positive and negative mass spectra, dominated by signal from $^{39,41}\mathrm{K^+}$, $^{63}\mathrm{PO_2^-}$, $^{79}\mathrm{PO_3^-}$, $^{42}\mathrm{CNO^-}$, $^{26}\mathrm{CN^-}$, and $^{35,37}\mathrm{Cl^-}$ without significant signal from the additional ion markers already listed (Figure 5.1c). Similar mass spectra have been generated when using elevated laser pulse energies in SPMS analysis of bacteria cells [*Steele et al.*, 2003, 2005] and have been attributed to microbial material or plant detritus in ambient particles and rainwater samples [*Holecek et al.*, 2007; *Creamean et al.*, 2014]. Note that the response from -4 to -23 *m/z* (Figure 5.1c) is due to an instrumental artifact and is not indicative of ion signal. All previously reported SPMS analyses of standards of bacterial cells and plant detritus [*Silva*, 2000] lack signal from chlorine ions or chlorine-containing ion clusters except when cultured in salt rich media or aerosolized from a salt solution [*Gaston*, 2012; *Cahill et al.*, 2015b]. Almost all BioSS identified in this study contained signal from $^{35,37}Cl^-$ and many also had signal from chlorine-containing ion clusters such as $^{129,131,133}MgCl_3^-$, $^{223,225,227,229}Mg_2Cl_5^-$, $^{81,83}Na_2Cl^+$, and $^{113,115}K_2Cl^+$. This suggests that signal from chlorine-containing ions could be unique markers used to distinguish ocean-derived from terrestrial microbial spectra in marine influenced air masses.

5.4.2 BioSS and Particle Size Dependence

The number fraction of particles generating BioSS relative to all mass spectra generating particles increased drastically with size, growing over an order of magnitude from 0.2% (0.5-1 μm) to 12% (4-4.5 μm) over the size range of the ATOFMS (Figure 5.6). This is consistent with field measurements which have suggested that bacteria are found predominantly in very large supermicron SSA particles [*Dueker et al.*, 2011]. For comparison the size dependent number fraction was also calculated for all remaining particles with at least a 5% contribution of potassium ($^{39}K^+$) and phosphate ($^{79}PO_3^-$, $^{63}PO_2^-$, $^{97}H_2PO_4^-$) ions to the positive and negative mass spectra respectively. The number fraction for these potassium- and phosphate-rich particles that were not identified as BioSS remains flat over the instrument size range (Figure 5.6). Representative mass spectra for these particles are provided in Figure 5.7. Because these particles do not display any size dependence, it suggests the phosphate and potassium were transferred as dissolved ions from the seawater into the aerosol phase rather than within a cell or associated with particulates. This is the first utilization of particle size in SPMS analysis to distinguish between SSA containing particulates versus dissolved ions. The novel results stemming from this approach highlight the importance of careful data treatment when trying to identify cellular spectra within a SSA or marine aerosol population, as the presence of ion markers such as $^{39,41}K^+$ and $^{79}PO_3^-$ cannot be used alone as indicative of aerosolized microbes.

5.4.3 Dependence of SSA BioSS Signatures on Total Ion Intensity and Laser Pulse Energy

Many previous SPMS studies of well-characterized and chemically and morphologically uniform aerosol particles have illustrated how differences in laser fluence yield variations in mass spectral signatures due to changes in both the ionization processes and degree of particle desorption [*Weiss et al.*, 1997; *Wenzel and Prather*, 2004; *Cai et al.*, 2006; *Zelenyuk et al.*, 2008b]. For particles of similar composition, the total ion intensities of mass spectra generally increase when particles encounter higher laser fluence [*Wenzel and Prather*, 2004; *Zelenyuk et al.*, 2008b]. However, analyses utilizing total ion signal or variable laser pulse energies have never been leveraged previously to help discriminate or confirm a distinct particle type within a larger chemically complex aerosol population. Due to the nominally Gaussian beam profile of the desorption/ionization laser utilized in this study, the laser fluence that each particle experiences upon ionization is variable even when the total pulse energy is relatively constant.

All BioSS identified for the entire experiment, generated at 1.22+-0.04 mJ laser pulse energy, were grouped by total ion intensity. Subsequently, the distributions of relative ion signals for a variety of *m/z* (Table 5.2) were calculated for all BioSS within these total ion intensity bins (Figure 5.2 and Figure 5.8). While this analysis utilizes total ion intensity as a proxy for laser fluence, this assumption was further confirmed by directly varying the laser pulse energy from 0.2 to 1.2 mJ on September 17th. BioSS were binned based upon relative signal from the ions previously described. The results for the lowest (0.21+-0.03) and highest (1.28+-0.06) laser pulse energies are shown in Figure 5.3 and for all laser pulse energies in Figure 5.9. The distribution of relative ion signals for the low and high pulse energies mimics the distribution for the low and high ion intensities respectively. This supports the use of total ion signal as a proxy for laser fluence for BioSS.

BioSS with low (0-5) total ion intensity or generated utilizing using low laser pulse energy more frequently have high relative ion signal from +*m/z 74* ($^{74}N(CH_3)_4^+$) compared to BioSS with high (35-100) total ion intensity (Figure 5.2a) or generated with high pulse energy (Figure 5.3a). The opposite trend is observed for the sum of - *m/z* 26 and 42 ($^{26}CN^-$, $^{42}CNO^-$) and the sum of +*m/z* 104, 120, 141, 157, 175, 197, for which large relative ion signal is more common for BioSS with high total ion intensity compared to low total ion intensity (Figure 5.2c,d and Figure 5.3c,d). It has been suggested that trends in these ion markers, indicative of amino acids, with respect to laser fluence are simply a result in changes in the fragmentation of the molecules, rather than illustrative of differences in the chemical species desorbed from the particle.[*Steele et al.*, 2003, 2005] The trends in relative ion signal described here (+*m/z* 74, 104, 120, 141, 157, 175, 197 and -*m/z* -26, -42) are entirely consistent with prior reports on the influence of laser fluence on bacterial cell single particle mass spectra and further confirm BioSS as indeed generated from microbial containing particles [*Steele et al.*, 2003, 2005].

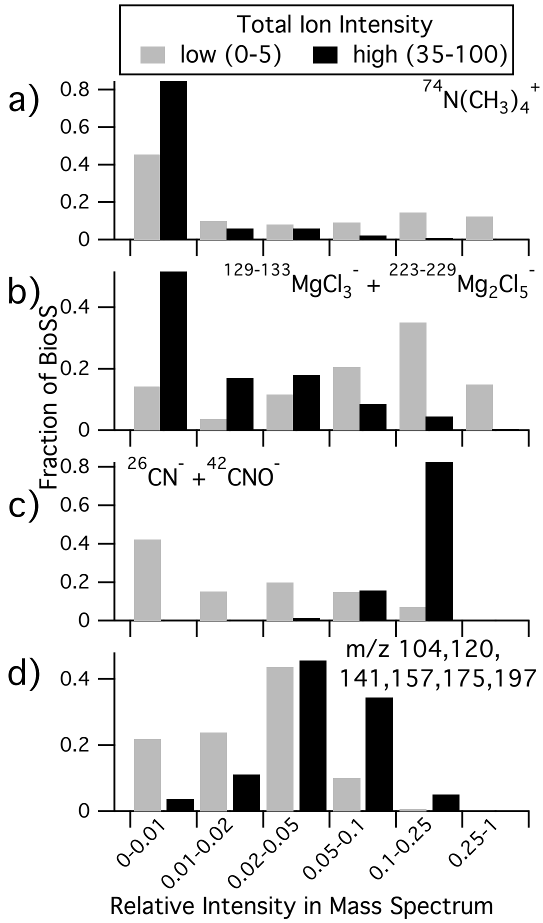

Figure 5.2 Relative ion signals for BioSS with either low or high total ion intensity. Results shown are for all BioSS generated during the experiment with 1.22+-0.04 mJ laser pulse energy.

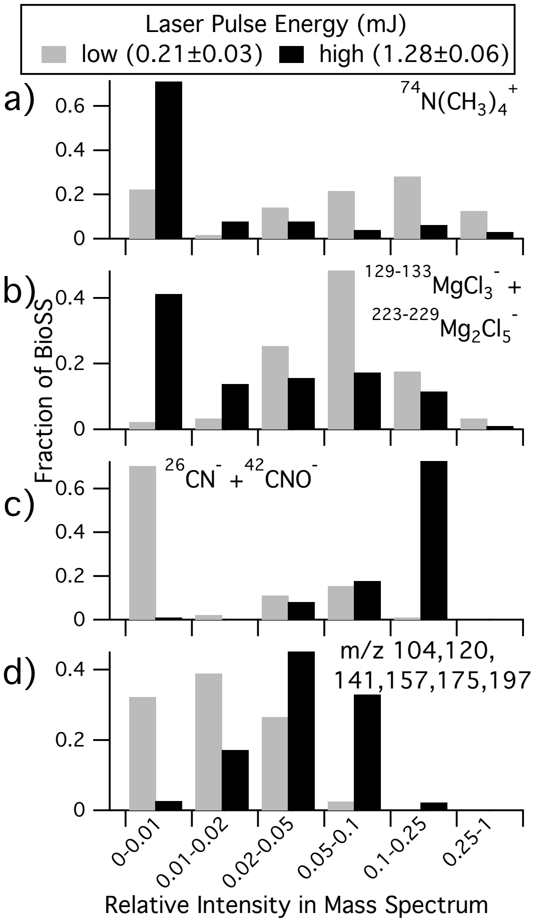

Figure 5.3 Distributions of relative ion signals on September 17th for BioSS generated with either low or high laser pulse energies.

5.4.4 Utilizing BioSS Signatures and Total Ion Intensity to Understand the Structure of Microbial Containing SSA Particles

Mass spectral peaks due to *-Mg* ($^{129,131,133}\mathrm{MgCl_3}$, $^{-223,225,227,229}\mathrm{Mg_2Cl_5}$), *-Cl* ($^{35,37}\mathrm{Cl}^-$), and *+Na* ($^{23}\mathrm{Na}^+$,$^{81,83}\mathrm{Na_2Cl}^+$) ion markers were also seen to have a strong dependence on total ion intensity and laser pulse energy. BioSS with low total ion intensity more frequently had high relative signal from *-Mg*. In contrast, at very high total ion intensity (>75) the relative contribution from *+Na* and *-Cl* to BioSS increased dramatically (Figure 5.4a). While chlorine-containing ion markers ($^{35,37}\mathrm{Cl}^-$, $^{129,131,133}\mathrm{MgCl_3}$, $^{-223,225,227,229}\mathrm{Mg_2Cl_5}$, $^{81,83}\mathrm{Na_2Cl}^+$) have never been noted in microbial or biological SPMS mass spectra, except when cultured in salt rich media, they are common in SSA mass spectra [*Gaston et al.*, 2011; *Prather et al.*, 2013; *Lee et al.*, 2015]. This suggests that these inorganic ion signals largely originate from chemical species present in the microbe-containing SSA particle but external to the microbial cell. It has been frequently noted that at the laser pulse energies commonly utilized in SPMS, desorption of supermicron particles is incomplete [*Weiss et al.*, 1997; *Carranza and Hahn*, 2002; *Vera et al.*, 2005; *Dall'Osto et al.*, 2006; *McJimpsey et al.*, 2008; *Wade et al.*, 2008]. The BioSS total ion intensity distribution is similar across the ATOFMS size range (0.5-4.5 µm) and only shifts slightly to higher values with increasing size (Figure 5.4b). Assuming spherical particles and complete particle desorption and ionization, the total ion intensity should have a third order dependence on diameter, which would result in a 700 fold increase in ion yield from 0.5 to 4.5 µm (d_{va}). The minimal increase in ion yield with particle diameter suggests that desorption of biological SSA particles is not complete over the range of laser fluences used in this study.

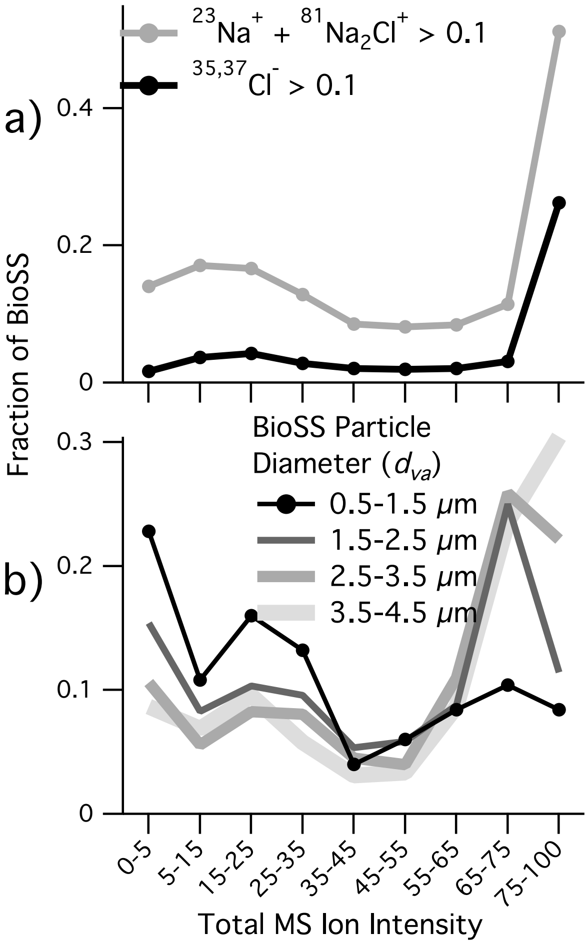

Figure 5.4 (a) The fraction of BioSS, grouped by total ion intensity, with large *-Cl* or *+Na* relative ion signal. (b) The total ion intensity distribution of BioSS grouped by particle diameter. Results shown are for all BioSS generated during the experiment with 1.22+-0.04 mJ laser pulse energy.

Coupling the trends in total ion intensity and *-Mg, -Cl, and +Na* ion signals allows us to offer a conceptual picture of the structure of BioSS SSA particles. First, it is well documented that dried seawater and model salt solution droplets exhibit a chemical spatial heterogeneity with a core rich in sodium chloride while the outer layer is enriched in organics and all minor inorganic components [*Ge et al.*, 1996, 1998a; *Cziczo et al.*, 1997; *Xiao et al.*, 2008; *Liu et al.*, 2008; *Russell et al.*, 2010; *Harmon et al.*, 2010; *Tong et al.*, 2011; *Ault et al.*, 2013a, 2013c; *Gupta et al.*, 2015; *Patterson et al.*, 2016]. Microbes are likely ejected in droplets of seawater, that upon drying will chemically segregate in the same manner with microbes adhered to sodium chloride rich nodes, surrounded by a magnesium-rich coating. Theoretical studies of laser desorption/ionization processes indicate that desorption propagates from the surface of the laser illuminated particle face [*Schoolcraft et al.*, 2000, 2001]. Therefore if desorption of the microbe-containing SSA particle is incomplete, the orientation of the particle within the laser beam will affect the mass spectrum generated. The laser beam could hypothetically illuminate the microbe face of the particle and generate little to no signal from sodium chloride in the shadow of the microbe. BioSS would only have relatively more intense signal from sodium chloride when much more complete desorption and ionization of the total particle occurs generating higher ion yields. In addition when very low degrees of desorption and ionization occurs, the mass spectrum could be rich in signal from the magnesium abundant coating relative to signal associated with ionization of the microbial cell. This is in good agreement with previous studies of supermicron SSA particles; low laser pulse energies generate low intensity mass spectra with high magnesium signal relative to sodium due to the enrichment of magnesium at the particle surface and concentration of sodium within the core [*Ault et al.*, 2013a; *Sultana et al.*, 2017c]. While there is strong evidence that BioSS identified in this paper are generated by microbe-containing SSA particles, future studies will focus on refining the structural paradigm above to more conclusively understand variability of inorganic markers within BioSS. Further the model presented here illustrates the possibility that microbe-containing SSA particles could generate mass spectra that have little to no BioSS signature.

5.4.5 Influence of Seawater Chemistry on BioSS signatures

The fraction of BioSS out of all single particle mass spectra generated was determined over the course of the phytoplankton bloom and found to be at a maximum close to the first peak in both the heterotrophic bacteria and chlorophyll-a and before the rise in total organic carbon (Figure 5.5). Previous studies of SSA particles generated during phytoplankton blooms show that as the bloom progresses and the dissolved organic carbon content increases in the seawater, dry supermicron SSA particles show increasingly thick organic and magnesium-rich coatings surrounding the sodium chloride cores [*Prather et al.*, 2013; *Lee et al.*, 2015]. ATOFMS data in this study indicate that the magnesium-rich coatings, proposed in the previous section to coat the biological SSA particles also increased in thickness over the course of the phytoplankton bloom. As already noted, BioSS with high *-Mg* relative signal generally had relatively low total ion intensities. However, as the phytoplankton bloom progressed not only did the fraction of BioSS with relatively high *-Mg* signal (>0.1) increase, but also the distribution of total ion intensities for *-Mg* rich BioSS shifted to higher values (Figure 5.5). Higher total ion intensities of *-Mg* rich BioSS indicate that more of the magnesium-rich coating had to be desorbed and ionized before reaching the microbial cell. This also suggests that very thick organic and magnesium coatings of dry microbe-containing SSA particles could possibly prevent the generation of recognizable BioSS signatures. This consideration is more critical in the examination of dense laboratory generated phytoplankton blooms where the dissolved organic carbon content of the seawater is much higher than commonly found in the natural environment in regions with elevated biological activity.

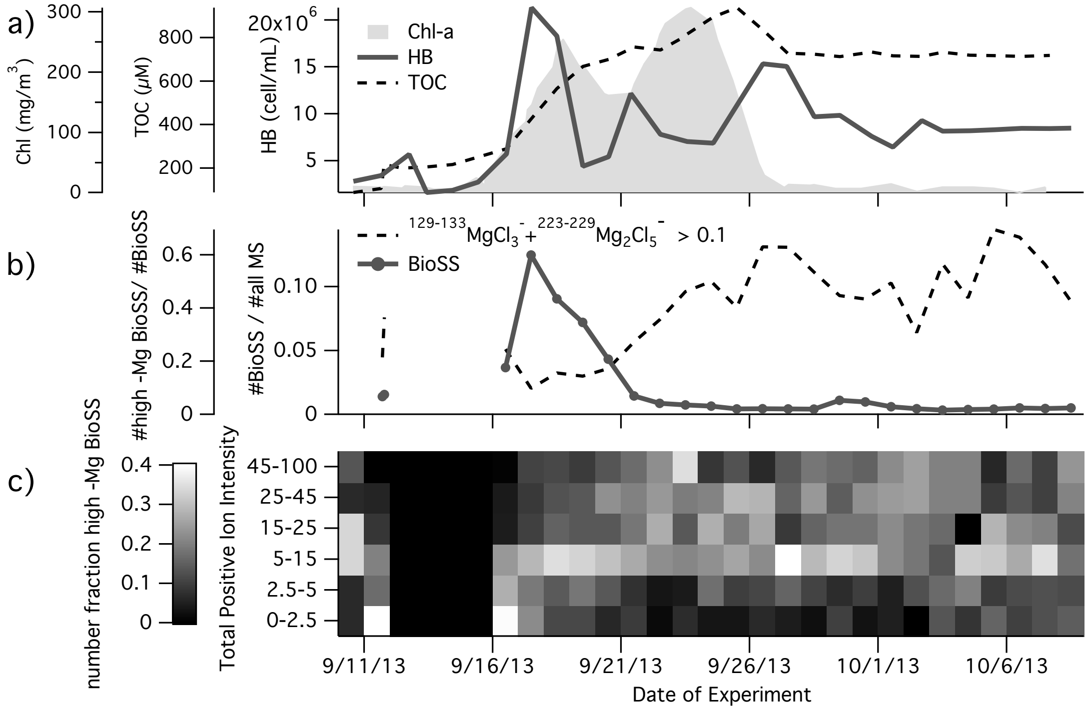

Figure 5.5 Temporal trends of (a) chlorophyll-a (Chl-a), heterotrophic bacteria (HB), and dissolved organic carbon (DOC) concentrations in the seawater as well as (b) the fraction of particles generating BioSS. In addition for each day (b) the fraction of BioSS with relatively intense *-Mg* ion signal and (c) the total ion intensity distribution for the *-Mg* rich BioSS is shown.

5.5 Conclusions

Identification and quantification of microorganisms originating from seawater is important due to their potential role as ice nuclei within clouds. However, while it has been shown that microbes are ejected into sea spray aerosols [*Blanchard*, 1978; *Blanchard and Syzdek*, 1982; *Aller et al.*, 2005; *Leck and Bigg*, 2005a; *Hultin et al.*, 2011; *Patterson et al.*, 2016], mass spectra with characteristic microbial signatures have never been uniquely identified within SPMS SSA datasets. This is the first report to distinguish BioSS, a likely microbial mass spectra, from the abundant SSA mass spectra with significant potassium and phosphate ion signals likely resultant from dissolved chemical species. Reported in this work are an array of identifying size and mass spectral characteristics for SSA BioSS which will support the identification of microbe-containing SSA particles in future laboratory and field studies. We utilize these ATOFMS results to propose that dry SSA generating BioSS are likely particles containing a microbial cell adhered to a sodium chloride node encompassed by a magnesium-rich coating. Such *in situ* descriptions of microbial SSA are rare as details of the structure of SSA are lost utilizing impinger or filter collection techniques commonly employed with offline analysis of aerosolized microbes. Finally, the chlorine and chlorine-containing ion clusters ubiquitous in the SSA BioSS population are the first ion markers proposed to be useful in distinguishing terrestrial from ocean-derived aerosolized microbes in marine influenced air masses.

In addition the analytical techniques applied herein while specifically employed for the identification of microbe-containing SSA particles could be applied to the wider examination of SSA, ambient, and other chemically complex aerosol populations. Our work suggests that particle size can be utilized to help discriminate mass spectral types generated by SSA containing insoluble residues beyond microbes, such as dust or soot. In addition we introduce mass spectral signature dependence on total ion intensity as a useful tool to support the classification of distinct particle types within a realistic mixed aerosol population. This technique is especially valuable as it can be applied to existing SPMS datasets and does not require explicit variable laser pulse energy experiments. The expansion of SPMS data analyses beyond the grouping of particles by comparison of mass spectral signatures could not only improve the robustness of scientific conclusions but also expand the limits of knowledge discovery within the field.

5.6 Acknowledgements

This work was supported by the National Science Foundation through the Centers of Chemical Innovation Program via the Center for Aerosol Impacts on Climate and the Environment (CHE-1305427). The authors would like to thank all collaborators involved in the MART microcosm study, notably C. Lee and D. B. Collins.

Chapter 5, in full, is material that has been submitted for publication to Analytical Chemistry. Printed with permission from Sultana, C.M., Al-Mashat, H., Prather, K. A. Expanding Single Particle Mass Spectrometer Analyses for the Identification of Microbe Signatures in Sea Spray Aerosols. The dissertation author was the primary investigator and author of this paper.

5.7 Supporting Information

Table 5.1 Final concentration of nutrients in the growth media (Proline Aquatic Ecosystems) added to the seawater. $Na_2SiO_3 \cdot 9H_2O$ is not part of the nutrient mix, and was added separately.

Components	*Molar Concentration* (M)
$NaNO_3$	8.82×10^{-4}
$NaH_2PO_4 \cdot H_2O$	3.62×10^{-5}
$Na_2SiO_3 \cdot 9H_2O$	1.06×10^{-4}
$FeCl_3 \cdot 6H_2O$	1.17×10^{-5}
$Na_2EDTA \cdot 2H_2O$	1.17×10^{-5}
$CuSO_4 \cdot 5H_2O$	3.93×10^{-8}
$Na_2MoO_4 \cdot 2H_2O$	2.60×10^{-8}
$ZnSO_4 \cdot 7H_2O$	7.65×10^{-8}
$CoCl_2 \cdot 6H_2O$	4.20×10^{-8}
$MnCl_2 \cdot 4H_2O$	9.10×10^{-7}
Thiamine HCl (vit. B_1)	2.96×10^{-7}
Biotin (vit. H)	2.05×10^{-9}
Cyanocobalamin (vit. B_{12})	3.69×10^{-10}

Table 5.2 Mass-to-charge of ions summed to calculate relative positive or negative ion signal.

m/z summed	**ion marker assignment**	**mass spectra polarity**
26, 42	$^{42}\mathrm{CNO}^{-}$, $^{26}\mathrm{CN}^{-}$	negative
74	$^{74}\mathrm{N(CH_3)_4}^{+}$	positive
104, 120, 141, 157, 175, 197	$^{120}\mathrm{C_8H_{10}NO_2}^{+}$, $^{175}\mathrm{C_6H_{15}N_4O_2}^{+}$	positive
129, 131, 133, 223, 225, 227, 229	$^{129,131,133}\mathrm{MgCl_3},^{-}$ $^{223,225,227,229}\mathrm{Mg_2Cl_5}$	negative
23, 81, 83	$^{23}\mathrm{Na}^{+}$, $^{81,83}\mathrm{Na_2Cl}^{+}$	positive

Table 5.3 Ion markers common to the various representative mass spectra shown in Figure 5.1. The ion markers are roughly grouped by the intensity of their signal relative to the total positive or total negative ion intensity. Note that a great amount of particle-to-particle variation exists in the mass spectra and the descriptions given are not definitive.

Figure 5.1 panel	Positive mass spectra	Negative mass spectra
a	High: $^{39,41}K^{+}$, $^{59}N(CH_3)_3^{+}$, $^{74}N(CH_3)_4^{+}$, Medium: $^{43}CHNO^{+}$, 58 Low: $^{19}H_3O^{+}$, $^{23}Na^{+}$, $^{24}Mg^{+}$, $^{91}C_7H_7^{+}$, 104	High: $^{79}PO_3^{-}$, Medium: $^{26}CN^{-}$, $^{35,37}Cl^{-}$, $^{42}CNO^{-}$, $^{63}PO_2^{-}$, -66, $^{90}C_4N_3^{-}$, $^{97}H_2PO_4^{-}$, $^{111,113}KCl_2^{-}$, $^{129,131,133}MgCl_3^{-}$, $^{146}C_5H_8NO_4^{-}$ $^{223,225,227,229}Mg_2Cl_5$ Low: $^{17}OH^{-}$, -43, 71, $^{107}C_4N_4H_3^{-}$, $^{117}C_5N_4H^{-}$
b	High: $^{39,41}K^{+}$ Medium: $^{23}Na^{+}$ Low: $^{19}H_3O^{+}$, $^{24}Mg^{+}$, $^{59}N(CH_3)_3^{+}$, $^{74}N(CH_3)_4^{+}$,104, $^{113,115}K_2Cl^{+}$, $^{120}C_8H_{10}NO_2^{+}$, 141, 157, $^{175}C_6H_{15}N_4O_2^{+}$, 197, 213, 215, 224, 275	High: $^{26}CN^{-}$, $^{42}CNO^{-}$, $^{79}PO_3^{-}$, Medium: $^{35,37}Cl^{-}$, 40, 41, $^{63}PO_2^{-}$, -66, $^{97}H_2PO_4^{-}$, Low: $^{17}OH^{-}$, 43, 58, 71, $^{90}C_4N_3^{-}$, $^{97}H_2PO_4^{-}$, $^{129,131,133}MgCl_3^{-}$, $^{146}C_5H_8NO_4^{-}$
c	High: $^{39,41}K^{+}$ Low: $^{23}Na^{+,}$ $^{56}KOH^{+}$	High: $^{26}CN^{-}$, $^{42}CNO^{-}$, $^{79}PO_3^{-}$, Medium: $^{35,37}Cl^{-}$, $^{63}PO_2^{-}$ Low: 40, 41, 43

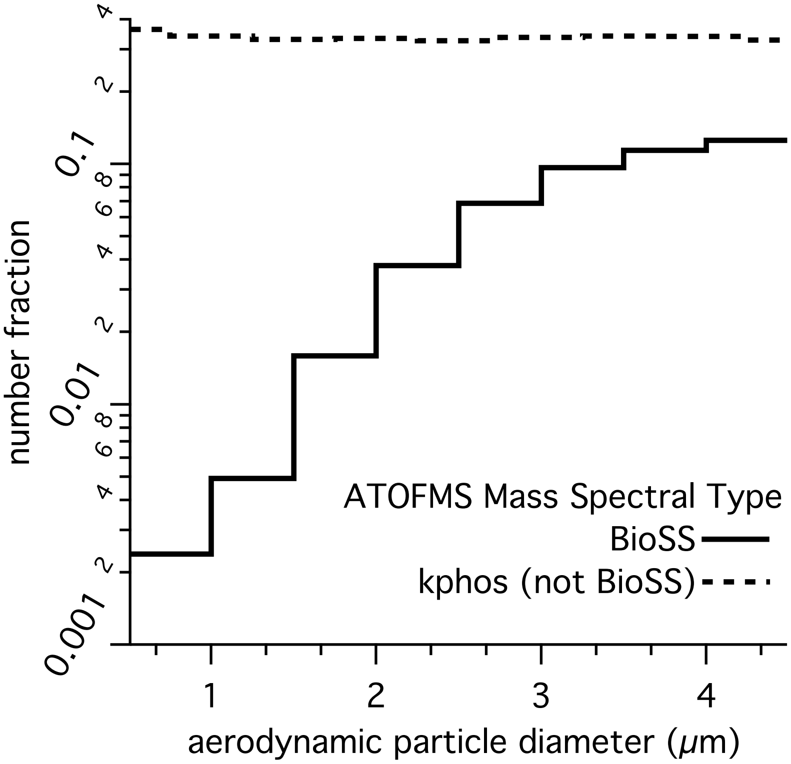

Figure 5.6 The number fraction of select SSA particles over the size range of the ATOFMS: particles generating biological mass spectra (BioSS), particles with potassium and phosphate rich mass spectra that were not classified as BioSS (kPhos).

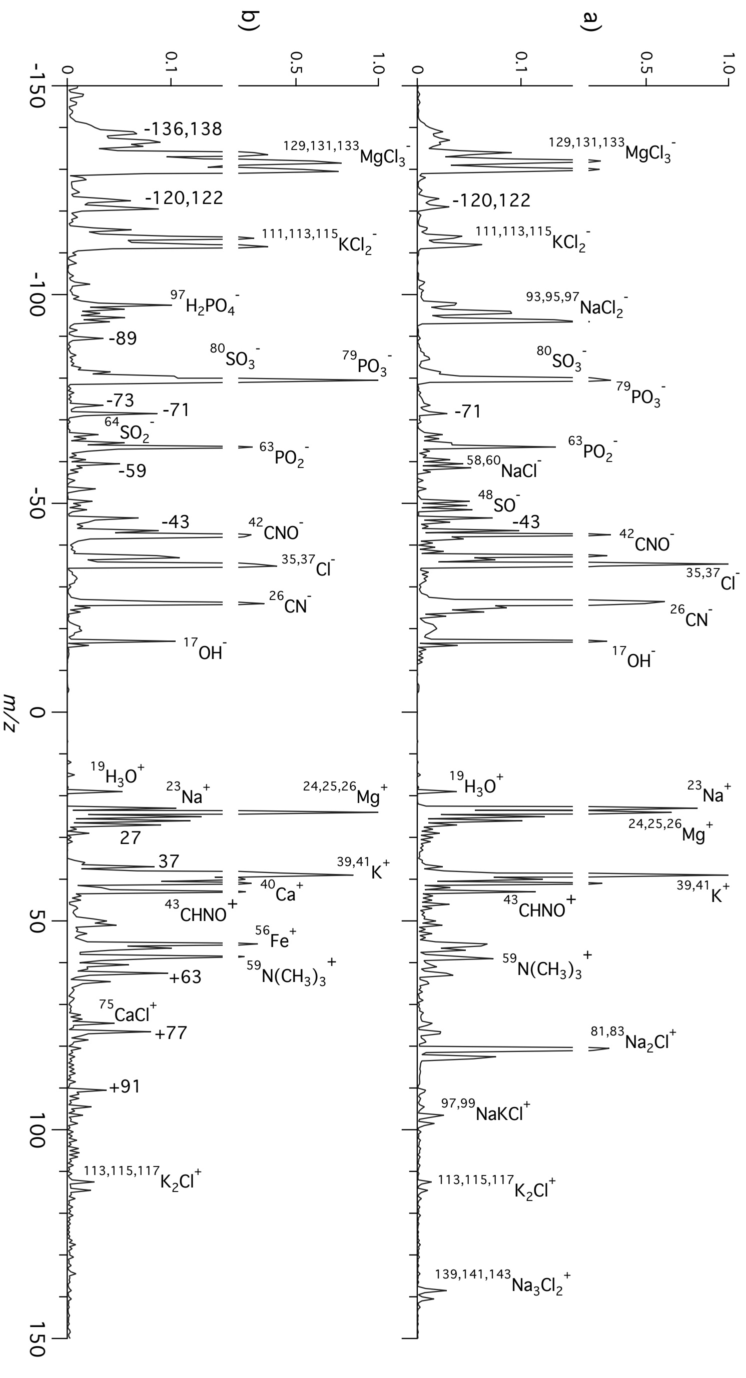

Figure 5.7 Two representative dual-polarity mass spectra illustrating the continuum of SSA ion signatures with strong potassium and phosphate ion signals but not identified as BioSS. To help eliminate noise, these representative mass spectra are made up of an average of 19788 (a) and 34711 (b) single particle mass spectra.

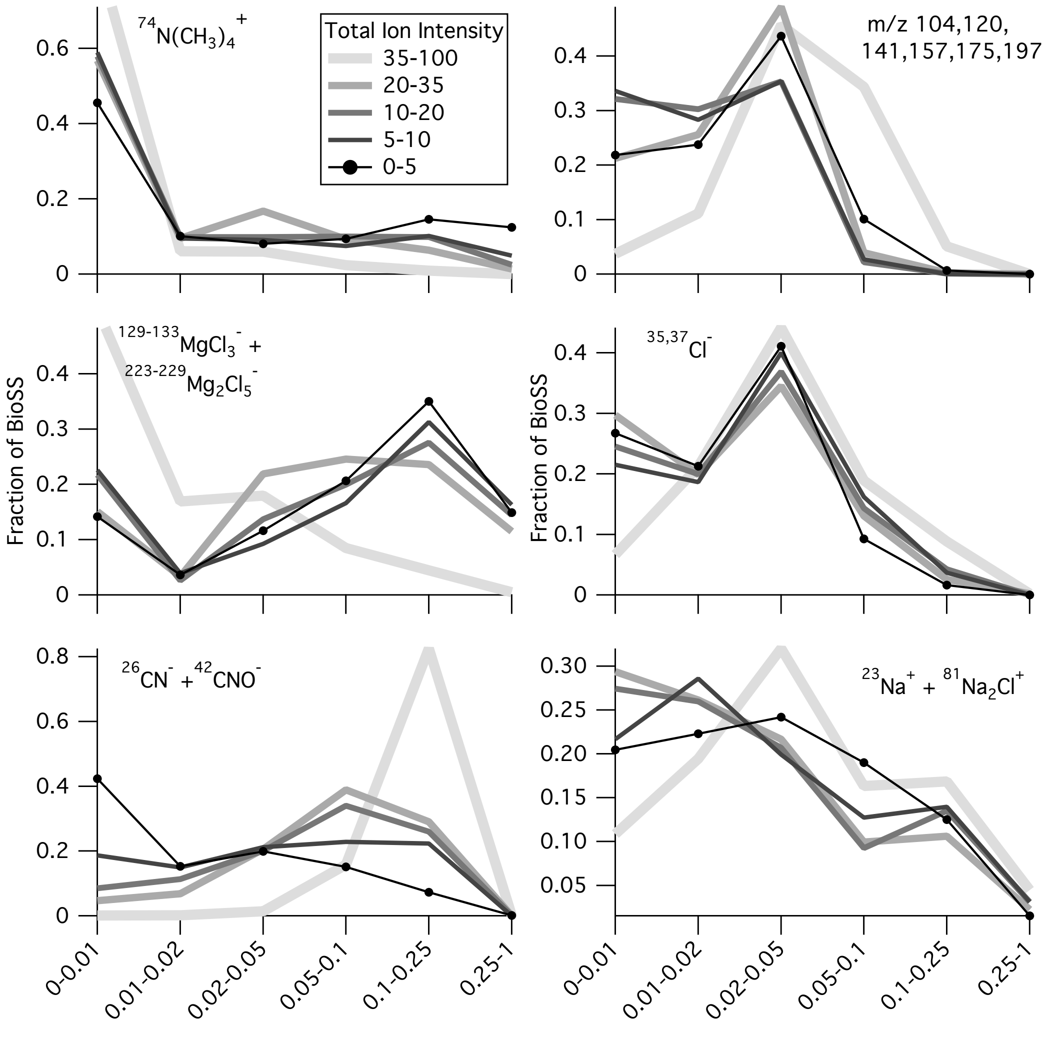

Figure 5.8 Distributions of relative ion signals for BioSS grouped by total ion intensity. Results shown are for all BioSS generated during the experiment with 1.22+-0.04 mJ laser pulse energy.

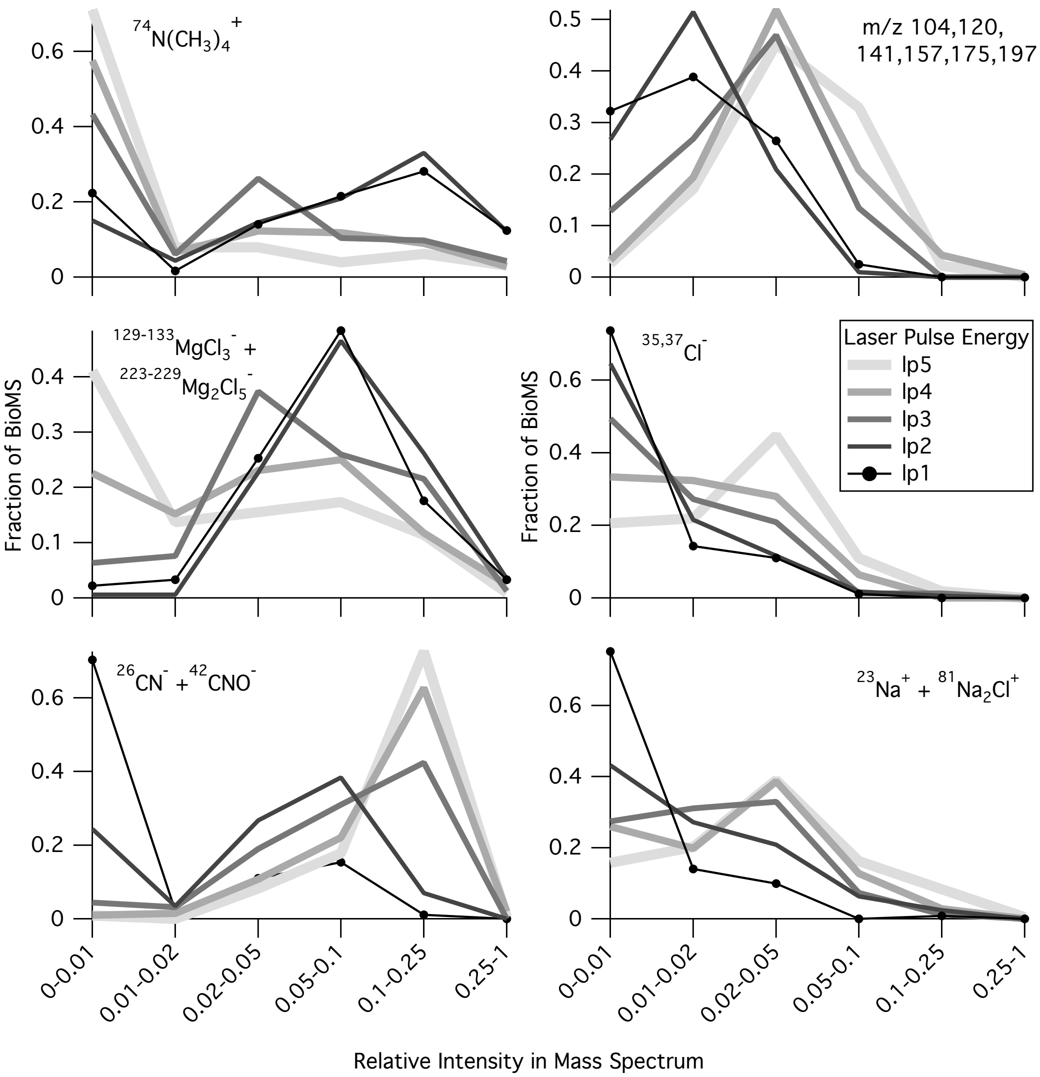

Figure 5.9 Distributions of relative ion signals on September 17th for BioSS for all laser pulse energies utilized.

Chapter 6. Microbial Control of Sea Spray Aerosol Composition: A Tale of Two Blooms

Reproduced by permission of the American Chemical Society

6.1 Abstract

With the oceans covering 71% of the Earth, sea spray aerosol (SSA) particles profoundly impact climate through their ability to scatter solar radiation and serve as seeds for cloud formation. The climate properties can change when sea salt particles become mixed with insoluble organic material formed in ocean regions with phytoplankton blooms. Currently, the extent to which SSA chemical composition and climate properties are altered by biological processes in the ocean is uncertain. To better understand the factors controlling SSA composition, we carried out a mesocosm study in an isolated ocean-atmosphere facility containing 3,400 gallons of natural seawater. Over the course of the study, two successive phytoplankton blooms resulted in SSA with vastly different composition and properties. During the first bloom, aliphatic-rich organics were enhanced in submicron SSA and tracked the abundance of phytoplankton as indicated by chlorophyll-a concentrations. In contrast, the second bloom showed no enhancement of organic species in submicron particles. A concurrent increase in ice nucleating SSA particles was also observed only during the first bloom. Analysis of the temporal variability in the concentration of aliphatic-rich organic species, using a kinetic model, suggests that the observed enhancement in SSA organic content is set by a delicate balance between the rate of phytoplankton primary production of labile lipids and enzymatic induced degradation. This study establishes a mechanistic framework indicating that biological processes in the ocean

and SSA chemical composition are coupled not simply by ocean chlorophyll-a concentrations, but are modulated by microbial degradation processes. This work provides unique insight into the biological, chemical, and physical processes that control SSA chemical composition, that when properly accounted for may explain the observed differences in SSA composition between field studies.

6.2 Introduction

Sea spray aerosols (SSA) represent a major atmospheric aerosol particle type [*Lewis and Schwartz*, 2004c; *Stier et al.*, 2005; *O'Dowd et al.*, 2007; *Knopf et al.*, 2011]. SSA play a crucial role in affecting climate through reducing direct radiative forcing [*Murphy et al.*, 1998] and by modulating cloud properties through their ability to act as cloud condensation nuclei [*Partanen et al.*, 2014] and ice nuclei particles (INP) [*DeMott et al.*, 2010]. Estimates of the impact of SSA on the Earth's radiation budget are highly uncertain due to an overall lack of understanding of the physical and chemical factors controlling SSA concentration, size, and composition [*O'Dowd et al.*, 2008; *de Leeuw et al.*, 2011; *Jaeglé et al.*, 2011; *Partanen et al.*, 2014]. This limits our ability to untangle the extent to which human activities versus the natural background have altered the impacts of particles on the global radiation budget and climate, and thus hampers assessments of future climate change [*IPCC*, 2013]. Freshly emitted SSA are composed both of sea salt and organic material, and under certain conditions the organic species comprise a substantial fraction of the total particle mass, especially for smaller diameter particles (< 1 mm) [*Hoffman and Duce*, 1974; *O'Dowd et al.*, 2004]. The lower solubility organic components can strongly affect the climate-relevant properties of SSA [*O'Dowd et al.*, 2004; *Collins et al.*, 2013; *Prather et al.*, 2013; *Quinn et al.*, 2014]. However, due to a limited understanding of the mechanisms that control the transfer of organic matter from seawater to SSA, it is currently not possible to predict the organic composition of SSA.

Ideally, the organic content of SSA could be predicted using some measured seawater chemical or biological parameter. Significant effort has been put into developing relationships between the organic fraction of SSA and chlorphyll-a (Chl-a) concentrations, an indicator of seawater phytoplankton concentrations, because Chl-a in surface waters can be measured from space using satellites [*McClain*, 2009]. Results from previous studies have been ambiguous. Some field studies have shown a relationship between the organic fraction of SSA and Chl-a concentrations for monthly and seasonal time scales in ambient marine aerosols [*O'Dowd et al.*, 2004; *Rinaldi et al.*, 2010], while others have reported no differences in sea spray composition [*Bates et al.*, 2012; *Quinn et al.*, 2014]. Further, the coefficient of determination (r^2) between Chl-a and organic fraction in SSA is usually below 0.5 [*Rinaldi et al.*, 2013]. This suggests that the organic enrichment of SSA is controlled not only by phytoplankton primary production, but also by other biological and chemical processes. Nevertheless, Chl-a is still commonly used to estimate the organic fraction of SSA in large-scale climate models [*Spracklen et al.*, 2008; *Vignati et al.*, 2010; *Partanen et al.*, 2014]. Thus, if sea spray composition and the associated properties are to be properly treated in models, it is crucial to elucidate the mechanisms that link oceanic biological activity, surface ocean chemical composition and concentrations, and the organic fraction of SSA.

Herein new insights into these mechanistic linkages have been achieved through the use of a unique ocean-atmosphere facility [*Prather et al.*, 2013] that allows for detailed characterization of seawater and the associated SSA produced from wave breaking during a 29-day mesocosm experiment utilizing real ocean water. Using a kinetic model, we have established a mechanistic explanation tying the control of seawater organic composition by the measured biological metrics of chlorophyll-a and heterotrophic bacteria enzyme activity to submicron SSA organic concentration and composition. The results from this study provide a possible explanation for the conflicting results in field studies investigating the factors controlling the organic content of SSA and the associated climate properties.

6.3 Results and Discussion

6.3.1 Overview of Mesocosm Experiment and Measurements

A mesocosm experiment was performed in a wave channel filled with 13,000 liters of natural seawater obtained off the California coast. This unique ocean-atmosphere facility allowed for simulation of ocean seawater conditions representative of typical oceanic phytoplankton blooms with respect to the Chl-a concentrations [*Wernand et al.*, 2013]. Dynamic oceanic chemical processes associated with biological activity were stimulated by addition of nutrients at the beginning of the experiment, which initiated phytoplankton growth (6.5.1-6.5.4). Two successive, yet distinct, phytoplankton blooms resulted as evidenced by two major Chl-a peaks over the 29-day experimental period (Figure 6.1A). Seawater biological activity was characterized by measurements of Chl-a and heterotrophic bacteria concentrations and ectoenzyme activities (6.5.5).

Throughout this entire study, realistic nascent SSA were generated from the seawater using actual breaking waves [*Partanen et al.*, 2014] (Figure 6.5) and the SSA size distributions and composition, both bulk and size-resolved, were measured (Methods S6-S9). Size-resolved bulk chemical composition of non-refractory SSA components (in particular, organic matter, OM) of dry particles in the size range 0.04 to 2 μm (vacuum aerodynamic diameter, D_{va}) was measured online using an Aerodyne high-resolution time-of-flight aerosol mass spectrometer (AMS; 6.5.7). The normalized OM mass fraction of SSA, f_{OM}, was determined as f_{OM} = $[OM]/[PM_1]_{dry}$, normalized to the maximum value of f_{OM}, where $[PM_1]_{dry}$ is the dry sub-micrometer particulate mass concentration estimated from the size distributions (6.5.8). The chemical compositions of dried individual SSA particles from 0.25 to 3 μm (D_{va}) were additionally characterized online using an aerosol time-of-flight mass spectrometer (ATOFMS), which measures the size-resolved chemical mixing state of particles and allows for determination of variations in the relative fractions and concentrations of particles with distinct compositions (Methods S7). These online measurements were complemented by offline measurements of individual particle organic composition using micro-Raman spectroscopy (Methods S9).

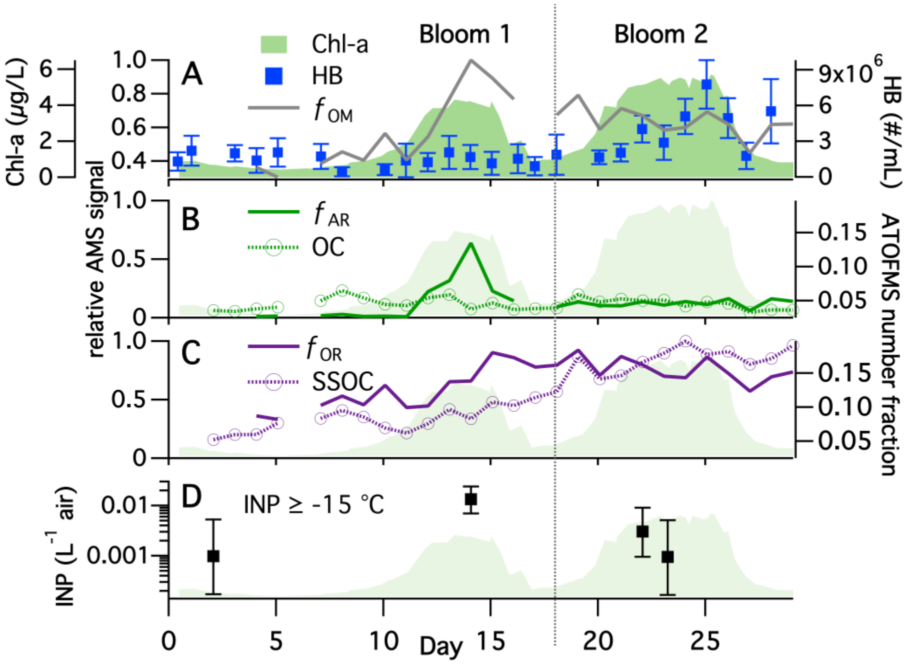

Figure 6.1 Time series for the mescosom experiment in the wave channel of (A) of Chl-a and heterotrophic bacteria (HB) concentrations in bulk seawater and as fOM, the relative organic mass fraction of SSA as determined by the AMS (B) fAR, the relative aliphatic-rich factor mass concentration and the number fraction of the OC particle type (C) fOR, the relative oxygen-rich factor mass concentration and the number fraction of the SSOC particle type as determined by the AMS and ATOFMS respectively and (D) the concentration of ice nucleating particles (INP).

6.3.2 Impact of Mesocosm Dynamics on SSA Composition

The behavior of the f_{OM} time series was distinct between the two phytoplankton blooms; f_{OM} peaked during the first bloom, then decreased and remained constant throughout the second bloom (Figure 6.1A). The variability in f_{OM} suggests a difference in the organic composition of the seawater between the two blooms, examined further below, and helps to explain why previous studies have found inconsistent correlations between organic enrichment in SSA and phytoplankton blooms or Chl-a concentrations in seawater [*O'Dowd et al.*, 2004; *Vignati et al.*, 2010; *Bates et al.*, 2012; *Quinn et al.*, 2014]. Further insights come from consideration of the average size distribution of AMS organic species ion signals (Figure 6.2A). The peaks at *m/z* 43, 57 and 44 are used as indicators of total, aliphatic-rich, and oxidized organic species, respectively [*Canagaratna et al.*, 2007]. The study-average total organic size distribution was bimodal, with clear chemical differences between the classes of organic compounds in these two modes. The submicron mode peaked at D_{va} = 300 nm and was dominated by aliphatic-rich organic species, whereas the supermicron mode peaked at D_{va} = 1500 nm and was dominated by oxidized organic species, consistent with the size-resolved mass spectra (Figure 6.6).

SSA are formed when bubbles burst at the air-sea interface, producing both film drops and jet drops [*Lewis and Schwartz*, 2004c]. Film drops are formed from the bursting of the bubble film, which is enriched in surface active organic species [*Blanchard*, 1989], while jet drops may originate from the sea surface microlayer (SSML) or underlying bulk seawater. These differences in production mechanisms can lead to differences in the resulting SSA composition. It is typically assumed that most submicron SSA originate from film drops, while most supermicron SSA originate from jet drops [*Blanchard*, 1989; *Grythe et al.*, 2014]. Aliphatic-rich organic species, such as lipids, are typically surface active, allowing them to partition strongly to bubble surfaces and the air-sea interface. This can lead to organic enrichment in film drops, especially if bubble drainage of water occurs [*Burrows et al.*, 2014], although there can be a complex relationship between enrichment in the SSML and the bulk concentrations of surface active species [*Marty et al.*, 1988; *Wurl et al.*, 2011]. In contrast, the more oxidized organic species in the supermicron mode were chemically similar to the dissolved organics in the seawater, as evidenced by comparison with the AMS organic spectrum of atomized bulk seawater (Figure 6.7). Given the differences in the size and composition of the two organic modes of SSA, we postulate that the

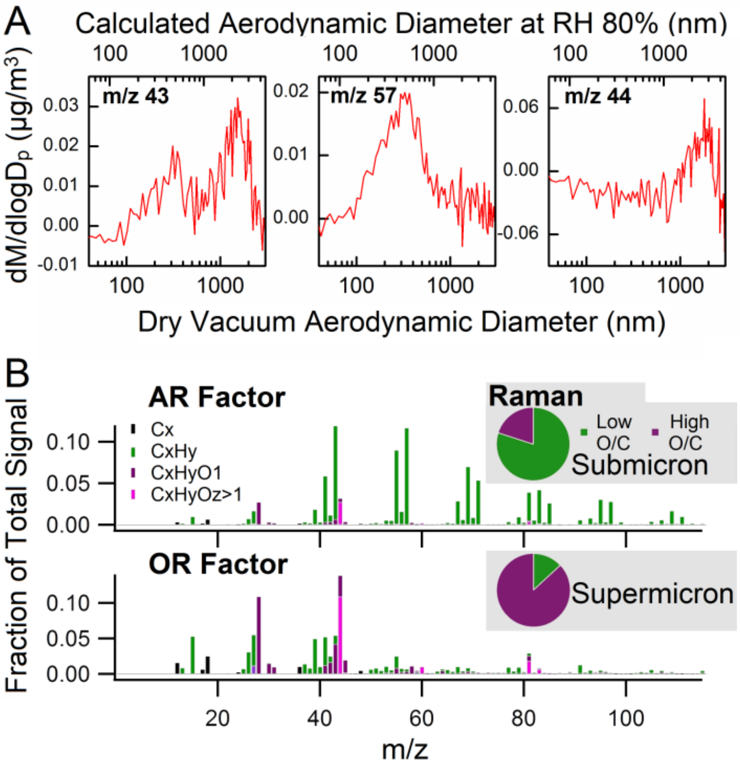

Figure 6.2 Two organic size modes in SSA produced from the wave-channel experiment: (A) mass size distributions of AMS organic ion signals: m/z 43 ($C_3H_7^+$ or $C_2H_3O^+$), an indicator of total organic species; m/z 57 ($C_4H_9^+$), an indicator of aliphatic-rich organic species and m/z 44 (CO_2^+), an indicator of oxidized organic species. The AMS measured particle size as dry D_{va}, and the aerodyanmic diameter (D_a) at RH 80% was calculated (6.5.8) and shown on the top x-axis; and (B) AMS mass spectra of the two organic component factors, aliphatic-rich and oxygen-rich, which were separated by positive matrix factorization (PMF); and (inset) classification of submicron (D_a: 0.56-1 µm) and supermicron (D_a: 1.8-3.2 µm) particles based on micro-Raman spectra of individual SSA particles collected on day 14. The data shown accounts for 94% and 81% respectively of all the submicron and supermicron particles analyzed on day 14.

aliphatic-rich submicron mode particles were mainly generated from film drops, while jet drops contributed to the supermicron mode particles that contained the more soluble oxidized organic compounds. It should be noted that this is the first time the production mechanism has been shown to distribute different classes of organic species to different size modes.

The AMS organic signals were separated into two factor components using positive matrix factorization (6.5.8, Figure 6.2B), and the oxygen-to-carbon (O/C) and hydrogen-to-carbon (H/C) atomic ratios of the total organic matter were extracted through analysis of the high-resolution mass spectra. The mass spectrum for one of the factors was dominated by hydrocarbon peaks ($C_xH_y^+$), similar to that of the organics in the submicron mode (Figure 6.7); this factor will be referred to as the aliphatic-rich (AR) factor. The mass spectrum for the second factor was similar to the average supermicron mode organic mass spectrum (Figure 6.7) and contained many oxygen-containing organic peaks ($C_xH_yO_z^+$); this factor will be referred to as the oxygen-rich (OR) factor. Thus, the AR and OR factors are representative of the organic species comprising the submicron and supermicron modes, respectively.

Figure 6.1B-C shows the time series of the AR and OR factor mass concentrations, normalized to $[PM_1]_{dry}$ and the maximum value of f_{OM}, referred to as f_{AR} and f_{OR} [6.5.8]. Both f_{AR} (Figure 6.1B) and the H/C ratio of the total organic matter (Figure 6.8) exhibited a sharp peak during the first phytoplankton bloom, quickly declined, and then remained nearly constant throughout the second bloom. The sudden decrease in the f_{AR} peak was nearly concurrent with the decline of the Chl-a concentrations in the first bloom, suggesting that the submicron mode became enriched in labile organic species that underwent rapid transformations through microbial activity in the seawater. The observation that f_{AR} peaked only during one of the blooms indicates there were clear differences in the production and degradation of the organic species that made up most of the submicron organic mass. The half-life of these labile species was <1 day, as f_{AR} decreased by more than 50% within one day of the peak. Known labile species in seawater include amino acids, proteins, free sugars, fatty acids, and other lipids [*Goutx et al.*, 2009]. The AR factor was rich in aliphatic character, and thus lipids seem a more likely source of the submicron organics than do proteins or free sugars. The f_{OR} time series exhibited distinctly different behavior from that of f_{AR}, increasing from the onset of the first bloom after which it remained relatively constant (Figure 6.1C), suggesting that the more oxidized organic species in the supermicron mode had comparably much longer residence times in seawater than AR species. These findings demonstrate that organic species in seawater cannot be considered a homogenous pool in terms of how they influence organic enrichment in SSA, and that complex dynamics and differences in the production mechanism lead to partitioning of distinct classes of organic species into different SSA size modes at different times over the course of a phytoplankton bloom.

The general organic type identifications (aliphatic-rich and oxygen-rich) are further supported by offline measurements using micro-Raman spectroscopy of individual, substrate-deposited particles in different size ranges (6.5.9). During the peak of the first bloom (day 14), submicron particles (aerodynamic diameter D_a: 0.56-1 μm) were dominated by compounds having low O/C ratios (O/C < 0.25), while supermicron particles (D_a: 1.8-3.2 μm) contained mostly compounds having a high O/C ratio (O/C > 0.5) (Figure 6.2B). The O/C ratio of individual particles was estimated from the molecular formulas of representative compounds (Figure 6.10). Thus, the micro-Raman results further support the mass spectrometry results showing different classes of organic species contributing to particles in the two SSA size modes.

Analysis of the ATOFMS mass spectra led to identification of two distinct organic-enriched SSA particle types (6.5.7): sea salt mixed with organic carbon species (SSOC) and organic carbon species largely free of sea salt (OC) (Figure 6.9A), both of which are similar to previously described particle types [*Prather et al.*, 2013]. Whereas the AMS allowed for characterization of the bulk organic composition, the ATOFMS characterizes individual particle types, making these two online mass spectrometry approaches complementary. Supermicron particles (1-3 mm) were dominated by the SSOC type, with SSOC particles 2 to 3 times more abundant than OC type particles in this size range. Further, the time series of the total SSOC number fraction was similar to that of f_{OR} (Figure 6.1C), which suggests a relationship between oxygen-rich species and SSOC type particles. The relative number fraction of the OC particle type increased steeply with decreasing size, making up a greater fraction of total particles than SSOC in the smallest size bin (0.25-0.5 μm). This indicates a connection between OC type particles and the AR organics in the submicron mode, although the time series of the total OC number fraction was fairly constant over time, in contrast to the sharp peak in f_{AR} (Figure 6.1B). However, the total OC number fraction time series is not necessarily representative of the behavior of particles with dry $D_{va} < 0.5\mu m$, which make up <1% of the total particle counts due to the size-dependent sampling bias of the ATOFMS (Figure 6.9B). The particle sampling statistics do not lend themselves to a presentation of the time series in the relevant submicron size range (dry $D_{va} \sim 0.3\mu m$). Based on the combined AMS and ATOFMS results, the aliphatic-rich organic species in the submicron particles most likely occur in particles largely free of sodium chloride (i.e. OC type) while the oxygen-rich organic species in the supermicron mode were more likely to be internally mixed with sea salt (i.e. SSOC type).

6.3.3 Explaining the Differences in SSA Organic Content Between the Two Blooms

The second phytoplankton bloom in the wave channel did not lead to organic enrichment in the submicron mode, suggesting some process other than phytoplankton primary production must have played a role in controlling the abundance and chemical composition of organic material transferred to submicron SSA. Heterotrophic bacteria (HB) concentrations (Figure 6.1A) and enzymatic activity as characterized by the lipase activity (Figure 6.3) were much higher during the second bloom than during the first, and both exhibited similar temporal variations. It is therefore possible that primary production by phytoplankton introduced surface-active, aliphatic-rich, highly-labile (ARL) organic species to the seawater that led to the sharp increase in f_{AR} (i.e. in aliphatic-rich organics in submicron SSA) during the first bloom. However, this build up in ARL species—and thus in f_{AR}—was halted and reversed as the HB concentration and enzymatic activity increased, leading to an increased rate of transformation of ARL species into less surface active, more soluble species. Although these degradation products likely remained in the seawater [*Duflos et al.*, 2009], they were transferred less efficiently into submicron SSA by film drops thereby causing f_{AR} to decrease and remain low throughout the second bloom. It is likely that the more soluble degradation products, likely fatty acid salts, contributed to organics species in the supermicron mode which began to increase after the first bloom. The most likely identity of the ARL organic species was lipids such as glyceroglycolipids, phospholipids, and triacylglycerols, which make up the majority of lipids produced by phytoplankton in seawater [*Gupta et al.*, 2004; *Harwood and Guschina*, 2009]. Fatty acids are less likely to be the ARL organic species because they are generally more soluble, less surface active than other lipids classes, and lack ester bonds [*Gašparovic et al.*, 1998]. Additionally, the turnover time for free fatty acids in the ocean is around 10 days [*Burrows et al.*, 2014; *Grythe et al.*, 2014], much longer than the 1 day observed in the first bloom. Consistent with the above ideas, it is well established that heterotrophic bacteria in seawater use ectoenzymatic lipase to transform ester-containing lipids by hydrolysis into smaller molecular weight and comparably more soluble free fatty acids or their salts. Thus, we suggest that the sharp decrease in f_{AR} at the end of the first bloom and the sustained low level throughout the second bloom resulted from the increase in heterotrophic bacteria concentrations and the associated lipase enzymatic activity.

This hypothesis is quantitatively examined using a box model in which it is assumed that ARL species are produced by phytoplankton and transformed by bacteria via lipase (6.5.11). More specifically, ARL production is assumed to correlate with the death and disruption (cell lysis) of the phytoplankton, which usually results from programmed cell death or virus or zooplankton attack, which serves as a major source of dissolved organic matter (DOM) in seawater [*Kujawinski et al.*, 2002; *Burrows et al.*, 2014]. In this study, zooplankton likely do not play an important role since most zooplankton were removed by filtering at the start of the experiment (6.5.2). Additionally viral lysis of phytoplankton was excluded from the model because the observed virus concentration correlated with the HB concentration (r^2 = 0.60), indicating that most of the viruses in the mesocosm experiment, which were at typical ocean concentrations [*Breitbart*, 2012], were likely bacteriophage that do not attack phytoplankton [*Wilcox and Fuhrman*, 1994; *Suttle*, 2007]. Therefore for this mesocosm experiment, programmed cell death is thought to control phytoplankton cell lysis, and the production rate of ARL was assumed to be first order and proportional to the Chl-a (and phytoplankton mass) concentrations. The transformation rate of the ARL species was assumed to follow Michaelis-Menten kinetics. Thus, the model is governed by the following equation:

$$\frac{d[\mathrm{ARL}]}{dt} = k^{+}[\text{Chl-a}] - R_{max} \cdot [\mathrm{ARL}]/(C_{1/2} + [\mathrm{ARL}]) \,, \qquad [1]$$

where k^{+} is the ARL production rate constant and $C_{1/2}$ is the ARL concentration at half of its maximum consumption rate, both of which are adjustable parameters. The observed [Chl-a] time series is used as a model input. The parameter R_{max} is the maximum transformation rate of ARL, which is related to the enzymatic activity. Here, R_{max} is assumed to be equal to the measured time series of lipase activity.

The model parameters have been adjusted to determine an [ARL] time series that reproduces the shape of the f_{AR} time series (Figure 6.3). This comparison implicitly assumes that variations in [ARL] are linearly related to f_{AR}, which is reasonable if the surface-active ARL species are below the surface saturation threshold; this assumption may break down at high ARL concentrations [*Marty et al.*, 1988; *Wurl et al.*, 2011]. This model shows good agreement between the calculated [ARL] and the observed f_{AR}, after tuning (Figure 6.3), which strongly supports our hypothesis that enzymatic degradation, driven by bacterial lipases, led to the rapid reduction in f_{AR} after the first bloom and the sustained low concentrations during the second bloom. Ectoenzyme activities besides lipase, including protease, chitinase, and alkaline phosphatase, were also measured. However, these ectoenzyme activities showed very different temporal trends from lipase (Figure 6.11), and no values of the adjustable model parameters were found that yielded a good fit to the f_{AR} time series when these were used either individually or when summed together. This further supports the idea that bacterial lipase activity was specifically responsible for the degradation of ARL species. Thus, bacterial enzymes are responsible for converting insoluble lipids into more soluble free fatty acids as the primary ARL transformation pathway [*Gupta et al.*, 2004; *Harwood and Guschina*, 2009]. The change in solubility induced by the enzymes results in different classes of organic species being released in different SSA size modes, as described above.

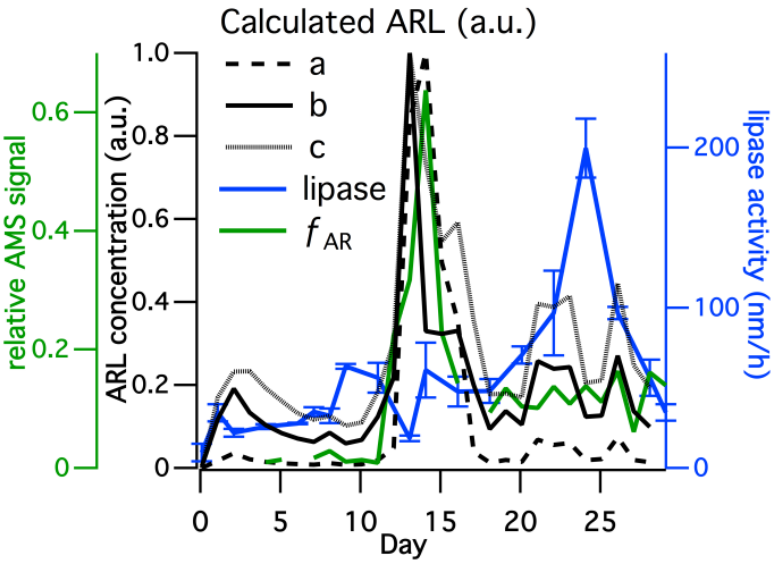

Figure 6.3 Lipase activity and calculated aliphatic-rich labile (ARL) species concentration (Model parameters: a: $k^+ = 250$ a.u. μg^{-1} l day^{-1} and $C_{1/2} = 30$ a.u.; b: $k^+ = 6$ a.u. μg^{-1} l day^{-1} and $C_{1/2} = 5$ a.u.; and c: $k^+ = 6$ a.u. μg^{-1} l day^{-1} and $C_{1/2} = 500$ a.u. (a.u. means arbitrary unit)

The above model excludes processes resulting from cell lysis of heterotrophic bacteria which could be a source of mostly phospholipids, rather than triacylglycerols and glyceroglycolipids [*Kaneda*, 1991; *Van Mooy and Fredricks*, 2010], although it is unlikely that contributions from bacteria cell lysis would compete globally with primary lipid production from phytoplankton [*Burrows et al.*, 2014]. Also of consideration is the level of lipase activity during the blooms, which was ~50 nM h^{-1} during the first bloom with a peak of 200 nm h^{-1} during the second bloom. Unpublished measurements of lipase activity of the natural seawater at the SIO pier range from 8-30 nM h^{-1}. Lower values have been observed in more oligotrophic sites [*Bourguet et al.*, 2003], while similarly high values have been observed in the northern Adriatic Sea [*Celussi and Del Negro*, 2012] and in other mesocosm experiments [*Riemann et al.*, 2000]. The implication of having high lipase activity, relative to oceanic blooms, is that the ARL transformation may have proceeded more rapidly during the mesocosm experiment, thus limiting the duration of the submicron SSA organic enrichment.

Taking all the results together, the contribution of organics to the submicron SSA mode (here, exemplified by f_{AR}) is determined by the combined effects of the production and transformation of key surface-active species. Thus, the use of Chl-a as an indicator of organic enrichment in submicron SSA consequently only provides one piece of the story. Based on our findings, we recommend future studies include measurements of bacterial enzyme activities to provide a more complete picture of the production and formation pathways for organic species in seawater to explain submicron SSA composition.

6.3.4 Impact of Phytoplankton Bloom on Ice Nucleation Properties

As SSA particles influence clouds and represent the dominant particle type available to serve as cloud nucleating particles in remote marine environments [*Murphy et al.*, 1998; *Burrows et al.*, 2013], variations in SSA chemical composition induced by biological activity have been suggested to lead to the observed changes in cloud properties in these regions [*Prather et al.*, 2013]. Here we investigate how concentrations of ice nucleating particles (INP) changed during the mesocosm experiment through SSA collection and release into liquid for immersion freezing studies in solution (6.5.10). The observed INP concentrations (0.001-0.014 L^{-1} at -15°C) were similar to those observed in remote (>45°S) marine air [*Harwood and Guschina*, 2009]. The maximum warm-temperature INP concentration (i.e. ice nucleation at ≥ -15 °C) occurred concurrent with the peak in f_{AR} during the first bloom (Figure 6.1D). The INP activity during this period was reduced from 0.014 L^{-1} to below the detection limit for this sample by pre-heating the solution to 95°C, suggesting that biological particles were released concurrently with the AR organics in SSA. Additionally, monolayers of surface-active long-chain molecules could also have triggered ice nucleation on SSA; for example, amphiphilic long-chain alcohol monolayers have been shown to trigger heterogeneous freezing of water [*Gavish et al.*, 1990; *Popovitz-Biro et al.*, 1991]. It is important to note that the INP which appear to be biological particles based on the heat treatment results could have been released concurrently with the change in SSA composition of submicron particles. Although the exact species that led to the increased INP concentrations during the first bloom are not yet confirmed, the observation that the INP concentration peaked during a phytoplankton bloom suggests that changes in the chemical composition and complexity of seawater, induced by biological processes, can influence the release of ice nucleating particles, a finding which has significant implications for marine cloud properties and global climate.

6.3.5 Factors Controlling SSA Composition and Climate Relevant Properties

A mechanistic overview of the major findings of this mesocosm experiment is provided in Figure 6.4. Chemically distinct pools of different organic compounds are proposed to exist in seawater. Differences in chemical composition between these pools determine both their biological availability and transfer to the aerosol phase, leading to clear distinctions in organic speciation and mixing state of organic-containing submicron and supermicron SSA. As evident from the mesocosm experiment here, these separate organic pools were transferred to SSA at different times and in different particle size ranges over the course of two successive phytoplankton blooms.

During the first bloom only, aliphatic-rich organic species in SSA peaked sharply and generally tracked Chl-a concentrations. The AR organics were primarily in submicron particles with little, if any, contribution from NaCl, indicating they were most likely generated primarily from the bursting of the bubble film cap as purely organic particles. A similar mechanism was proposed recently based on the observation that the organic fraction of artificially generated sea spray from natural waters in the field was more aliphatic-rich from areas of higher Chl-a concentrations [*Frossard et al.*, 2014]. Increased concentrations of ice nucleating particles were associated with the increase of these aliphatic-rich organic species, thus illustrating the potential climatic impacts of variations in SSA chemical composition. However, no enrichment in AR organics occurred during the second bloom despite higher peak Chl-a concentrations. It is proposed here that the AR organics are phytoplankton-produced, surface-active, labile organic

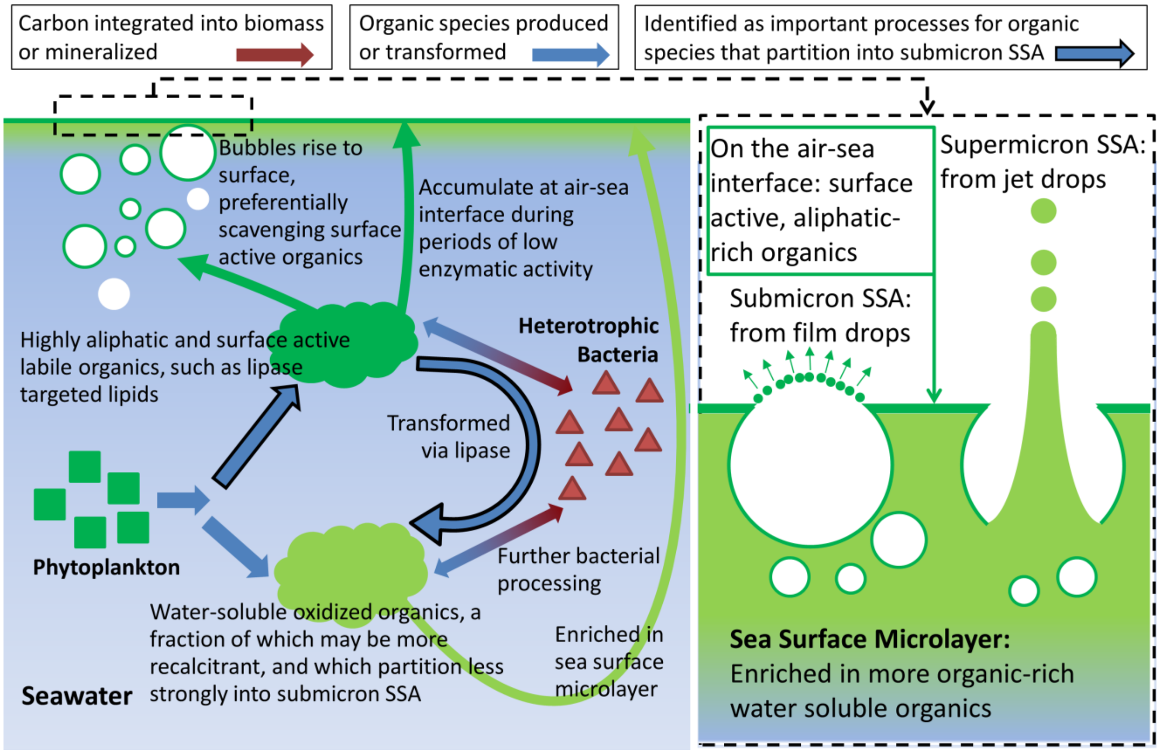

Figure 6.4 Schematic for the pathways of organic enrichment in SSA and their possible relationships with biological processes in seawater.

species, such as ester-containing lipids, that are subject to hydrolysis by enzymatic activity of bacterial lipase. This mechanism is supported by a kinetic box model that was constrained by measured Chl-a concentrations and lipase activity and that associates variations in calculated seawater labile AR organics with variations in the observed AR organics in submicron SSA for the two phytoplankton blooms in the wave channel. In contrast, the supermicron mode SSA organics were identified as being comparably oxygen rich and likely mixed with sea salt. These OR organics are likely more soluble than the AR organics and less surface active, and it is proposed that the OR organics are transferred to SSA primarily via jet drop production. The organic precursors contributing to the supermicron SSA are likely relatively more recalcitrant in nature and products of either phytoplankton primary production, bacteria degradation or secondary production making their temporal behavior difficult to model. Future mesocosm studies should focus on obtaining a more complete understanding of the factors contributing to the fate of these OR organic species in seawater.

A recent study [*Quinn et al.*, 2014] detected no difference in the amount of organic enrichment in SSA in areas of high and low biological activity, leading the authors to conclude that background levels of organic species overwhelm those produced by biological activity in seawater and make up the organic content of SSA. However, the current study demonstrates that biological processes can indeed impact the organic content of SSA. Firstly it is shown here that the organic species contributing to submicron and supermicron SSA are different chemical classes and show different temporal behavior over the course of the bloom. Secondly, the extent of organic enrichment in submicron SSA particles depends on a competition between phytoplankton production and bacterial degradation of surface-active organic species. This study therefore provides a mechanistic explanation as to why Chl-a has proven to be an inconsistent predictor of organic enrichment in SSA particles. Clearly, predictions of organic enrichment and the resulting impacts on cloud properties in marine environments require that additional measurements besides Chl-a levels are needed. Specifically, the history of the phytoplankton bloom, timing of the SSA measurements relative to the bloom lifecycle, heterotrophic bacteria concentrations, and the associated level of enzymatic activity also play determinant roles.

6.4 Acknowledgements

This material is based upon work supported by the National Science Foundation through the Centers of Chemical Innovation Program under Grant CHE1305427. Farooq Azam and Francesca Malfatti were partially supported by a Gordon and Betty Moore Foundation, MMI grant. Yanyan Zhou was partially supported by China Scholarship Council. We would like to thank Paul Harvey and the entire staff of the Scripps Institution of Oceanography Hydraulics Laboratory for facilitating use of the laboratory and technical support in maintaining the wave channel. We would also like to thank Susannah Burrows, Douglas Collins, Luisa Galgani, Renee Williams and Richard Cochran for helpful discussion.

Chapter 6, in full is a reprint of material as it appears in ACS Central Science, 2015. Reprinted with permission from Wang, X., Sultana, C. M., Trueblood, J., Hill, T.C.J., Malfatti, F., Lee, C., Laskina, O., Moore, K.A., Beall, C.M., McCluskey, C.S., Cornwell, G.C., Zhou, Y., Cox, J.L., Pendergraft, M.A., Santander, M.V., Bertram, T.H., Cappa, C.D., Azam, F., DeMott, P.J., Grassian, V.H., Prather, K. A. Microbial Control of Sea Spray Aerosol Composition: A Tale of Two Blooms. ACS Central Science. 2015, 1, 124–131. The dissertation author was a primary investigator and author of this paper.

6.5 Supporting Information

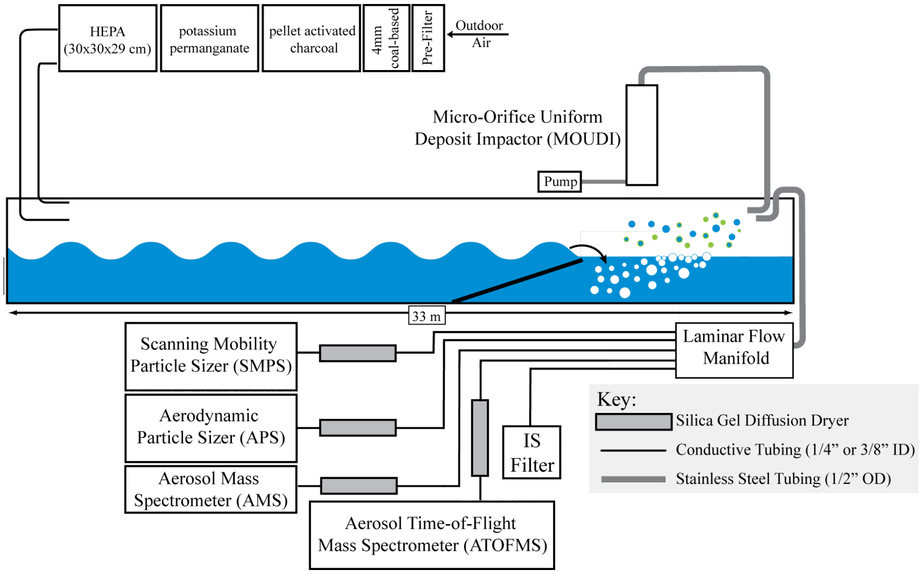

Figure 6.5 Schematic drawing of the IMPACTS experiment set-up.

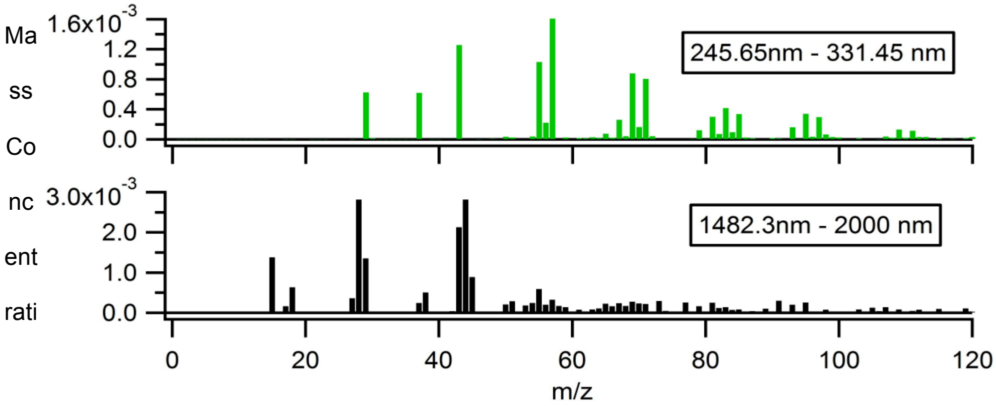

Figure 6.6 Size resolved organic AMS spectra of SSA from the wave-channel: The major peaks in the mass spectrum for the submicron mode are 43, 55, 57, 79, 81 and 83, which are typical hydrocarbon fragments [*Canagaratna et al.*, 2007]. Since the concentration of pure hydrocarbon in natural unpolluted seawater is low [*Ratte et al.*, 2011], the organics from this mode were likely from molecules with long hydrocarbon chains, such as lipids. Conversely, the mass spectrum for the supermicron mode shows a large peak at m/z 44 and m/z 28, indicators of oxidized organic matter. The hydrocarbon peaks were much smaller compared to the submicron mode.

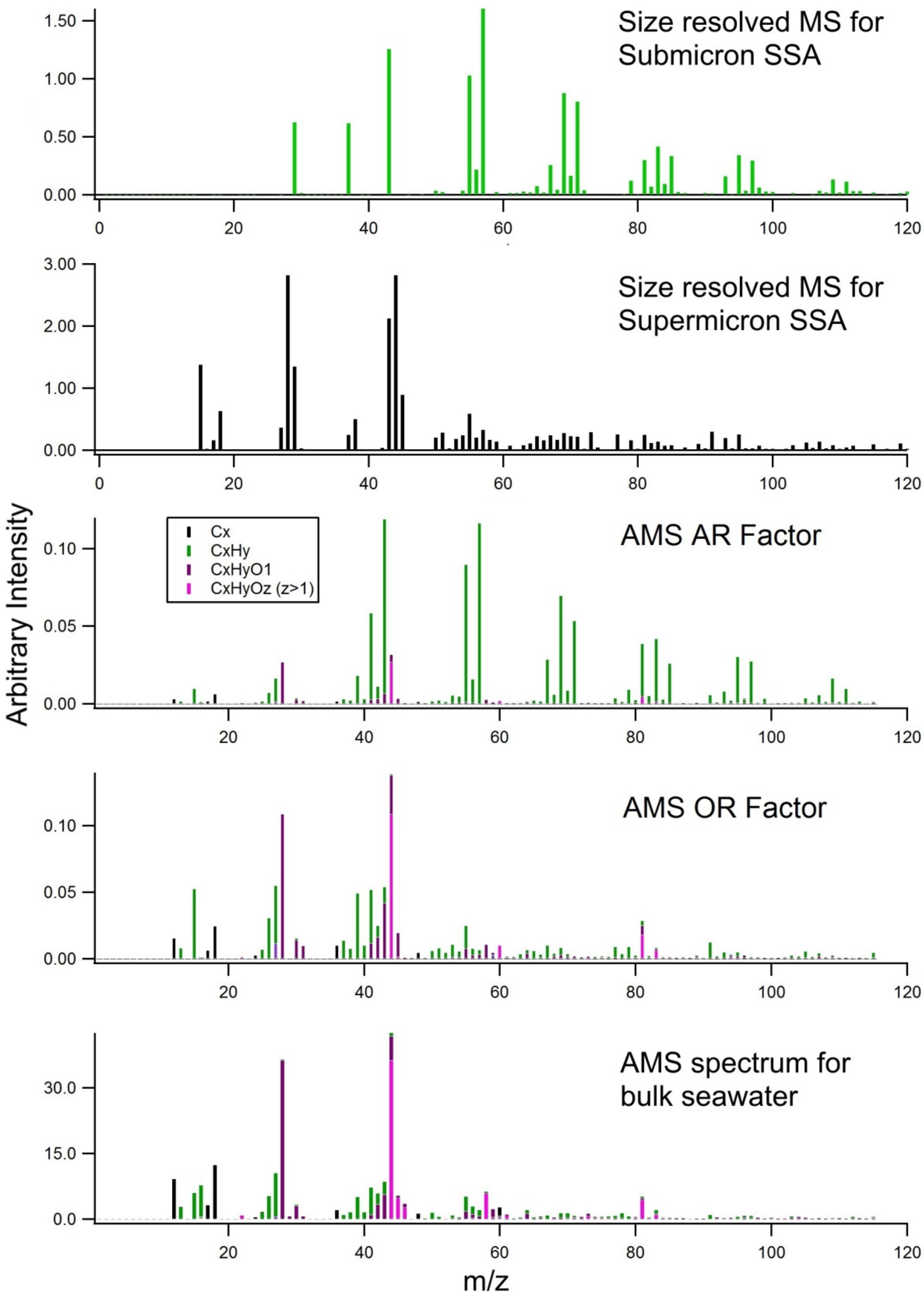

Figure 6.7 AMS organic spectrum of the bulk seawater (last panel): seawater from the wave channel was atomized to produce droplets, which were then dried and sampled by the AMS. All other AMS spectra used in this study (including Figure 6.2B and 6.5) are compared here.

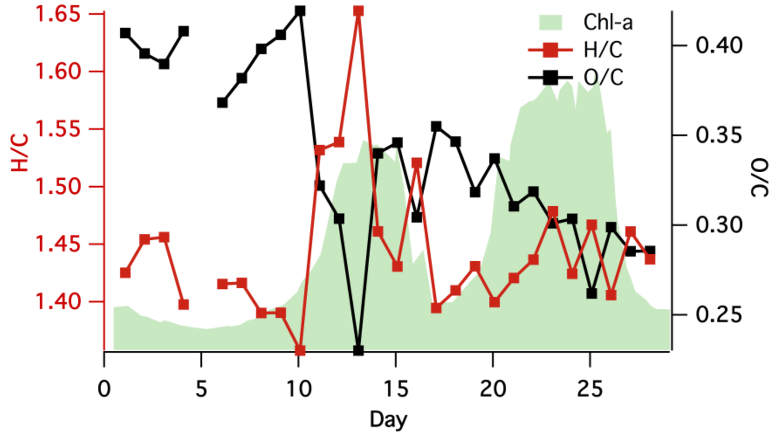

Figure 6.8 Elemental ratios of organics in SSA, calculated from the high resolution AMS mass spectra (C: carbon, H: hydrogen, and O: oxygen).

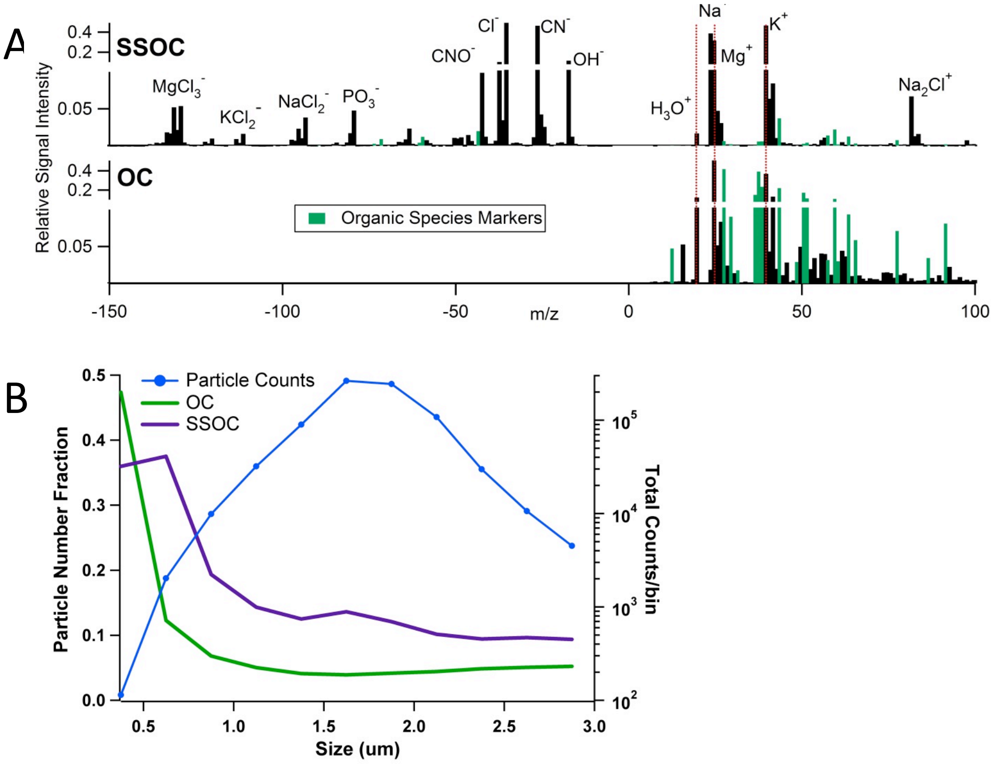

Figure 6.9 (A) ATOFMS spectra (weight matrices) and (B) size (D_{va}) resolved number fraction of the SSOC and OC SSA types from the wave channel experiment. The mass-to-charge spectra for particles designated as OC is dominated by signal from organic species with significant signal from magnesium and potassium as well. However, the relative ion intensity from sodium is <1% that observed in SSOC particles. In contrast particles classified as SSOC yield mass spectra with strong signal from NaCl ion markers, as well as enrichment in organic species and biological markers relative to particles defined as sea salt.

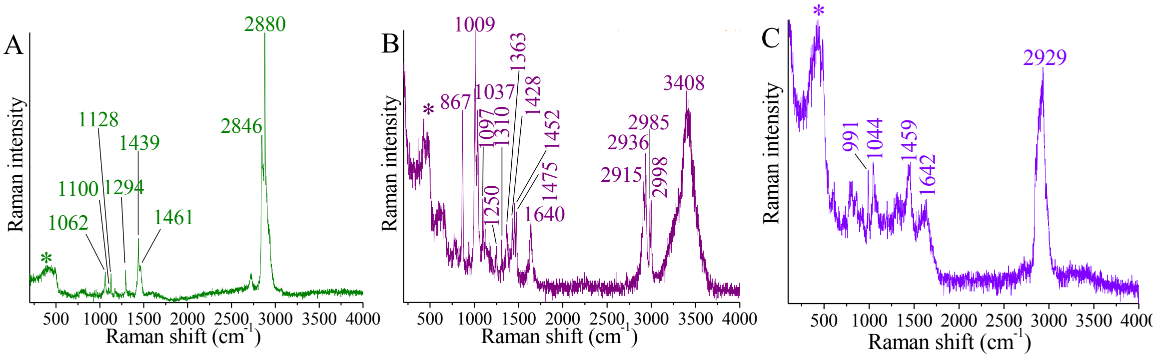

Raman shift, cm^{-1}	Assignment
1062, 1100, 1128	υ(C-C)
1294, 1439, 1461	δ(CH_2)
2846	$υ_s(CH_2)$
2880	$υ_{as}(CH_2)$

Raman shift, cm^{-1}	Assignment
867	δ(COH)
1009, 1037, 1097	υ(C–O) and υ(C–C)
1310, 1363, 1428, 1452, 1475	δ(CH_2) and δ (CH_2OH)
1250, 1640	amide III and I bands
2915, 2936, 2985, 2998	υ(C-H)
3408	υ(O-H)

Raman shift, cm^{-1}	Assignment
991, 1044	υ(C-C), υ(C-O) and υ(C-C-O)
1459	δ(CH_2)
1642	amide I band overlapping with υ(C=C)
2929	υ(C–H)

Low O/C

High O/C

Figure 6.10 Representative Raman spectra of SSA particles and assignments to the vibrational peaks are provided in each table. A peak marked with an asterisk in each spectrum is due to the quartz substrate (6.5.9).

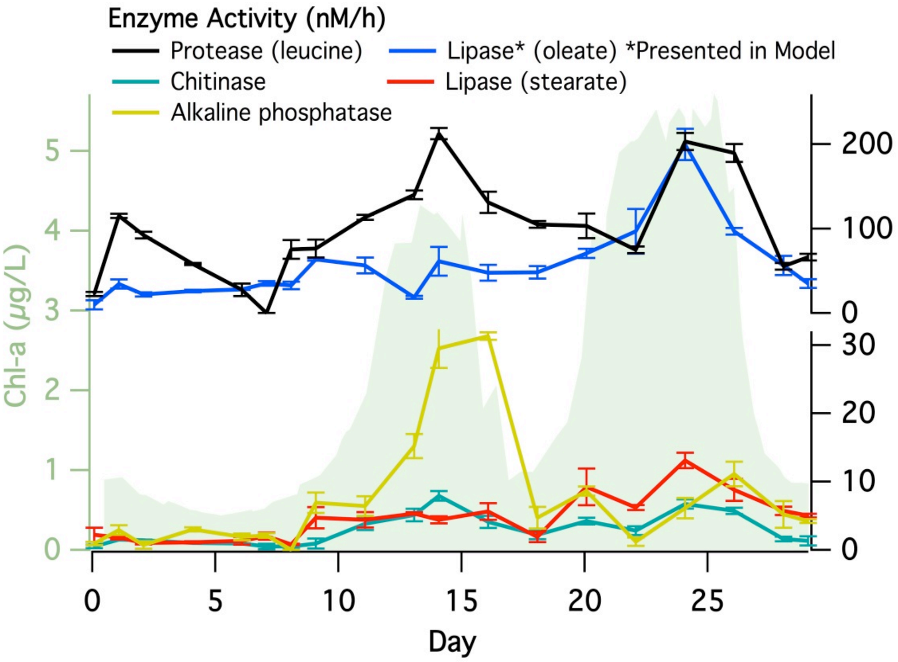

Figure 6.11 Measured ectoenzyme activity of the bulk seawater with target sites of the substrates given in parentheses where necessary (6.5.5).

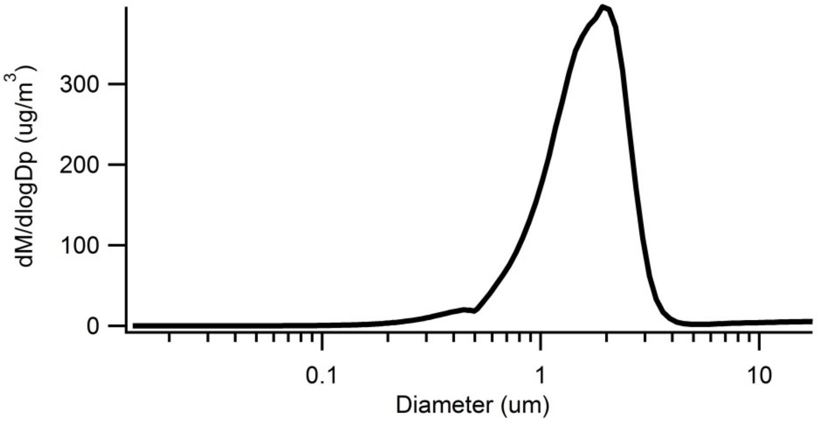

Figure 6.12 Average mass size distribution (calculated from the particle number size distribution, 6.5.6) of SSA produced from the wave channel during the entire experiment.

6.5.1 General Experiment Summary

Natural phytoplankton blooms were initiated in a wave channel in July 2014. Nutrients were added to natural seawater that was illuminated continuously to stimulate phytoplankton growth. SSA particles were generated through wave breaking and measured continuously throughout the course of the experiments. Chemical and biological bulk seawater measurements were also taken daily. Details of the experimental methods are given below.

6.5.2 Water Collection

All seawater was collected from Scripps Pier (La Jolla, CA; 32°51´56.8"N: 117° 15´38.48"W) and filtered through a 50 µm mesh to remove debris and zooplankton before addition to the wave channel. The pump inlet was at least 5 meters below the surface of the water.

Table 6.1 Summarizing collection times and volumes for the experiment.

Experiment	**Date**	**Time**	**Volume**	**t = 0 for plots**
Wave channel	7/3/14	7:00-16:00	13000 L	7/3/14 10:00:00

6.5.3 Nutrient Addition

All experiments used f/2 algae growth medium (Proline, Aquatic Eco-Systems, Apopka, FL) in addition to solutions of sodium metasilicate. Species concentrations have been detailed in previous work [*Lee et al.*, 2015]. An additional 9 μM sodium phosphate was added to the wave flume on 7/25/14 01:00 to maintain enriched levels of phosphate.

6.5.4 Wave Channel Set-up

Nutrients were added simultaneously with the freshly collected seawater to ensure adequate mixing. The wave channel was illuminated continuously for the entirety of the experiment with 5700 K full spectrum lights. Measurement of photosynthetically active radiation (PAR) within the wave channel was roughly 45 μE m^{-2} s^{-1}. To ensure low background particle counts and clean conditions, hydrocarbon, oxidant, and particle filtered air was delivered to the headspace of the channel with an average along-channel airflow velocity of approximately 5 cm/s. Breaking waves were used to generate SSA. The aerosol sampling manifold was approximately 4 feet from the location where the waves broke. Details of the air handling system and wave generation mechanism have been previously described [*Prather et al.*, 2013; *Collins et al.*, 2014]. Bulk seawater samples were collected daily between where the waves broke and the aerosol sampling manifold and at least 6 inches below the water surface.

6.5.5 Bulk Seawater Measurements

Bulk chlorophyll-a concentrations were measured fluorometrically using a Wetlabs ECO BBFL2 sensor and Turner AquaFluor handheld unit. The Wetlabs sensor was integrated into a flow-through system with a pump, housing, and additional sensors for continuous measurements; the AquaFluor was used with discrete samples. The Wetlabs sensor was calibrated at the factory against *T. weissflogii* cultures, and used as received. Measurements made with the AquaFluor were calibrated against simultaneous values recorded by the Wetlabs sensor, and then the two datasets were combined into a single timeseries.

Heterotrophic bacteria and viruses were enumerated via epifluorescence microscopy (Keyence BZ-X700) with SYBR Green-I nucleic acid gel stain (Life Technologies, S-7563).[4] Seawater samples were pipetted into sterile cryogenic vials and preserved with 0.05% electron microscopy grade glutaraldehyde. After incubation at 4 ºC for 15 min, samples were flash frozen in liquid nitrogen and then stored at -80 °C until analysis.

The fluorogenic substrate method was used to measure the enzymatic activities of lipase, protease, alkaline phosphatase and chitinase [*Hoppe*, 1983]. All the substrates (Sigma-Aldrich) were used to a final concentration at 20 µM [*Martinez et al.*, 1996]. Lipase activity was measured using 4-Methyl-umbelliferone oleate and 4-Methyl-umbelliferone stearate. Protease was measured using L-Leucine-7-amino-4-methyl-coumarin. The alkaline phosphatase activity was measured using 4-Methyl-umbelliferone-phosphate. The chitinase was measured using 4-methyl-umbelliferone-N-acetyl-β-D-glucosaminide. After the addition of the substrate, the samples were incubated at the *in situ* temperature in the dark for one hour. Assays were performed in microtiter plates (SpectraMax M3, Molecular Device) in triplicate. Fluorescence was measured immediately after adding substrates and again at the end of the incubation [*Danovaro et al.*, 2005], at 355/460 nm (excitation/emission). The fluorescence signal after blank correction was calibrated against 4-MUF and 7-AMC standards. The activities were computed as nmol substrate hydrolyzed L^{-1} h^{-1}.

6.5.6 Measurement of Aerosol Size Distributions

Aerosol size distributions were measured using a Scanning Mobility Particle Sizer (SMPS, TSI Inc. Model 3936) and Aerodynamic Particle Sizer (APS, TSI Inc. Model 3321). SMPS measurements were made of particles with dry (RH<40%) mobility diameters (D_m) in the range 0.013-0.750 μm; assuming sphericity implies the measured D_m is equivalent to physical diameter (D_p). APS measurements were adjusted from aerodynamic diameter (D_a) to D_p assuming spherical particles with an effective density of 1.8 g cm^{-3} [*Zelenyuk et al.*, 2007]. After density adjustment, APS measurements were of particles with dry (RH<40%) D_p in the range 0.460-17.930 μm. SMPS and APS (after adjustment) distributions were merged at a diameter of 0.540 μm, with SMPS sizes greater and APS sizes smaller than the cutoff being truncated. Size distributions were used to estimate $[PM_1]_{dry}$ by integrating the merged distribution up to 1 μm and calculating the expected mass, again assuming particle sphericity and an effective density of 1.8 g cm^{-3}.

6.5.7 Measurement of SSA Composition via an ATOFMS

The chemical composition of individual SSA particle (D_{va} = 0.25-3 μm, vacuum aerodynamic diameter) was measured in real time via ATOFMS which yielded dual-polarity mass spectra. As particle phase water has been shown to reduce the negative ion signal [*Neubauer et al.*, 1997], the sampled SSA passed through a silica gel diffusion dryer before the instrument inlet. A brief description of the ATOFMS follows here; more detailed discussion of the ATOTMS has been provided previously [*Noble and Prather*, 1996; *Gard et al.*, 1997]. Aerosol particles enter the instrument through a converging nozzle inlet and are then accelerated to their size-dependent terminal velocity in a differentially pumped vacuum chamber. The time for particles to transit two continuous wave laser beams (532 nm) that are separated by a fixed distance is measured. A calibration with polystyrene latex spheres of known diameter is used to convert the velocity to vacuum aerodynamic diameter. The velocity of the particles is used to trigger a pulsed, Q-switched, UV desorption-ionization laser. The particle's chemical components are desorbed and ionized in the ion source region by the Nd:YAG laser (266 nm, 8 ns, 1.3 mJ) pulse. The positive and negative ions produced are detected by a dual-polarity reflectron time-of-flight mass spectrometer.

Single particle spectra and size data were loaded into Matlab (The MathWorks, Inc.) and analyzed via the software toolkit YAADA (http://www.yaada.org/). Particles were divided into clusters based on their spectra via an adaptive neural network (ART-2a) and the resultant clusters were recombined into types based on their characteristic mass spectra and size distributions [*Song and Hopke*, 1999].

6.5.8 Measurement of SSA Composition via AMS

SSA produced from the wave channel were first dried by a diffusional dryer, and then introduced into an AMS, which is equipped with a high resolution time-of-flight mass spectrometer. Its detailed description can be found in *DeCarlo et al.* [2006]. A brief introduction to the AMS is given here. Aerosol particles (D_{va} = 0.04 ~ 1 μm) can efficiently enter the AMS through an aerodynamic lens (AFL), which focuses particles into a narrow beam. Noticeably, the AMS also samples some supermicron particles although with a relatively low collection efficiency [*Jayne et al.*, 2000; *Liu et al.*, 2007], especially when the total aerosol mass is mainly located in the supermicron size range, as is the case for SSA in this study (Figure 6.12). Next, particles are resolved based on their measured velocities, which are used to calculate their vacuum aerodynamic particle diameters. Then, particles are collected on a hot vaporizer (set to 600 °C) where organics and other non-refractory matter are vaporized. Electron impact ionization is used to ionize the vapor and produce ions, which are analyized by a mass spectrometer. The organic signals at m/z 28 and 44 were adjusted based on the CO_2 concentration in air, which was monitored by a CO_2 gas analyzer (Model LI-820, LI-COR, Inc., Nebraska, USA). The exact ion formula of peaks (e.g. $C_xH_yO_z$) were calculated based on their accurate mass. Overall elemental ratios for all organic signals were also obtained [*Aiken et al.*, 2007].

The AMS measured dry vacuum aerodyanmic particle diameter. Assuming the SSA were spherical, their density (ρ) was 1.8 g/cm^3, and their growth factor (GF) at a relative humidity (RH) of 80% was 2 [*Hämeri et al.*, 2001], the aerodyanmic diameter at RH 80% was calculated based on the relationship between vacuum aerodyanmic particle diameter (D_{va}) and aerodyanmic diameter (D_a) [*DeCarlo et al.*, 2006]:

$$D_{a@RH\ 80\%} = GF_{@RH\ 80\%} \times D_{a,dry} = GF_{@RH\ 80\%} \times D_{va,dry}/SQRT(\rho)$$

The AMS data were loaded into Igor Pro (Wavemetrics) and analyized using SQUIRREL and PIKA, which are the standard AMS data analysis toolkits. Postive matrix factorization (PMF) technique [*Paatero and Tapper*, 1994; *Ulbrich et al.*, 2009] was applied to the high resolution organic signals from the V-mode. The data for PMF was pre-treated, including removing the organic peaks with a signal-to-noise ratio (SNR) < 0.2, down-weighting the peaks (0.2 < SNR < 2), and further down-weighting the peaks with duplicated information related to CO_2^+. The total AMS organic signals were seperated into two PMF factors: the aliphatic-rich (AR) factor and oxygen-rich (OR) factor.

In the paper, f_{OM} is defined as the relative organic mass fraction of SSA:

$$f_{OM} = \left[\frac{[OM]}{[PM_1]_{dry}}\right] / \left[\frac{[OM]}{[PM_1]_{dry}}\right]_{max}$$

f_{AR} and f_{OR} are defined as the relative aliphatic-rich factor or oxygen-rich factor mass concentrations, respectively:

$$f_{AR} = \left[\frac{[AR]}{[PM_1]_{dry}}\right] / \left[\frac{[OM]}{[PM_1]_{dry}}\right]_{max}$$

$$f_{OR} = \left[\frac{[OR]}{[PM_1]_{dry}}\right] / \left[\frac{[OM]}{[PM_1]_{dry}}\right]_{max}$$

where [OM] is the total AMS organic signal. [AR] and [OR] are the aliphatic-rich (AR) factor and oxygen-rich (OR) factor, respectively. $[PM_1]_{dry}$ is the dry sub-micrometer particulate mass concentration estimated from the size distributions. “max” means maximum value.

6.5.9 Measurement of SSA Composition via Micro-Raman Spectroscopy

Individual SSA particles were collected on quartz discs (Ted Pella Inc., part no. 16001-1) placed on different stages of a Micro-Orifice Uniform Deposition Impactor (MOUDI, MSP Corp. Model 110) operating at a flow rate of 30 LPM, at RH ~72%. Particles collected on the the fourth stage, with aerodynamic diameters between 1.8 and 3.2 μm, and the sixth stage, with aerodynamic diameters between 0.56 and 1 μm, were analyzed. A LabRam HR Evolution Raman spectrometer (Horiba) with a 530 nm laser (30 mW) was used with a laser exposure time of 5-10 s. Two successive exposures were averaged to obtain each individual particle spectrum.

The sample for Raman data shown in this paper was taken 1:12 pm-2:06 pm (Local Time) on July 17, 2014 (day 14), while the AMS was sampling from 9-11am, 1-4 pm and 6-9 pm (Local Time) on this day.

Particles that contained Raman peaks associated with organic compounds were further analyzed and compared to representative standards. For example, the spectrum shown in Figure S6A has prominent peaks in the C-H stretching region at 2846 and 2880 cm^{-1} that correspond to symmetric and asymmetric stretches of the CH_2 group respectively. Additional peaks of lower intensity are associated with C-C stretching (1062 cm^{-1}, 1129 cm^{-1}), CH_2 twisting (1295 cm^{-1}) and bending (1439 cm^{-1} and 1461 cm^{-1}) modes [*Spiker and Levin*, 1975; *Hill and Levin*, 1979; *Pemberton and Chamberlain*, 2000; *De Gelder et al.*, 2007; *Gomes et al.*, 2013]. These spectra have been compared to spectra of saturated fatty acids with chain lengths between 12 and 18. Spectra of all standard acids are very similar with prominent peaks. Based on this comparison, the Raman spectra shown in Figure S6A are assigned to long chain fatty acids with a chain length between 12 and 18. From this analysis, the oxygen to carbon ratio (O/C) is between 0.11 and 0.17. These molecular species are referred to as "low O/C" species.

The Raman spectrum shown in Figure S6B features four peaks in the CH stretching region (2915 cm^{-1}, 2936 cm^{-1}, 2985 cm^{-1}, 2998 cm^{-1}), a large 3408 cm^{-1} peak due to OH stretch, stretching vibrations of C-O and C-C bonds characteristic of the carbohydrate nature (1009 cm^{-1}, 1037 cm^{-1}, 1097 cm^{-1}), bending deformations of COH group (867 cm^{-1}) and CH_2 and CH_2OH groups (1310 cm^{-1}, 1363 cm^{-1}, 1428 cm^{-1}, 1452 cm^{-1}, 1475 cm^{-1}) as well as amide I and III bands at 1250 cm^{-1} and 1640 cm^{-1} respectively [*She and Tu*, 1974; *Lin and Koenig*, 1976; *Amharref et al.*, 2007; *De Gelder et al.*, 2007; *Wu et al.*, 2011]. This spectrum can be compared to spectra associated with carbohydrates typically found in the marine environment [*Compiano et al.*, 1993; *Hawkins and Russell*, 2010; *Russell et al.*, 2010; *Gao et al.*, 2012; *Van Pinxteren et al.*, 2012; *Cunliffe et al.*, 2013]. In particular, carbohydrate model compounds analyzed with Raman spectroscopy have similar characteristic peaks in the C-H stretching region although some of the relative intensities of these peak can differ. Based on the peak assignments and comparison to standard spectra, this SSA particle is associated with carbohydrates. Some common carbohydrates in marine environment include ribose (O/C=1), heptose (O/C=1), glucose (O/C=1), glucosamine (O/C=0.83), fucose (O/C=0.83), mannose (O/C=1), galactose (O/C=1), and sialic acid (O/C=0.82) [*Compiano et al.*, 1993; *Hawkins and Russell*, 2010; *Russell et al.*, 2010; *Gao et al.*, 2012; *Van Pinxteren et al.*, 2012; *Cunliffe et al.*, 2013]. These carbohydrates all have oxygen to carbon ratios between 0.82 and 1 and therefore are referred to as "high O/C" species.

A third particle type gives a Raman spectrum that is shown in Figure S6C. The Raman peaks in this spectrum are identified as a having skeletal C-C, C-O and stretching C-C-O bands at 991 cm^{-1} and 1044 cm^{-1}, CH_2 bending modes at 1459 cm^{-1} that is common for proteins and lipids, a peak at 1642 cm^{-1} that can be assigned as either an amide I band or C=C stretching vibration of unsaturated fatty acid chains, and a broad peak at 2929 cm^{-1} identified as the C–H stretching modes of CH, CH_2 and CH_3 groups of fatty acid chains [*Kamnev et al.*, 2001; *Laucks et al.*, 2005]. This spectrum compares well with the spectrum of commercially available lipopolysaccharide (LPS) derived from *E. coli*. Indeed spectra of E. coli LPS features similar peaks and therefore, based on the peak assignments and comparison with standards, the type of spectra shown in Figure S6C has been associated with LPS. LPS consist of approximately 70% of carbohydrates and 30% of fatty acids [*Weckesser et al.*, 1972; *Carlson et al.*, 1987]. Assuming the O/C ratio of carbohydrates is 0.85 and O/C ratio of fatty acids is 0.15 (*vide supra*) it can be inferred that the O/C ratio of LPS is approximately 0.6. Using a cutoff of 0.5, to identify “low” and “high” oxygen to carbon ratio containing molecules, LPS here is referred to as a “high O/C” species.

In addition to these three most common types of particles identified by the Raman spectra shown in Figure S6, other types of particles were either highly fluorescent under the laser beam during data collection or had uncommon organic signatures that did not allow them to be characterized or grouped further. These particles collectively accounted for 6% and 19% of total particles measured in the submicron and supermicron size range respectively.

6.5.10 Measurement of INP with CSU-IS

Samples were obtained by filtering between 6-7 L min^{-1} of flume headspace air for 3-7 h through a 47 mm diameter in-line aluminum filter holder (Pall) fitted with a 0.05 μm diameter pore Nuclepore polycarbonate membrane (Whatman). A 3 μm Nuclepore membrane was placed below the sampling membrane as an additional cleanliness measure. Filter holders were cleaned between events, after disassembly, by soaking in 10% H_2O_2 for 60 min followed by three rinses in deionized water (18 MΩ and 0.2 μm diameter-pore filtered) and removal of excess water with a gas duster before drying. Filters were cleaned and any contaminating DNA removed by soaking in 10% H_2O_2 for 10 min in a sterile, 150 mm petri dish (CELLTREAT) followed by three rinses in deionized water, the last of which had been filtered through a 0.02 μm pore diameter filter (Anotop 25 mm syringe filter, Whatman). Filters were then dried on foil. Cleaning and drying were performed in a laminar flow cabinet (<0.01 particles mL^{-1}).

After particle collection, filters were transferred using clean, acetyl plastic forceps (Fine Science Tools) to sterile, 60 mm petri dishes (CELLTREAT) and stored at -20°C until processed. For the release of particles, filters were placed in sterile 50 mL Falcon polypropylene tubes (Corning Life Sciences), 5 mL of deionized water (18 MΩ and 0.2 μm diameter-pore filtered with ~2 INP mL^{-1} at -22°C) added and particles re-suspended by tumbling end-over-end on a Roto-Torque (Cole-Palmer) at 60 cycles min^{-1} for 20 min. To assess the heat labile fraction, 1.8 mL of the suspension solution was transferred to a 50 mL Falcon centrifuge tube and immersed in water heated to 95°C for 20 min (after allowing time for equilibration). Immersion freezing temperature spectra of INP were obtained using 24-32 aliquots of 50 or 60 μL dispensed into sterile, 96-well polymerase chain reaction (PCR) trays (LS-9796, Life Science Products Inc.) in a laminar flow cabinet. Trays were capped with polystyrene lids (Nunc microwell plates, Thermo Fisher Scientific Inc.) and then transferred to the CSU-IS. Based on aliquot size and number, the detection limit for INP was calculated to be 0.001 L^{-1} and 0.002 L^{-1} air in untreated and heated sample experiments, respectively.

The CSU-IS is constructed using two 96-well aluminum incubation blocks (VWR), designed for cooling or heating PCR plates, placed end-to-end and encased on their sides and base by cold plates (Lytron). A ULT-80 low temperature bath (Thermo Neslab) circulating SYLTHERM XLT heat transfer fluid (Dow Corning Corporation) is used for cooling the plates via copper coils. Loaded PCR plates were placed in the blocks, the device covered with a plexiglass window and the headspace purged with 1.5 L min^{-1} of filtered (HEPA-CAP, Whatman) nitrogen. Temperature was then lowered at 0.33°C min^{-1}, and measured using a thermistor verification probe (Bio-Rad, Hercules, CA, VPT-0300) inserted into a side well. Temperature uncertainty was ±0.2°C, mostly from temperature variation across the blocks due to gradients in cooling. Frozen wells were counted at 0.5 or 1°C degree intervals, and cumulative numbers of INP mL^{-1} of suspension estimated using the formula $\ln(f)/V$, where f is the proportion of droplets not frozen and V is the volume of each aliquot [*Vali*, 1971]. This was converted to INP L^{-1} air using the volume of air filtered. Filter blanks were used to obtain a mean background INP spectrum.

Binomial sampling confidence intervals (95%) were derived using the following formula [*Agresti and Coull*, 1998]:

$$\mathrm{CI}_{95\%} = \left(\hat{p} + \frac{1.96^2}{2n} \pm 1.96\sqrt{\left[\hat{p}(1-\hat{p}) + {1.96^2}/{4n}\right]/n}\right) / \left(1 + {1.96^2}/{n}\right),$$

where $\hat{p}$ is the proportion of droplets frozen and n is the total number of droplets.

6.5.11 Calculating Labile Organic Species in Seawater during the Mesocosm Experiment

It is assumed that aliphatic-rich labile organic species (ARL) are only produced by phytoplankton and transformed by lipase enzyme activity. Below is a list of assumptions:

(1) The production rate of ARL is linearly dependent on the concentration of phytoplankton. Thus the production rate can be expressed in the following form: $d[\mathrm{ARL}]/dt = k^{+}[\mathrm{Chl\_a}]$, where k^{+} is a first-order reaction constant.

(2) The transformation of ARL follows Michaelis–Menten kinetics: $d[\mathrm{ARL}]/dt = \mathrm{R\_max} \times [\mathrm{ARL}] / (C_{1/2} + [\mathrm{ARL}])$, where R_max is the maximum transformation rate of ARL. $C_{1/2}$ is the ARL concentration at half of its maximum transformation rate.

(3) The lipase activity was measured (shown in Figure 6.3) based on the decomposition rate of MUF-oleate at a saturating concentration (Method S12) in nM/h. However, phytoplankton produced ARL must include non-oleate compound lipids. Thus, in this model, only the trend of the lipase activity is used with units of a.u./day (a.u. means arbitrary unit).

Therefore, the governing equation of ARL concentration takes the following form:

$$\frac{d[\mathrm{ARL}]}{dt} = k^{+}[Chl\_a] - R_{max} \cdot [\mathrm{ARL}]/(C_{1/2} + [\mathrm{ARL}])$$

There are 3 rate constants in the above equation: k^{+}, R_max and $C_{1/2}$. k+ and $C_{1/2}$ are unknown. The concentration of Chl-a and R_max are known and input into the model from measurements during the mesocosm.

Chapter 7. Biologically-mediated influences on the climate impacts of SSA

7.1 Abstract

A series of phytoplankton bloom experiments were conducted during the Investigation in Marine Particle Chemistry and Transfer Science (IMPACTS) campaign during July and August of 2014. To better understand the influence of seawater chemistry on the climate impacts of sea spray aerosol (SSA), a wide array of SSA particle chemical and physical properties were measured. During two studies conducted in a marine aerosol reference tank (MART), the average chemical composition of the SSA population, measured utilizing an aerosol mass spectrometer, decreased after the peak in the phytoplankton bloom. Paradigms for interpreting the bulk of SSA aerosol time-of-flight mass spectrometer (ATOFMS) data sets were utilized helped inform how these average changes manifested at the single particle level. ATOFMS results helped illustrate that that increases in the organic content of particles across the SSA population likely resulted the measured decreased particle hygroscopicity. During the mesocosm wave channel experiment, ATOFMS analyses provided chemical identification of rare particles, fulfilling a gap between the seawater chemistry and ice nucleation measurements, which would have otherwise been lacking. Increases in the number fraction of the *BioSS* mass spectral type, first described in Chapter 5, corresponded well in time with high concentrations of ice nucleating particles that are active at warmer temperatures. However, *BioSS* made up less than 1.5% of all SSA mass spectra generated during the wave channel experiment, suggesting that the ice nucleating capacity of SSA may be influenced by rare-microbe containing particles.

7.2 Introduction

Atmospheric aerosols impact global climate directly, via scattering and adsorbing incoming solar radiation, and indirectly, by influencing cloud properties by acting as cloud condensation (CCN) and ice nucleating particles (INPs) [*Haywood and Boucher*, 2000; *Lohmann and Feichter*, 2005; *Pöschl*, 2005]. A large source of the uncertainty on the total radiative forcing of aerosols [IPCC, 2013], is a lack of understanding regarding the impact of large natural sources of aerosols , such as sea spray aerosols [*Raes et al.*, 2000; *Carslaw et al.*, 2013]. Sea spray aerosols are generated from bubble bursting at the ocean surface and are one of the largest sources of natural aerosol particles into the atmosphere [*Textor et al.*, 2006; *O'Dowd et al.*, 2007]. The direct light scattering ability of SSA is dependent on the particle size [*Pilinis et al.*, 1995; *Kleefeld et al.*, 2002; *Forestieri et al.*, 2016], which is modified by the particle's hygroscopicity or ability to take up or lose water. Except for very small particles (< 100 nm), particle hygroscopicity at subsaturated ambient relative humidities (RH) is almost entirely dependent upon particle chemical composition, with increases in the organic to salt ratio within SSA associated with decreases in the particle water uptake ability [*Petters and Kreidenweis*, 2007; *Fuentes et al.*, 2011; *Vaishya et al.*, 2013; *Zhang et al.*, 2014]. SSA can also potentially alter cloud properties in remote marine regions by acting as ice nucleating particles [*Burrows et al.*, 2013; *Wilson et al.*, 2015]. Ice nucleating particles (INPs) are required for ice nucleation of supercooled liquid droplets before the homogeneous freezing point limit near -38°C, and therefore have a profound influence on precipitation potential, lifetime and optical properties of clouds [*Pruppacher and Klett*, 1997]. While most SSA have the capacity to directly scatter solar radiation, with the degree of interaction modified by the particle size (and therefore particle hygroscopicity), only very few marine aerosol particles have the capacity to act as efficient ice nuclei [*DeMott et al.*, 2015; *Wilson et al.*, 2015]. Less than 1 in one 100,000 SSA particles nucleate ice at warmer than -25°C [*DeMott et al.*, 2015]. To understand the climate impacts of SSA, it is important to be able to both describe the general chemical composition, which influences direct light scattering, and identify rare ice nucleating particle types. In addition, both particle hygroscopicity [*Fuentes et al.*, 2011; *Ovadnevaite et al.*, 2011; *Vaishya et al.*, 2013] and ice nucleation (IN) ability [*DeMott et al.*, 2015; *Wilson et al.*, 2015; *McCluskey et al.*, 2017a] have been shown to be influenced by biologically mediated changes in seawater chemistry.

To better understand the link between changing seawater chemistry and the climate impact of SSA, the chemical and physical properties of SSA were simultaneously characterized during the Investigation in Marine Particle Chemistry and Transfer Science (IMPACTS) campaign conducted in July and August of 2014. During IMPACTS, a series of phytoplankton blooms were generated in natural seawater and SSA was generated by intermittent wave breaking mechanisms. Variation in SSA particle hygroscopicity at subsaturated RH, determined from UC-Davis cavity ring-down spectrometer (CRD) measurements, and INP concentrations, determined by offline and online measurements made by researchers from Colorado State University (CSU), were informed by size resolved measurements of single particle chemical composition, determined utilizing an aerosol time-of-flight mass spectrometer (ATOFMS).

7.3 Methods

7.3.1 General Experiment Description

A series of phytoplankton blooms were studied during 2014, utilizing natural seawater collected off the Pacific Coast from the Scripps Pier. Growth of naturally occurring phytoplankton was encouraged by the addition of nutrients and illumination, following the general procedures outlined by *Lee et al.* [2015]. SSA particles were generated via intermittent plunging or breaking wave mechanism [*Stokes et al.*, 2013] and then dried with diffusional driers (relative humidity (RH) <20%) before sampling by the online instrumentation. Specifics of the distinct hygroscopicity and IN studies are provided below.

7.3.1.1 Hygroscopicity Experiment

During the Investigation in Marine Particle Chemistry and Transfer Science (IMPACTS) campaign in July 2014 two separate phytoplankton bloom microcosm experiments were completed utilizing marine aerosol reference tanks (MARTs). Comprehensive details of the experimental conditions and sampling procedures are provided in *Forestieri et al.* [2016]. During the growth phase of the phytoplankton bloom, one MART was incubated indoors ("indoor MART") and illuminated continuously with 5700K full spectrum lights and the second MART was located outdoors ("outdoor MART") and therefore experienced natural daily variations in sunlight. SSA particles were generated via the MART's intermittent plunging wave mechanism [*Stokes et al.*, 2013].

7.3.1.2 IN Experiment

A phytoplankton bloom mesocosm experiment was conducted as part of the IMPACTS campaign, during July and August of 2014, utilizing a wave channel filled with 3,400 gallons of natural seawater, with more experimental details provided by *McCluskey et al.* [2016] and *Wang et al.* [2015]. The wave channel was continuously illuminated with 5700 K full spectrum lights. SSA particles were generated by intermittent wave breaking [*Stokes et al.*, 2013; *Wang et al.*, 2015] in the wave channel.

7.3.2 ATOFMS

Size resolved dual-polarity mass spectra of the SSA particles were generated utilizing a nozzle-ATOFMS [*Gard et al.*, 1997], operating at a laser pulse energy of 1-1.3 mJ. Silica gel diffusional driers were utilized to dry the SSA particles before sampling, reducing the relative humidity of the sampled air to less than 15%. Mass spectral peak assignments correspond to the most likely ion produced at a specific mass-to-charge (*m*/*z*) value.

7.3.2.1 Hygroscopicity Experiment

Single particle mass spectra were initially grouped utilizing the artificial neural network clustering algorithm (ART-2a). These groups were then further refined and combined utilizing expert knowledge and referencing previous classifications [*Gaston et al.*, 2011; *Prather et al.*, 2013; *Guasco et al.*, 2014] into broad SSA mass spectral categories. The size distribution (vacuum aerodynamic diameter (d_{va})) of particles generating mass spectra, which is strongly influenced by the d_{va} dependent transmission efficiency of the nozzle ATOFMS, is shown in Figure 7.1. Greater than 85% percent of all detected particles were larger than 1μm (d_{va}).

7.3.2.2 IN Experiment

BioSS were classified by user-guided visual analysis of the mass spectra utilizing guiFATES a graphical user interface within FATES [*Sultana et al.*, 2017b]. BioSS mass spectral signatures have a narrow range closely matching those of previously described likely microbe-containing SSA particles [*Sultana et al.*, 2017a]. The Bio-Ag mass spectral type was generated based only on the presence of silver ion markers. It has been suggested that, in the wave channel, bacterial cells bioaccumulate silver nanoparticles, which are present as contamination [*Guasco et al.*, 2014]. Wave channel mass spectra were initially filtered selecting for ion signatures with

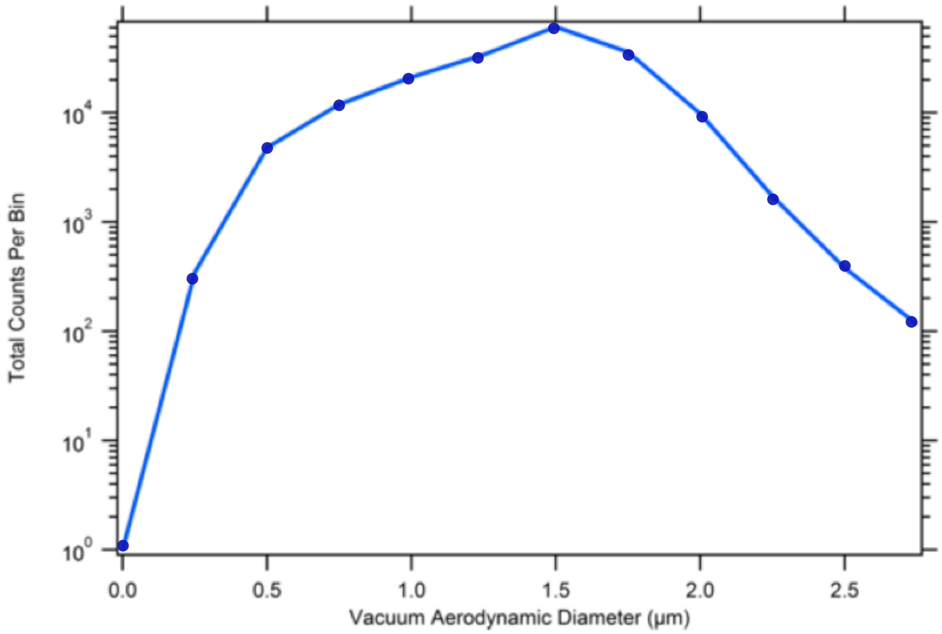

Figure 7.1 Size resolved ATOFMS particle counts during the hygroscopicity MART experiments.

greater than 1% of the total positive ion intensity generated from a sum of +107, 109, 214, 216, and 218, ion markers for silver ($^{107,109}Ag^+$, $^{214,216,218}Ag_2^+$). However, it is possible that isobaric interference from other ion species or simply noise in low ion intensity mass spectra could result in selecting for mass spectra above the filter threshold. The initially filtered (sum of +107, 109, 214, 216, 218 >1%) mass spectra were imported into guiFATES to visually discriminate mass spectra without the distinct silver isotopic ratios at the ion peaks noted above. Total positive and negative ion intensities are the summation of all peak areas from 0 to 300 and 0 to -300 *m/z*, respectively. No mass spectra with silver ion markers were included in the BioSS classification.

7.3.3 Additional Measurements: Hygroscopicity Experiment

7.3.3.1 Aerosol Mass Spectrometer

An Aerodyne aerosol mass spectrometer (AMS) was utilized to calculate the non-refractory (NR) organic matter volume fractions (ε_{org}) of SSA. NR species are defined as those that volatilize within a few seconds at ~600 ◦C under vacuum conditions. The AMS aerodynamic lens imposes a 50% cut at ~40 nm and ~1 μm with quantitative sampling nominally between 90 and 700 nm (d_{va}). Xiaofei Wang was responsible for the operation of the AMS and all following data analyses, which are described in *Forestieri et al.* [2016].

7.3.3.2 Growth Factor Analysis

Simultaneous light scattering measurements made at a wavelength of 532 nm by the UC-Davis cavity ring-down spectrometer (CRD) of dry (RH<20%) and wet (RH~85%) SSA particles were utilized to characterize the hygroscopicity of the SSA particles. Specifics of the instrument operation and all ensuing calculations, performed by Sara Forestieri, are provided in *Forestieri et al.* [2016] and briefly summarized here. The optically weight growth factor (GF) for the sampled particles was calculated, where at a given particle size the GF is defined as

$$\mathrm{GF(RH)} = \frac{d_p(\mathrm{RH_{high}})}{d_p(\mathrm{RH_{low}})} \qquad [2]$$

where d_p is the geometric particle diameter. Variations in the GF are driven by variations in particle composition. The light scattering measurements made here are most sensitive to particles from 400 nm to 800 nm (d_p). Particles less than 200 nm and greater than 1 μm (d_p) contributed roughly 0% and 10%, respectively, to total light scattering. It is important to note that d_{va} = 1 μm corresponds to a d_p of roughly 560 nm. Note only 15% of all particles detected by the ATOFMS were larger than d_{va} = 1.8 μm (d_p = 1 μm).

7.3.4 Additional Measurements: Hygroscopicity Experiment

7.3.4.1 INP concentrations

The concentration of immersion freezing ice nucleating particles (INPs) was monitored online by the Colorado State University (CSU) continuous flow diffusion chamber (CFDC) and offline with the CSU ice spectrometer (IS). Extensive details of instrument operation, sample collection, and data analysis are given in [*McCluskey et al.*, 2017a] so only a short summary follows here. The CFDC draws dried particles through an impactor, which removes larger particles (50% aerodynamic cutoff d_{va} = 1.5 μm), into an ice thermal diffusion chamber. Chamber conditions are such that particles are exposed to supersaturation with respect to water, driving cloud droplet activation and growth. The ice-coated chamber is temperature controlled (-16°C to -30°C), allowing for droplets containing INPs to nucleate into ice crystals via immersion and condensation freezing. In the final stage of the chamber liquid droplets are evaporated, resulting in a distribution that contains particles without condensed water and ice crystals. Ice crystals are counted based on their size with an optical particle counter at the base of the chamber. Ice crystal concentrations are also measured from filtered air in 10 minute increments to account for background crystals that form in the chamber.

For the offline detection of ice nucleating particles, total suspended SSA particles are first collected onto a filter (pore size 0.05 μm). Due to depositional losses in the collection line only particles less than 2.5 μm were considered to be transferred efficiently to the IS filters. Filters were then suspended in deionized water and the collected SSA matter was removed via shaking into solution for analysis by the IS. Aliquots of the liquid sample are transferred into wells of PCR trays that are then placed into the IS aluminum blocks, which are slowly cooled (0°C to -25°C). The number of wells that freeze at each temperature is recorded and number concentrations of INPs are calculated following methods of *Vali* [1971].

The CFDC was operated by Paul DeMott and Christina McCluskey and subsequent data analyses was performed by Christina McCluskey. Tom Hill was responsible for all offline IS analysis.

7.3.4.2 INP characterization

On Day 26 of the IMPACTS study, ice crystals were collected via impaction at the base of the CFDC and the remaining residuals were later analyzed by micro-Raman spectromicroscopy to characterize the organic components of the ice crystal residuals (ICRs). The composition was determined for residuals with diameters of approximately 1 μm by comparing the Raman spectrum of each ICR particle with a library of spectra. Details of ICR collection and analysis can be found in [*McCluskey et al.*, 2017b]. John Trueblood was responsible for collecting all Raman spectra and ensuing analyses.

7.4 Results and Discussion

7.4.1 Hygroscopicity Studies

7.4.1.1 Description of ATOFMS spectral types

Leveraging algorithmic clustering, ATOFMS mass spectra were categorized into five broad mass spectral types based upon ion signatures: sea salt (SS), sea salt with organic carbon (SSOC), organic carbon (Org), magnesium (Mg), and iron (Fe). These categorizations are similar to previous classifications of SSA by ATOFMS [*Gaston et al.*, 2011; *Prather et al.*, 2013; *Guasco et al.*, 2014]. Mass spectra not classified into one of these categories are referred to as "Other". Mass spectra with black carbon, nitrate, and dust ion signatures were also identified and attributed to contamination.

An average mass spectrum for each SSA mass spectral type is shown in Figure 7.2. A brief description of the ion signatures is also provided here: *SS*, with most signal attributed to sodium and chloride ions ($^{23}\mathrm{Na}^{+}$, $^{46}\mathrm{Na}_2^{+}$, $^{81,83}\mathrm{Na}_2\mathrm{Cl}^{+}$, $^{139,141,143}\mathrm{Na}_3\mathrm{Cl}_2^{+}$, $^{35,37}\mathrm{Cl}^{-}$, $^{58,60}\mathrm{NaCl}^{-}$, $^{93,95,97}\mathrm{NaCl}_2^{-}$) and a moderate potassium ion peak ($^{39}\mathrm{K}^{+}$); *SSOC*, with intense signal from sodium and chloride ions as well as from magnesium ($^{24,25,26}\mathrm{Mg}^{+}$, $^{129,131,133}\mathrm{MgCl}_3^{-}$), potassium, and organic nitrogen ions ($^{26}\mathrm{CN}^{-}$, $^{42}\mathrm{CNO}^{-}$) and less intense ion markers associated with other organic carbon species (e.g. +43, +27, +50, +51, -43) and calcium ($^{40}\mathrm{Ca}^{+}$, $^{56}\mathrm{CaO}^{+}$, $^{57}\mathrm{CaOH}^{+}$, $^{75,77}\mathrm{CaCl}^{+}$), and phosphate ($^{63}\mathrm{PO}_2^{-}$, $^{79}\mathrm{PO}_3^{-}$); *OC*, moderate intensity ion markers associated with magnesium, potassium, calcium, and phosphate, and an array of organic ion markers varying in intensity; *Mg*, with signal dominated by magnesium, chloride, and organic nitrogen ion signal, with moderate response from potassium and a relatively weak response from other organic ion markers; *Fe*, with mass spectra dominated by iron ($^{54,56}\mathrm{Fe}^{+}$) and phosphate ion markers, likely a result of nutrient addition at the beginning of each experiment, with strong signal also from magnesium and calcium and relatively weak ion peaks associated with potassium and chloride.

It should be emphasized that there is a great amount of variability within the mass spectral categorizations. In addition, based upon the depth profiling experiments detailed in Chapter 3 [*Sultana et al.*, 2017c], these mass spectral groups should not be considered representative of distinct particle types. Rather most of the variability in the mass spectral signatures is likely a result of varying degrees of particle desorption and ionization from a single SSA particle type. Offline spectromicroscopy analyses have demonstrated that most supermicron SSA particles have a chemically separated morphology once dry, with sodium chloride rich cores surrounding a coating enriched in organic species and minor inorganic components [*Posfai et al.*, 1995; *Leck and Bigg*, 2008; *Wise et al.*, 2009; *Russell et al.*, 2010; *Hawkins and Russell*, 2010; *Maskey et al.*, 2011; *Laskin et al.*, 2012; *Ault et al.*, 2013a, 2013b, 2013c; *Gantt and Meskhidze*, 2013; *Collins et al.*, 2014; *Chi et al.*, 2015; *Lee et al.*, 2015; *Patterson et al.*, 2016]. However, changes in the number fraction of each mass spectral type over time are still likely illustrative of changing chemistry of the particle population. Increases in the organic content of each particle are expected to result in increasing thickness of the sodium-deficient outer layer encompassing each dry particle [*Ault et al.*, 2013c; *Lee et al.*, 2015; *Ryder et al.*, 2015], and therefore a higher fraction of mass spectra with relatively weak sodium ion signals (i.e. *SSOC, Mg, Org*), as demonstrated in Chapter 4 (cite in prep paper here).

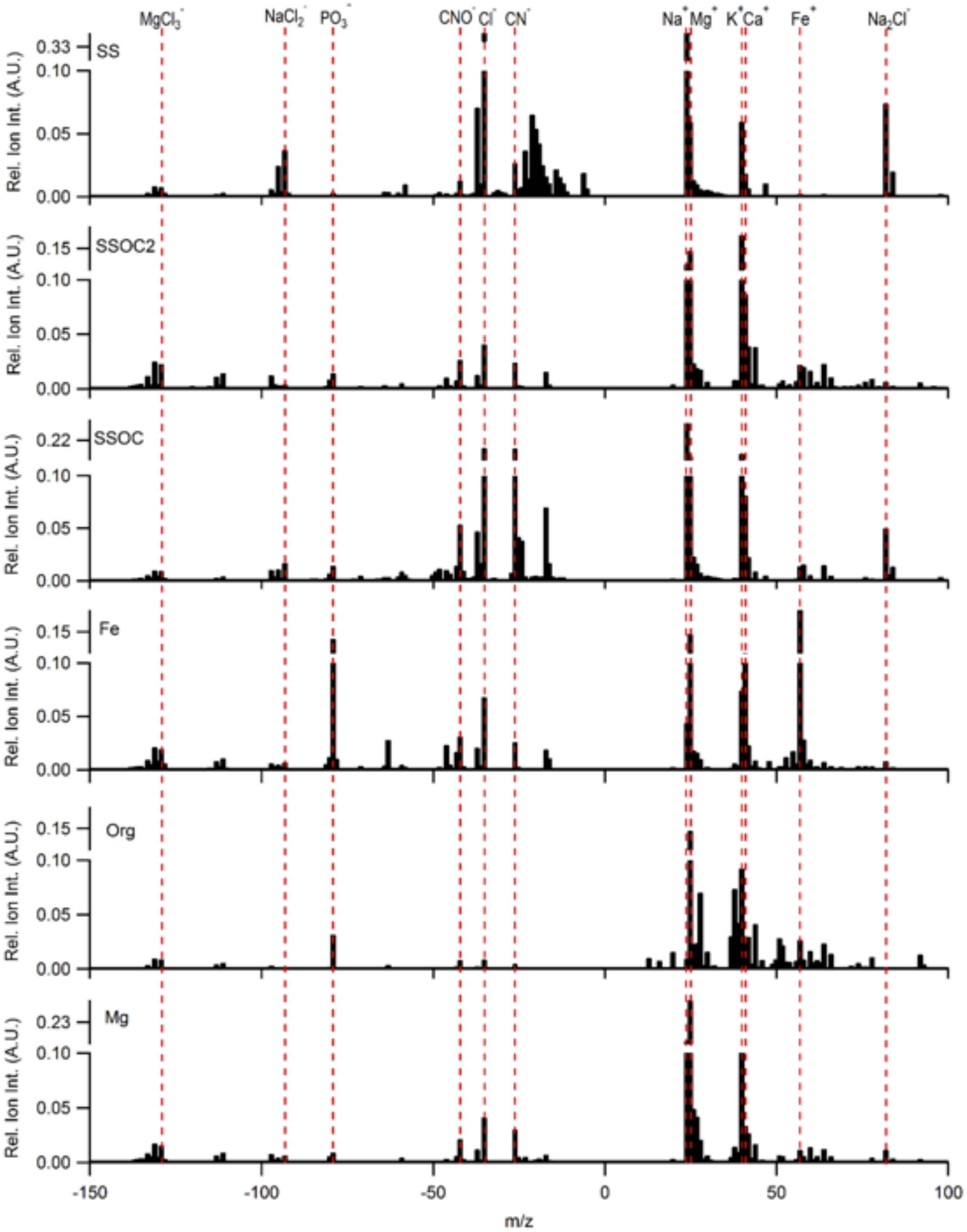

Figure 7.2 The average relative mass spectrum for each mass spectral category generated in the hygroscopicity MART experiments. The SSOC category was split into two groups with relatively strong sodium (SSOC) or magnesium (SSOC2) ion markers to illustrate the intra-category variation.

7.4.1.2 Changing chemistry and hygroscopicity of SSA particles

For each MART phytoplankton microcosm the number fraction of SS, and therefore sodium rich, mass spectra decreased after the peak in chlorophyll-a, reaching a minimum value 1 and 5 days after the collapse of the bloom (Figure 7.3 and Figure 7.4). Corresponding increases were observed in a combination of the SSOC and Mg spectral types. The relatively high fraction of *Fe* mass spectra on the first day of collection for the indoor MART is a result of nutrient addition on that day and is not indicative of biological or biologically mediated chemical changes in the seawater composition. The increase in organic particle content suggested by the qualitative ATOFMS results are supported by corresponding increases in the volume fraction of non-refractory organic matter (ε_{org}) for submicron SSA as calculated from AMS data. Increases in organic content as demonstrated by both the ATOFMS and AMS results corresponded to decreases in the SSA particle growth factors at 85% relative humidity. However, the AMS generates data for submicron SSA as an ensemble, rather than for single particles as with ATOFMS. The changes in the single particle mass spectral signatures presented in this chapter coupled with the paradigm established in Chapter 3 [*Sultana et al.*, 2017c] for interpreting ATOFMS SSA data sets, indicate that the changes in ε_{org} are probably driven by broad increases in organic content across most particles in the SSA population, rather than isolated to increased generation of a distinct, extremely organic-rich particle type. As detailed thoroughly in [*Forestieri et al.*, 2016], these results indicate a clear link between particle chemistry and water uptake: organic compounds transferred from seawater into SSA by bubble bursting can affect the hygroscopicity of the particles and thus the ability of SSA to scatter solar radiation.

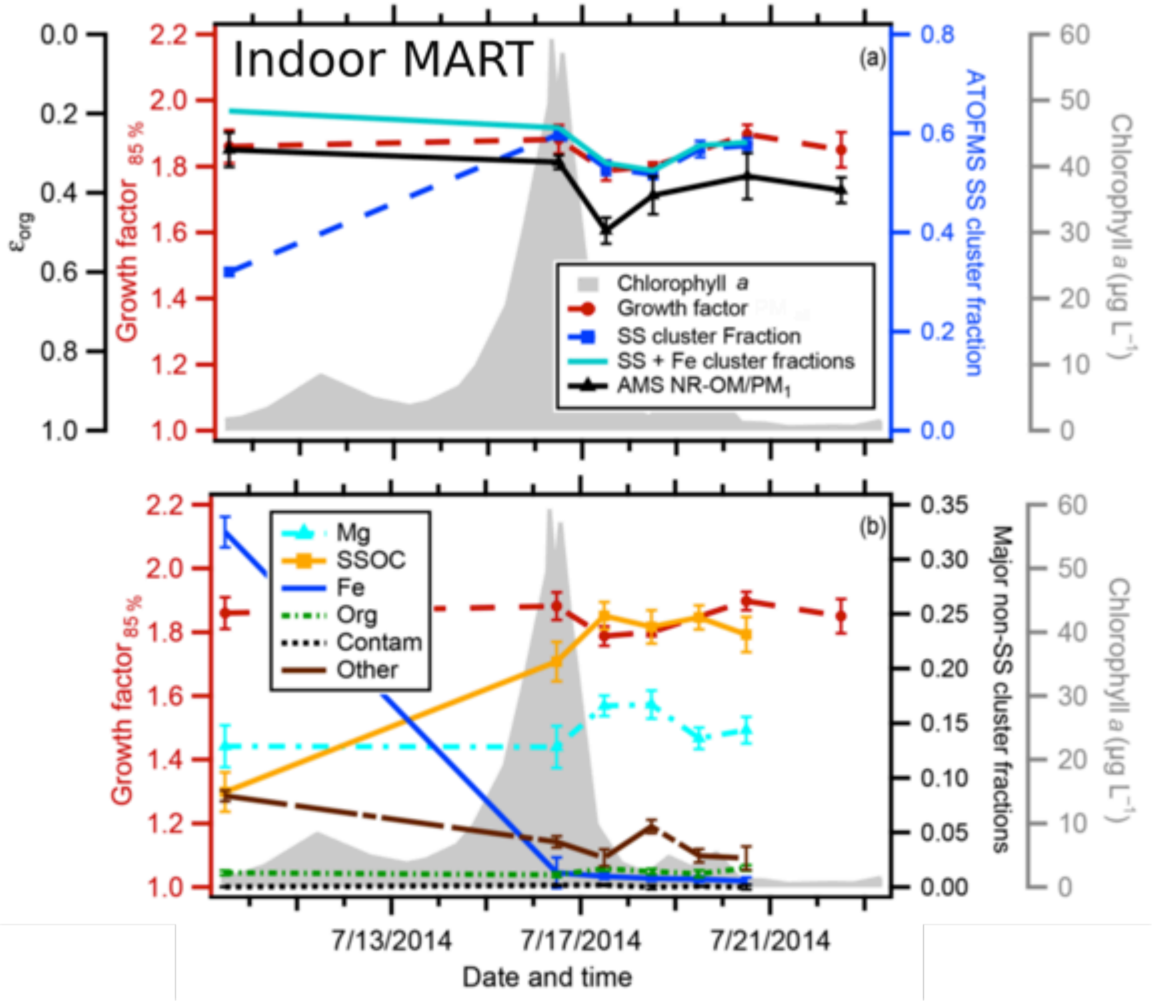

Figure 7.3 Reproduced from [*Forestieri et al.*, 2016]. Time series for the indoor MART chlorophyll-a along with physical and chemical measurements of the SSA population. The SSA GF(85%), organic volume fraction (εorg), and number fractions of ATOFMS mass spectral types are plotted over the course of the microcosm. The reported standard deviation for all properties is 1σ of the individual measurements over each sampling period.

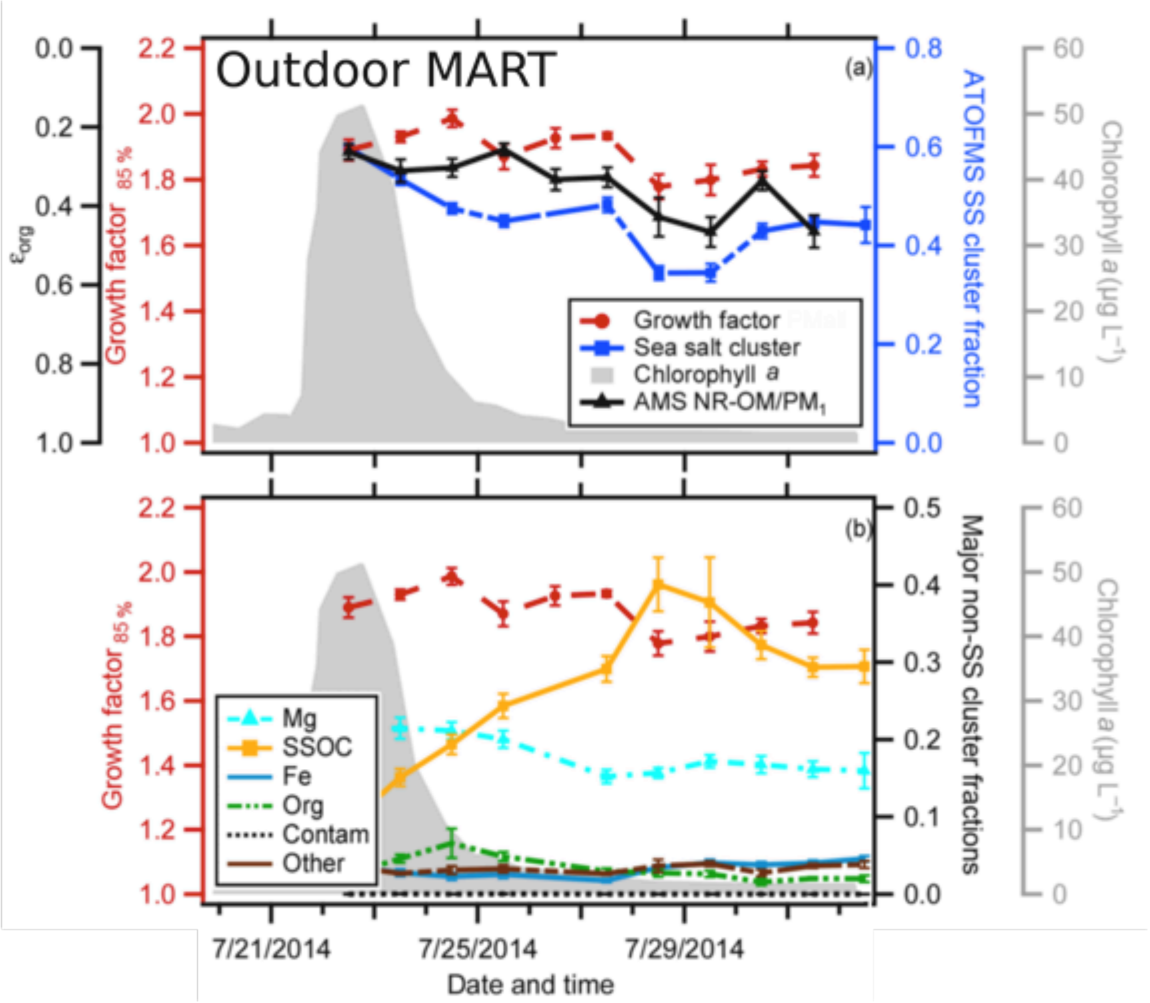

Figure 7.4 Reproduced from [*Forestieri et al.*, 2016]. Time series for the indoor MART chlorophyll-a along with physical and chemical measurements of the SSA population. The SSA GF(85%), organic volume fraction (εorg), and number fractions of ATOFMS mass spectral types are plotted over the course of the microcosm. The reported standard deviation for all properties is 1σ of the individual measurements over each sampling period.

7.4.2 IN Studies

7.4.2.1 Description of ATOFMS spectral types

A narrow set of particles with mass spectral signatures and properties closely matching those of likely microbe-containing SSA particles (BioSS), as detailed in Chapter 5 [*Sultana et al.*, 2017a], were identified within the IMPACTS study. BioSS mass spectra were dominated by potassium ($^{39}K^+$) and phosphate ion ($^{63}PO_2^-$, $^{79}PO_3^-$, $^{97}PO_4^-$) markers and also contained an array of organic and organic nitrogen ion markers ($^{26}CN^-$, $^{42}CNO^-$, -66, -71, $^{90}C_4N_3^-$, $^{59}N(CH_3)_3^+$, $^{74}N(CH_3)_4^+$, $^{120}C_8H_{10}NO_2^+$) (Figure 7.5). In addition the BioSS mass spectra were grouped by total positive ion intensity into low (0-2E5), medium (2E5-6E5), and high (6E5-12E5) bins. As for the *BioSS* mass spectra described in Chapter 5 [*Sultana et al.*, 2017a] ion markers +59 and +74 had high relative signals at low total positive ion intensities. In contrast the relative signal from sodium ($^{23}Na^+$,$^{23}Na_2Cl^+$), chloride ($^{35,37}Cl^-$), organic nitrogen ($^{26}CN^-$, $^{42}CNO^-$), and a set of low intensity positive ion markers (104, 120, 141, 157, 175) increased with increasing total positive ion intensity (Figure 7.5).

A group of mass spectra with positive silver ($^{107,109}Ag^+$, $^{214,216,218}Ag_2^+$) ion markers were also identified (Bio-Ag) (Figure 7.6). In a previous wave channel experiment silver-rich mass spectra were suggested to be generated from aerosolized bacterial cells into which silver nanoparticles, present in the wave channel, had bioaccumulated [*Guasco et al.*, 2014]. Note Bio-Ag and BioSS are exclusive classifications. Because only silver ion markers were utilized to select for Bio-Ag mass spectra, there is a wide degree of variation in the ion signatures as a whole. However most mass spectra were characterized by large potassium ($^{39}K^+$) and phosphate ($^{63}PO_2^-$, $^{79}PO_3^-$) ion signal with significant contributions from a wide array of peaks from sea salt ions ($^{23}Na^+$, $^{24,25,26}Mg^+$, $^{129,131,133}MgCl_3^-$, $^{93,95,97}NaCl_2^-$) and organic and organic nitrogen ion species. The relative intensity of the summation of relative intensity of the silver ion markers also varied greatly within the BioAg mass spectral type (0.015-0.99) and was not consistent over the course of the experiment (Figure 7.7).

Distinct from the BioSS and Bio-Ag types, were particles with mass spectra dominated by potassium ($^{39,41}K^+$, $^{56}KOH^+$, $^{113,115}K_2Cl^+$) and phosphate ($^{63}PO_2^-$, $^{79}PO_3^-$) ion markers (KP-lowOrg), but with little to no signal from the organic or organic nitrogen markers associated with BioSS signatures (Figure 7.6). Finally mass spectra typical of dust particles (Dust) and atmospherically aged aerosols (NO_x), attributed to contamination of the wave channel headspace, were also identified (Figure 7.8). Titanium ($^{46\text{-}50}Ti^+$, $^{62\text{-}66}TiO^+$), aluminum silicate ($^{27}Al^+$, $^{76}SiO_3^-$, $^{77}HSiO_3^-$), and zirconium ($^{90\text{-}96}Zr^+$, $^{106\text{-}112}ZrO^+$) ion markers were utilized to distinguish the *Dust* particle type. Nitrate ($^{46}NO_2^-$, $^{62}NO_3^-$) and sulfate ion markers ($^{165}Na_3SO_4^-$) were used to identify particles that had undergone atmospheric processing, and thus were not freshly produced SSA in the wave channel. Dust mass spectra may be partially attributed to ejection of dust particles present in the seawater. However, several spikes in the number fraction of the Dust and NO_x mass spectral types coincided with each other in time (Figure 7.10), indicating dust particles may also have been present as a result of headspace contamination. Note that only very few mass spectra during the entire wave channel study were classified into the relatively strict mass spectral types described above made up (<1%). The vast majority of the ion signatures resembled the broad SSA mass spectral categories (SS, SSOC, Org, or Mg) described in section 7.4.1 for the MART hygroscopicity studies.

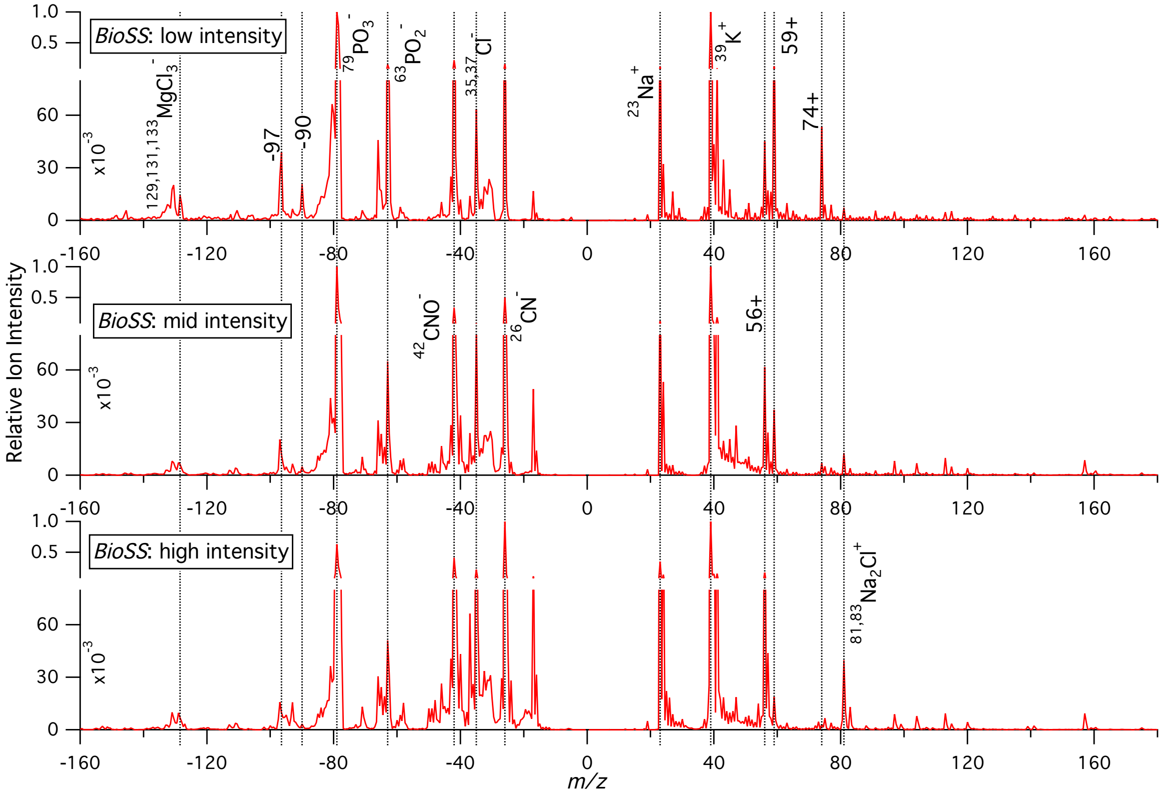

Figure 7.5 Average relative mass spectra for the *BioSS* mass spectral type, identified during the wave channel IMPACTS experiment, split by total positive ion intensity (low: 0-2E5, medium: 2E5-6E5, high: 6E5-12E5).

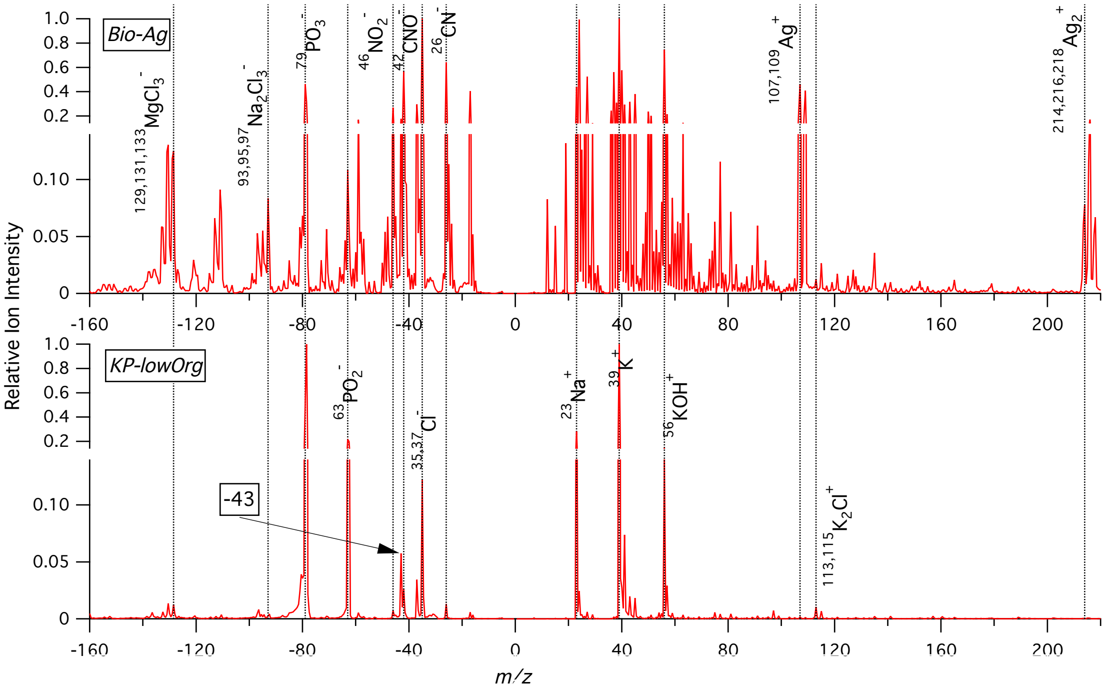

Figure 7.6 Average relative mass spectra for the Bio-Ag and KP-lowOrg mass spectral types identified during the wave channel IMPACTS experiment.

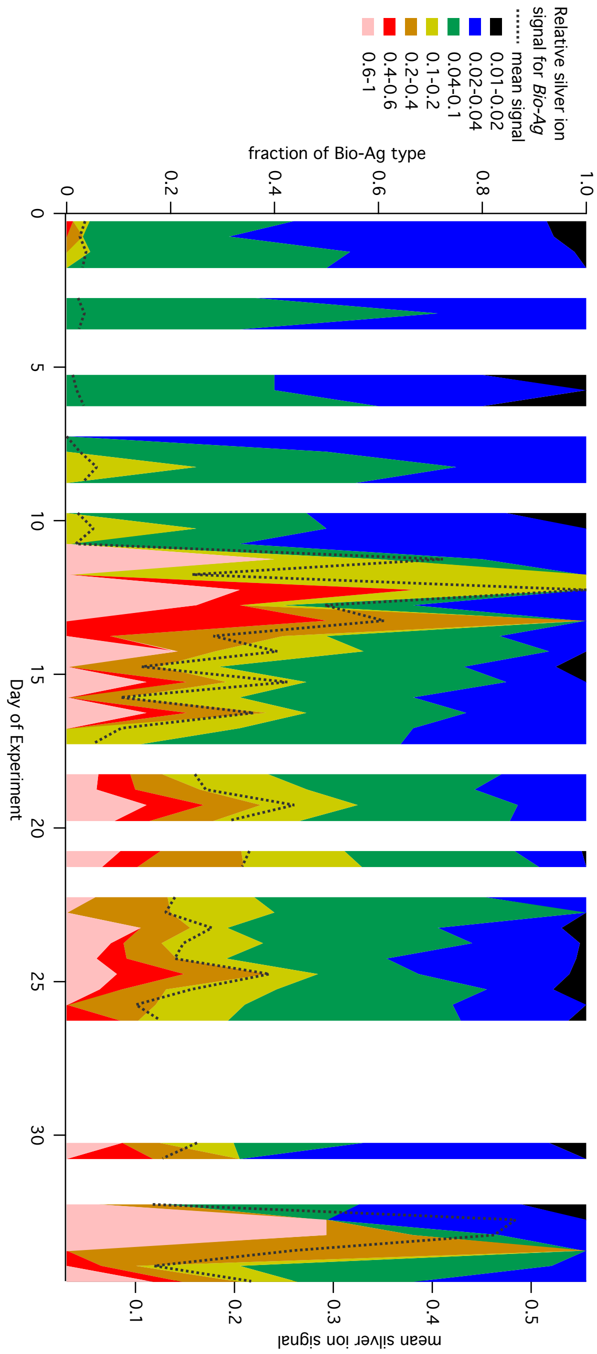

Figure 7.7 For each sampling period the mean relative positive silver ion signal was calculated for the BioAg type (dotted line). In addition the distribution of the relative silver ion signal for the BioAg mass spectral type is also shown for each time period. The positive silver ion signal is the sum of $^{107,109}Ag^+$ and $^{214,216,218,}Ag_2^+$ relative peak intensities.

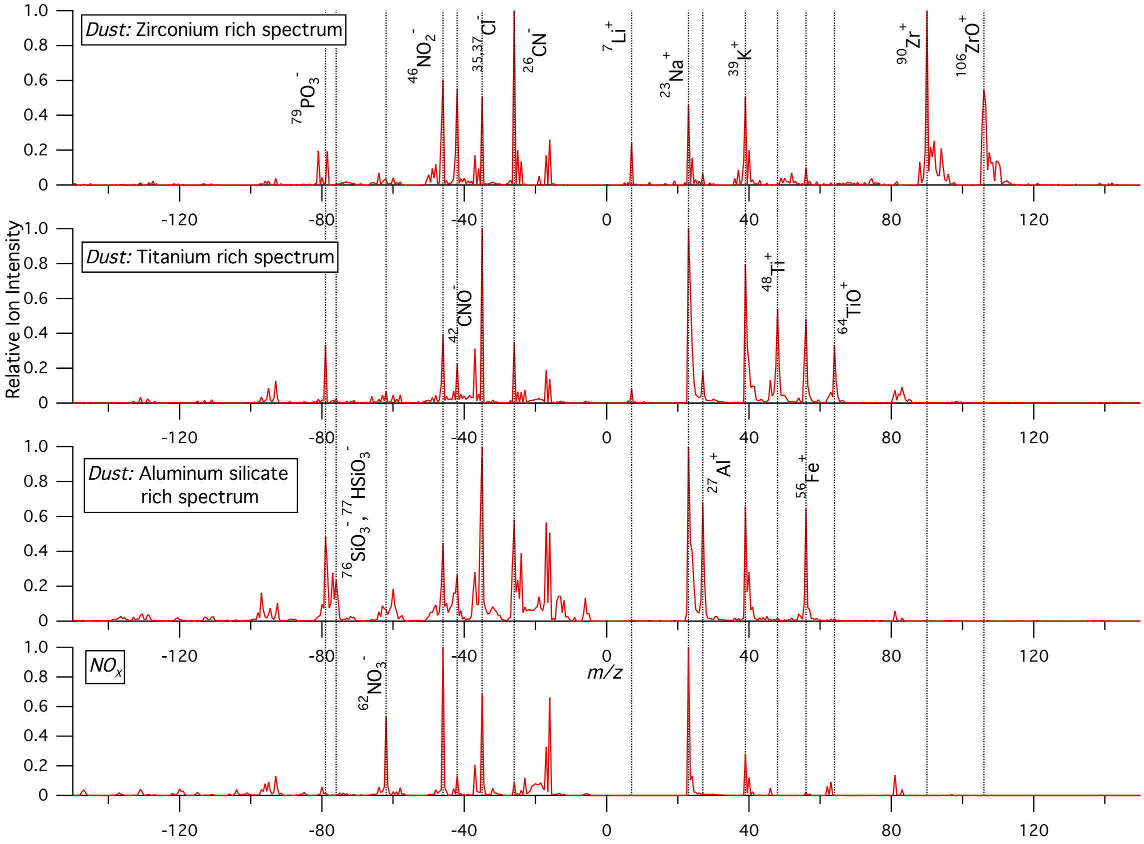

Figure 7.8 Average relative mass spectra for the Dust and NO_x mass spectral types, identified during the wave channel IMPACTS experiment. The Dust mass spectra were grouped by whether zirconium, titanium, or aluminum silicate were the dominant dust-indicative ion markers.

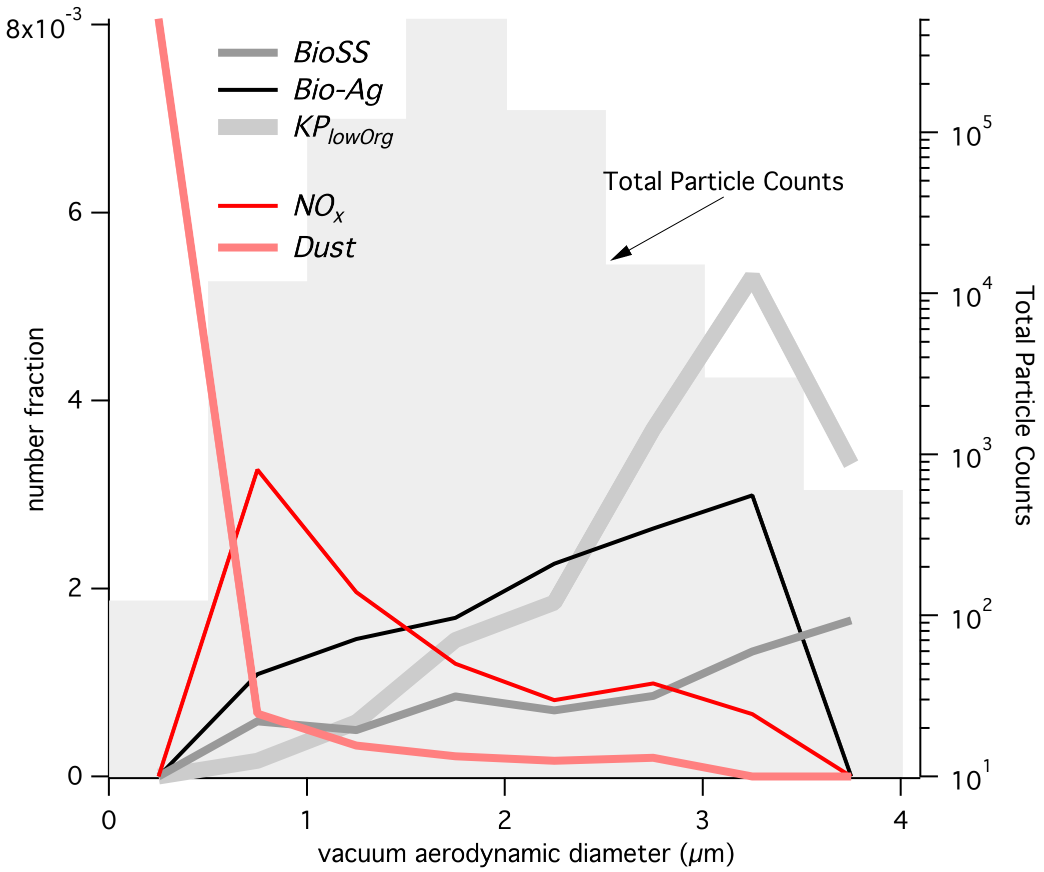

Figure 7.9 The number fraction for the mass spectral types, identified during the wave channel IMPACTS experiment, over the size range of the ATOFMS. In addition the size resolved total particle counts are shown for the entirety of the dataset.

The number fraction of each particle type relative to all mass spectra generated by sampling the SSA population in the wave channel headspace is shown with respect to particle size (d_{va}) in Figure 7.9. The number fraction of the BioSS and Bio-Ag increased with size. In Chapter 5 [*Sultana et al.*, 2017a], BioSS mass spectra identified during a MART study had a similar size trend. In addition, a previous field study suggested that bacteria transfer into SSA occurs dominantly in large supermicron SSA particles [*Dueker et al.*, 2011]. Therefore these results are consistent with the theory that BioSS and Bio-Ag mass spectral signatures are from SSA particles that contain microbial cells transferred from seawater during the bubble bursting process. However, the number fraction of particles with the KP-lowOrg mass spectral signature also increased dramatically with size. This result suggests that the KP-lowOrg mass spectra may also be generated from insoluble particles transferred from seawater into SSA during the bubble bursting process. Yet, the lack of organic and organic nitrogen markers in these mass spectra implies that the SSA particles may not contain cells or cellular material.

7.4.2.2 Changing chemistry and ice nucleation of particles

During the IMPACTS wave channel study the peaks in the BioSS and Bio-Ag particle types were usually coincident with high concentrations of warm INP (>-25°C) detected in the SSA (Figure 7.10). BioSS and Bio-Ag never exceeded 1.5% of all mass spectra and frequently made up less than 0.2% of the population. These results suggest that a rare SSA particle type, potentially microbe-containing particles, can have a profound influence on the INP populations associated with SSA. This conclusion is further supported by micro-Raman spectroscopy analysis of the ICR's collected downstream of the CFDC. On Day 26 of the experiment 60% of ICR's were characterized as "siliceous" [*McCluskey et al.*, 2017b]. In addition, a number of studies have indicated that both bacterial and diatom cells and cellular material effectively nucleate ice [*Maki et al.*, 1974; *Knopf et al.*, 2011; *Hill et al.*, 2014; *Wilson et al.*, 2015]. The

BioSS and *Bio-Ag* types' temporal correlations with increases in warm INP, size trends, and ion signatures support their classification as microbe-containing SSA particles. The presence of silver ion markers is most likely result of silver contamination within the waveflume, therefore the Bio-Ag mass spectral type is unlikely to be relevant in other studies. However, the evidence presented in this chapter illustrates that the paradigms for identifying BioSS mass spectra (Chapter 5) can be leveraged in future studies which couple INP and SPMS measurements of aerosol populations.

It is interesting to note that the temporal trend of the KP-lowOrg mass spectral type was distinct from those of both BioSS and Bio-Ag, suggesting that SSA particles generating KP-lowOrg mass spectral signatures do not contain microbes. The source of this mass spectral type is an area of ongoing research, however it appears that particles generating KP-lowOrg may not have a strong influence in increasing the concentration of warm INPs in SSA. A small fraction of sampled mass spectra had ion signatures similar to previously characterized dust particles, with strong signal from titanium, zinc or aluminum. Various types of dust have been shown to be effective INP at colder temperatures [*DeMott et al.*, 2003; *Cziczo et al.*, 2009]. However, there appears to be no correspondence between the *Dust* and INP temporals. The ATOFMS results help eliminate the conclusion that the periods of elevated warm INP concentrations were due to trace dust particles, either ejected during the bubble bursting process or a result of headspace contamination. A manuscript is currently in prep, which discusses at length the possible identities of ice nucleating particles in SSA generated during the wave channel IMPACTS study [*McCluskey et al.*, 2017b].

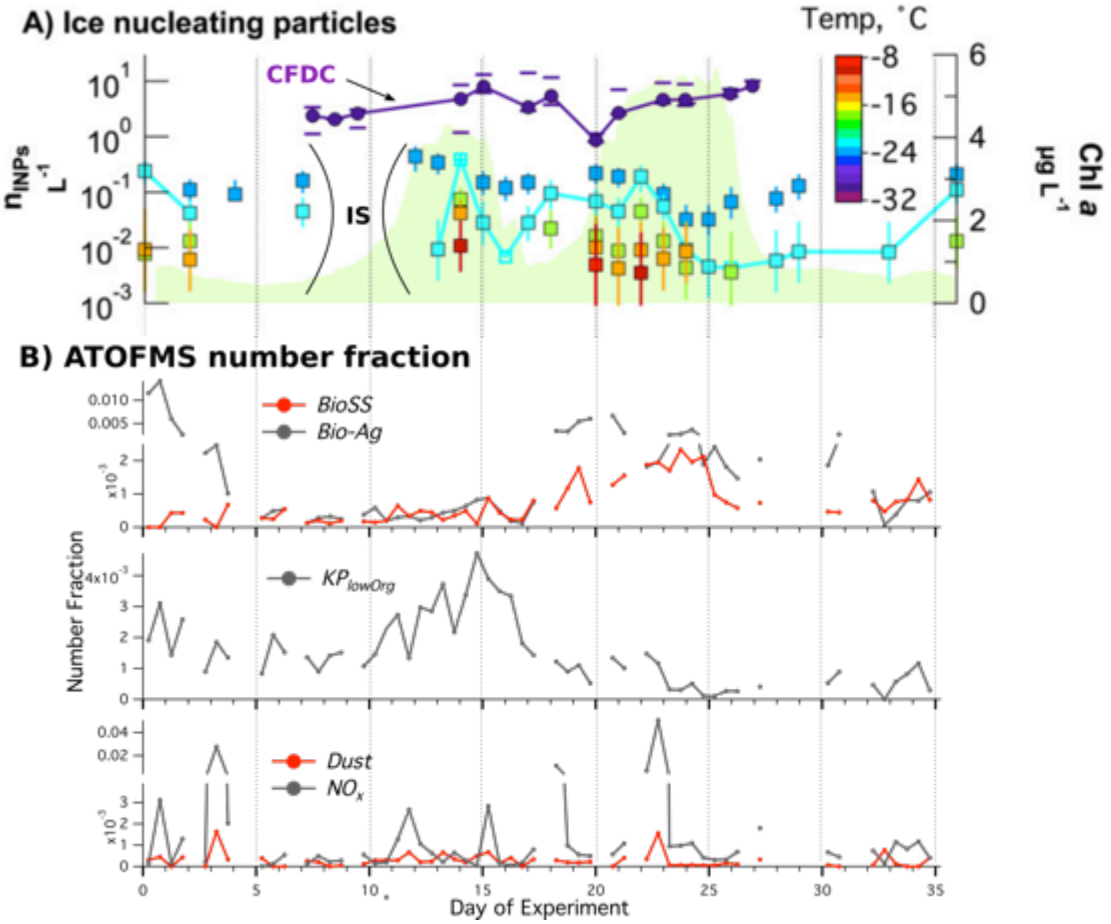

Figure 7.10 Panels (a) from *McCluskey et al.* [2017a]. (a) Timeline of INP number concentrations (n_{INPs}; per liter of air; left axis). Colors indicate activation temperature denoted by the color scale. (b) Number fraction of the ATOFMS mass spectral types.

7.5 Conclusions

ATOFMS couples online high throughput analysis with single particle resolution. These capabilities make them well-suited to studying aerosol populations where capturing broad changes in particle chemistry as well as distinguishing exceedingly rare particle types are both necessary. This dichotomy is present when studying the physical processes that controls SSA impact on climate and the environment.

Light scattering capabilities of SSA are controlled by the ability of particles to take up water. Above roughly 100 nm, particle hygroscopicity is independent of dry particle size and controlled by particle chemical composition [*Forestieri et al.*, 2016], with increases in organic particle content, regardless of molecular species, generating decreases in particle hygroscopicity [*Petters and Kreidenweis*, 2007]. Therefore at a given size, roughly understanding variations in organic to salt ratio of the major SSA particle types can help inform changes in the overall light scattering of the population. During two microcosm phytoplankton bloom experiments, conducted during the IMPACTS study, decreases in the frequency of sodium rich single particle SSA mass spectra, a broad change in the mass spectral signatures, corresponded to increases in the organic volume fraction of the SSA particles as well as decreases in the particle hygroscopicity [*Forestieri et al.*, 2016].

In contrast, the number of INPs in SSA has been shown to be very low, with fewer than 1 particle nucleating ice at -25 °C per liter of sampled air [*DeMott et al.*, 2015]. Because sea salt, which makes up the majority of supermicron SSA mass does not nucleate ice, INP concentrations are thought to be very sensitive to rare SSA particles types and molecular species, which may be more common during periods of elevated biological activity [*DeMott et al.*, 2015; *McCluskey et al.*, 2017a]. To help elucidate the identity of ice nucleating SSA particles chemical techniques with single particle resolution are critical. In addition, high instrument throughput is necessary to generate enough data to identify discernable temporal and size dependent trends of this presumably rare particle type within the greater SSA population. During the wave channel IMPACTS mesocosm study, the BioSS mass spectral type, established in Chapter 5 [*Sultana et al.*, 2017a], and the Bio-Ag mass spectral type, identified in [*Guasco et al.*, 2014], combined made up less than 1.5% of all mass spectra during any given sampling period. However, periods of elevated warm INP concentrations corresponded well to relatively high number fractions of the BioSS and Bio-Ag mass spectral types. These ATOFMS results have been critical in informing the identification of marine ice nucleating particles [*McCluskey et al.*, 2017b].

The IMPACTS campaign brought together researchers from 8 separate institutions and enabled simultaneous measurement of a wide array of chemical and physical SSA properties. Over 2 million SSA single particle mass spectra were generated utilizing ATOFMS during this campaign. New paradigms established for the interpretation of this chemically and morphologically complex aerosol population (Chapters 3 [*Sultana et al.*, 2017c] and 5[*Sultana et al.*, 2017a]) helped generate descriptions of the SSA mixing state and chemical composition, which were utilized to inform both hygroscopicity and ice nucleation measurements of the SSA population. This collaborative effort enabled new connections to be drawn between changes in SSA particle chemistry and their climate impacts [*Forestieri et al.*, 2016; *McCluskey et al.*, 2017b].

7.6 Acknowledgments

This work was supported by the National Science Foundation through the Centers of Chemical Innovation Program via the Center for Aerosol Impacts on Climate and the Environment (CHE-1305427).

The hygroscopicity study in Chapter 7 is material that appears in Atmospheric Chemistry and Physics, 2016. Reprinted with permission from Forestieri, S. D., Cornwell, G. C., Helgestad,

T. M., Moore, K. A., Lee, C., Novak, G.A., Sultana, C. M., Wang, X., Bertram, T. H., Prather, K. A., Cappa, C. D. Linking variations in sea spray aerosol particle hygroscopicity to composition during two microcosm experiments. Atmos. Chem. Phys. 2016, 16, 9003-9018. Portions of the ice nucleation study results in Chapter 7 contribute to a manuscript, which has been submitted for publication to the Journal of the Atmospheric Sciences. Printed with permission from McCluskey, C. S., Hill, T. C. J., Sultana, C. M., Laskina, O., Trueblood, J., Santander, M. V., Beall, C. M., Michaud, J. M., Prather, K. A., Grassian, V., DeMott, P. J. A mesocosm double feature: revealing the identity of marine ice nucleating particles.

Sara Forestieri and Christina McCluskey are acknowledged for assisting in the editing of this chapter.

Chapter 8. Conclusions and Future Directions

8.1 Synopsis

This dissertation focuses on the elucidation of single particle sea spray aerosol (SSA) chemistry and morphology via analysis by an aerosol time-of-flight mass spectrometer (ATOFMS). Chapter 2 describes FATES, a new open-source single particle mass spectrometer (SPMS) data analysis toolkit, which was utilized to generate the results described in Chapters 3, 4, 5, and 7. Chapters 3 and 4 illustrate that the core-shell morphology of dry supermicron SSA particles, a result of phase separation during particle deliquescence, can result in wide variability in the mass spectral signatures of the population. Chapter 5 provides a refined definition for the discrimination of mass spectra generated from rare microbe-containing SSA particles from the greater population. Chapters 6 and 7 illustrate connections between biologically-mediated changes in seawater chemical composition and the chemistry and climate impacts of SSA particles.

8.2 Conclusions

8.2.1 New SPMS data analysis toolkit

The complexity and size of the ATOFMS SSA data sets generated during a series of phytoplankton bloom studies performed in 2013 and 2014 exposed the need for more efficient and sophisticated data analysis tools. Chapter 2 describes the development of the Flexible Analysis Toolkit for the Analysis of SPMS datasets (FATES), which was publicly released along with a detailed user manual. FATES is implemented completely in MATLAB for ease of use, is optimized for both speed and memory considerations, and was intentionally designed to be simply extensible to the evolving and varied implementations of SPMS. FATES is the first open-source SPMS toolkit to allow users to explore their data without constraints using creative script-based data mining alongside robust interactive GUIs for data visualizations, all within a single programming environment. The initial release of FATES (v1.0.0) can read in data sets from three SPMS designs: ATOFMS, TSI-ATOFMS, and ALABAMA. FATES is shared online via GitHub, a popular platform for hosting open-source software. Utilizing GitHub, the SPMS community will be able to keep its codebase synced with updates and also can help maintain the toolkit and contribute new features. All ATOFMS users within the Prather lab are now using FATES. It is expected that many in the SPMS community will adopt this software and FATES will greatly improve the efficiency of data processing and knowledge discovery from single particle mass spectrometer datasets.

8.2.2 Influence of SSA particle morphology on mass spectral signatures

Spectromicroscopy studies of nascent SSA have generally found the most common type of dry supermicron particles by far to be inorganic cuboids with amorphous coatings [e.g. *Russell et al.*, 2010; *Ault et al.*, 2013c; *Collins et al.*, 2014; *Chi et al.*, 2015]. However, previous SPMS analyses of SSA have revealed several mass spectral ion patterns, suggesting that there may be a number of chemically distinct particle types contributing significantly to the population [*Gaston et al.*, 2011; *Prather et al.*, 2013; *Collins et al.*, 2014; *Guasco et al.*, 2014]. Chapter 3 combined new experimental data from laboratory generated SSA and new interpretations of previously published field study datasets to investigate the factors controlling single particle mass spectra of dried supermicron SSA. Results from a depth profiling study, the first to be performed explicitly on SSA particles, are paired with a binned total ion intensity analysis to provide information on the three-dimensional chemical morphology of the particles. These analyses reveal that single particle mass spectra with weak sodium ion signals can be produced by surface desorption of typical SSA particles comprised of salt cores and organic rich coatings. This study unifies the description of supermicron SSA from offline spectromicroscopy and online SPMS measurements as well as lab and field studies of SSA mixing state. This new understanding can serve as a foundation for the online study of the surface chemistry of SSA and could be extended in the future to the more complex submicron SSA population. It should be noted an array of atmospheric aerosols, such as biomass burning aerosols, dust, and aerosol particles which have undergone atmospheric processing, have all been shown to exhibit heterogeneous chemical morphologies [*Pöhlker et al.*, 2012; *Li et al.*, 2016]. While this study focused on SSA, the results reveal that SPMS analysis of any aerosol particles with spatial chemical heterogeneity could potentially generate an array of distinct mass spectral ion signatures. This should be taken into consideration when trying to infer aerosol mixing state from SPMS data sets.

The paradigm established in Chapter 3 enabled further discovery-based science utilizing ATOFMS data sets of synthetic core-shell SSA particles, as described in Chapter 4. Particle morphology, composition, and mass spectral signatures were examined for SSA generated from a synthetic carboxylic acid seawater solution. Quantitative measurements of the chemical composition of the ensemble SSA population [*Cochran et al.*, 2016b] were utilized to calculate particle organic volume fractions (OVF). By coupling OVF values with model particle morphologies, it was shown that the organic-rich particle shell thickness increases over the size range of the ATOFMS. The particle size dependence of the organic-rich shell thickness was expressed in ATOFMS mass spectra. Smaller particles generated more sodium-rich spectra due to thinner organic-rich coatings, in agreement with the offline ensemble and atomic force microscopy results. Also, it is suggested that the exceptional calcium ion signal in the ATOFMS mass spectra is a result of calcium ion coordination to the carboxylate functional groups in the dried SSA particles. These results illustrate a level of detail in the description of the chemical morphology of SSA particles that had not been previously attained utilizing SPMS analysis.

8.2.3 Identification of microbial ion signatures in SSA populations

Due to their high throughput, single particle resolution, and portability, SPMSs are particularly well suited to detecting aerosolized microbial cells in both ground-based and aircraft studies, which require high temporal resolution measurements on the order of seconds to minutes. However, isolating microbial mass spectra in marine or laboratory generated SSA presents a particular challenge due to the extreme rarity of aerosolized microbes coupled with the ubiquity of dissolved chemical species that are commonly associated with "microbial signatures", such as phosphate and potassium [e.g. *Fergenson et al.*, 2004; *Czerwieniec et al.*, 2005; *Cahill et al.*, 2015b], in seawater and thus SSA.

The study detailed in Chapter 5 is the first to distinguish a narrow set of single particle mass spectra (BioSS) that are likely generated by microbes ejected in seawater droplets within a larger, realistic, and chemically complex SSA population. This study also presents the first application of laser pulse energy experiments and data analyses utilizing mass spectral total ion intensities to support the classification of BioSS as a microbe-containing particle type. These techniques progress beyond typical methods of comparing ambient SPMS mass spectra to standard microbial signatures and provide the first multivariate analysis of SPMS data to identify microbial signatures within a complex aerosol population. Furthermore, particle size is used as a novel metric to verify the separation of microbial mass spectra from the larger population of typical potassium and phosphate-rich mass spectra generated by SSA. These approaches were leveraged to describe the influence of changing seawater chemical composition on both the chemical morphology and mass spectral signatures of BioSS particles. The results shown are also pertinent for atmospheric scientists due to the potential influence of microbes on ice nucleating processes [*Maki et al.*, 1974; *Knopf et al.*, 2011; *Burrows et al.*, 2013; *Hill et al.*, 2014; *Wilson et al.*, 2015].

8.2.4 Influence of seawater biology and SSA chemical composition

The Investigation into Marine Particle Chemistry and Transfer Science (IMPACTS) campaign was conducted to explore the impact of changing seawater chemistry on the chemical composition and climate impacts of SSA particles. Phytoplankton blooms were induced from natural seawater and SSA were produced utilizing realistic intermittent wave breaking or plunging sheet mechanisms. In Chapter 6, during two successive phytoplankton blooms in a 3,400 gallon wave-channel, the behavior of organic material in SSA was determined to be class-specific. Aliphatic-rich organics, which were concentrated in submicron SSA, probably originated from labile phytoplankton produced organic species. However, the concentration of this labile organic material is controlled by both phytoplankton and bacteria and was modeled with consideration of enzymatic activity in seawater. More recalcitrant oxygenated organic species were mainly enriched in supermicron SSA particles and increased gradually over the course of the experiment and persisted for days after phytoplankton senescence. To the best of my knowledge, this is the first time that reports different phytoplankton blooms leading to generation of chemically distinct organic containing SSA within a single isolated system.

In Chapter 7 of this dissertation, the paradigms for interpreting SPMS SSA data sets established in Chapters 3, 4, and 5, were applied to the dynamic systems studied during the IMPACTS campaign. Descriptions of the SSA mixing state and chemical composition, generated from an ATOFMS data set made up over 2 million SSA single particle mass spectra, were utilized to inform the water uptake and ice nucleation capabilities of the SSA population. Broad changes in the mass spectral signatures of the SSA population, namely a decrease in the relative sodium ion intensity, corresponded to increases in the SSA organic volume fraction and decreases in the particle hygroscopicity, occurring after the peak in the phytoplankton blooms. Periods of elevated warm INP concentrations corresponded well to relatively high number fractions of rare mass spectral types, likely generated by microbe-containing SSA particles. This collaborative effort between researchers measuring climate relevant properties of SSA and online analysis of single particle SSA chemistry enabled new insights of how the chemical and biological composition of seawater can impact cloud formation and the atmospheric scattering of solar radiation.

8.3 Future Work

8.3.1 Extending FATES to offline spectroscopic single particle data sets

Single particle mass spectrometers produce large and highly complex data sets, with thousands to millions of single particle mass spectra generated in an experiment or field study. Therefore, while SPMS generate mass spectra with single particle resolution, by necessity the complexity of the data set is often reduced by algorithmically clustering particles based upon similarity of ion signatures [e.g. *Dallosto and Harrison*, 2006; *Pratt and Prather*, 2009; *Qin et al.*, 2012]. Temporal trends, size distributions, and the average mass spectra for these clusters can then be easily calculated and examined. Yet, by only examining average cluster mass spectra, single particle mass spectral variability within each group is masked, potentially obscuring important information and patterns. In addition, users can be tempted to treat particles grouped into algorithmically generated clusters as chemically distinct particle types without understanding the mathematical similarity or dissimilarity between clusters. To overcome these limitations, interactive tools have been developed to visualize SPMS data sets of hundreds of thousands of particles while still maintaining the single particle resolution of the mass spectra and particle metadata. These tools enable efficient user-guided exploration of large data sets and can help enable more accurate elucidation of particle types [*Zelenyuk et al.*, 2006, 2008a]. Chapter 3 of this dissertation describes FATES, a new toolkit for SPMS analysis, which includes guiFATES a visualization tool for SPMS data sets as described above.

While, FATES was developed with a flexible framework to enable utilization with a wide array of SPMS designs and data formats, this robust data architecture means it could be easily extended to accommodate data from offline single particle techniques. Raman and energy-dispersive X-ray spectroscopic single particle studies often generate data sets with hundreds to several thousand spectra [e.g. *Rogers et al.*, 2001; *Ault et al.*, 2013c; *Deng et al.*, 2014; *Chi et al.*, 2015; *Cochran et al.*, 2017]. Similar to treatments of SPMS datasets, offline single particle spectra are frequently grouped by algorithmic clustering or empirically generated thresholds and then average spectra for each group are provided [e.g. *Deng et al.*, 2014; *Chi et al.*, 2015; *Cochran et al.*, 2017]. The difficulty of creating accurate particle types and dilemmas inherent to grouping mass spectra have been an active area of discussion in the SPMS community [*Murphy et al.*, 2003; *Zelenyuk et al.*, 2006; *Rebotier and Prather*, 2007; *Gross et al.*, 2010; *Giorio et al.*, 2012; *Zawadowicz et al.*, 2016]. However, this does not appear to be a current area of discussion among researchers utilizing offline spectroscopy techniques. As these techniques become more popular and associated instrumentation improves the size of offline spectroscopic single particle data sets will continue to grow. Sophisticated data analysis techniques should be employed to be maximize the efficiency of data analysis while maintaining complexity of these single particle datasets. FATES, with its associated tools for user-guided visual analysis of single particle datasets, is positioned as a potentially powerful toolkit for spectroscopists studying single particle chemistry.

8.3.2 Chemistry at the air-particle interface of hydrated aerosols

Chapters 3 through 5 of this dissertation focused on deconvoluting SPMS data sets of SSA particles that had been dried before analysis. Particle phase water is known to inhibit ionization in SPMS systems [*Neubauer et al.*, 1997, 1998]. Therefore, when sampling time is limited, it is essential to dry particles before analysis to be able to generate mass spectra from an adequate number of particles. However, SSA particles are generated as wet droplets and will likely remain so in marine regions, which have relatively high relative humidities. SSA undergo phase separation as a result of drying processes [*Ge et al.*, 1996, 1998a; *Cziczo and Abbatt*, 2000; *Liu et al.*, 2008; *Xiao et al.*, 2008; *Tong et al.*, 2011; *Gupta et al.*, 2015] and the surface chemistry of a dry particle is not comparable to the surface chemistry of nascent hydrated SSA. While laser desorption/ionization of wet particles has a poor efficiency, mass spectra of hydrated particles have been generated utilizing SPMS [*Neubauer et al.*, 1997, 1998; *Ge et al.*, 1998a] and could potentially be improved by addition of trace amounts of material that has a high absorption cross section at the ionizing wavelength. The chemistry of hydrated SSA particles is an area of active research. Particular focus has been given to the propensity of organic material to partition to the air-particle interface and their interactions with dissolved cations in the particle bulk [*Cochran et al.*, 2016b; *Jayarathne et al.*, 2016]. However, most studies motivated by this atmospherically relevant particle chemistry have leveraged spectroscopic experiments on model bulk liquid systems [e.g. *Hua et al.*, 2015; *Adams et al.*, 2016; *Casper et al.*, 2016; *Zhang et al.*, 2016]. Very recently a few studies have begun to connect surface chemistry of hydrated particles with actual measurements of particle surface tension, using both online and offline techniques [*Forestieri et al.*, n.d.; *Lee et al.*, 2017]. Nonetheless, the potential exists to directly describe the surface chemistry of hydrated particles via variable laser pulse energy (depth profiling) SPMS studies of model particles with trace amounts of dissolved highly adsorptive species, such as iodide. The ionization of the particles could also be improved by utilizing aromatic highly surface-active organic species. With careful selection of anionic, aromatic, surface-active organic species and low desorption/ionization pulse energies, interactions between cations in the particle bulk with the anionic surfactants could potentially be elucidated. Notably, while this dissertation focuses on the chemistry of SSA particles, the chemical composition at the air-particle interface of any hydrated aerosol is key to that particle's chemical reactions within the atmosphere and climatic impacts.

8.3.3 Definitive identification of microbial cells in SSA

Microbe-containing SSA particles, though likely rare within the SSA population, are of interest due to their ill-defined potential to act as ice nucleating particles [*Maki et al.*, 1974; *Fall and Schnell*, 1985; *Alpert et al.*, 2011a, 2011b; *Knopf et al.*, 2011; *Burrows et al.*, 2013; *Hill et al.*, 2014; *Wilson et al.*, 2015; *McCluskey et al.*, 2017a]. Chapter 5 of this dissertation provides a description of a narrowly defined biological mass spectral signature (BioSS) generated by SSA. An array of evidence is provided in Chapter 5 and Chapter 7 that strongly suggests BioSS mass spectra are generated by microbe-containing SSA particles, although definitive evidence supporting this conclusion has yet to be provided. In addition, as explained in Chapter 5, mass spectra falling outside of this classification may have been also generated from microbe-containing SSA particles. Definitive identification of all microbe-containing particles within SSA populations is fraught as ions common in microbial SPMS mass spectral signatures can also be generated by dissolved chemical species ubiquitous in seawater. However, some SPMS instruments, in an effort to improve detection of biological aerosols, have integrated measurement of the intrinsic particle fluorescence before desorbing and ionizing the particle's chemical components [*Mcjimpsey et al.*, 2006]. Integration of fluorescence measurements within ATOFMS instruments or parallel measurement of the fluorescence of the SSA population with instruments such as the wideband integrated bioaerosol sensor [*Kaye et al.*, 2005], appears to be an intuitive next step in the definitive identification of microbe-containing SSA particles.

8.3.4 Semi-quantitative descriptions of SSA particle morphology

In Chapters 3, 4, and 5 of this dissertation, the spatial chemical heterogeneity of dry supermicron SSA particles was qualitatively illustrated by total positive ion intensity analyses of ATOFMS SSA datasets and also in experiments which directly varied the desorption/ionization laser pulse energy. Although, because of the nominally Gaussian profile of the desorption/ionization laser utilized, these analyses depended upon investigating trends in the ion signatures of the population of mass spectra collected. Single mass spectra of individual particles were relatively uninformative because of the likely wide variance in particle desorption at any given laser pulse energy because of inconsistent laser fluence within the beam profile. Recently, atomic force microscopy images were leveraged to calculate the organic volume fraction of individual particles SSA particles with core-shell morphologies [*Ryder et al.*, 2015]. While innovative, these offline measurements are extremely time-consuming compared to the high throughput, which can be achieved with online single particle analysis by SPMS. However, achieving a semi-quantitative description of the thickness of the organic-rich sodium-deficient shell on individual SSA particles via analysis by SPMS would likely require a more consistent degree of particle desorption than achieved in this dissertation. Mass spectral consistency between chemically uniform particles has been improved by utilizing lasers with relatively homogeneous beam profiles [*Wenzel and Prather*, 2004; *Steele et al.*, 2005]. A number of methods to generate relatively uniform fluences across the beam profile for the lasers currently installed in the ATOFMS systems are described in *Cahill*, [2014]. To generate mass spectra which could be utilized to estimate the organic-rich shell thickness of single particles, rather than simply providing general descriptions and trends in the SSA population, analysis with more homogenous laser beams would need to be informed by results from calibration studies of synthetic controlled core-shell model particles and supported by concurrent offline morphological analyses.

8.4 Acknowledgments

Gavin Cornwell is acknowledged for assisting in the editing of this chapter.

References

Adams, E. M., C. B. Casper, and H. C. Allen (2016), Effect of cation enrichment on dipalmitoylphosphatidylcholine (DPPC) monolayers at the air-water interface, *J. Colloid Interface Sci.*, *478*, 353–364, doi:10.1016/j.jcis.2016.06.016.

Agresti, A., and B. A. Coull (1998), Approximate is better than “exact” for interval estimation of binomial proportions, *Am. Stat.*, *52*, 119–126.

Aiken, A. C., A. DeCarlo, P. F., and J. L. Jimenez (2007), Elemental analysis of organic species with electron ionization high-resolution mass spectrometry, *Anal. Chem.*, *79*, 8350–8358.

Albert, M. F. M. A, M. Schaap, A. M. M. Manders, C. Scannell, C. D. O’Dowd, and G. de Leeuw (2012), Uncertainties in the determination of global sub-micron marine organic matter emissions, *Atmos. Environ.*, *57*, 289–300, doi:10.1016/j.atmosenv.2012.04.009.

Allen, J. O. (2005), *YAADA - Software Toolkit to Analyze Single-Particle Mass Spectral Data: Reference Manual Versions 1.3 and 2.0*, Tempe.

Aller, J. Y., M. R. Kuznetsova, C. J. Jahns, and P. F. Kemp (2005), The sea surface microlayer as a source of viral and bacterial enrichment in marine aerosols, *J. Aerosol Sci.*, *36*(5–6), 801–812, doi:10.1016/j.jaerosci.2004.10.012.

Alpert, P. A., J. Y. Aller, and D. A. Knopf (2011a), Ice nucleation from aqueous NaCl droplets with and without marine diatoms, *Atmos. Chem. Phys.*, *11*(12), 5539–5555, doi:10.5194/acp-11-5539-2011.

Alpert, P. A., J. Y. Aller, and D. A. Knopf (2011b), Initiation of the ice phase by marine biogenic surfaces in supersaturated gas and supercooled aqueous phases., *Phys. Chem. Chem. Phys.*, *13*, 19882–19894, doi:10.1039/c1cp21844a.

Amharref, N., A. Bejebbar, S. Dukie, L. Venteo, L. Schneider, M. Pluot, and M. Manfait (2007), Discriminating healthy from tumor and necrosis tissue in rat brain tissue samples by Raman spectral imaging, *Biopolymers*, *1768*, 2605–2615.

IPCC (2013), Cambridge, UK and New York, NY, USE.

Ault, A. P., C. R. Williams, A. B. White, P. J. Neiman, J. M. Creamean, C. J. Gaston, F. M. Ralph, and K. A. Prather (2011), Detection of Asian dust in California orographic precipitation, *J. Geophys. Res. Atmos.*, *116*(16), 1–15, doi:10.1029/2010JD015351.

Ault, A. P., T. L. Guasco, O. S. Ryder, J. Baltrusaitis, L. A. Cuadra-Rodriguez, D. B. Collins, M. J. Ruppel, T. H. Bertram, K. A. Prather, and V. H. Grassian (2013a), Inside versus outside: Ion redistribution in nitric acid reacted sea spray aerosol particles as determined by single particle analysis, *J. Am. Chem. Soc.*, *135*, 14528–14531, doi:10.1021/ja407117x.

Ault, A. P., D. Zhao, C. J. Ebben, M. J. Tauber, F. M. Geiger, K. A. Prather, and V. H. Grassian (2013b), Raman microspectroscopy and vibrational sum frequency generation spectroscopy as probes of the bulk and surface compositions of size-resolved sea spray aerosol particles, *Phys. Chem. Chem. Phys.*, *15*(207890), 6206–6214, doi:10.1039/c3cp43899f.

Ault, A. P., R. C. Moffet, J. Baltrusaitis, D. B. Collins, M. J. Ruppel, L. A. Cuadra-Rodriguez, D. Zhao, T. L. Guasco, C. J. Ebben, F. M. Geiger, T. H. Bertram, K. A. Prather, and V. H. Grassian (2013c), Size-dependent changes in sea spray aerosol composition and properties with different seawater conditions, *Environ. Sci. Technol.*, *47*, 5603–5612, doi:10.1021/es400416g.

Ault, A. P., T. L. Guasco, J. Baltrusaitis, O. S. Ryder, J. V. Trueblood, D. B. Collins, M. J. Ruppel, L. A. Cuadra-Rodriguez, K. A. Prather, and V. H. Grassian (2014), Heterogeneous reactivity of nitric acid with nascent sea spray aerosol: Large differences observed between and within individual particles, *J. Phys. Chem. Lett.*, *5*(15), 2493–2500, doi:10.1021/jz5008802.

Bassett, D. R., E. A. Boucher, and A. C. Zettlemoyer (1970), Adsorption studies on ice-nucleating substrates. Hydrophobed silicas and silver iodide, *J. Colloid Interface Sci.*, *34*(3), 436–446, doi:10.1016/0021-9797(70)90203-1.

Bates, T. S., P. K. Quinn, A. A. Frossard, L. M. Russell, J. Hakala, T. Petäjä, M. Kulmala, D. S. Covert, C. D. Cappa, S.-M. Li, K. L. Hayden, I. Nuaaman, R. McLaren, P. Massoli, M. R. Canagaratna, T. B. Onasch, D. Sueper, D. R. Worsnop, and W. C. Keene (2012), Measurements of ocean derived aerosol off the coast of California, *J. Geophys. Res. Atmos.*, *117*(D21), D00V15, doi:10.1029/2012JD017588.

Bhave, P. V., J. O. Allen, B. D. Morrical, D. P. Fergenson, G. R. Cass, and K. A. Prather (2002), A field-based approach for determining ATOFMS instrument sensitivities to ammonium and nitrate, *Environ. Sci. Technol.*, *36*(22), 4868–4879, doi:10.1021/es015823i.

Blanchard, D., and L. Syzdek (1974), Bubble tube: apparatus for determining rate of collection of bacteria by an air bubble rising in water, *Limnol. Oceanogr.*, *19*(1), 133–138, doi:10.4319/lo.1974.19.1.0133.

Blanchard, D., and L. Syzdek (1978), Seven problems in bubble and jet drop researches, *Limnol. Oceanogr.*, *23*(3), 389–400.

Blanchard, D. C. (1975), Bubble scavenging and the water-to-air transfer of organic material in the sea, in *Applied Chemistry at Protein Interfaces*, pp. 360–387, American Chemical Society, Washington, DC.

Blanchard, D. C. (1978), Jet drop enrichment of bacteria, virus, and dissolved organic material, *Pure Appl. Geophys.*, *116*, 302–308, doi:10.1007/BF01636887.

Blanchard, D. C. (1989), The ejection of drops from the sea and their enrichment with bacteria and other materials: a review, *Estuaries*, *12*(3), 127–137.

Blanchard, D. C., and L. D. Syzdek (1982), Water-to-air transfer and enrichment of bacteria in drops from bursting bubbles, *Appl. Environ. Microbiol.*, *43*(5), 1001–1005.

Blanchard, D. C., and A. H. Woodcock (1957), Bubble formation and modification in the sea and its meteorological significance, *Tellus IX*, *9*(2), 145–158, doi:10.3402/tellusa.v9i2.9094.

Bourguet, N., J.-P. Torréton, O. Galy, V. Arondel, and M. Goutx (2003), Application of a specific and sensitive radiometric assay for microbial lipase activities in marine water samples from the Lagoon of Nouméa, *Appl. Environ. Microbiol.*, *69*(12), 7395–7400, doi:10.1128/AEM.69.12.7395.

Brands, M., M. Kamphus, T. Böttger, J. Schneider, F. Drewnick, A. Roth, J. Curtius, C. Voigt, A. Borbon, M. Beekmann, A. Bourdon, T. Perrin, and S. Borrmann (2011), Characterization of a newly developed Aircraft-Based Laser Ablation Aerosol Mass Spectrometer (ALABAMA) and first field deployment in urban pollution plumes over paris during MEGAPOLI 2009, *Aerosol Sci. Technol.*, *45*(1), 46–64, doi:10.1080/02786826.2010.517813.

Breitbart, M. (2012), Marine viruses: truth or dare, *Ann. Rev. Mar. Sci.*, *4*(1), 425–448, doi:10.1146/annurev-marine-120709-142805.

Burrows, S. M., C. Hoose, U. Pöschl, and M. G. Lawrence (2013), Ice nuclei in marine air: biogenic particles or dust?, *Atmos. Chem. Phys.*, *13*(1), 245–267, doi:10.5194/acp-13-245-2013.

Burrows, S. M., O. Ogunro, A. A. Frossard, L. M. Russell, P. J. Rasch, and S. M. Elliott (2014), A physically-based framework for modelling the organic fractionation of sea spray aerosol from bubble film Langmuir equilibria, *Atmos. Chem. Phys.*, *14*, 13601–13629, doi:10.5194/acpd-14-5375-2014.

Burrows, S. M., E. Gobrogge, L. Fu, K. Link, S. M. Elliott, H. Wang, and R. Walker (2016), OCEANFILMS-2: Representing coadsorption of saccharides in marine films and potential impacts on modeled marine aerosol chemistry, *Geophys. Res. Lett.*, *43*, 8306–8313, doi:10.1002/2016GL069070.

Cahill, J. F. (2014), Novel techniques and applications in single particle mass spectrometry, University of California, San Diego.

Cahill, J. F., H. Fei, S. M. Cohen, and K. A. Prather (2015a), Characterization of core–shell MOF particles by depth profiling experiments using on-line single particle mass spectrometry, *Analyst*, *140*(5), 1510–1515, doi:10.1039/C4AN01913J.

Cahill, J. F., T. K. Darlington, C. Fitzgerald, N. G. Schoepp, J. Beld, M. D. Burkart, and K. A. Prather (2015b), Online analysis of single cyanobacteria and algae cells under nitrogen-limited conditions using aerosol time-of-flight mass spectrometry, *Anal. Chem.*, *87*(16), 8039–8046, doi:10.1021/acs.analchem.5b02326.

Cai, Y., A. Zelenyuk, and D. Imre (2006), A high resolution study of the effect of morphology on the mass spectra of single PSL particles with Na-containing layers and nodules, *Aerosol Sci. Technol.*, *40*(12), 1111–1122, doi:10.1080/02786820601001677.

Canagaratna, M. R., J. T. Jayne, J. L. Jimenez, J. D. Allan, M. R. Alfarra, Q. Zhang, T. B. Onasch, F. Drewnick, H. Coe, A. Middlebrook, A. Delia, L. R. Williams, A. M. Trimborn, M. J. Northway, P. F. DeCarlo, C. E. Kolb, P. Davidovits, and D. R. Worsnop. (2007), Chemical and microphysical characterization of ambient aerosols with the Aerodyne aerosol mass spectrometer, *Mass Spectrom. Rev.*, *26*, 185–222.

Carlson, R. W., S. Kalembasa, D. Turowski, P. Pachori, and K. D. Noel (1987), Characterization of the lipopolysaccharide from a Rhizobium Phaseoli mutant that is defective in infection thread development, *J. Bacteriol.*, *169*, 4923–4928.

Carranza, J. E., and D. W. Hahn (2002), Assessment of the upper particle size limit for quantitative analysis of aerosols using laser-induced breakdown spectroscopy, *Anal. Chem.*, *74*(21), 5450–5454, doi:10.1021/ac020261m.

Carslaw, K. S., L. A. Lee, C. L. Reddington, K. J. Pringle, A. Rap, P. M. Forster, G. W. Mann, D. V. Spracklen, M. T.Woodhouse, L. A. Regayre, and J. R. Pierce (2013), Large contribution of natural aerosols to uncertainty in indirect forcing., *Nature*, *503*, 67–71, doi:10.1038/nature12674.

Carson, P. G., K. R. Neubauer, M. V. Johnston, and A. S. Wexler (1995), On-line chemical analysis of aerosols by rapid single-particle mass spectrometry, *J. Aerosol Sci.*, *26*(2–4), 535–545, doi:10.1016/0168-1176(95)04312-8.

Carson, P. G., M. V Johnston, and A. S. Wexler (1997a), Laser desorption / ionization of ultrafine aerosol particles, *Rapid Commun. Mass Spectrom.*, *11*, 993–996.

Carson, P. G., M. V. Johnston, and A. S. Wexler (1997b), Real-time monitoring of the surface and total composition of aerosol particles, *Aerosol Sci. Technol.*, *26*(4), 291–300, doi:10.1080/02786829708965431.

Casillas-Ituarte, N. N., X. Chen, H. Castada, and H. C. Allen (2010), Na(+) and Ca(2+) effect on the hydration and orientation of the phosphate group of DPPC at air-water and air-hydrated silica interfaces., *J. Phys. Chem. B*, *114*(29), 9485–95, doi:10.1021/jp1022357.

Casper, C. B., D. Verreault, E. M. Adams, W. Hua, and H. C. Allen (2016), Surface potential of DPPC monolayers on concentrated aqueous salt solutions., *J. Phys. Chem. B*, *120*(8), 2043–2052, doi:10.1021/acs.jpcb.5b10483.

Celussi, M., and P. Del Negro (2012), Microbial degradation at a shallow coastal site: Long-term spectra and rates of exoenzymatic activities in the NE Adriatic Sea, *Estuar. Coast. Shelf Sci.*, *115*, 75–86, doi:10.1016/j.ecss.2012.02.002.

Chen, H., Z. Ouyang, and R. G. Cooks (2006), Thermal production and reactions of organic ions at atmospheric pressure, *Angew. Chemie - Int. Ed.*, *45*(22), 3656–3660, doi:10.1002/anie.200600660.

Chen, X., W. Hua, Z. Huang, and H. C. Allen (2010), Interfacial water structure associated with phospholipid membranes studied by phase-sensitive vibrational sum frequency generation spectroscopy., *J. Am. Chem. Soc.*, *132*(32), 11336–42, doi:10.1021/ja1048237.

Chi, J. W., W. J. Li, D. Z. Zhang, J. C. Zhang, Y. T. Lin, X. J. Shen, J. Y. Sun, J. M. Chen, X. Y. Zhang, Y. M. Zhang, and W. X. Wang (2015), Sea salt aerosols as a reactive surface for inorganic and organic acidic gases in the Arctic troposphere, *Atmos. Chem. Phys.*, *15*(19), 11341–11353, doi:10.5194/acp-15-11341-2015.

Claereboudt, J., M. Claeys, H. Geise, R. Gijbels, and A. Vertes (1993), Laser microprobe mass spectrometry of quaternary phosphonium salts: Direct versus matrix-assisted laser desorption, *J. Am. Soc. Mass Spectrom.*, *4*(10), 798–812, doi:10.1016/1044-0305(93)80038-Z.

Cochran, R. E., O. Laskina, T. Jayarathne, A. Laskin, J. Laskin, P. Lin, C. Sultana, C. Lee, K. A. Moore, C. D. Cappa, T. H. Bertram, K. A. Prather, V. H. Grassian, and E. A. Stone (2016a), Analysis of organic anionic surfactants in fine and coarse fractions of freshly emitted sea spray aerosol, *Environ. Sci. Technol.*, *50*, 2477–2486, doi:10.1021/acs.est.5b04053.

Cochran, R. E., T. Jayarathne, E. A. Stone, and V. H. Grassian (2016b), Selectivity across the interface: A test of surface activity in the composition of organic-enriched aerosols from bubble bursting., *J. Phys. Chem. Lett.*, *7*, 1692–1696, doi:10.1021/acs.jpclett.6b00489.

Cochran, R. E., O. Laskina, J. V. Trueblood, A. D. Estillore, H. S. Morris, T. Jayarathne, C. M. Sultana, C. Lee, P. Lin, J. Laskin, A. Laskin, J. A. Dowling, Z. Qin, C. D. Cappa, T. H. Bertram, A. V. Tivanski, E. A. Stone, K. A. Prather, and V. H. Grassian (2017), Molecular diversity between individual sea spray aerosol particles : Influence of ocean biology on particle composition and hygroscopicity, *Chem*, *In Press.*

Collins, D. B., A. P. Ault, R. C. Moffet, M. J. Ruppel, L. A. Cuadra-Rodriguez, T. L. Guasco, C. E. Corrigan, B. E. Pedler, F. Azam, L. I. Aluwihare, T. H. Bertram, G. C. Roberts, V. H. Grassian, and K. A. Prather (2013), Impact of marine biogeochemistry on the chemical mixing state and cloud forming ability of nascent sea spray aerosol, *J. Geophys. Res. Atmos.*, *118*, 1–13, doi:10.1002/jgrd.50598.

Collins, D. B., D. F. Zhao, M. J. Ruppel, O. Laskina, J. R. Grandquist, R. L. Modini, M. D. Stokes, L. M. Russell, T. H. Bertram, V. H. Grassian, G. B. Deane, and K. A. Prather (2014), Direct aerosol chemical composition measurements to evaluate the physicochemical differences between controlled sea spray aerosol generation schemes, *Atmos. Meas. Tech.*, *7*(11), 3667–3683, doi:10.5194/amt-7-3667-2014.

Compiano, A. M., J. C. Romano, F. Garabetian, P. Laborde, and I. Delagiraudiere (1993), Monosaccharide compostion of particulate hydrolyzable sugar fraction in surface microlayers from brackish and marine waters, *Mar. Chem.*, *42*, 237–251.

Cotter, R. J., and A. L. Yergey (1981), Thermal desorption of quaternary ammonium cations, *J. Am. Chem. Soc.*, *103*, 1596–1598, doi:10.1017/CBO9781107415324.004.

Creamean, J. M., K. J. Suski, D. Rosenfeld, A. Cazorla, P. J. DeMott, R. C. Sullivan, A. B. White, F. M. Ralph, P. Minnis, J. M. Comstock, J. M. Tomlinson, K. A. Prather (2013), Dust and biological aerosols from the Sahara and Asia influence precipitation in the Western U.S., *Science*, *339*(6127), 1572–1578, doi:10.1126/science.1227279.

Creamean, J. M., C. Lee, T. C. Hill, A. P. Ault, P. J. DeMott, A. B. White, F. M. Ralph, and K. A. Prather (2014), Chemical properties of insoluble precipitation residue particles, *J. Aerosol Sci.*, *76*, 13–27, doi:10.1016/j.jaerosci.2014.05.005.

Cunliffe, M., A. Engel, S. Frka, B. Gašparović, C. Guitart, J. C. Murrell, M. Salter, C. Stolle, R. Upstill-Goddard, and O. Wurl (2013), Sea surface microlayers: A unified physicochemical and biological perspective of the air–ocean interface, *Prog. Oceanogr.*, *109*, 104–116, doi:10.1016/j.pocean.2012.08.004.

Czerwieniec, G. A., S. C. Russell, H. J. Tobias, M. E. Pitesky, D. P. Fergenson, P. Steele, A. Srivastava, J. M. Horn, M. Frank, E. E. Gard, and C. B. Lebrilla (2005), Stable isotope labeling of entire Bacillus atrophaeus spores and vegetative cells using bioaerosol mass spectrometry, *Anal. Chem.*, *77*(4), 1081–1087, doi:10.1021/ac0488098.

Cziczo, D. J., and J. P. D. Abbatt (2000), Infrared observations of the response of NaCl, MgCl2, NH4HSO4, and NH4NO3 aerosols to changes in relative humidity from 298 to 238 K, *J. Phys. Chem. A*, *104*(10), 2038–2047, doi:10.1021/jp9931408.

Cziczo, D. J., J. B. Nowak, J. H. Hu, and J. P. D. Abbatt (1997), Infrared spectroscopy of model tropospheric aerosols as a function of relative humidity: Observation of deliquescence and crystallization, *J. Geophys. Res.*, *102*(D15), 18843, doi:10.1029/97JD01361.

Cziczo, D. J., K. D. Froyd, S. J. Gallavardin, O. Moehler, S. Benz, H. Saathoff, and D. M. Murphy (2009), Deactivation of ice nuclei due to atmospherically relevant surface coatings, *Environ. Res. Lett.*, *4*, 44013, doi:10.1088/1748-9326/4/4/044013.

Cziczo, D. J., K. D. Froyd, C. Hoose, E. J. Jensen, M. Diao, M. a Zondlo, J. B. Smith, C. H. Twohy, and D. M. Murphy (2013), Clarifying the dominant sources and mechanisms of cirrus cloud formation., *Science*, *340*, 1320–1324, doi:10.1126/science.1234145.

Dall'Osto, M., D. C. S. Beddows, R. P. Kinnersley, and R. M. Harrison (2004), Characterization of individual airborne particles by using aerosol time-of-flight mass spectrometry at Mace Head, Ireland, *J. Geophys. Res.*, *109*(D21), D21302, doi:10.1029/2004JD004747.

Dall'Osto, M., R. M. Harrison, D. C. S. Beddows, E. J. Freney, M. R. Heal, and R. J. Donovan (2006), Single-particle detection efficiencies of aerosol time-of-flight mass spectrometry during the North Atlantic marine boundary layer experiment., *Environ. Sci. Technol.*, *40*(16), 5029–35.

Dall'Osto, M., D. Ceburnis, C. Monahan, D. R. Worsnop, J. Bialek, M. Kulmala, T. Kurten, M. Ehn, J. Wenger, J. Sodeau, R. Healy, and C. O'Dowd (2012), Nitrogenated and aliphatic organic vapors as possible drivers for marine secondary organic aerosol growth, *J. Geophys.*

Res., *117*, doi:10.1029/2012JD017522.

Dallosto, M., and R. Harrison (2006), Chemical characterisation of single airborne particles in Athens (Greece) by ATOFMS, *Atmos. Environ.*, *40*(39), 7614–7631, doi:10.1016/j.atmosenv.2006.06.053.

Danovaro, R., M. Armeni, G. M. Luna, C. Corinaldesi, A. Dell'Anno, C. R. Ferrari, C. Fiordelmondo, C. Gambi, M. Gismondi, E. Manini, M. Mecozzi, F. M. Perrone, A. Pusceddu, and M. Giani (2005), Exo-enzymatic activities and dissolved organic pools in relation with mucilage development in the Northern Adriatic Sea, *Sci. Total Environ.*, *353*, 189–203.

DeCarlo, P. F., J. G. Slowik, D. R. Worsnop, P. Davidovits, and J. L. Jimenez (2004), Particle morphology and density characterization by combined mobility and aerodynamic diameter measurements. Part 2: Application to combustion-generated soot aerosols as a function of fuel equivalence ratio, *Aerosol Sci. Technol.*, *38*, 1206-121185–120522, doi:10.1080/02786826.2004.10399462.

DeCarlo, P. F., J. R. Kimmel, A. Trimborn, M. J. Northway, J. T. Jayne, A. C. Aiken, M. Gonin, K. Fuhrer, T. Horvath, K. S. Docherty, D. R. Worsnop, and J. L. Jimenez (2006), Field-deployable, high-resolution, time-of-flight aerosol mass spectrometer, *Anal. Chem.*, *78*, 8281–8289.

DeMott, P. J., D. J. Cziczo, A. J. Prenni, D. M. Murphy, S. M. Kreidenweis, D. S. Thomson, R. Borys, and D. C. Rogers (2003), Measurements of the concentration and composition of nuclei for cirrus formation., *Proc. Natl. Acad. Sci. U. S. A.*, *100*(25), 14655–60, doi:10.1073/pnas.2532677100.

DeMott, P. J., A. J. Prenni, X. Liu, S. M. Kreidenweis, M. D. Petters, C. H. Twohy, M. S. Richardson, T. Eidhammer, and D. C. Rogers (2010), Predicting global atmospheric ice nuclei distributions and their impacts on climate., *Proc. Natl. Acad. Sci. U. S. A.*, *107*(25), 11217–22, doi:10.1073/pnas.0910818107.

DeMott, P. J., T. C. J. Hill, C. S. McCluskey, K. A. Prather, D. B. Collins, R. C. Sullivan, M. J. Ruppel, R. H. Mason, V. E. Irish, T. Lee, C. Y. Hwang, T. S. Rhee, J. R. Snider, G. R. McMeeking, S. Dhaniyala, E. R. Lewis, J. J. B. Wentzell, J. Abbatt, C. Lee, C. M. Sultana, A. P. Ault, J. L. Axson, M. D. Martinez, I. Venero, G. Santos-Figueroa, M. D. Stokes, G. B. Deane, O. L. Mayol-Bracero, V. H. Grassian, T. H. Bertram, A. K. Bertram, B. F. Moffett, and G. D. Franc (2015), Sea spray aerosol as a unique source of ice nucleating particles, *Proc. Natl. Acad. Sci.*, *113*(21), 5797–5803, doi:10.1073/pnas.1514034112.

Deng, C., S. D. Brooks, G. Vidaurre, and D. C. O. Thornton (2014), Using Raman microspectroscopy to determine chemical composition and mixing state of airborne marine aerosols over the Pacific Ocean, *Aerosol Sci. Technol.*, *48*(2), 193–206, doi:10.1080/02786826.2013.867297.

Dueker, M. E., K. C. Weathers, G. D. O'Mullan, A. R. Juhl, and M. Uriarte (2011), Environmental controls on coastal coarse aerosols: Implications for microbial content and deposition in the near-shore environment, *Environ. Sci. Technol.*, *45*, 3386–3392, doi:10.1021/es1035128.

Duflos, M., M. Goutx, and F. Van Wambeke (2009), Determination of lipid degradation by marine lipase-producing bacteria: Critical evaluation of lipase activity assays, *Lipids*, *44*(12), 1113–1124, doi:10.1007/s11745-009-3358-7.

Erdmann, N., A. Dell'Acqua, P. Cavalli, C. Grüning, N. Omenetto, J.-P. Putaud, F. Raes, and R. Van Dingenen (2005), Instrument characterization and first application of the Single Particle Analysis and Sizing System (SPASS) for atmospheric aerosols, *Aerosol Sci. Technol.*, *39*(5), 377–393, doi:10.1080/027868290935696.

Fall, R., and R. C. Schnell (1985), Association of an ice-nucleating psuedomonad with cultures of the marine dinoflagellate, heterocapsa-niei, *J. Mar. Res.*, *43*(1), 257–265.

Fan, T., and O. B. Toon (2011), Modeling sea-salt aerosol in a coupled climate and sectional microphysical model: Mass, optical depth and number concentration, *Atmos. Chem. Phys.*, *11*(9), 4587–4610, doi:10.5194/acp-11-4587-2011.

Fergenson, D. P., M. E. Pitesky, H. J. Tobias, P. T. Steele, G. A. Czerwieniec, S. C. Russell, C. B. Lebrilla, J. M. Horn, K. R. Coffee, A. Srivastava, S. P. Pillai, M. P. Shih, H. L. Hall, A. J. Ramponi, J. T. Chang, R. Langlois, P. L. Estacio, R. T. Hadley, M. Frank, and E. E. Gard (2004), Reagentless detection and classification of individual bioaerosol particles in seconds., *Anal. Chem.*, *76*(2), 373–378, doi:10.1021/ac034467e.

Forestieri, S. D., G. C. Cornwell, T. M. Helgestad, K. A. Moore, C. Lee, G. A. Novak, C. M. Sultana, X. Wang, T. H. Bertram, K. A. Prather, and C. D. Cappa (2016), Linking variations in sea spray aerosol particle hygroscopicity to composition during two microcosm experiments, *Atmos. Chem. Phys.*, *16*, 9003–9018, doi:10.5194/acp-16-9003-2016.

Forestieri, S. D., T. M. Kuborn, S. M. Staudt, R. E. Cochran, T. H. Bertram, and C. D. Cappa, Establishing the impact of model surfactants on cloud condensation nuclei activity of sea spray aerosols, *In Prep*.

Frossard, A. A., L. M. Russell, S. M. Burrows, S. M. Elliott, T. S. Bates, and P. K. Quinn (2014), Sources and composition of submicron organic mass in marine aerosol particles, *J. Geophys. Res. Atmos.*, *119*, 12,977–13,003, doi:10.1002/2014JD021913.

Fuentes, E., H. Coe, D. Green, G. de Leeuw, G. McFiggans, G. De Leeuw, and G. McFiggans (2010a), Laboratory-generated primary marine aerosol via bubble-bursting and atomization, *Atmos. Meas. Tech.*, *3*, 141–162, doi:10.5194/amt-3-141-2010.

Fuentes, E., H. Coe, D. Green, G. de Leeuw, and G. McFiggans (2010b), On the impacts of phytoplankton-derived organic matter on the properties of the primary marine aerosol – Part 1: Source fluxes, *Atmos. Chem. Phys.*, *10*(19), 9295–9317, doi:10.5194/acp-10-9295-2010.

Fuentes, E., H. Coe, D. Green, and G. McFiggans (2011), On the impacts of phytoplankton-derived organic matter on the properties of the primary marine aerosol – Part 2: Composition, hygroscopicity and cloud condensation activity, *Atmos. Chem. Phys.*, *11*(6), 2585–2602, doi:10.5194/acp-11-2585-2011.

Gantt, B., and N. Meskhidze (2013), The physical and chemical characteristics of marine primary organic aerosol: a review, *Atmos. Chem. Phys.*, *13*(8), 3979–3996, doi:10.5194/acp-13-3979-2013.

Gantt, B., N. Meskhidze, M. C. Facchini, M. Rinaldi, D. Ceburnis, and C. D. O'Dowd (2011), Wind speed dependent size-resolved parameterization for the organic mass fraction of sea spray aerosol, *Atmos. Chem. Phys.*, *11*(16), 8777–8790, doi:10.5194/acp-11-8777-2011.

Gantt, B., M. S. Johnson, N. Meskhidze, J. Sciare, J. Ovadnevaite, D. Ceburnis, and C. D. O'Dowd (2012), Model evaluation of marine primary organic aerosol emission schemes, *Atmos. Chem. Phys.*, *12*(18), 8553–8566, doi:10.5194/acp-12-8553-2012.

Gao, Q., C. Leck, C. Rauschenberg, and P. A. Matrai (2012), On the chemical dynamics of extracellular polysaccharides in the high Arctic surface microlayer, *Ocean Sci.*, *8*(4), 401–418, doi:10.5194/os-8-401-2012.

Gard, E., J. E. Mayer, B. D. Morrical, T. Dienes, D. P. Fergenson, and K. A. Prather (1997), Real-time analysis of individual atmospheric aerosol particles: Design and performance of a portable ATOFMS, *Anal. Chem.*, *69*(20), 4083–4091, doi:10.1021/ac970540n.

Garrett, W. D. (1967), Stabilization of air bubbles at the air-sea interface by surface-active material, *Deep Sea Res. Oceanogr. Abstr.*, *14*(6), 661–672, doi:10.1016/S0011-7471(67)80004-4.

Gašparovic, B., Z. Kozarac, A. Saliot, B. Ćosović, and D. Möbius (1998), Physicochemical characterization of natural and ex-situ reconstructed sea-surface microlayers., *J. Colloid Interface Sci.*, *208*, 191–202, doi:10.1006/jcis.1998.5792.

Gaston, C. J. (2012), Direct measurements of marine aerosols to examine the influence of biological activity, anthropogenic emissions, and secondary processing on particle chemistry, University of California, San Diego.

Gaston, C. J., H. Furutani, S. A. Guazzotti, K. R. Coffee, T. S. Bates, P. K. Quinn, L. I. Aluwihare, B. G. Mitchell, and K. A. Prather (2011), Unique ocean-derived particles serve as a proxy for changes in ocean chemistry, *J. Geophys. Res.*, *116*(D18), D18310, doi:10.1029/2010JD015289.

Gavish, M., R. Popovitz-biro, M. Lahav, and L. Leiserowitz (1990), Ice nucleation by alcohols arranged in monolayers at the surface of water drops, *Science*, *250*(4983), 973–975.

Ge, Z., A. S. Wexler, and M. V Johnston (1998a), Deliquescence behavior of multicomponent aerosols, *J. Phys. Chem. A*, *5639*(97), 173–180.

Ge, Z., A. S. Wexler, and M. V. Johnston (1998b), Laser desorption/ionization of single ultrafine multicomponent aerosols, *Environ. Sci. Technol.*, *32*(20), 3218–3223, doi:10.1021/es980104y.

Ge, Z. Z., A. S. Wexler, and M. V. Johnston (1996), Multicomponent aerosol crystallization, *J. Colloid Interface Sci.*, *183*(1), 68–77, doi:10.1006/jcis.1996.0519.

De Gelder, J., K. De Gussem, P. Vandenabeele, and L. Moens (2007), Reference database of Raman spectra of biological molecules, *J. Raman. Spectrosc.*, *38*, 1133–1147.

Giorio, C., A. Tapparo, M. Dall'Osto, R. M. Harrison, D. C. S. Beddows, C. Di Marco, and E. Nemitz (2012), Comparison of three techniques for analysis of data from an Aerosol Time-of-Flight Mass Spectrometer, *Atmos. Environ.*, *61*, 316–326, doi:10.1016/j.atmosenv.2012.07.054.

Gomes, H., P. Rosina, P. Holakooei, T. Solomon, and C. Vaccaro (2013), Identification of pigments used in rock art paintings in Gode Roriso-Ethiopia using Micro-Raman spectroscopy, *J. Archaeol. Sci.*, *40*, 4073–4082.

Goutx, M., C. Guigue, D. Aritio, J. F. Ghiglione, M. Pujo-Pay, V. Raybaud, M. Duflos, and L. Prieur (2009), Short term summer to autumn variability of dissolved lipid classes in the Ligurian Sea (NW Mediterranean), *Biogeosciences*, *6*, 1229–1246, doi:10.1029/2002GB001947.

Gouw, J. De, and C. Warneke (2007), Measurements of volatile organic compounds in the Earth's atmosphere use proton-transfer-reaction mass spectrometry, *Mass Spectrom. Rev.*, *26*, 223–257, doi:10.1002/mas.

Gross, D. S., M. E. Gälli, P. J. Silva, and K. A. Prather (2000), Relative sensitivity factors for alkali metal and ammonium cations in single-particle aerosol time-of-flight mass spectra., *Anal. Chem.*, *72*(2), 416–22.

Gross, D. S., R. Atlas, J. Rzeszotarski, E. Turetsky, J. Christensen, S. Benzaid, J. Olson, T. Smith, L. Steinberg, J. Sulman, A. Ritz, B. Anderson, C. Nelson, D. R. Musicant, L. Chen, D. C. Snyder, and J. J. Schauer (2010), Environmental chemistry through intelligent atmospheric data analysis, *Environ. Model. Softw.*, *25*(6), 760–769, doi:10.1016/j.envsoft.2009.12.001.

Grythe, H., J. Ström, R. Krejci, P. Quinn, and A. Stohl (2014), A review of sea-spray aerosol source functions using a large global set of sea salt aerosol concentration measurements, *Atmos. Chem. Phys.*, *14*(3), 1277–1297, doi:10.5194/acp-14-1277-2014.

Guasco, T. L., L. A. Cuadra-Rodriguez, B. E. Pedler, A. P. Ault, D. B. Collins, D. Zhao, M. J. Kim, M. J. Ruppel, S. C. Wilson, R. S. Pomeroy, V. H. Grassian, F. Azam, T. H. Bertram, and K. A. Prather (2014), Transition metal associations with primary biological particles in sea spray aerosol generated in a wave channel, *Environ. Sci. Technol.*, *48*, 1324–1333, doi:10.1021/es403203d.

Gupta, D., H. J. Eom, H. R. Cho, and C. U. Ro (2015), Hygroscopic behavior of NaCl-MgCl2 mixture particles as nascent sea-spray aerosol surrogates and observation of efflorescence during humidification, *Atmos. Chem. Phys.*, *15*(19), 11273–11290, doi:10.5194/acp-15-11273-2015.

Gupta, R., N. Gupta, and P. Rathi (2004), Bacterial lipases: An overview of production, purification and biochemical properties, *Appl. Microbiol. Biotechnol.*, *64*, 763–781, doi:10.1007/s00253-004-1568-8.

Hämeri, K., A. Laaksonen, M. Väkevä, and T. Suni (2001), Hygroscopic growth of ultrafine sodium chloride particles, *J. Geophys. Res. Atmos.*, *106*, 20749–20757.

Hardie, L. A., and H. P. Eugster (1980), Evaporation of seawater: calculated mineral sequences, *Science*, *208*, 498–500, doi:10.1126/science.208.4443.498.

Harmon, C. W., R. L. Grimm, T. M. McIntire, M. D. Peterson, B. Njegic, V. M. Angel, A. Alshawa, J. S. Underwood, D. J. Tobias, R. B. Gerber, M. S. Gordon, J. C. Hemminger, and S. A. Nizkorodov (2010), Hygroscopic growth and deliquescence of NaCl nanoparticles mixed with surfactant SDS., *J. Phys. Chem. B*, *114*(7), 2435–49, doi:10.1021/jp909661q.

Harwood, J. L., and I. A. Guschina (2009), The versatility of algae and their lipid metabolism, *Biochimie*, *91*(6), 679–684, doi:10.1016/j.biochi.2008.11.004.

Hawkins, L. N., and L. M. Russell (2010), Polysaccharides , proteins , and phytoplankton fragments : four chemically distinct types of marine primary organic aerosol classified by single particle spectromicroscopy, *Adv. Meteorol.*, *2010*, 612132, doi:10.1155/2010/612132.

Haywood, J., and O. Boucher (2000), Estimates of the direct and indirect radiative forcing due to tropospheric aerosols: A review, *Rev. Geophys.*, *38*(4), 513–543.

Healy, R. M., S. Hellebust, I. Kourtchev, A. Allanic, I. P. O'Connor, J. M. Bell, D. A. Healy, J. R. Sodeau, and J. C. Wenger (2010), Source apportionment of PM2.5 in Cork Harbour, Ireland using a combination of single particle mass spectrometry and quantitative semi-continuous measurements, *Atmos. Chem. Phys.*, *10*(19), 9593–9613, doi:10.5194/acp-10-9593-2010.

Heinen, H. J. (1981), On ion formation with LAMMA in laser desorption mass spectrometry, *Int. J. Mass Spectrom. Ion Phys.*, *38*, 309–322.

Hill, I. R., and I. W. Levin (1979), Vibrational spectra and carbon hydrogen stretching mode assignments for a series of normal alkyl carboxylic acids, *J. Chem. Phys.*, (70), 842–851.

Hill, T. C. J., B. F. Moffett, P. J. DeMott, D. G. Georgakopoulos, W. L. Stump, and G. D. Franc (2014), Measurement of ice nucleation-active bacteria on plants and in precipitation by quantitative PCR, *Appl. Environ. Microbiol.*, *80*(4), 1256–1267, doi:10.1128/AEM.02967-13.

Hinz, K., and B. Spengler (2007), Instrumentation, data evaluation and quantification in on-line aerosol mass spectrometry, *J. Mass Spectrom.*, *42*, 843–860, doi:10.1002/jms.1262.

Hinz, K., R. Kaufmann, and B. Spengler (1994), Laser-induced mass analysis of single particles in the airborne state, *Anal. Chem.*, *66*(13), 2071–2076.

Hinz, K. P., N. Erdmann, C. Grüning, and B. Spengler (2006), Comparative parallel characterization of particle populations with two mass spectrometric systems LAMPAS 2 and SPASS, *Int. J. Mass Spectrom.*, *258*(1–3), 151–166, doi:10.1016/j.ijms.2006.09.008.

Hinz, K. P., E. Gelhausen, K. C. Schäfer, Z. Takats, and B. Spengler (2011), Characterization of surgical aerosols by the compact single-particle mass spectrometer LAMPAS 3, *Anal. Bioanal. Chem.*, *401*(10), 3165–3172, doi:10.1007/s00216-011-5465-6.

Hoffman, E. J., and R. A. Duce (1974), The organic carbon content of marine aerosols collected on Bermuda, *J. Geophys. Res.*, *79*(30), 4474–4477.

Holecek, J. C., M. T. Spencer, and K. A. Prather (2007), Analysis of rainwater samples: Comparison of single particle residues with ambient particle chemistry from the northeast Pacific and Indian oceans, *J. Geophys. Res. Atmos.*, *112*(22), doi:10.1029/2006JD008269.

Hoppe, H. (1983), Significance of exoenzymatic activities in the ecology of brackish water: measurements by means of methylumbelliferyl-substrates, *Mar. Ecol. - Prog. Ser.*, *11*, 299–308, doi:10.3354/meps011299.

Hua, W., D. Verreault, and H. C. Allen (2015), Solvation of calcium-phosphate headgroup complexes at the DPPC/aqueous interface, *ChemPhysChem*, *16*(18), 3910–3915, doi:10.1002/cphc.201500720.

Hultin, K. A. H., R. Krejci, J. Pinhassi, L. Gomez-Consarnau, E. M. Mårtensson, Å. Hagström, and E. D. Nilsson (2011), Aerosol and bacterial emissions from Baltic Seawater, *Atmos. Res.*, *99*(1), 1–14, doi:10.1016/j.atmosres.2010.08.018.

Jaeglé, L., P. K. Quinn, T. S. Bates, B. Alexander, and J. T. Lin (2011), Global distribution of sea salt aerosols: New constraints from in situ and remote sensing observations, *Atmos. Chem. Phys.*, *11*(7), 3137–3157, doi:10.5194/acp-11-3137-2011.

Jayarathne, T., C. E. Stockwell, R. J. Yokelson, S. Nakao, and E. A. Stone (2014), Emissions of fine particle fluoride from biomass burning, *Environ. Sci. Technol.*, *48*, 12636–12644, doi:10.1021/es502933j.

Jayarathne, T., C. M. Sultana, C. Lee, F. Malfatti, J. L. Cox, M. A. Pendergraft, K. A. Moore, F. Azam, A. V. Tivanski, C. D. Cappa, T. H. Bertram, V. H. Grassian, K. A. Prather, and E. A. Stone (2016), Enrichment of saccharides and divalent cations in sea spray aerosol during two phytoplankton blooms, *Environ. Sci. Technol.*, *50*(21), 11511–11520, doi:10.1021/acs.est.6b02988.

Jayne, J. T., D. C. Leard, X. F. Zhang, P. Davidovits, K. A. Smith, C. E. Kolb, and D. R. Worsnop (2000), Development of an aerosol mass spectrometer for size and composition analysis of submicron particles, *Aerosol Sci. Technol.*, *33*, 49–70.

Junge, K., and B. D. Swanson (2007), High-resolution ice nucleation spectra of sea-ice bacteria: implications for cloud formation and life in frozen environments, *Biogeosciences Discuss.*, *4*(NOVEMBER), 4261–4282, doi:10.5194/bgd-4-4261-2007.

Kamnev, A. A., P. A. Tarantilis, L. P. Antonyuk, L. A. Bespalova, M. G. Polissiou, M. Colina, P. H. E. Gardiner, and V. V. Ignatov (2001), Fourier transform Raman spectroscopic characterisation of cells of the plant-associated soil bacterium Azospirillum brasilense, *J. Mol. Struct.*, *563*, 199–207.

Kane, D. B., J. Wang, K. Frost, and M. V. Johnston (2002), Detection of negative ions from individual ultrafine particles, *Anal. Chem.*, *74*(9), 2092–2096, doi:10.1021/ac011126x.

Kaneda, T. (1991), Iso- and anteiso-fatty acids in bacteria: biosynthesis, function, and taxonomic significance., *Microbiol. Rev.*, *55*(2), 288–302.

Kaye, P. H., W. R. Stanley, and E. Hirst (2005), Single particle multichannel bio-aerosol fluorescence sensor, *Opt. Express*, *13*(10), 3583–3593.

Keene, W. C., H. Maring, J. R. Maben, D. J. Kieber, A. A. P. Pszenny, E. E. Dahl, M. A. Izaguirre, A. J. Davis, M. S. Long, X. Zhou, L. Smoydzin, and R. Sander (2007), Chemical and physical characteristics of nascent aerosols produced by bursting bubbles at a model air-sea interface, *J. Geophys. Res.*, *112*, D21202, doi:10.1029/2007JD008464.

Kelsall, G. H., S. Tang, A. L. Smith, and S. Yurdakulz (1996), Measurement of rise and electrophoretic velocities of gas bubbles, *J. Chem. Soc., Faraday Trans.*, *92*(5), 3879–3885.

Kleefeld, C., C. D. O'Dowd, S. O'Reilly, S. G. Jennings, P. Aalto, E. Becker, G. Kunz, and G. De Leeuw (2002), Relative contribution of submicron and supermicron particles to aerosol light scattering in the marine boundary layer, *J. Geophys. Res. Atmos.*, *107*(19), 1–13, doi:10.1029/2000JD000262.

Klimach, T. (2012), Chemische Zusammensetzung der Aerosole- Design und Datenauswertung eines Einzelpartikel- Laserablationsmassenspektrometers, University of Mainz.

Knopf, D. A., P. A. Alpert, B. Wang, and J. Y. Aller (2011), Stimulation of ice nucleation by marine diatoms, *Nat. Geosci.*, *4*, 88–90, doi:10.1038/ngeo1037.

Kujawinski, E. B., J. W. Farrington, and J. W. Moffett (2002), Evidence for grazing-mediated production of dissolved surface-active material by marine protists, *Mar. Chem.*, *77*(2–3), 133–142, doi:10.1016/S0304-4203(01)00082-2.

Lake, D. A., M. P. Tolocka, M. V. Johnston, and A. S. Wexler (2003), Mass spectrometry of individual particles between 50 and 750 nm in diameter at the Baltimore supersite, *Environ. Sci. Technol.*, *37*(15), 3268–3274, doi:10.1021/es026270u.

Langmann, B., C. Scannell, and C. O'Dowd (2008), New Directions: Organic matter contribution to marine aerosols and cloud condensation nuclei, *Atmos. Environ.*, *42*(33), 7821–7822, doi:10.1016/j.atmosenv.2008.09.002.

Laskin, A., R. C. Moffet, M. K. Gilles, J. D. Fast, R. A. Zaveri, B. Wang, P. Nigge, and J. Shutthanandan (2012), Tropospheric chemistry of internally mixed sea salt and organic particles: Surprising reactivity of NaCl with weak organic acids, *J. Geophys. Res. Atmos.*, *117*(15), 1–12, doi:10.1029/2012JD017743.

Laskina, O., H. S. Morris, J. R. Grandquist, A. D. Estillore, E. A. Stone, V. H. Grassian, and A. V. Tivanski (2015), Substrate-deposited sea spray aerosol particles: Influence of analytical method, substrate, and storage conditions on particle size, phase, and morphology, *Environ. Sci. Technol.*, *49*, 13447–13453, doi:10.1021/acs.est.5b02732.

Laucks, M. L., A. Sengupta, K. Junge, E. J. Davis, and B. D. Swanson (2005), Comparison of psychro-active arctic marine bacteria and common mesophillic bacteria using surface-enhanced Raman spectroscopy, *Appl. Spectrosc.*, *59*, 1222–1228.

Leck, C., and E. K. Bigg (2005a), Biogenic particles in the surface microlayer and overlaying atmosphere in the central Arctic Ocean during summer, *Tellus*, *57B*(4), 305–316.

Leck, C., and E. K. Bigg (2005b), Source and evolution of the marine aerosol—A new perspective, *Geophys. Res. Lett.*, *32*(19), L19803, doi:10.1029/2005GL023651.

Leck, C., and E. K. Bigg (2008), Comparison of sources and nature of the tropical aerosol with the summer high Arctic aerosol, *Tellus*, *60B*(1), 118–126, doi:10.1111/j.1600-0889.2007.00315.x.

Lee, C., C. M. Sultana, D. B. Collins, M. V. Santander, J. L. Axson, F. Malfatti, G. C. Cornwell, J. R. Grandquist, G. B. Deane, M. D. Stokes, F. Azam, V. H. Grassian, and K. A. Prather (2015), Advancing model systems for fundamental laboratory studies of sea spray aerosol using the microbial loop, *J. Phys. Chem. A*, *119*, 8860–8870, doi:10.1021/acs.jpca.5b03488.

Lee, H. D., A. D. Estillore, H. S. Morris, K. K. Ray, A. Alejandro, V. H. Grassian, and A. V. Tivanski (2017), Direct surface tension measurements of individual submicrometer particles using Atomic Force Microscopy, *J. Phys. Chem. A*.

de Leeuw, G., E. L. Andreas, M. D. Anguelova, C. W. Fairall, E. R. Lewis, C. O. Dowd, M. Schulz, and S. E. Schwartz (2011), Production flux of sea spray aerosol, *Rev. Geophys.*, *49*(RG2001), doi:10.1029/2010RG000349.1.INTRODUCTION.

Lewis, E. R., and S. E. Schwartz (2004a), Measurements and models of quantities required to evaluate sea salt aerosol production fluxes, in *Sea Salt Aerosol Production: Mechanisms, Methods, Measurements and Models*, pp. 119–297, American Geophysical Union, Washington, DC.

Lewis, E. R., and S. E. Schwartz (2004b), Methods of determining size-dependent sea salt aerosol, in *Sea Salt Aerosol Production: Mechanisms, Methods, Measurements and Models*, pp. 101–118.

Lewis, E. R., and S. E. Schwartz (2004c), *Sea Salt Aerosol Production: Mechanisms, Methods, Measurements and Models-A Critical Review*, American Geophysical Union, Washington, DC.

Li, W., L. Shao, D. Zhang, C. Ro, M. Hu, X. Bi, H. Geng, A. Matsuki, H. Niu, and J. Chen (2016), A review of single aerosol particle studies in the atmosphere of East Asia : morphology , mixing state , source , and heterogeneous reactions, *J. Clean. Prod.*, *112*, 1330–1349, doi:10.1016/j.jclepro.2015.04.050.

Lin, V. J. C., and J. L. Koenig (1976), Raman studies of bovine serum albumin, *Biopolymers*, *15*, 203–218.

Liu, P. S. K., R. Deng, K. A. Smith, L. R. Williams, J. T. Jayne, M. R. Canagaratna, K. Moore, T. B. Onasch, D. R. Worsnop, and T. Deshler (2007), Transmission efficiency of an aerodynamic focusing lens system: Comparison of model calculations and laboratory measurements for the Aerodyne Aerosol Mass Spectrometer, *Aerosol Sci. Technol.*, *41*, 721–733.

Liu, Y., Z. Yang, Y. Desyaterik, P. L. Gassman, H. Wang, and A. Laskin (2008), Hygroscopic behavior of substrate-deposited particles studied by micro-FT-IR spectroscopy and complementary methods of particle analysis, *Anal. Chem.*, *80*(3), 633–642, doi:10.1021/ac701638r.

Lohmann, U., and H. Feichter (2005), Global indirect aerosol effects: a review, *Atmos. Chem. Phys.*, *5*, 715–737.

Maki, L. R., E. L. Galyan, M. M. Chang-Chien, and D. R. Caldwell (1974), Ice nucleation induced by pseudomonas syringae., *Appl. Microbiol.*, *28*(3), 456–459, doi:10.1111/1462-2920.12668.

Martin, A. C., G. C. Cornwell, S. A. Atwood, K. A. Moore, N. E. Rothfuss, H. Taylor, P. J. DeMott, S. M. Kreidenweis, M. D. Petters, and K. A. Prather (2017), Transport of pollution to a remote coastal site during gap flow from California's interior: impacts on aerosol composition, clouds, and radiative balance, *Atmos. Chem. Phys.*, *17*(2), 1491–1509, doi:10.5194/acp-17-1491-2017.

Martinez, J., D. C. Smith, G. F. Steward, and F. Azam (1996), Variability in ectohydrolytic enzyme activities of pelagic marine bacteria and its significance for substrate processing in the sea, *Aquat. Microb. Ecol.*, *10*, 223–230, doi:10.3354/ame010223.

Marty, J. C., V. Zutic, R. Precali, A. Saliot, B. Cosovic, N. Smodlaka, and G. Cauwet (1988), Organic matter characterization in the northern Adriatic Sea with special reference to the sea surface microlayer, *Mar. Chem.*, *25*, 243–263.

Maskey, S., H. Geng, Y. C. Song, H. Hwang, Y. J. Yoon, K. H. Ahn, and C. U. Ro (2011), Single-particle characterization of summertime antarctic aerosols collected at King George island using quantitative energy-dispersive electron probe X-ray microanalysis and attenuated total reflection Fourier transform-infrared imaging techniques, *Environ. Sci. Technol.*, *45*(15), 6275–6282, doi:10.1021/es200936m.

McClain, C. R. (2009), A decade of satellite ocean color observations, *Ann. Rev. Mar. Sci.*, *1*, 19–42, doi:10.1146/annurev.marine.010908.163650.

McCluskey, C. S., T. C. J. Hill, F. Malfatti, C. M. Sultana, C. Lee, M. V. Santander, C. M. Beall, K. A. Moore, G. C. Cornwell, D. B. Collins, K. A. Prather, T. Jayarathne, E. A. Stone, F. Azam, S. M. Kreidenweis, and P. J. DeMott (2017a), A dynamic link between ice nucleating particles released in nascent sea spray aerosol and oceanic biological activity during two mesocosm experiments, *J. Atmos. Sci.*, *74*, 151–165, doi:10.1175/JAS-D-16-0087.1.

McCluskey, C. S., T. C. J. Hill, O. Laskina, J. Trueblood, V. H. Grassian, M. V. Santander, C. M. Beall, C. M. Sultana, K. A. Prather, and P. J. DeMott (2017b), A mesocosm double feature: revealing the identity of marine ice nucleating particles, *Submitted to Journal of the Atmospheric Sciences*.

McCoy, D. T., S. M. Burrows, R. Wood, D. P. Grosvenor, S. M. Elliott, P.-L. Ma, P. J. Rasch, and D. L. Hartmann (2015), Natural aerosols explain seasonal and spatial patterns of Southern Ocean cloud albedo., *Sci. Adv.*, *1*(6), e1500157, doi:10.1126/sciadv.1500157.

Mcjimpsey, E. L., P. T. Steele, K. R. Coffee, D. P. Fergenson, V. J. Riot, B. W. Woods, E. E. Gard, M. Frank, H. J. Tobias, and C. Lebrilla (2006), Detection of biological particles in ambient air using Bio-Aerosol Mass Spectrometry, *Proc. SPIE*, *6218*, 62108B–1, doi:10.1117/12.666459.

McJimpsey, E. L., W. M. Jackson, C. B. Lebrilla, H. Tobias, M. J. Bogan, E. E. Gard, M. Frank, and P. T. Steele (2008), Parameters contributing to efficient ion generation in aerosol MALDI mass spectrometry, *J. Am. Soc. Mass Spectrom.*, *19*(3), 315–324, doi:10.1016/j.jasms.2007.11.009.

Meskhidze, N., J. Xu, B. Gantt, Y. Zhang, A. Nenes, S. J. Ghan, X. Liu, R. Easter, and R. Zaveri (2011), Global distribution and climate forcing of marine organic aerosol: 1. Model improvements and evaluation, *Atmos. Chem. Phys.*, *11*(22), 11689–11705, doi:10.5194/acp-11-11689-2011.

Modini, R. L., L. M. Russell, G. B. Deane, and M. D. Stokes (2013), Effect of soluble surfactant on bubble persistence and bubble-produced aerosol particles, *J. Geophys. Res. Atmos.*, *118*, 1388–1400, doi:10.1002/jgrd.50186.

Van Mooy, B. A. S., and H. F. Fredricks (2010), Bacterial and eukaryotic intact polar lipids in the eastern subtropical South Pacific: Water-column distribution, planktonic sources, and fatty acid composition, *Geochim. Cosmochim. Acta*, *74*(22), 6499–6516, doi:10.1016/j.gca.2010.08.026.

Mopper, K., J. Zhou, K. Sri Ramana, U. Passow, H. Dam, and T. Drapeau (1995), The role of surface-active carbohydrates in the flocculation of a diatom bloom in a mesocosm, *Deep. Res. II*, *42*(1), 47–73.

Morris, H. S., V. H. Grassian, and A. V Tivanski (2015), Humidity-dependent surface tension measurements of individual inorganic and organic submicrometre liquid particles, *Chem. Sci.*, *6*, 3242–3247, doi:10.1039/C4SC03716B.

Morris, H. S., A. D. Estillore, O. Laskina, V. H. Grassian, and A. V. Tivanski (2016), Quantifying the hygroscopic growth of individual submicrometer particles with Atomic Force Microscopy, *Anal. Chem.*, *88*(7), 3647–3654, doi:10.1021/acs.analchem.5b04349.

Murphy, D. M., J. R. Anderson, P. K. Quinn, L. M. McInnes, F. J. Brechtel, S. M. Kreidenweis, A. M. Middlebrook, M. Pósfai, D. S. Thomson, and P. R. Buseck (1998), Influence of sea-salt on aerosol radiative properties in the Southern Ocean marine boundary layer, *Nature*, *392*(6671), 62–65, doi:10.1038/32138.

Murphy, D. M., A. M. Middlebrook, and M. Warshawsky (2003), Cluster analysis of data from the Particle analysis by Laser Mass Spectrometry (PALMS) Instrument, *Aerosol Sci. Technol.*, *37*(April 2014), 382–391, doi:10.1080/02786820300971.

Nash, D. G., T. Baer, and M. V. Johnston (2006), Aerosol mass spectrometry: An introductory review, *Int. J. Mass Spectrom.*, *258*(1–3), 2–12, doi:10.1016/j.ijms.2006.09.017.

Neubauer, K. R., M. V. Johnston, and A. S. Wexler (1997), On-line analysis of aqueous aerosols by laser desorption ionization, *Int. J. Mass Spectrom. Ion Process.*, *163*(1–2), 29–37, doi:10.1016/S0168-1176(96)04534-X.

Neubauer, K. R., M V Johnston, and A. S. Wexler (1998), Humidity effects on the mass spectra of single aerosol particles, *Atmos. Environ.*, *32*(14–15), 2521–2529, doi:10.1016/S1352-2310(98)00005-3.

Noble, C. A., and K. A. Prather (1996), Real-Time Measurement of Correlated Size and Composition Profiles of Individual Atmospheric Aerosol Particles, *Environ. Sci. Technol.*, *30*(9), 2667–2680, doi:10.1021/es950669j.

O'Dowd, C. D., M. C. Facchini, F. Cavalli, D. Ceburnis, M. Mircea, S. Decesari, S. Fuzzi, Y. J. Yoon, and J.-P. Putaud (2004), Biogenically driven organic contribution to marine aerosol, *Nature*, *431*(October), 676–680, doi:10.1038/nature02970.1.

O'Dowd, C. D., G. de Leeuw, C. D. O. Dowd, and G. De Leeuw (2007), Marine aerosol production: a review of the current knowledge, *Philos. Trans. R. Soc. A*, *365*, 1753–74, doi:10.1098/rsta.2007.2043.

O'Dowd, C. D., B. Langmann, S. Varghese, C. Scannell, D. Ceburnis, and M. C. Facchini (2008), A combined organic-inorganic sea-spray source function, *Geophys. Res. Lett.*, *35*, L01801, doi:10.1029/2007GL030331.

Orellana, M. V, P. A. Matrai, C. Leck, C. D. Rauschenberg, and A. M. Lee (2011), Marine microgels as a source of cloud condensation nuclei in the high Arctic, *Proc. Natl. Acad. Sci. U. S. A.*, *108*(33), 13612–13617, doi:10.1073/pnas.1102457108/-/DCSupplemental.www.pnas.org/cgi/doi/10.1073/pnas.1102457108.

Otten, P., F. Bruynseels, and R. Van Grieken (1987), Study of inorganic ammonium compounds in individual marine aerosol particles by Laser Microprobe Mass Spectrometry, *Anal. Chim. Acta*, *195*, 117–124.

Ovadnevaite, J., D. Ceburnis, G. Martucci, J. Bialek, C. Monahan, M. Rinaldi, M. C. Facchini, H. Berresheim, D. R. Worsnop, and C. O'Dowd. (2011), Primary marine organic aerosol: A dichotomy of low hygroscopicity and high CCN activity, *Geophys. Res. Lett.*, *38*(21), doi:10.1029/2011GL048869.

Paatero, P., and U. Tapper (1994), Positive matrix factorization: A non-negative factor model with optimal utilization of error estimates of data values, *Environmetrics*, *5*, 111–126.

Park, J. Y., S. Lim, and K. Park (2014), Mixing state of submicrometer sea spray particles enriched by insoluble species in bubble-bursting experiments, *J. Atmos. Ocean. Technol.*, *31*(1), 93–104, doi:10.1175/JTECH-D-13-00086.1.

Partanen, A.-I., E. M. Dunne, T. Bergman, A. Laakso, H. Kokkola, J. Ovadnevaite, L. Sogacheva, D. Baisnée, J. Sciare, A. Manders, C. O'Dowd, G. de Leeuw, and H. Korhonen (2014), Global modelling of direct and indirect effects of sea spray aerosol using a source function encapsulating wave state, *Atmos. Chem. Phys.*, *14*(4), 11731–11752, doi:10.5194/acpd-14-4537-2014.

Patterson, J. P., D. B. Collins, J. M. Michaud, J. L. Axson, C. M. Sultana, T. Moser, A. C. Dommer, J. Conner, V. H. Grassian, M. D. Stokes, G. B. Deane, J. E. Evans, M. D. Burkart, K. A. Prather, N. C. Gianneshi (2016), Sea spray aerosol structure and composition using Cryogenic Transmission Electron Microscopy, *ACS Cent. Sci.*, *2*, 40–47, doi:10.1021/acscentsci.5b00344.

Pegus, A., D. Kirkwood, D. B. Cairns, S. P. Armes, and A. J. Stace (2005), Depth profiling of sterically-stabilised polystyrene nanoparticles using laser ablation/ionisation mass spectrometric methods, *Phys Chem Chem Phys*, *7*(12), 2519–2525, doi:10.1039/b502837j.

Pemberton, J. E., and J. R. Chamberlain (2000), Raman spectroscopy of model membrane monolayers of dipalmitoylphosphatidic acid at the air-water interface using surface enhancement from buoyant thin silver films, *Biopolymers*, *57*, 103–116.

Petters, M. D., and S. M. Kreidenweis (2007), A single parameter representation of hygroscopic growth and cloud condensation nucleus activity, *Atmos. Chem. Phys.*, *7*, 1961–1971, doi:10.5194/acp-13-1081-2013.

Phares, D. J., K. P. Rhoads, A. S. Wexler, D. B. Kane, and M. V. Johnston (2001), Application of the ART-2a algorithm to Laser Ablation Aerosol Mass Spectrometry of particle standards, *Anal. Chem.*, *73*(10), 2338–2344, doi:10.1021/ac0015063.

Phares, D. J., K. P. Rhoads, and A. S. Wexler (2002), Performance of a single ultrafine particle mass spectrometer, *Aerosol Sci. Technol.*, *36*(5), 583–592, doi:10.1080/02786820252883829.

Pilinis, C., S. N. Pandis, and J. H. Seinfeld (1995), Sensitivity of direct climate forcing by atmospheric aerosols to aerosol size and composition, *J. Geophys. Res.*, *100*(D9), 18739, doi:10.1029/95JD02119.

Pöhlker, C., K. T. Wiedemann, D. Sinha, M. Shiraiwa, S. S. Gunthe, M. Smith, H. Su, P. Artaxo, Q. Chen, Y. Cheng, W. Elbert, M. K. Gilles, A. L. D. Kilcoyne, R. C. Moffet, M. Weigand, S. T. Martin, U. Poschl, and M. O. Andreae (2012), Biogenic potassium salt particles as seeds for secondary organic aerosol in the Amazon, *Science, 337*, 1075–1078.

Popovitz-Biro, R., M. Lahav, and L. Leiserowitz (1991), Ice nucleation: a test to probe the packing of amphiphilic alcohols at the oil-water interface, *J. Am. Chem. Soc.*, *113*(4), 8943–8944, doi:10.1021/ja00023a050.

Pöschl, U. (2005), Atmospheric aerosols: Composition, transformation, climate and health effects, *Angew. Chem. Int. Ed. Engl.*, *44*, 7520–40, doi:10.1002/anie.200501122.

Posfai, M., J. R. Anderson, and P. R. Buseck (1995), Compositional variations of sea-salt-mode aerosol particles from the North Atlantic, *J. Geophys. Res.*, *100*(D11), 23063–23074.

Prather, K. A., T. H. Bertram, V. H. Grassian, G. B. Deane, M. D. Stokes, P. J. DeMott, L. I. Aluwihare, B. P. Palenik, F. Azam, J. H. Seinfeld, R. C. Moffet, M. J. Molina, C. D. Cappa, F. M. Geiger, G. C. Roberts, L. M. Russell, A. P. Ault, J. Baltrusaitis, D. B. Collins, C. E. Corrigan, L. A. Cuadra-Rodriguez, C. J. Ebben, S. D. Forestieri, T. L. Guasco, S. P. Hersey, M. J. Kim, W. F. Lambert, R. L. Modini, W. Mui, B. E. Pedler, M. J. Ruppel, O. S. ryder, N G. Schoepp, R. C. Sullivan, and D. Zhao (2013), Bringing the ocean into the laboratory to probe the chemical complexity of sea spray aerosol, *Proc. Natl. Acad. Sci. U. S. A.*, *110*(19), 7550–7555, doi:10.1073/pnas.1300262110.

Pratt, K. A., L. E. Hatch, and K. A. Prather (2009a), Seasonal volatility dependence of ambient particle phase amines., *Environ. Sci. Technol.*, *43*(14), 5276–81.

Pratt, K. A., P. J. DeMott, J. R. French, Z. Wang, D. L. Westphal, A. J. Heymsfield, C. H. Twohy, A. J. Prenni, and K. A. Prather (2009b), In situ detection of biological particles in cloud ice-crystals, *Nat. Geosci.*, *2*(6), 398–401, doi:10.1038/ngeo521.

Pratt, K. A., and K. A. Prather (2009), Size and chemical composition measurements of aged urban Aerosols, *Environ. Sci. Technol.*, *43*(21), 8276–8282.

Pruppacher, H. R., and J. D. Klett (1997), *Microphysics of Clouds and Precipitation*, 2nd ed., Springer, New York.

Qin, X., and K. A. Prather (2006), Impact of biomass emissions on particle chemistry during the California Regional Particulate Air Quality Study, *Int. J. Mass Spectrom.*, *258*(1–3), 142–150, doi:10.1016/j.ijms.2006.09.004.

Qin, X., K. A. Pratt, L. G. Shields, S. M. Toner, and K. A. Prather (2012), Seasonal comparisons of single-particle chemical mixing state in Riverside, CA, *Atmos. Environ.*, *59*, 587–596, doi:10.1016/j.atmosenv.2012.05.032.

Quinn, P. K., T. S. Bates, K. S. Schulz, D. J. Co, A. A. Frossard, L. M. Russell, W. C. Keene, and D. J. Kieber (2014), Contribution of sea surface carbon pool to organic matter enrichment in sea spray aerosol, *Nat. Geosci.*, *7*(March), 228–232, doi:10.1038/NGEO2092.

Quinn, P. K., D. B. Collins, V. H. Grassian, K. A. Prather, and T. S. Bates (2015), Chemistry and related properties of freshly emitted sea spray aerosol, *Chem. Rev.*, *115*(4383–4399), 150406123611007, doi:10.1021/cr500713g.

Raes, F., R. Van Dingenen, E. Vignati, J. Wilson, J.-P. Putaud, J. H. Seinfeld, and P. Adams (2000), Formation and cycling of aerosols in the global troposphere, *Atmos. Environ.*, *34*, 4215–4240, doi:10.1016/S1352-2310(00)00239-9.

Ratte, M., C. Plass-Dulmer, R. Koppmann, and J. Rudolph (2011), Horizontal and vertical profiles of light hydrocarbons in sea water related to biological, chemical and physical parameters, *Tellus B*, *47*, 607–623.

Rebotier, T. P., and K. A. Prather (2007), Aerosol time-of-flight mass spectrometry data analysis: a benchmark of clustering algorithms., *Anal. Chim. Acta*, *585*(1), 38–54, doi:10.1016/j.aca.2006.12.009.

Reents, W. D., and M. J. Schabel (2001), Measurement of individual particle atomic composition by aerosol mass spectrometry, *Anal. Chem.*, *73*(22), 5403–5414, doi:10.1021/ac010436c.

Reinard, M. S., and M. V Johnston (2008), Ion formation mechanism in laser desorption ionization of individual nanoparticles., *J. Am. Soc. Mass Spectrom.*, *19*(3), 389–399, doi:10.1016/j.jasms.2007.11.017.

Riemann, L., G. F. Steward, and F. Azam (2000), Dynamics of bacterial community Composition and activity during a mesocosm diatom bloom, *Appl. Environ. Microbiol.*, *66*(2), 578–587, doi:10.1128/AEM.66.2.578-587.2000.Updated.

Rinaldi, M., S. Decesari, E. Finessi, L. Giulianelli, C. Carbone, S. Fuzzi, C. D. O'Dowd, D. Ceburnis, and M. C. Facchini (2010), Primary and secondary organic marine aerosol and pceanic biological activity: Recent results and new perspectives for future studies, *Adv. Meteorol.*, 310682, doi:10.1155/2010/310682.

Rinaldi, M., S. Fuzzi, S. Decesari, S. Marullo, R. Santoleri, A. Provenzale, J. von Hardenberg, D. Ceburnis, A. Vaishya, C. D. O'Dowd, and M. C. Facchini (2013), Is chlorophyll- a the best surrogate for organic matter enrichment in submicron primary marine aerosol?, *J. Geophys. Res. Atmos.*, *118*(10), 4964–4973, doi:10.1002/jgrd.50417.

Rogers, D. C., P. J. Demott, and S. M. Kreidenweis (2001), Airborne measurements of tropospheric ice-nucleating aerosol particles in the Arctic spring, *J. Geophys. Res.*, *106*(D14), 15053–15063, doi:10.1029/2000JD900790.

Rollgen, F. W., U. Giessmann, and R. Stoll (1982), On the formation of molecular ions from liquids and solids, *Nucl. Instruments Methods*, *198*, 93–99.

Russell, L. M., L. N. Hawkins, A. A. Frossard, P. K. Quinn, and T. S. Bates (2010), Carbohydrate-like composition of submicron atmospheric particles and their production from ocean bubble bursting, *Proc. Natl. Acad. Sci.*, *107*(15), 6652–6657, doi:10.1073/pnas.0908905107.

Russell, S. C. (2009), Microorganism characterization by single particle mass spectrometry., *Mass Spectrom. Rev.*, *28*(2), 376–387, doi:10.1002/mas.20198.

Russell, S. C., G. Czerwieniec, and C. Lebrilla (2004), Toward understanding the ionization of biomarkers from micrometer particles by bio-aerosol mass spectrometry, *J. Am. Soc. Mass Spectrom.*, *15*(6), 900–909, doi:10.1016/j.jasms.2004.02.013.

Ryder, O. S., N. R. Campbell, H. Morris, S. Forestieri, M. J. Ruppel, C. Cappa, A. Tivanski, K. Prather, and T. H. Bertram (2015), Role of organic coatings in regulating N2O5 reactive uptake to sea spray aerosol, *J. Phys. Chem. A*, *119*(48), 11683–11692, doi:10.1021/acs.jpca.5b08892.

Sansonetti, J. E., and W. C. Martin (2005), Handbook of basic atomic spectroscopic data, *J. Phys. Chem. Ref. Data*, *34*(4), 1559–2259, doi:10.1063/1.1800011.

Saxena, P., L. M. Hildemann, P. H. McMurry, and J. H. Seinfeld (1995), Organics alter hygroscopic behavior of atmospheric particles, *J. Geophys. Res.*, *100*(D9), 18755, doi:10.1029/95JD01835.

Schnell, R. C. (1977), Ice nuclei in seawater, fog water and marine air off the coast of Nova Scotia: Summer 1975, *J. Atmos. Sci.*, *34*(8), 1299–1305, doi:10.1175/1520-0469(1977)034<1299:INISFW>2.0.CO;2.

Schoolcraft, T. A., G. S. Constable, L. V Zhigilei, and B. J. Garrison (2000), Molecular dynamics simulation of the laser disintegration of aerosol particles, *Anal. Chem.*, *72*(21), 5143–5150.

Schoolcraft, T. A., G. S. Constable, B. Jackson, L. V Zhigilei, and B. J. Garrison (2001), Molecular dynamics simulations of laser disintegration of amorphous aerosol particles with spatially nonuniform absorption, *Nucl. Instruments Methods Phys. Res. B*, *180*, 245–250.

Schwier, A. N., C. Rose, E. Asmi, A. M. Ebling, W. M. Landing, S. Marro, M.-L. Pedrotti, A. Sallon, F. Iuculano, S. Agusti, A. Tsiola, P. Pitta, J. Louis, C. Guieu, F. Gazeau, and K. Sellegri (2015), Primary marine aerosol emissions from the Mediterranean Sea during pre-bloom and oligotrophic conditions: Correlations to seawater chlorophyll a from a mesocosm study, *Atmos. Chem. Phys.*, *15*, 7961–7976, doi:10.5194/acp-15-7961-2015.

Scott, B. J. C. (1975), The preparation of water for surface-clean fluid mechanics, *J. Fluid Mech.*, *69*(2), 339–351.

Sellegri, K., C. D. O'Dowd, Y. J. Yoon, S. G. Jennings, and G. de Leeuw (2006), Surfactants and submicron sea spray generation, *J. Geophys. Res. Atmos.*, *111*(22), 1–12, doi:10.1029/2005JD006658.

She, C. Y., and A. T. Tu (1974), Laser Raman scattering of glucosamine N-acetylglucosamine, and glucuronic acid, *Biochim. Biophys. Acta.*, *372*, 345–357.

Sierau, B., R. Y.-W. W. Chang, C. Leck, J. Paatero, and U. Lohmann (2014), Single-particle characterization of the high-Arctic summertime aerosol, *Atmos. Chem. Phys.*, *14*(14), 7409–7430, doi:10.5194/acp-14-7409-2014.

Silva, P., and K. Prather (2000), Interpretation of mass spectra from organic compounds in aerosol time-of-flight mass spectrometry, *Anal. Chem.*, *72*(15), 3553–62.

Silva, P. J. (2000), Source profiling and apportionment of airborne particles: A new approach using Aerosol Time-of-Flight Mass Spectrometry, University of California, Riverside.

Silva, P. J., K. Prather, C. A. Noble, and K. A. Prather (1999), Size and chemical characterization of individual particles resulting from biomass burning of local Southern California species, *Environ. Sci. Technol.*, *33*(18), 3068–3076, doi:10.1021/es980544p.

Song, X.-H., and P. K. Hopke (1999), Classification of single particles analyzed by ATOFMS using an Artificial Neural Network, ART-2A, *Anal. Chem.*, *71*(4), 860–865.

Spencer, M. T., and K. A. Prather (2006), Using ATOFMS to determine OC/EC mass fractions in particles, *Aerosol Sci. Technol.*, *40*(8), 585–594, doi:10.1080/02786820600729138.

Spiker, R. C., and I. W. Levin (1975), Raman spectra and vibrational assignments for dipalmitoyl phosphatidylcholine and structurally related molecules, *Biochim. Biophys. Acta.*, *388*, 361–373.

Spracklen, D. V., S. R. Arnold, J. Sciare, K. S. Carslaw, and C. Pio (2008), Globally significant oceanic source of organic carbon aerosol, *Geophys. Res. Lett.*, *35*(12), L12811, doi:10.1029/2008GL033359.

Srivastava, A., M. E. Pitesky, P. T. Steele, H. J. Tobias, D. P. Fergenson, J. M. Horn, S. C. Russell, G. A. Czerwieniec, C. B. Lebrilla, E. E. Gard, and M. Frank (2005), Comprehensive assignment of mass spectral signatures from individual spores in matrix-free laser desorption/ionization bioaerosol mass spectrometry, *Anal. Chem.*, *77*(10), 3315–3323, doi:10.1021/ac048298p.

Steele, P. T., H. J. Tobias, D. P. Fergenson, M. E. Pitesky, J. M. Horn, G. A. Czerwieniec, S. C. Russell, C. B. Lebrilla, E. E. Gard, and M. Frank (2003), Laser power dependence of mass spectral signatures from individual bacterial spores in bioaerosol mass spectrometry, *Anal. Chem.*, *75*(20), 5480–5487.

Steele, P. T., A. Srivastava, M. E. Pitesky, D. P. Fergenson, H. J. Tobias, E. E. Gard, and M. Frank (2005), Desorption / ionization fluence thresholds and improved mass spectral consistency measured using a flattop laser profile in the bioaerosol mass spectrometry of single bacillus endospores, *Anal. Chem.*, *77*(22), 7448–7454.

Stier, P., J. Feichter, E. Roeckner, S. Kloster, and M. Esch (2005), The evolution of the global aerosol system in a transient climate simulation from 1860 to 2100, *Atmos. Chem. Phys. Discuss.*, *5*(6), 12775–12814, doi:10.5194/acpd-5-12775-2005.

Stocker, T. F., D. Qin, G. K. Plattner, M. Tignor, S. K. Allen, J. Boschung, A. Nauels, Y. Xia, V. Bex, and P. M. Midgley (2013), *IPCC, 2013: Summary for Policymakers. IPCC WG1 5th Assessment Report.*

Stokes, M. D., G. B. Deane, K. Prather, T. H. Bertram, M. J. Ruppel, O. S. Ryder, J. M. Brady, and D. Zhao (2013), A Marine Aerosol Reference Tank system as a breaking wave analogue for the production of foam and sea-spray aerosols, *Atmos. Meas. Tech.*, *6*, 1085–1094, doi:10.5194/amt-6-1085-2013.

Su, Y., M. F. Sipin, H. Furutani, and K. A. Prather (2004), Development and characterization of an aerosol time-of-flight mass spectrometer with increased detection efficiency, *Anal. Chem.*, *76*(3), 712–719, doi:10.1021/ac034797z.

Sullivan, R. C., and K. A. Prather (2005), Recent advances in our understanding of atmospheric chemistry and climate made possible by on-line aerosol analysis instrumentation, *Anal. Chem.*, *77*(12), 3861–3886, doi:10.1021/ac050716i.

Sultana, C. M., H. Al-Mashat, and K. A. Prather (2017a), Expanding single particle mass spectrometer analyses for the identification of microbe signatures in sea spray aerosols, *Submitt. to Anal. Chem.*

Sultana, C. M., G. C. Cornwell, P. Rodriguez, and K. A. Prather (2017b), FATES: a flexible analysis toolkit for the exploration of single-particle mass spectrometer data, *Atmos. Meas. Tech.*, *10*, 1323–1334, doi:10.5194/amt-10-1323-2017.

Sultana, C. M., D. B. Collins, and K. A. Prather (2017c), The effect of structural heterogeneity in chemical composition on online single particle mass spectrometry analysis of sea spray Aerosol Particles, *Environ. Sci. Technol.*, *51*, 3660–3668, doi:10.1021/acs.est.6b06399.

Suttle, C. A (2007), Marine viruses--major players in the global ecosystem., *Nat. Rev. Microbiol.*, *5*(10), 801–812, doi:10.1038/nrmicro1750.

Tang, C. Y., Z. Huang, and H. C. Allen (2010), Binding of Mg(2+) and Ca(2+) to palmitic acid and deprotonation of the COOH headgroup studied by vibrational sum frequency generation spectroscopy., *J. Phys. Chem. B*, *114*(51), 17068–76, doi:10.1021/jp105472e.

Tang, C. Y., Z. Huang, and H. C. Allen (2011), Interfacial water structure and effects of Mg2+ and Ca2+ binding to the COOH headgroup of a palmitic acid monolayer studied by sum frequency spectroscopy., *J. Phys. Chem. B*, *115*(1), 34–40, doi:10.1021/jp1062447.

Textor, C., M. Schulz, S. Guibert, S. Kinne, Y. Balkanski, S. Bauer, T. Berntsen, T. Berglen, O. Boucher, M. Chin, F. Dentener, T. Diehl, R. Easter, H. Feichter, D. Fillmore, S. Ghan, P. Ginoux, S. Gong, A. Grini, J. Hendricks, L. Horowitz, P. Huang, I. Isaksen, T. Iversen, S. Kloster, D. Koch, A. Kirkevag, J. E. Kristjansson, M. Krol, A. Lauer, J. F. Lamarque, X. Liu, V. Montanaro, G. Myhre, J. Penner, G. Pitari, S. Reddy, Ø. Seland, P. Stier, T.

Takemura, and X. Tie. (2006), Analysis and quantification of the diversities of aerosol life cycles within AeroCom, *Atmos. Chem. Phys.*, *6*, 1777–1813, doi:10.5194/acp-6-1777-2006.

Thomson, D. S., M. E. Schein, and D. M. Murphy (2000), Particle analysis by laser mass spectrometry WB-57F instrument overview, *Aerosol Sci. Technol.*, *33*(1–2), 153–169, doi:10.1080/027868200410903.

Tobias, H. J., M. E. Pitesky, D. P. Fergenson, P. T. Steele, J. Horn, M. Frank, and E. E. Gard (2006), Following the biochemical and morphological changes of Bacillus atrophaeus cells during the sporulation process using Bioaerosol Mass Spectrometry, *J. Microbiol. Methods*, *67*, 56–63, doi:10.1016/j.mimet.2006.03.001.

Tong, H. J., Z. G. Qian, P. Reid Jonathan, and Y. H. Zhang (2011), High temporal and spatial resolution measurements of the rapid efflorescence of sea salt droplets, *Wuli Huaxue Xuebao/ Acta Phys. - Chim. Sin.*, *27*(11), 2521–2527.

Trimborn, A., K.-P. Hinz, and B. Spengler (2000), Online analysis of atmospheric particles with a transportable laser mass spectrometer, *Aerosol Sci. Technol.*, *33*(1–2), 191–201, doi:10.1080/027868200410921.

Tseng, R.-S., J. T. Viechnicki, R. A. Skop, and J. W. Brown (1992), Sea-to-air transfer of surface-active organic compounds by bursting bubbles, *J. Geophys. Res.*, *97*(C4), 5201–5206, doi:10.1029/91JC00954.

Ulbrich, I. M., M. R. Canagaratna, Q. Zhang, D. R. Worsnop, and J. L. Jimenez (2009), Interpretation of organic components from Positive Matrix Factorization of aerosol mass spectrometric data, *Atmos. Chem. Phys.*, *9*, 291–2918.

Van Breemen, R. B., M. Snow, and R. J. Cotter (1983), Time-resolved laser desorption mass spectrometry. I. Desorption of preformed ions, *Int. J. Mass Spectrom. Ion Phys.*, *49*(1), 35–50, doi:10.1016/0020-7381(83)85074-8.

Van Pinxteren, M., C. Müller, Y. Linuma, C. Stolle, and H. Herrmann (2012), Chemical characterization of dissolved organic compounds from coastal sea surface microlayers, *Environ. Sci. Technol.*, *46*, 10455–10462.

Van Vaeck, L., J. Bennett, P. Van Epsen, E. Schweikert, R. Gijbels, F. Adams, and W. Lauwers (1989a), Structural characterization of organic molecules by negative ions in laser mass spectrometry, *Org. Mass Spectrom.*, *24*, 782–796.

Van Vaeck, L., J. Bennett, P. Van Espen, E. Schweikert, R. Gijbels, F. Adams, and W. Lauwers (1989b), Structural characterization of organic molecules by negative ions in laser microprobe mass spectrometry- Part 2--Salts, *Org. Mass Spectrom.*, *24*, 797–806.

Vaishya, A., J. Ovadnevaite, J. Bialek, S. G. Jennings, D. Ceburnis, and C. D. O'Dowd (2013), Bistable effect of organic enrichment on sea spray radiative properties, *Geophys. Res. Lett.*, *40*(24), 6395–6398, doi:10.1002/2013GL058452.

Vali, G. (1971), Quantitative evaluation of experimental results and the heterogeneous freezing nucleation of supercooled liquids, *J. Atmos. Sci.*, *28*, 402–409, doi:10.1175/1520-0469(1971)028<0402:QEOERA>2.0.CO;2.

Vera, C., A. Trimborn, K. Hinz, and B. Spengler (2005), Initial velocity distributions of ions generated by in-flight laser desorption / ionization of individual polystyrene latex microparticles as studied by the delayed ion extraction method, *Rapid Commun. Mass Spectrom.*, *19*, 133–146, doi:10.1002/rcm.1753.

Vignati, E., M. C. Facchini, M. Rinaldi, C. Scannell, D. Ceburnis, J. Sciare, M. Kanakidou, S. Myriokefalitakis, F. Dentener, and C. D. O'Dowd (2010), Global scale emission and distribution of sea-spray aerosol: Sea-salt and organic enrichment, *Atmos. Environ.*, *44*(5), 670–677, doi:10.1016/j.atmosenv.2009.11.013.

Wade, E. E., G. R. Farquar, P. T. Steele, E. L. McJimpsey, C. B. Lebrilla, and D. P. Fergenson (2008), Wavelength and size dependence in single particle laser aerosol mass spectra, *J. Aerosol Sci.*, *39*(8), 657–666, doi:10.1016/j.jaerosci.2008.03.007.

Wang, X., C. M. Sultana, J. Trueblood, T. C. J. Hill, F. Malfatti, C. Lee, O. Laskina, K. A. Moore, C. M. Beall, C. S. McCluskey, G. C. Cornwell, Y. Zhou, J. L. Cox, M. A. Pendergraft, M. V. Santander, T. H. Bertram, C. D. Cappa, F. Azam, P. J. DeMott, V. H. Grassian, and K. A. Prather (2015), Microbial control of sea spray aerosol composition: A tale of two blooms, *ACS Cent. Sci.*, *1*(3), 124–131, doi:10.1021/acscentsci.5b00148.

Weckesser, J., G. Drews, and I. Fromme (1972), Chemical analysis of and degradation studies on cell wall lipopolysaccharide of Rhodopseudomonas capsulata, *J. Bacteriol.*, *109*, 1106.

Weiss, M., P. J. T. Verheijen, J. C. M. Marijnissen, and B. Scarlett (1997), On the performance of an on-line time-of-flight mass spectrometer for aerosols, *J. Aerosol Sci.*, *28*(1), 159–171, doi:10.1016/S0021-8502(96)00067-5.

Wenzel, R. J., and K. A. Prather (2004), Improvements in ion signal reproducibility obtained using a homogeneous laser beam for on-line laser desorption/ionization of single particles, *Rapid Commun. Mass Spectrom.*, *18*, 1525–1533, doi:10.1002/rcm.1509.

Wernand, M. R., H. J. van der Woerd, and W. W. C. Gieskes (2013), Trends in ocean colour and chlorophyll concentration from 1889 to 2000, Worldwide, *PLoS One*, *8*(6), doi:10.1371/journal.pone.0063766.

Westervelt, D. M., R. H. Moore, A. Nenes, and P. J. Adams (2012), Effect of primary organic sea spray emissions on cloud condensation nuclei concentrations, *Atmos. Chem. Phys.*, *12*(1), 89–101, doi:10.5194/acp-12-89-2012.

Wilcox, R. M., and J. A. Fuhrman (1994), Bacterial viruses in coastal seawater: Lytic rather than lysogenic production, *Mar. Ecol. Prog. Ser.*, *114*(1–2), 35–46, doi:10.3354/meps114035.

Wilson, T. W., L. A. Ladino, P. A. Alpert, M. N. Breckels, I. M. Brooks, J. Browse, S. M. Burrows, K. S. Carslaw, J. Alex Huffman, C. Judd, W. P. Kilthau, R. H. Mason, G.

McFiggans, L. A. Miller, J. J. Na ́jera, E. Polishchuk, S. Rae, C. L. Schiller, M. Si, J. Vergara Temprado, T. F. Whale, J. P. S. Wong, O. Wurl, J. D. Yakobi-Hancock, J. P. D. Abbatt, J. Y. Aller, A. K. Bertram, D. A. Knopf, and B. J. Murray (2015), A marine biogenic source of atmospheric ice-nucleating particles, *Nature*, *525*(7568), 234–238, doi:10.1038/nature14986.

Wise, M. E., E. J. Freney, C. A. Tyree, J. O. Allen, S. T. Martin, L. M. Russell, and P. R. Buseck (2009), Hygroscopic behavior and liquid-layer composition of aerosol particles generated from natural and artificial seawater, *J. Geophys. Res. Atmos.*, *114*(3), 1–8, doi:10.1029/2008JD010449.

Woods, E. I., G. D. Smith, R. E. Miller, and T. Baer (2002), Depth profiling of heterogeneously mixed aerosol particles using single-particle mass spectrometry, *Anal. Chem.*, *74*(7), 1642–1649.

Wu, H., V. J. Volponi, A. E. Oliver, A. N. Parikh, B. A. Simmons, and S. Singh (2011), In vivo lipidomics using single-cell Raman spectroscopy, *Proc. Natl. Acad. Sci.*, *108*, 3809–3814.

Wurl, O., E. Wurl, L. Miller, K. Johnson, and S. Vagle (2011), Formation and global distribution of sea-surface microlayers, *Biogeosciences*, *8*(1), 121–135, doi:10.5194/bg-8-121-2011.

Xiao, H. S., J. L. Dong, L. Y. Wang, L. J. Zhao, F. Wang, and Y. H. Zhang (2008), Spatially resolved micro-raman observation on the phase separation of effloresced sea salt droplets, *Environ. Sci. Technol.*, *42*(23), 8698–8702, doi:10.1021/es801181f.

Yergeyt, A. L., and R. J. Cotter (1982), Thermal desorption mass spectrometry of organic salts, *Biomed. Mass Spectrom.*, *9*(7), 286–292.

Yoon, Y. J., D. Ceburnis, F. Cavalli, O. Jourdan, J. P. Putaud, M. C. Facchini, S. Decesari, S. Fuzzi, K. Sellegri, S. G. Jennings, and C. D. O’Dowd (2007), Seasonal characteristics of the physicochemical properties of North Atlantic marine atmospheric aerosols, *J. Geophys. Res.*, *112*(D4), D04206, doi:10.1029/2005JD007044.

Zábori, J., R. Krejci, J. Ström, P. Vaattovaara, A. M. L. Ekman, M. E. Salter, E. M. Mårtensson, and E. D. Nilsson (2013), Comparison between summertime and wintertime Arctic Ocean primary marine aerosol properties, *Atmos. Chem. Phys.*, *13*(9), 4783–4799, doi:10.5194/acp-13-4783-2013.

Zawadowicz, M. A., K. D. Froyd, D. M. Murphy, and D. J. Cziczo (2016), Proper identification of primary biological aerosol particles using single particle mass spectrometry, *Atmos. Chem. Phys. Discuss.*, doi:10.5194/acp-2016-1119.

Zelenyuk, A., and D. Imre (2005), Single particle laser ablation time-of-flight mass spectrometer: an introduction to SPLAT, *Aerosol Sci. Technol.*, *39*(6), 554–568, doi:10.1080/027868291009242.

Zelenyuk, A., D. Imre, Y. Cai, K. Mueller, Y. Han, and P. Imrich (2006), SpectraMiner, an interactive data mining and visualization software for single particle mass spectroscopy: A laboratory test case, *Int. J. Mass Spectrom.*, *258*, 58–73, doi:10.1016/j.ijms.2006.06.015.

Zelenyuk, A., D. Imre, L. A. Cuadra-Rodriguez, and B. Ellison (2007), Measurements and interpretation of the effect of a soluble organic surfactant on the density, shape and water uptake of hygroscopic particles, *J. Aerosol Sci.*, *38*, 903–923, doi:10.1016/j.jaerosci.2007.06.006.

Zelenyuk, A., D. Imre, E. J. Nam, Y. Han, and K. Mueller (2008a), ClusterSculptor: Software for expert-steered classification of single particle mass spectra, *Int. J. Mass Spectrom.*, *275*, 1–10, doi:10.1016/j.ijms.2008.04.033.

Zelenyuk, A., Y. Juan, S. Chen, R. A. Zaveri, and D. Imre (2008b), “Depth-profiling” and quantitative characterization of the size, composition, shape, density, and morphology of fine particles with SPLAT, a single-particle mass spectrometer, *J. Phys. Chem. A*, *112*(4), 669–671, doi:10.1021/jp077308y.

Zelenyuk, A., J. Yang, E. Choi, and D. Imre (2009), SPLAT II: an aircraft compatible, ultra-sensitive, high precision instrument for in-situ characterization of the size and composition of fine and ultrafine particles, *Aerosol Sci. Technol.*, *43*(5), 411–424, doi:10.1080/02786820802709243.

Zelenyuk, A., D. Imre, J. Wilson, Z. Zhang, J. Wang, and K. Mueller (2015), Airborne single particle mass spectrometers (SPLAT II & miniSPLAT) and new software for data visualization and analysis in a geo-spatial context, *J. Am. Soc. Mass Spectrom.*, *26*(2), 257–270, doi:10.1007/s13361-014-1043-4.

Zhang, G., B. Han, X. Bi, S. Dai, W. Huang, D. Chen, X. Wang, G. Sheng, J. Fu, and Z. Zhou (2015), Characteristics of individual particles in the atmosphere of Guangzhou by single particle mass spectrometry, *Atmos. Res.*, *153*, 286–295, doi:10.1016/j.atmosres.2014.08.016.

Zhang, T., M. G. Cathcart, A. S. Vidalis, and H. C. Allen (2016), Cation effects on phosphatidic acid monolayers at various pH conditions, *Chem. Phys. Lipids*, *200*, 24–31, doi:10.1016/j.chemphyslip.2016.06.001.

Zhang, X., P. Massoli, P. K. Quinn, T. S. Bates, and C. D. Cappa (2014), Hygroscopic growth of submicron and supermicron aerosols in the marine boundary layer, *J. Geophys. Res. Atmos.*, *119*, 8384–8399, doi:10.1002/2013JD021213.